ABSTRACT

Title of Dissertation: THE ROLE OF THE INDIAN OCEAN SECTOR AND SEA SURFACE SALINITY FOR PREDICTION OF THE COUPLED INDO-PACIFIC SYSTEM

Eric C. Hackert, Doctor of Philosophy, 2016

Dissertation directed by: Professor Antonio J. Busalacchi
Department of Atmospheric and Oceanic Sciences

The purpose of this dissertation is to evaluate the potential downstream influence of the Indian Ocean (IO) on El Niño/Southern Oscillation (ENSO) forecasts through the oceanic pathway of the Indonesian Throughflow (ITF), atmospheric teleconnections between the IO and Pacific, and assimilation of IO observations. Also the impact of sea surface salinity (SSS) in the Indo-Pacific region is assessed to try to address known problems with operational coupled model precipitation forecasts. The ITF normally drains warm fresh water from the Pacific reducing the mixed layer depths (MLD). A shallower MLD amplifies large-scale oceanic Kelvin/Rossby waves thus giving ~10% larger response and more realistic ENSO sea surface temperature (SST) variability compared to observed when the ITF is open. In order to isolate the impact of the IO sector atmospheric teleconnections to ENSO, experiments are contrasted that selectively couple/decouple the interannual forcing in the IO. The interannual variability of IO SST

forcing is responsible for 3 month lagged widespread downwelling in the Pacific, assisted by off-equatorial curl, leading to warmer NINO3 SST anomaly and improved ENSO validation (significant from 3-9 months). Isolating the impact of observations in the IO sector using regional assimilation identifies large-scale warming in the IO that acts to intensify the easterlies of the Walker circulation and increases pervasive upwelling across the Pacific, cooling the eastern Pacific, and improving ENSO validation ($r \sim 0.05$, RMS~0.08^{o}C). Lastly, the positive impact of more accurate fresh water forcing is demonstrated to address inadequate precipitation forecasts in operational coupled models. Aquarius SSS assimilation improves the mixed layer density and enhances mixing, setting off upwelling that eventually cools the eastern Pacific after 6 months, counteracting the pervasive warming of most coupled models and significantly improving ENSO validation from 5-11 months. In summary, the ITF oceanic pathway, the atmospheric teleconnection, the impact of observations in the IO, and improved Indo-Pacific SSS are all responsible for ENSO forecast improvements, and so each aspect of this study contributes to a better overall understanding of ENSO. Therefore, the upstream influence of the IO should be thought of as integral to the functioning of ENSO phenomenon.

THE ROLE OF INDIAN OCEAN SECTOR AND SEA SURFACE SALINITY FOR PREDICTIONS OF THE COUPLED INDO-PACIFIC SYSTEM

by

Eric C. Hackert

Dissertation submitted to the Faculty of the Graduate School of the
University of Maryland, College Park, in partial fulfillment
of the requirements for the degree of
Doctor of Philosophy
2016

Advisory Committee:

Professor Antonio J. Busalacchi, Chair
Dr. Phillip Arkin
Professor James Carton
Professor Raghu Murtugudde
Professor Michael Evans, Dean's Representative

Acknowledgements

First and foremost, I would like to thank Dr. Busalacchi for his unfailing encouragement to follow my research interests, for guiding my professional career, and allowing me the scientific freedom to pursue the PhD research. In addition, I would like to thank my research committee, Drs. Arkin, Carton, Evans, and Murtugudde, for their helpful comments to improve this dissertation. I would like to thank all the many colleagues, post-docs, and visiting scientists who mentored me to improve my research skills over the years. In particular, I would like to thank Joaquim Ballabrera-Poy who provided much of the data assimilation software and my longtime officemate and friend, Jim Beauchamp. In addition, I would like to thank Dr. Fred Kucharski who provided all software and guidance on implementing SPEEDY into our coupled model, Dr. Hugo Berbery who assisted with atmospheric model questions, and Stephanie Schollaert Uz who shepherded me through the student aspects of the PhD process. I would also like to acknowledge NASA for supporting much of the research contained in this dissertation (NASA Grants NNX13AM61G, NN09AU74G, NNX09AF41G, and NNX16AH62G) and the Department of Atmospheric and Oceanic Sciences for initiating the Accomplished Scientists Program. I am especially grateful to my parents who instilled in me a scientific curiosity and a strong work ethic. Last but not least I'd like to thank my wife, Sandra, who has patiently encouraged me to pursue my goals and remains the most important blessing in my life.

Table of Contents

List of Tables

List of Figures

List of Abbreviations

AGCM – atmospheric general circulation model
AQ – Aquarius
AQ@IS – Aquarius data at in situ locations and time
ARPEGE - Action de Recherche Petite Echelle Grande Echelle, (research project on small and large scales)
AS – Arabian Sea
ASSIM_SL_SST_SSS_T_z_S_z - experiment that assimilates sea level, sea surface temperature, sea surface salinity and subsurface temperature and salinity
ASSIM_SL_SST_SSS_T_z_S_z_MASKIND - experiment that assimilates sea level, sea surface temperature, sea surface salinity and subsurface temperature and salinity only in the Pacific
ASSIM_T_z - experiment that assimilates subsurface temperature
ASSIM_Tz_SSS_{AQ} - experiment that assimilates subsurface temperature and Aquarius sea surface salinity
ASSIM_Tz_$SSS_{AQ@IS}$ - experiment that assimilates subsurface temperature and optimal interpolation product created from Aquarius sea surface salinity subsampled at in situ locations
ASSIM_T_z_SSS_{IS} - experiment that assimilates subsurface temperature and weekly in situ near surface salinity optimal interpolation product
ASSIM_T_z_SSS_{ISMON} - experiment that assimilates subsurface temperature and monthly in situ near surface salinity optimal interpolation product
AVHRR – advanced very high resolution radiometer
AVISO – Archiving Validation and Interpretation of Satellite Oceanographic Center
BLT – barrier layer thickness
BOB – Bay of Bengal
CFSRR – Climate Forecast System Reanalysis Reforecast
CFSV2 – Climate Forecast System version 2
CLIM_PAC, CLIM_IO – experiment with climatological SST forcing throughout Indo-Pacific region
CLIM_PAC, INT_IO – experiment with climatological forcing in the Pacific and interannual SST forcing in the Indian Ocean
CMT – cumulus momentum transport
Cryosat2 – CRYosphere SATellite 2
CTD – Conductivity Temperature Depth (ocean profile data)
D20 – depth of the 20^{o}C isotherm (depth of thermocline)
df – effective degrees of freedom
DECOUPIO – decoupled Indian Ocean
DMI – Dipole Mode Index
ECHAM – ECMWF/Hamburg atmospheric model
ECMWF – European Center for Medium Range Weather Forecasts
EIO – eastern Indian Ocean
ENSO – El Niño/Southern Oscillation
Envisat – environmental satellite
EOF – Empirical Orthogonal Function
ERBE – Earth Radiation Budget Experiment

EROKF – Ensemble Reduced Order Kalman Filter
ERS – European Remote Sensing satellite
G+C – Gent and Cane ocean model
GFO – Geosat Follow-On
GODAS – Global Ocean Data Assimilation System (NOAA's operational ocean data assimilation technique)
GPCP – Global Precipitation Climate Project
GTSPP – Global Temperature/Salinity Profile Project
H – Observational operator for data assimilation
HadISST – Hadley Centre Sea Ice and Sea Surface Temperature data set
IC – initial conditions
ILD – isothermal layer depth
INDOPAC – full atmospheric coupling over the entire Indo-Pacific
INSTANT – International Nusantara STratification ANd Transport
INT_PAC, CLIM_IO – experiment with interannual forcing in the Pacific and climatological SST forcing in the Indian Ocean
INT_PAC, INT_IO – experiment with interannual forcing throughout Indo-Pacific
IODZM – Indian Ocean Dipole Zonal Mode
IO – Indian Ocean
IP_NOITF – experiment with closed Indonesian Throughflow
IP_OPEN – experiment with the open Indonesian Throughflow
IS – in situ (weekly)
ISCCP – Interannual Satellite Cloud Climatology Project
ISMON – in situ (monthly)
ITCZ – Intertropical Convergence Zone
ITF – Indonesian ThroughFlow
LODYC – Laboratoire d'Oceanographie Dynamique et de Climatologie
MEOF – Multivariate Empirical Orthogonal Function
MLD – mixed layer depth
MPI – Max Planck Institute for Meteorology
MSS – mean sea surface
NCEP – National Center for Environmental Prediction
NINO3.4 – NINO3.4 region (120^oW-170^oW and 5^oS- 5^oN)
NINO3 – NINO3 region (90^oW-150^oW and 5^oS- 5^oN)
NODC – National Ocean Data Center
OGCM – ocean general circulation model
OI – optimal interpolation
P – Precipitation
PDO - Pacific Decadal Oscillation
PSU – practical salinity units
Q – model forecast error for the data assimilation
RAMA – Research Moored array for African-Asian-Australian Monsoon Analysis and Prediction
RCP – representative concentration pathways (for future climate scenarios)
RMS – Root mean square
RMSD – Root mean square difference

r= – correlation
SAM – statistical atmospheric model
S_{bottom} – salinity of the deep ocean
SL – sea level
SOI – Southern Oscillation Index
SPB – spring prediction barrier
SPCZ - South Pacific Convergence Zone
SPEEDY – Simplified Parameterizations, primitivE-Equation DYnamics
SST – sea surface temperature
SST' – sea surface temperature anomaly
Sv – Sverdrup ($1x10^6$ m^3/s)
S_z – subsurface salinity
TAO – Tropical Atmosphere Ocean Array
TAUX – zonal wind stress
TAUY – meridional wind stress
T_{bottom} – temperature of the deep layer
TP – TOPEX/Poseidon
TRMM - Tropical Rainfall Measuring Mission
T_z – subsurface temperature
WIO – western Indian Ocean
WOA09 – World Ocean Atlas 2009
WOD09 – World Ocean Database 2009
XBT – Expendable Bathythermograph (ocean profile data)

1 Introduction

1.1 Statement of the Problem

El Niño/Southern Oscillation (ENSO) is the single most important mode of global climate variability on interannual time scales. Based in the equatorial Pacific, ENSO-related anomalies impact global atmospheric circulation (e.g. [*Lau and Nath*, 2003]) and cause far-reaching socioeconomic ramifications (see e.g. [*Glantz*, 2001], [*Horel and Wallace*, 1981]). It is therefore an important goal to better understand mechanisms that could lead to successful extension of useful ENSO predictability. Despite the large body of existing work on ENSO, the state of the art for ENSO prediction still has much to improve upon (e.g. [*National Academies of Sciences and Medicine*, 2016], [*National Research Council*, 2010]). For example, in June 2014 the consensus forecast from IRI (http://iri.columbia.edu/our-expertise/climate/ forecasts/enso/2014-June-quick-look/) called for 78% chance for El Niño for December 2014 and the National Oceanic and Atmospheric Administration (NOAA) officially issued an El Niño watch (http://www.cpc.ncep.noaa.gov/products/analysis_monitoring/enso_disc_jun2014/ensodisc.pdf). Subsurface conditions and heat storage rivaled the big event of 1997. However, in reality this event was so short-lived that it did not even achieve El Niño status (i.e. it did not have 5 consecutive 3-month running means with > 0.5^{o}C). Instead, the big El Niño was delayed until December 2015 when the magnitude matched the 1997 event with a NINO3 SST anomaly of 2.3^{o}C (http://www.cpc.ncep.noaa.gov/products/analysis_monitoring/ensostuff/ensoyears.shtml). So why did the expected air/sea interaction in the Pacific fail to couple to produce a big El Niño in 2014 as predicted? [*McPhaden*, 2015] suggested that the lack of coupling between the atmosphere and ocean

was the main reason for this poor forecast. There are several possibilities for this prediction failure which include 1) initial triggering events (i.e. westerly wind bursts) were out of sync with an amplifying mode and with the typical El Niño development timing (occurring 1 month earlier than for 1997 event), 2) negative feedbacks such as upwelling ocean waves may have damped warm ENSO sea surface temperature anomalies, 3) stronger trade wind easterlies associated with the cool phase of the Pacific Decadal Oscillation (PDO) could have inhibited migration of the precipitation from the warm pool eastward thus increasing sea surface salinity, density, and mixed layer depth and reducing the impact of wind on ocean, and 4) Indian Ocean (IO) dynamics may have anchored deep convection over the Indo-Pacific warm pool rather than allowing it to migrate to the east and become coupled with central/eastern Pacific SST anomalies.

Within this dissertation we focus on the last item for better understanding ENSO predictability. Namely, it is the purpose of this dissertation to help to better understand the oceanic and atmospheric impacts of the IO and the role that fresh water flux via sea surface salinity may play in extending useful ENSO predictions.

A major feature of the IO is the dynamic coupled response known as the Indian Ocean Dipole Zonal Mode (IODZM) as coined by [*Saji et al.*, 1999]. During the positive phase of the IODZM anomalous cold water upwells off Sumatra shoaling the thermocline and lowering sea surface heights (SSH) in the eastern IO. At that same time, warm water is found west of 70^{o}E with deeper thermocline and higher SSH. This anomalous east-to-west SST gradient reverses the normal westerlies of the Walker circulation to easterlies near the equator. In summer, southeasterlies in the east enhance the local along-shore upwelling and in the west, weakened monsoon southeasterlies south of the equator

veering into southwesterlies north of the equator lead to weaker upwelling and warmer SST off Africa, thus reinforcing the dipole pattern. In the west, warm SST is associated with enhanced convection and unusually abundant rainfall. In the east, cold SST results in drought over the Maritime Continent. During the positive IODZM phase, anomalous easterlies along the equator drive anticyclonic curl off the equator in the Southern Hemisphere triggering downwelling oceanic Rossby waves with positive SSH roughly straddling 10^{o}S west of 70^{o}E (see e.g. Figure 2, [*Webster et al.*, 1999]). These Rossby waves propagate to the west, reflect to the equator as coastal Kelvin waves, and generate downwelling Kelvin waves that eventually act to counteract the upwelling in the east after they traverse the basin. Southeasterlies generated from cold SST south of the equator reinforce climatological southeasterlies and enhance upwelling in summer. However, in fall and winter these same southeasterly anomalies counteract climatological northwesterlies reducing upwelling and leading to warmer eastern IO SST anomalies (e.g. [*Hendon*, 2003]).

Because the Indonesian Throughflow (ITF) is the only low-latitude pathway for warm/fresh water to be transported from the Pacific to the IO, the ITF has been the focus of much attention for better understanding ENSO dynamics. Most of these studies adopt the experiment philosophy to either cut off the ITF ([*Hirst and Godfrey*, 1993], [*Murtugudde et al.*, 1998]) and compare model results, closed minus open, or prescribe the ITF flow (e.g. [*Rodgers et al.*, 1999]). These results show that when the ITF is closed the Pacific is warmer, fresher with a deeper thermocline, the IO is colder, saltier and shallower thermocline and the normal ITF flow is missing across the IO (i.e. anomalous counterclockwise circulation in the south IO). In addition, these studies

conclude that the Pacific is the source for interannual variability of the ITF. Using the same philosophy (i.e. ITF closed-open) [*Schneider*, 1998], [*Wajsowicz and Schneider*, 2001], [*Song et al.*, 2007], and [*Santoso et al.*, 2011] not only confirm the previous forced ocean model results using a coupled model, but they also find that the ITF regulates the position of the deep convection, surface pressure and winds over the entire tropics. When the ITF is closed, abundant rainfall and westerlies migrate from Indonesia out into the central Pacific, negative precipitation anomalies are found over Indonesia/eastern IO, and easterlies prevail over the equatorial IO changing the entire character of the Walker circulation and ENSO.

In addition to the oceanic component, many papers address the impact of atmospheric coupling in the IO to the functioning of ENSO. For these studies the general approach is to run coupled experiments with regional decoupling accomplished by simply forcing the atmosphere using climatological SST rather than interannual values. For example, the full Indo-Pacific coupling experiments are differenced with those that only couple the atmosphere to surface forcing in the Pacific (e.g. [*Yu et al.*, 2002], [*Wu and Kirtman*, 2004], [*Annamalai et al.*, 2005], and [*Annamalai et al.*, 2010]). Thus, the difference between the full Indo-Pacific minus the Pacific regional coupled experiments highlights the impact of the IO atmospheric coupling. In general, the authors simplify the SST structure (e.g. using the first EOF) and then force a simple linear atmospheric model to show how particular regional forcing might impact winds and precipitation associated with ENSO. For example, SST anomalies covering the IO and in the Indonesian Seas lead to, not only a same-sign local response (i.e. negative SST spawn easterlies over the IO), but also have opposite-sign impacts trapped near the equator over the entire Pacific

as well enhancing El Niño signal. On the other hand, the warm western/cold eastern dipole pattern of the Indian Ocean Dipole Zonal Mode (IODZM) results in an atmospheric response mostly limited to the IO sector. However, these coincident cold SST anomalies over Indonesia force a global precipitation response with negative anomalies over Indonesia and positive values near the dateline [*Annamalai et al.*, 2010]. Unfortunately, both the closed ITF oceanic and atmospheric coupling experiments have been run under idealized conditions rather than under realistic hindcast conditions. Therefore, examining the oceanic and atmospheric impacts of the IO on ENSO predictability under realistic ENSO prediction hindcast circumstances motivates this research.

Many studies have addressed how assimilation can improve ENSO predictions. For example, SL (e.g. [*Ji et al.*, 2000]), SST (e.g. [*Zhou et al.*, 2009]), subsurface temperature and salinity (e.g. [*Yang et al.*, 2010]) and SSS (e.g. [*Hackert et al.*, 2011]) have all been assimilated into initial conditions to improve coupled ENSO predictions for either the Pacific or globally (e.g. [*Balmaseda and Anderson*, 2009]). However, none of these studies have addressed what impact assimilation in the IO might play on extending useful ENSO predictions. Therefore, this dissertation investigates how assimilation of SL, SST, subsurface temperature (T_z) and salinity (S_z) in the IO impacts coupled Indo-Pacific ENSO predictions.

A component of this study is determining what impact the freshwater flux over the Indo-Pacific region plays in ENSO predictability. Unfortunately tracking changes in the fresh water flux using precipitation from coupled models is less than ideal. For example, validation of Climate Forecast System Reanalysis (CFSR - [*Saha et al.*, 2010])

precipitation using satellite estimates (i.e. [*Xie and Arkin*, 1997] and [*Adler et al.*, 2003]) show that the CFSR climate results are too wet over the Inter-Tropical and South Pacific Convergence Zones (ITCZ and SPCZ) in the Pacific, too dry over the western Pacific and Indonesia, and have the global mean bias of 3.14 mm/day ([*Wang et al.*, 2010]). In addition, the CFSR product typically has 25% higher variability than observed in the tropical rainy regions over the tropical IO, Indonesia, Pacific warm pool, SPCZ and ITCZ ([Wang et al., 2010]). As far as precipitation forecasts go, the positive biases over Indonesia, the Pacific ITCZ and SPZC grow over forecast lead times out to 7 months. The pattern of the errors remain robust over time and for all initialization seasons indicating that the errors are likely caused by model biases ([*Dirmeyer*, 2013]). For the most recent version of the CFSv2 forecasts, the zonal mean of the precipitation skill within 5^{o} of the equator is worse than the initial state (i.e. observed SST forced CFSR) and over the entire tropics (30^{o}N-30^{o}S) the correlation between oceanic precipitation and observations falls from r=0.3 to r=0.2 by roughly 20 day forecasts [*Kumar et al.*, 2010].

Poor representation of the model precipitation in a coupled model could have severe implications on coupled forecast results. Although other factors such as horizontal advection ([Foltz and McPhaden, 2008]) play an important role in the tropics, Evaporation minus Precipitation (E-P), is the major factor controlling the salinity budget in the tropics ([Yu, 2011]) especially in tropical convergence zones such as the ITCZ and SPCZ. Therefore, if precipitation is systematically mis-forecast (like CFSv2 - [Dirmeyer, 2013]) then the fresh water forcing is suboptimal, ocean sea surface salinity, and salinity within the mixed layer will also be incorrectly initialized and then forecasted. Inaccurate salinity would also mean that mixed layer density and upwelling would be inexact and

misrepresented in the ocean model. Systematic precipitation biases in coupled forecasts would have ramifications for ocean predictions but might also rectify in coupled forecasts. For example, if precipitation were too great in a given area, then mixed layer density would be too low. This would lead to a mixed layer that was too thin and would store too much heat, leading to anomalously warm SST, with atmospheric forecast consequences.

Although precipitation is an important variable to study since it represents the communication of SST to the atmosphere and tropical upper-level heat anomalies, it would be useful to address the reliance upon less-than-ideal precipitation forecasts and directly examine the impact of fresh water flux in the tropical Indo-Pacific by utilizing sea surface salinity (SSS). Therefore, the role that the freshwater budget of the Indo-Pacific plays in ENSO predictability is diagnosed using SSS in this study. Variation of the western Pacific salt budget associated with either IO regional atmospheric coupling or by salt transport of the ITF may impact the heat reservoir available for ENSO. For example, [*Maes et al.*, 2002] and [*Maes et al.*, 2005] show that the heat stored below the salinity stratified layer in the western Pacific is critical to the amplitude of the subsequent El Niño as well as the ENSO mean state ([*Maes and Belamari*, 2011]). Another way to improve vertical density structure in coupled models is via direct assimilation of salinity. [*Hackert et al.*, 2011] show that coupled hindcasts of the tropical Pacific are significantly improved by assimilation of observed SSS into the initial conditions. However, there remains a gap in the existing research to connect salinity and density improvements and concomitant improvements to barrier layer thickness (BLT – defined in Section 1.2.2), MLD, sea level, SST, etc. to coupled ENSO forecasts for the Indo-Pacific region.

Therefore, it is the purpose of this research to examine the impact of improved representation of near-surface salinity and density in the Indo-Pacific on the coupled ENSO predictions in a realistic hindcast setting.

The overriding hypothesis that we wish to test is that the upstream influence of the Indian Ocean, both through the oceanic flow of the ITF and the atmospheric bridge (as coined by [*Alexander et al.*, 2002]), improves validation statistics with respect to observations thus extending useful ENSO predictions. In addition, the impact of satellite and in situ observations in the IO, and the concomitant improvement in the IO circulation, will improve ENSO predictions. Finally, the impact of fresh water flux as estimated by assimilation of sea surface salinity along with improved density structure in the Indo-Pacific region will improve the near-surface ocean quantities such as mixed layer depth (MLD) and barrier layer thickness (BLT) at initialization leading to better ENSO predictions. Our approach is to use a combination of ocean models, data assimilation of in situ and satellite analyses, and coupled models to diagnose the impact of these various components on ENSO predictability.

1.2 Indo-Pacific Background State

1.2.1 Observations of the Indonesian Throughflow

The main oceanic link between the IO and Pacific is the Indonesian Throughflow (ITF) which is important to the global climate system since it moves roughly 15 Sv of warm, fresh water from the Pacific [*Sprintall et al.*, 2009] and thus is a major source of heat for the IO and a sink for the Pacific. In particular, ITF water enters the IO at 10^{o}S, propagates across the basin between 5-20^{o}S in the South Equatorial Current (SEC) and 1/3 exits through the Madagascar and Agulhas currents after 10 years residence time

[*Song et al.*, 2004]. The remaining 2/3 of the ITF water recirculates to the north and heat is eventually released to the atmosphere [*Vranes et al.*, 2002] or exits south of 30^{o}S through the Antarctic Circumpolar Current. In this way, the ITF contributes to the global heat conveyer belt [*Gordon*, 1986].

Assuming Sverdrup balance in interior ocean basins and a local balance between alongshore winds and pressure gradient at the coasts, [*Godfrey*, 1989] suggests that the line integral of wind stress along the circuit from South Australia, east to South America and north to the equator then east to New Guinea, through the ITF back to Australia should match ITF flow (known as the Island Rule). The ITF flow estimated using the island rule corresponds to about 14 Sv using QuikScat winds ([*Wijffels et al.*, 2008]).

Following the work of [*Wyrtki*, 1987], who first suggested that the pressure gradient across the ITF could be used to estimate its transport, [*Potemra*, 2005] utilizes SODA model output ([*Carton et al.*, 2000]) and altimetry to create indexes of upper layer ITF transport differencing sea level data east of the Philippines and southwest of Java. The mean ITF transport is 6-10 Sv using the sea level method, whereas SODA, forced by ERA40 ([*Uppala et al.*, 2005]) and assimilating SST, subsurface temperature and salinity (but not SL nor SSS), has a value of 12.7 Sv.

Peak ITF transport can be found during the Southwest monsoon (July-October) and minimum during Northwest monsoon confirming the local Ekman seasonal contribution. Although local wind forcing plays a minor role in the interannual variability of the ITF, remote wind forcing of equatorial/coastal Kelvin and Rossby waves have a major impact (60-90% sea level, 70% thermocline) in interannual variability of ITF [*Schiller et al.*, 2010]. Pacific winds force equatorial Rossby waves

that hit eastern New Guinea and propagate around the west coast as coastal Kelvin waves and down through the ITF along the west Australia Shelf coast ([*Shi et al.*, 2007]).

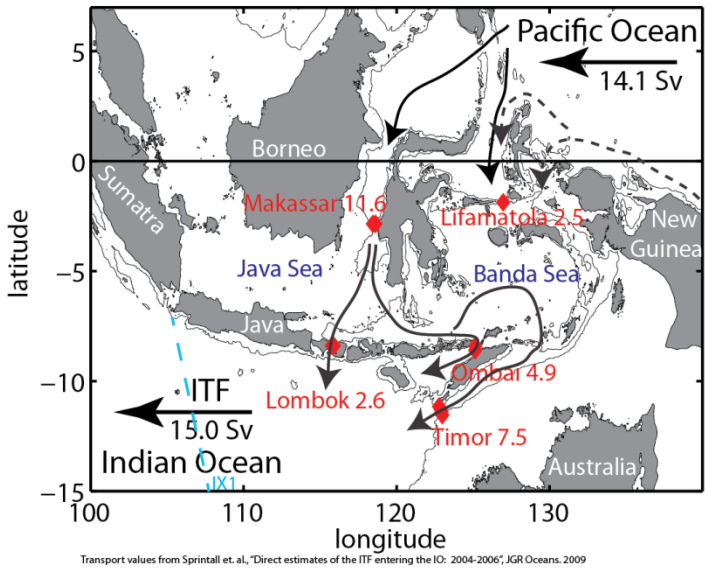

Figure 1.1: Schematic of the ITF. *Schematic of the ITF shows major passages, INSTANT mooring locations (red diamonds) and estimates of the flow (in Sverdrup from [Sprintall et al., 2009]). The WOCE line IX01 is indicated by the light blue dashed line.*

Seasonal to interannual variability of the ITF is highlighted using the International Nusantara Stratification and Transport (INSTANT) mooring data for 2004-2006 [*Sprintall et al.*, 2009]. Eleven moorings were deployed across the entrance (Makassar Strait, Lifamatola Passage but not Halmahera) and exit regions (Lombok, Ombai, and Timor) of the ITF and are dispersed to accurately measure each passage's contribution to the ITF. These mooring locations are shown in Figure 1.1 as red diamonds. Total inflow at Makassar is 11.6 Sv and Lifamatola contributes 2.5 Sv (deeper passage, 700-1200 m with saltier South Pacific water). Note that total ITF exit transport corresponds to 15.0 Sv (varying from 10.7 to 18.7 Sv) and is made up of Lombok (2.6 Sv), Ombai (4.9 Sv) and over half the flow comes from Timor (7.9 Sv). Two thirds of the total transport

comes from the upper 300 m mostly through Timor passage (5.3 Sv, Ombai 3.3 Sv and Lombok 2.6 Sv).

Since there are relatively sparse historical salinity observations, less is known about the ITFs role in the global hydrological cycle. [*Talley*, 2008] estimates global meridional ocean fresh water flux along repeat hydrographic sections using absolute geostrophic velocities from [*Reid*, 2003] and Ekman transports from NCEP reanalysis winds from 1979 to 2005 ([*Kalnay et al.*, 1996]). Assuming an ITF flow of 10 Sv and a reference salinity of 34.5 PSU, Talley finds that the net freshwater transport of the ITF sums to 0.11 Sv. Although this number appears small relative to the mass transport, it is roughly half the total transport of the southern subtropical gyre of the Pacific (0.23 Sv) thus demonstrating that the salinity budget in the Pacific is strongly impacted by the ITF flow.

Various studies attempt to directly measure the flow of the ITF and estimate the interannual variability. For example, [*Meyers et al.*, 1995] measure the mean ITF as 5 Sv for 1983-1989 using the geostrophic transport calculated from the IX01 WOCE XBT data (see Figure 1.1 for location of IX01 line). [*Vranes et al.*, 2002] use Makassar Strait moorings to estimate the ITF (10.8 Sv) from December 1996 to July 1998 and they find that heat flux of 0.55 PW (reference temperature 0^{o}C) and 0.41 PW (4^{o}C) is lower during El Niño and higher during La Niña. Thus, the ITF can be seen as a critical source to transfer heat from the equatorial Pacific to the southwestern IO. [*Meyers*, 1996] finds reduced ITF transport associated with warm ENSO due to low sea level in the western Pacific reducing the Pacific-to-Indian pressure head (e.g. note that the normal negative SL gradient from the Philippines to Java is reduced during El Niño). Observations are

assessed along the IX01 XBT track and most of the variability in the transport is annual and semi-annual but interannual variability is strongest at the southern end of the track (i.e. Australia) corresponding to direct Pacific forcing along New Guinea/west Australia wave guide.

Estimates of the net heat flux of the ITF from the Pacific to the IO varies from 0.55 PW [*Vranes et al.*, 2002] using mooring data to 1.09 PW [*Tozuka et al.*, 2007] using the SINTEX coupled model. In addition, [*England and Huang*, 2005] find the mean heat transport of 0.74 PW using SODA data but, more importantly, estimate the variability to be 0.21 PW. This variability of the ITF is generally attributed to the Pacific. ITF lags ENSO (as defined by the Southern Oscillation Index of [*Trenberth*, 1984]) by 5 months with r = -0.40 using an integration of our ocean model from 1985-2004 (c.f. Section 2.2.1 for details). These values compare favorably with those of [*England and Huang*, 2005] who find that ITF lags ENSO by 9 months with r = -0.32.

The ITF is generally weaker during El Niño in response to lower western Pacific sea level but less is known about the ITF response to the IO. During the positive IODZM, which coincided with El Niño in 2006, there is increased ITF flow in the upper 230 m increasing the net heat transport of the ITF. However, during the weak El Niño (2004), both Makassar and outflow channels are weak in the top 150 m (total ITF 13.8 Sv) whereas the flow is intensified at the surface during 2006 (a period of weak El Niño and positive IODZM conditions - 15.4 Sv). The ITF should be stronger since the Philippines-to-Java SL gradient is intensified during the positive phase of IODZM.

Modulation of the ITF, via remote Kelvin forcing in the IO, also plays an important role in heat transport from the Pacific to the IO and so may be instrumental in

the heat buildup prior to ENSO via the recharge paradigm of [*Jin*, 1997] or via direct wave dynamics across the Pacific. For example, Figure 1.2 illustrates how energy can transfer from the IO to the Pacific. Downwelling Kelvin waves, generated in the IO by monsoon transition westerlies or MJO (e.g. [*Zhou and Murtugudde*, 2010]), reflect off Sumatran coast, propagate along the coast through Lombok (< 300m) and then Makassar reversing the ITF flow. In addition, these coastal Kelvin waves continue along Suva Islands and penetrate Ombai with both surface and deep reversals and a deep signature in Timor. Using a combination of INSTANT moorings and model results to illustrate the IO remote forcing on the functioning of the ITF, [*Schiller et al.*, 2010] find that poleward propagating downwelling coastal Kelvin waves cause higher sea level along Java-Sumatra-Lesser Sunda waveguide, increasing eastward flow of South Java Current, and passes northward into the Lombok Strait (0-7 days). After 14-21 days, the downwelling Kelvin wave makes its way into the Banda, Flores, and Java seas through various straits. The reflected, downwelling Rossby wave detaches from the Sumatra coast and begins to propagate westward (e.g. [*Potemra et al.*, 1991]) into the IO (28-35 days). After 21 days, plots of lagged correlations (right) along the red line (left) are shown in Figure 1.2. As the Kelvin wave propagates along the Sumatra-Java-Lesser Sunda ray path, the correlation drops since energy is redirected to Flores Sea (through Lombok), Savu (through Ombai) and Timor Seas. It is interesting to note that the depth correlation drops off at the corresponding sill depth of Lombok (500 m), Ombai (800-1000 m) and only deeper energy makes it to Timor.

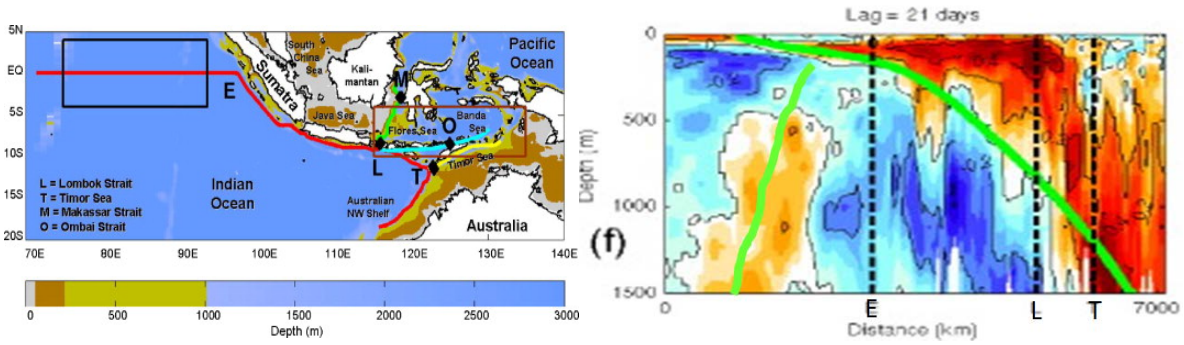

Figure 1.2: Kelvin passage through ITF. *Taken from [Schiller et al., 2010] Figure 1, 5f. Left panel shows the Indonesian region with the red line corresponding to one of the potential pathways (Sumatra-Java-Australia) of IO Kelvin waves propagating into/through the ITF. The right panel shows the correlation of IO wind stress anomaly index from the black box in left panel versus the potential temperature anomaly along the red line path shown in left panel. Correlation ranges from -0.5 to 0.5 and E, L, and T correspond to Equator, Lombok, and Timor, respectively on both figures. The positive and negative sloping green lines on the right panel correspond to the theoretical 1st mode Rossby and Kelvin waves, respectively. Model results are from 1/10^{o} resolution Bluelink ReANalysis (BRAN Version 2.1) comprised of MOM4p0 assimilating all available sea level, SST, subsurface data, and Australian tide gauge data forced by combination of ERA-40 and ECMWF analyses.*

Recently [*Yuan et al.*, 2013] showed the important inter-basin exchange between the IO to the Pacific for the large IODZM event in 1997. They utilized gridded fields of observed satellite sea level, SST and ECMWF winds and lagged correlation analysis to show that there are significant lagged correlations between the southeast tropical IO SL and SST (i.e. the eastern dipole of the DMI) in fall and Nino 3.4 values for the following summer to fall. They attributed the significant lagged correlations up to 1 year out to the propagation of an upwelling Kelvin wave, associated with the anomalous easterlies of the strong IODZM event, from the IO through the ITF into the western Pacific then along the equator to the eastern Pacific. Again using lagged correlation they showed that this Kelvin wave propagation was evident in subsurface temperature from TAO moorings as well. Using ocean and coupled models, [*Yuan et al.*, 2011] also showed that the negative

sea level associated with the IODZM in the eastern IO could generate enhanced ITF flow by increasing the pressure head from the Pacific to the IO (ala [*Wyrtki*, 1987]). Enhanced ITF flow leads to warm water venting from western Pacific, upwelling of the western Pacific thermocline, and initiation of an upwelling Kelvin wave that traverses the Pacific. Since these IODZM anomalies can persist for a year, this work suggests the importance of oceanic pathway of the ITF and the potential to increase ENSO lead forecasts. This component of how the IO could impact ENSO predictions has received little attention in the literature thus motivating this current dissertation research.

1.2.2 Barrier Layer Thickness Observations and Formation

As its name implies, Barrier Layer Thickness (BLT) is important to the tropical mixed layer budget because it acts to inhibit entrainment of deep cooler/saltier water into the base of the mixed layer. The first reference to a barrier layer is attributed to S. Godfrey (personal communication, 1987) in the paper by [*Lukas and Lindstrom*, 1991]. BLT is generally defined as the depth between an isothermal layer depth (ILD) and the depth of constant density (or distance separating the bottom of the Mixed Layer Depth (MLD) to the top of the thermocline).

[*Sprintall and Tomczak*, 1992] determine the criteria for BLT as the difference between an isothermal layer ($\Delta T=0.5^{o}C$) and the mixed layer depth (MLD) defined by the density criteria (i.e. depth that the Δdensity equals the surface density value plus the equivalent density change assuming $\Delta T=0.5^{o}C$ keeping salinity equal to SSS). In other words, $\sigma_{t,MLD=}\sigma_{t,0} + \Delta T \frac{\partial \sigma_t}{\partial T}$ or BLT is the depth difference between the MLD determined from density (with salinity held to surface values and Δdensity equivalent to

the value it would be using the same ΔT as the temperature criterion) and the MLD determined using temperature criterion (usually $\Delta T=0.5^{o}C$).

MLD can either shoal or deepen due to changes in turbulence which is in turn caused by potential or kinetic energy. Potential energy is measured by buoyancy flux that is due to density changes brought about by either freshwater or heat flux at the ocean surface. Kinetic energy is input at the sea surface by the action of wind via waves, entrainment and horizontal advection by currents. Presence of BLT means that any water entrained into the bottom of the ML is of the same temperature; no heat transfer into/out of the ML and so any additional surface heat flux would act to raise the temperature of the ML.

Figure 1.3 shows the BLT statistics calculated from an optimal interpolation of all available subsurface temperature and salinity for the tropical Indo-Pacific region. (See Section 2.1 for OI details). These results are consistent with [*Sprintall and Tomczak*, 1992] who used Levitus climatology. Several equatorial regions have persistent BLT. These include the western Pacific, the northern IO, and the eastern half of the Indian Ocean. For the western Pacific, the BLT is anchored just west of New Guinea (strongest in May to July), along $15^{o}N$ (February to April), and $12^{o}S$ (August to October) and these are associated with the warm pool, ITCZ, and SPCZ precipitation maximums, respectively. The spatial distribution of the ITCZ BLT is explained by the north and south migration of the ITCZ. This is also true for the SPCZ, the January maximum

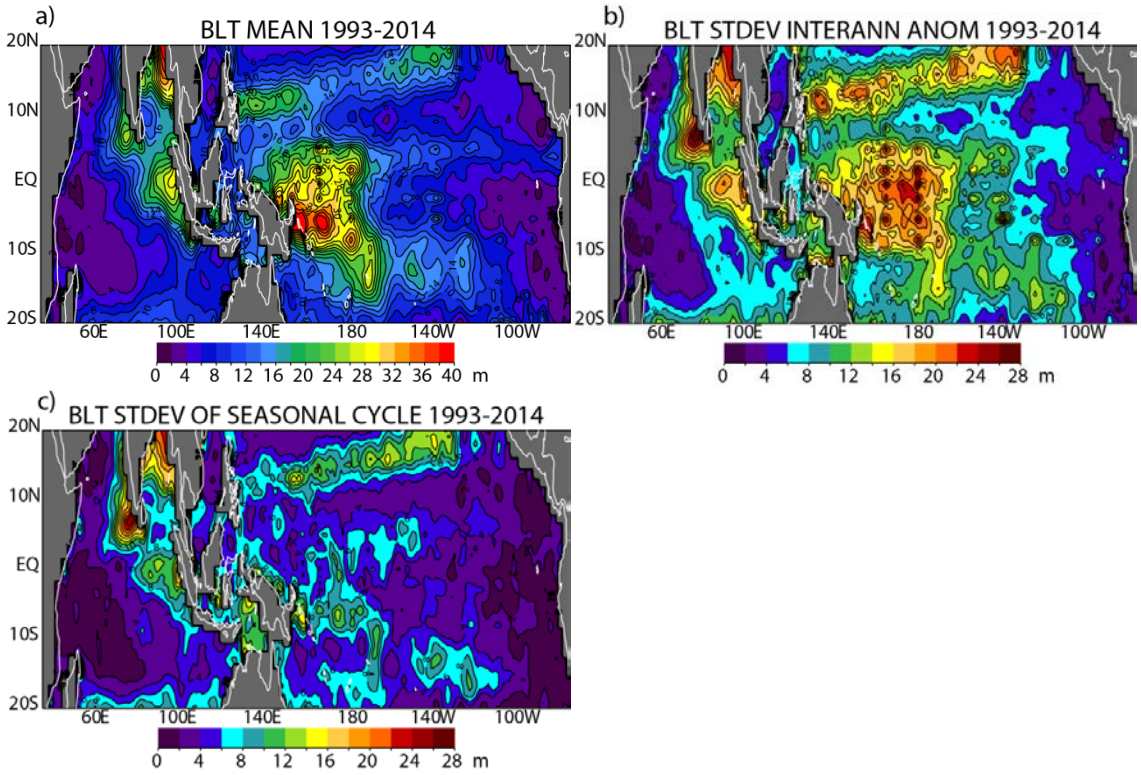

Figure 1.3: Observed BLT statistics. *Plots of observed BLT using optimal interpolation of temperature and salinity profiles at Levitus levels for a) mean, b) interannual variability of the anomaly with respect to the seasonal cycle, and c) variability of the mean seasonal cycle. BLT is defined as the difference between MLD determined using the 0.5°C temperature criterion minus MLD depth determined using the density criterion (assume SSS and equivalent density change corresponding to 0.5°C). The units are meters.*

precipitation is at 15°S and by September the SPCZ is located at 10°S and is generally oriented southeast to northwest. A simple model, constructed by [*Sprintall and Tomczak*, 1992], estimates that a net surplus of 2140 mm/yr of rainfall into the ocean is required to maintain the western Pacific BLT. Different estimates of evaporation minus precipitation (E-P) can easily explain these values. For example, [*Oberhuber*, 1988] finds that there is an excess of 2400 mm/yr precipitation for the western Pacific and this value adequately explains the fresh water content of the observed BLT. The warm pool in the western Pacific is dominated by the interannual signal (Figure 1.3b). The maximum variability

regions in the ITCZ and the western south Pacific are split between interannual and seasonal amplitudes.

Other tropical regions of BLT are found in the Bay of Bengal (BOB in August to October), Arabian Sea (AS in November to January) stretching south to the equator, and just west of Sumatra (May to January). For BOB and AS the total variability is dominated by the seasonal cycle (Figure 1.3c). The likely source for BOB BLT is the river outflow from the Ganges, Brahmaputra, and Irrawaddy that peaks just after the summer monsoon season. Fresh water from these rivers (~2545 mm/yr river flow) flows out into the BOB and overrides the saltier eastern IO water, forming the BLT layer. The Indus River supplies fresh water for the AS BLT. This lags the monsoon peak by one season, perhaps due to varying rain-to-river residence times for Indus versus Ganges. The variability maximum just to the west of Sumatra is split between interannual and seasonal values. The mechanism for the Sumatra BLT is likely an excess of rainfall, estimated to be 1800 mm/yr [*Sprintall and Tomczak*, 1992].

For the western Pacific, the mechanism for BLT formation is different. Along the equator, the eastern edge of the warm pool (typically 28^{o}C isotherm) is a demarcation region between warm fresh water to the west and cold salty, upwelled water in the central Pacific. A barrier layer is formed in the isothermal layer when either 1) abundant precipitation falls in weak wind conditions, 2) salty water is subducted from the east into the warm pool due to local convergence and warm fresh water overrides denser water to the east, 3) differential deepening of the ILD with respect to the MLD, or 4) vertical displacement of Kelvin and Rossby waves [*Cronin and McPhaden*, 2002]. Weak winds, heavy precipitation, eastward advection of low salinity water, westward subduction of

salty water and either downwelling Kelvin waves or Rossby waves are all factors that contribute to deep BLT formation in the western Pacific during 2000-2007 [*Bosc et al.*, 2009].

Prior to El Niño, the warm pool stores heat and is confined to the far western Pacific. During the El Niño, the warm pool expands eastward along with the concomitant precipitation and current anomalies because of relaxation of climatological easterlies. The fetch of the westerlies is increased during this time, reinforcing the event. [*Picaut et al.*, 1996], [*Delcroix and Picaut*, 1998] and [*Delcroix and McPhaden*, 2002] find a strong relationship between the east and west migration of the warm/fresh pool and ENSO. Using observations, [*Maes et al.*, 2006] show that there is a close positive relationship between SSS and SST in the western Pacific and the BLT is instrumental in maintaining heat and momentum in the warm pool within the salinity stratified layer. Later work, including Argo floats, confirm the relationship between eastward migration of the warm pool during El Niño and BLT heat storage in the western Pacific [*Mignot et al.*, 2007].

The study by [*Bosc et al.*, 2009] utilizes Argo, CTD and surface-only thermo-salinographs (TSG) from Volunteer Ships of Opportunity (VOS) to highlight the covariability of SSS, BLT, SST and other variables within 2^{o} of the equator in the western Pacific (130^{o}E-120^{o}W). Plots of SSS, SST, $\partial S/\partial x$ (zonal salinity gradient) and BLT are presented for 2000-2007 (Figure 1.4) and show that there is a close correspondence between SSS (identified by 34.7 PSU isohaline), SST (29.5^{o}C), zonal SSS gradient (maximum $\partial S/\partial x$), BLT, and the east and west migration of the warm/fresh pool. The warm/fresh pool moves eastward with El Niño (2002, 2004, and 2006) and

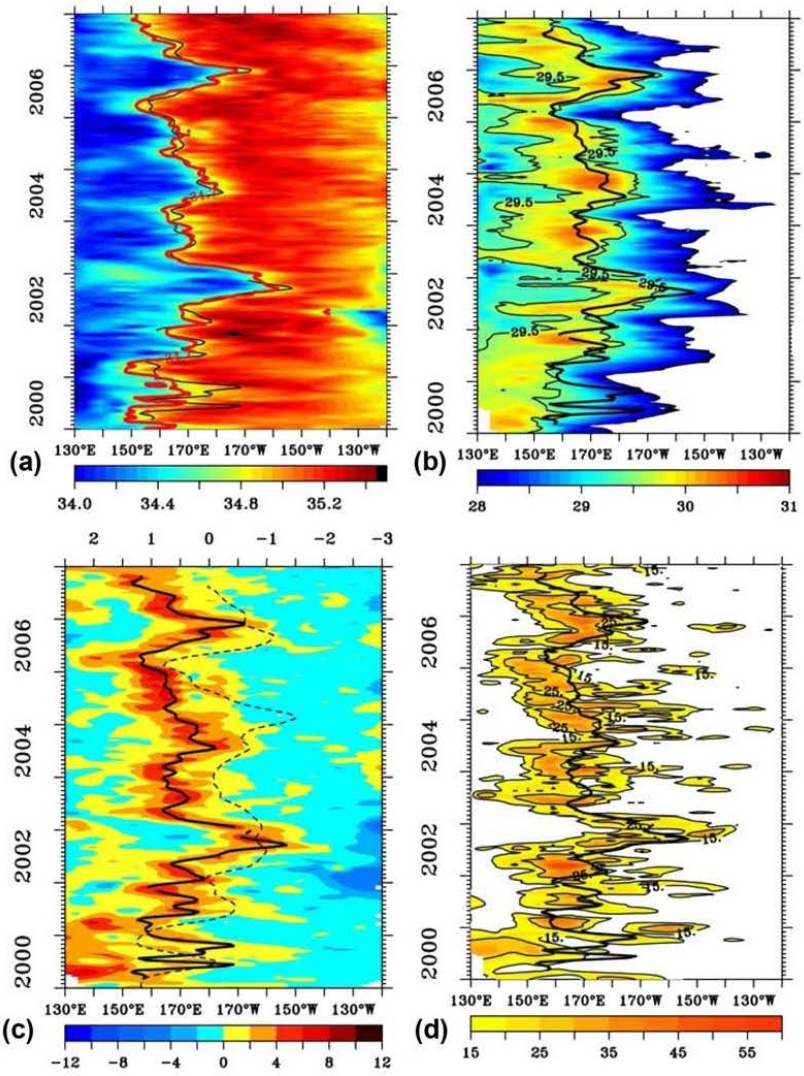

Figure 1.4: Interannual variability of tropical Pacific. *Longitude versus time plots of 2^oN-2^oS a) SSS, b) SST, c) ∂S/∂x, and d) BLT. For all panels the solid black line corresponds to the maximum of ∂S/∂x. Thinner solid lines correspond to a) 34.7 PSU, b) 29.5^{o}C, c) scaled SOI index. Units are PSU, ^{o}C, 10^{-7} PSU/m and m for the four panels, respectively. From [Bosc et al., 2009] Figure 6.*

westward with La Niña (2000-2001, 2007). In addition, the scaled SOI index (dashed line in Figure 1.4c) matches the east/west migration of this front. Close examination of these figures shows that warmest SST occurs just to the west of the salinity front. In addition, analysis of this data set indicates existence of permanent BLT that can be found

near the front (see Figure 1.4d) with the largest values generally to the west. Thus, warmest SST generally corresponds to deep BLT just to the west of the front.

[*Bosc et al.*, 2009] find that BLT is present for all periods 2000-2007 and has a close correspondence to maximum $\partial S/\partial x$, warmest SST, and east and west migrations of the salinity front in accordance with ENSO. All of the mechanisms for BLT formation proposed by [*Cronin and McPhaden*, 2002] are affirmed. Namely, high precipitation and low wind speeds are coincident with highest BLT; eastward advection of low SSS and zonal current vertical shear contributes to BLT formation; and higher differential impact on ILD versus MLD of Kelvin and Rossby waves also can form BLT. The main impact of BLT is to maintain a shallow mixed layer allowing an enhanced air-sea coupled response (e.g. [*Maes et al.*, 2005]). In addition, the BLT is the key factor in establishing the mean state that is perturbed during El Niño/La Niña [*Maes and Belamari*, 2011].

1.3 Modeling Indo-Pacific Interactions

1.3.1 Open/Closed ITF – Ocean Impacts

From observational studies cited in the previous section, we know that the ITF is important for global climate since it is the major route for mass to be transported from the western Pacific (~15 Sv) into the IO and a major source of heat (~0.74 PW) and freshwater (0.11 SV) for the IO. In particular, the input from the ITF can only return to the Pacific south of Tasmania where the mean temperature is 10^{o}C cooler so an ITF flow of 10 Sv would correspond to a net transport of 0.4 PW (assumes 10 Sv and 10^{o}C) from the Pacific to IO which may be as high as 60% of the total heat absorbed by the Pacific [*Hirst and Godfrey*, 1993]. In addition, calculations of the freshwater balances indicate that ITF water accounts for 0.23 Sv of evaporation within the IO [*Talley*, 2008].

Baroclinic coastal Kelvin and Rossby waves transport heat and fresh water from the Pacific into the IO and heat/fresh water is then dissipated over the broad areas of IO surface especially southwest of Australia. On the other hand, variations of the ITF from the IO due to equatorial Kelvin waves would modulate the ITF and impact the normal transport of heat and fresh water from the Pacific to the IO thus potentially impacting the predictability of ENSO.

Work by [*Hirst and Godfrey*, 1993] and [*Murtugudde et al.*, 1998] concentrate on the oceanic impact of closing the ITF on the Pacific and IO in forced ocean models. They conclude that closing the ITF leaves the Pacific warmer and saltier with a deeper equatorial thermocline and the IO is colder with a shallower thermocline. In addition, [*Rodgers et al.*, 1999] find that ventilation of Northern Hemisphere water via the relatively fresh Mindanao Current into the ITF (through Makassar), is a requirement to have the proper observed proportions of Northern Hemisphere versus Southern Hemisphere water in the tropical Pacific. Later work ([*Schneider*, 1998] and [*Wajsowicz and Schneider*, 2001]) use short coupled experiments to show that the ITF regulates the position of the deep convective precipitation, surface pressure and winds, and that these impact the entire tropics.

More recently, [*Song et al.*, 2007] use a 200 year simulation of the GFDL CM2.1 coupled model to further point out the impact of the ITF. Two experiments are performed and compared over 200 years with the difference being that the ITF is cut off (Lombok, Ombai, and Timor) by land bridges. Differences between ITF_{closed} and ITF_{open}

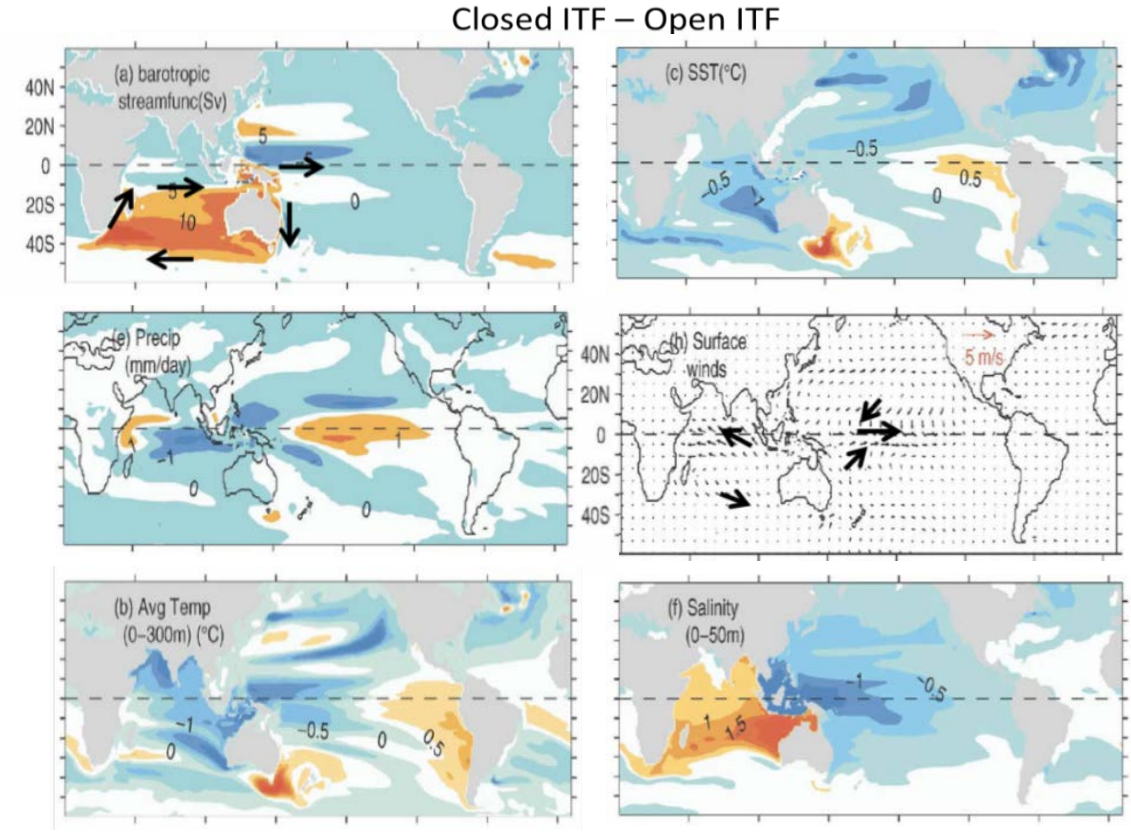

Figure 1.5: Closed minus Open ITF for CM2.1. *Annual mean differences ITF_{closed} minus ITF_{open} for a) barotropic stream function (Sv), c) SST (^oC), e) precipitation (mm/day), h) surface winds (m/s), b) 0-300 m average temperature (^oC), and f) 0-50 m salinity (PSU). Arrows are added for emphasis of the direction of the differences. Taken from Figure 4 [Song et al., 2007]. CM2.1 is made up of MOM4 (50 levels 10 m resolution above 220m and $1^o x 1^o$ resolution down to $1/3^o$ near the equator) with true freshwater fluxes and K-profile vertical mixing. The atmospheric component is made up of AM2p12b with 24 vertical layers and $2^o x 2.5^o$ resolution. (©American Meteorological Society. Used with permission.)*

are shown in Figure 1.5. Barotropic streamfunction (Figure 1.5a) shows decreased flow of the SEC in the southwestern Pacific and clockwise rotation over most of the IO corresponding to a reduced (i.e. eastward) SEC flow, transport of the Agulhas (i.e. northerly anomaly), and Agulhas retroflection currents, and increased southward flow of the East Australian current. Heat content from 0 to 300m (Figure 1.5b) is reduced in the IO due to surface cooling brought about by closing the ITF and increased in the eastern Pacific. In addition, the western Pacific cools which is inconsistent with previous

modeling studies but is explained by overall weakened trades and deeper thermocline. SST (Figure 1.5c) is decreased in the southeastern IO and western equatorial Pacific and warmed in the upwelling region in the Pacific serving to reduce the mean zonal SST gradient across the Pacific. Atmospheric pressure is increased over Indonesia leading to weaker trades (westerly anomalies, Figure 1.5h) and flatter thermocline in the Pacific and anticyclonic circulation in the south IO with easterlies prevailing over the equator. Precipitation differences (Figure 1.5e) reflect the fact that as SST warms in the east and cools in the western Pacific, the precipitation migrates out away from Indonesia, the ITCZ shifts south. The negative SST over the IO corresponds to deficit rainfall over most of the IO. The source waters for the ITF consist of low salinity north Pacific thermocline and intermediate waters so when the ITF is closed the salinity of the IO increases and the Pacific freshens (Figure 1.5f). This results in a reinforcement of the Pacific and a decrease in the eastern IO vertical fresh pool salinity gradient. In this region the shallower thermocline leads to reduced barrier layer thickness (BLT) in the western Pacific and eastern IO and thus may contribute to changing heat storage for ENSO along the lines of [*Maes and Belamari*, 2011]. Note that the dynamics of the ITF is the prominent driver of the salinity differences and not changes in precipitation or evaporation minus precipitation.

[*Santoso et al.*, 2011] extends the work by previous authors by running coupled experiments with the ITF_{open} and ITF_{closed}. EOF analysis of the different ENSO characteristics shows that for the ITF_{closed} experiment, the main amplitude of the SST signal is confined to the NINO3 region (5^oN-5^oS, 150^oW-90^oW) whereas for the ITF_{open} experiment, the highest variability is located in NINO3.4 region (5^oN-5^oS, 170^oW-

120°W) or to the west of ITF_{closed}. Unlike [*Song et al.*, 2007], who conclude that ITF_{closed} had higher variability by examining only the eastern Pacific response, [*Santoso et al.*, 2011] find that the ITF_{closed} example has weaker total variability: the interdecadal variability is less while the interannual variability is sustained at the same level as ITF_{open}. Differences in plots of variability ITF_{closed} minus ITF_{open} for zonal current, upwelling, zonal temperature gradient and zonal wind stress all show a dipole pattern, negative to the west and positive to the east, consistent with enhanced Bjerknes feedback for the ITF_{open} scenario. For ITF_{closed} the Bjerknes feedback is displaced eastward. The decreased amplitude of decadal ENSO in the ITF_{closed} case can be explained by a relatively shorter time it takes to recharge/discharge smaller upper ocean heat content in the ITF_{closed} example. The oceanic connection is attributed to possible draining of the warm pool (and subsequent discharging) of the ENSO via the ITF. For the IO sector, the eastern dipole of the IODZM, exhibits increased variability for the ITF_{closed} case. However, there is no such increase in the western tropical IO so the large negative correlation between these two (e.g. Dipole Mode Index) for the ITF_{open} experiment is eliminated thus breaking the dipole response of IODZM relationship [*Song et al.*, 2007]. In addition, [*Schneider*, 1998] finds that both IO monsoons were enhanced with ITF_{closed}.

The IO impacts the Indo-Pacific region via precipitation and concomitant sea surface salinity changes since the normal flow of fresh water to the IO is turned off by closing the ITF, resulting in a fresher Pacific (e.g. [*Song et al.*, 2007] and [*Santoso et al.*, 2011]). In addition, closing the ITF leads to less rainfall over Indonesia but more rainfall in the central Pacific (e.g. [*Schneider*, 1998] and [*Wajsowicz and Schneider*, 2001]). These changes in salinity in the fresh pool of the Pacific can modify near-surface density

anomalies and barrier layer heat storage, which in turn can have an impact on ENSO predictability. For example, [*Maes et al.*, 2005] showed that the western Pacific barrier layer stores heat to amplify ENSO. However, the impact of these salinity/precipitation features on ENSO predictability has not yet been fully addressed within the context of hindcast prediction experiments.

1.3.2 Pacific versus Indian Atmosphere/Ocean Coupling – Wind Impacts

In order to test the impact that the IO atmospheric coupling might have on ENSO, [*Wu and Kirtman*, 2004] use a coupled general circulation model (CGCM) to test the impact of the IO on ENSO. They compare two experiments. In one, the Indo-Pacific (INDOPAC) region atmosphere is coupled. In the other, the IO is decoupled (i.e. DECOUPIO) by setting SST to climatological forcing. They show that the ENSO variability is reduced significantly when the IO is decoupled. For the INDOPAC control experiment, the NINO3.4 variability is 0.56^{o}C whereas the DECOUPIO is only 0.27^{o}C. In addition, composite plots of longitude versus time show that the maximum for the INDOPAC coupled experiment (195^{o}E) is located to the east of the DECOUPIO (180^{o}E, matching [*Yu et al.*, 2002]) and that the eastern upwelling (i.e. Kelvin wave arrival) is slightly later (March versus April for INDOPAC and DECOUPIO, respectively). The dominant period of variability is extended by decoupling the IO (2.3 for INDOPAC to 2.8 years for PACONLY) which is inconsistent with earlier work of [*Yu et al.*, 2002]. The influence of the IO is via the convective heating and modulation of the Walker circulation. IO SST can induce anomalous Walker circulation over the eastern equatorial IO (EEIO) and western-central Pacific through anomalous heating over the IO. For

example, cold IO SST induces anomalous westerlies in the Pacific that serve to enhance El Niño.

To test why IO SST affects low level winds, a simple 2.5 layer linear atmospheric model is employed by [*Wu and Kirtman*, 2004]. The first EOF (38% explained variance) of the JJAS SST of the INDOPAC control is used to force the simple atmosphere (Figure 1.6a). This pattern has positive values over the central Pacific NINO3.4 region (0.4^{o}C), negative values over most of the IO (-0.4^{o}C) and positive values over the eastern IO (0.2^{o}C). Three experiments are initiated: full IO plus Pacific SST forcing (Figure 1.6b), Pacific only (Figure 1.6c) and IO only (Figure 1.6d). For the Pacific and IO SST forcing, the results show strong westerlies to the east of Indonesia and easterlies to the west (a negative Walker circulation). For the Pacific-only SST forcing the wind anomalies are limited to the Pacific region with westerlies over the western Pacific and easterlies over

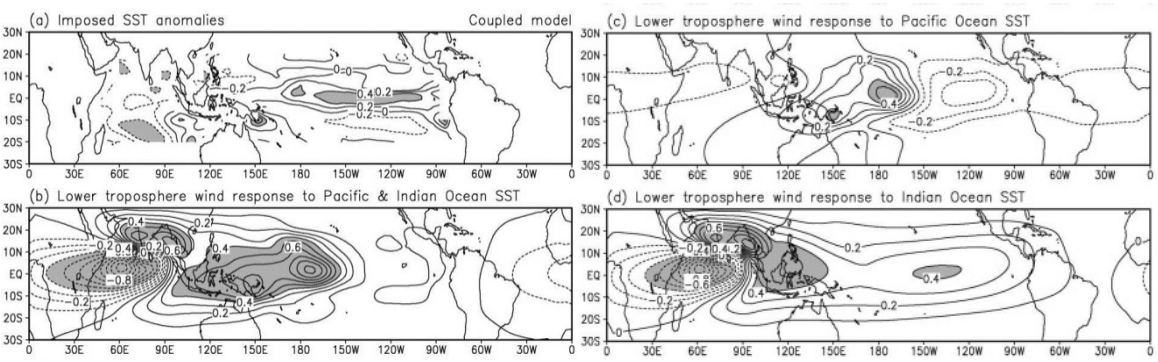

Figure 1.6: Simplified coupled model response. *Top) 1st EOF of the JJAS SST (0.2^{o}C) anomalies of the INDOPAC coupled model used to force the simple atmospheric model– 38% of the variance. b), c) and d) panels correspond to INDOPAC, PACONLY and IO-ONLY SST forcing on zonal winds (0.1m/s). Taken from Figure 7, [Wu and Kirtman, 2004]. The coupled GCM of the Center for Ocean-Land-Atmosphere Studies (COLA) uses an atmospheric model with T42 resolution. This is coupled to the GFDL Modular Ocean Model (MOM) version 3. Years 71-392 of the fully coupled experiment serve as the control. For the DECOUPIO experiments, climatological SST from the control is used to force the IO sector and then these are run for 45 years and the last 40 is then used for analysis. (©American Meteorological Society. Used with permission.)*

the eastern Pacific. This pattern reflects the lower level convergence forced by the warm SST in the central Pacific. Interestingly, the wind pattern from the IO negative SST forcing (Figure 1.6d) is easterly over the western IO but strong westerlies reside over Indonesia extending over the entire Pacific giving the well-known atmospheric Kelvin wave pattern. A westerly node associated with an atmospheric Rossby wave is demonstrated by westerlies over the Bay of Bengal. Therefore, the IO SST forcing results indicate a mechanism that can enhance westerlies over the western Pacific resulting in more intense El Niño.

[*Annamalai et al.*, 2010] find that El Niño is much stronger when it occurs with IODZM events than when only El Niño occurs. They call the former class 1 and the latter class 2 events. Plots of CM2.1 coupled model results for class 1 minus class 2 composite El Niños show cold SST over the EIO and in the Indonesian Seas (110^{o}E-140^{o}E, 10^{o}S-0^{o}) and the eastern Pacific thermocline deepens and SST warms east of the dateline for IODZM + El Niño cases (Figure 1.7a). Precipitation (Figure 1.7b) is decreased from the central IO to 160^{o}E in the Pacific (with minimum off Java and Indonesian Seas) and increased just east of 160^{o}E and in the western Pacific. Note that this region corresponds to the same area mentioned by [*Bosc et al.*, 2009] where the fresh water front migration is highly correlated with ENSO (from Section 1.2.2). Winds are westerly from 130^{o}E east to 120^{o}W and easterly over Indonesia west over the central IO indicating a weaker Walker circulation (Figure 1.7c).

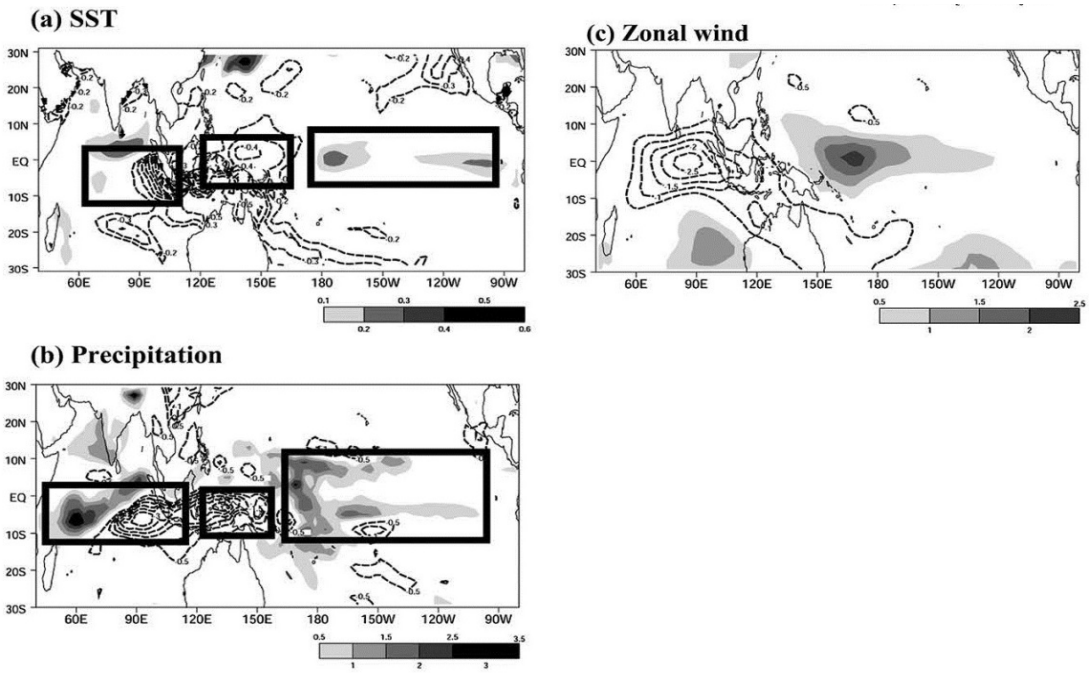

Figure 1.7: El Niño differences with and without IODZM. *Differences between class 1 (i.e. Strong El Niño with IODZM) minus class 2 El Niño (i.e. no IODZM) for a) SST (^oC), b) precipitation (mm/day), and c) 850 mb zonal wind (m/s). Dashed lines are negative. Boxes in a) represent EIO, Indonesian Seas, and equatorial Pacific forcing regions, respectively. From Figure 2 [Annamalai et al., 2010]. The GFDL Climate Model version 2.1 uses climate of the 20th century forcing from 1861 to 2000 and is GFDL's contribution to the IPCC AR4. NINO3 (90^{o}W-150^{o}W, 5^{o}N-5^{o}S) from DJF and EEIO (90^{o}E-110^{o}E, 0^o-10^{o}S) from JJASON were formulated to define El Niño and IODZM, respectively. Monthly anomalies were formulated with respect to the 1971-2000 mean seasonal cycle and any trend was removed. (©American Meteorological Society. Used with permission.)*

Next a simple atmospheric model, the Linear Baroclinic Model (LBM) of [*Watanabe and Jin*, 2003] is utilized by [*Annamalai et al.*, 2010] that is linearized about the CM2.1 mean state and forced by SST anomalies in Figure 1.8 in order to highlight the impact of the various regions. The forcing for the regions corresponds to the boxes in Figure 1.7a. EIO forcing generates an atmospheric Rossby wave signature in the eastern IO (i.e. easterlies at the equator and westerlies to north and south with the BOB winds significantly stronger – Figure 1.8a) but no signal in the Pacific similar to the idealized

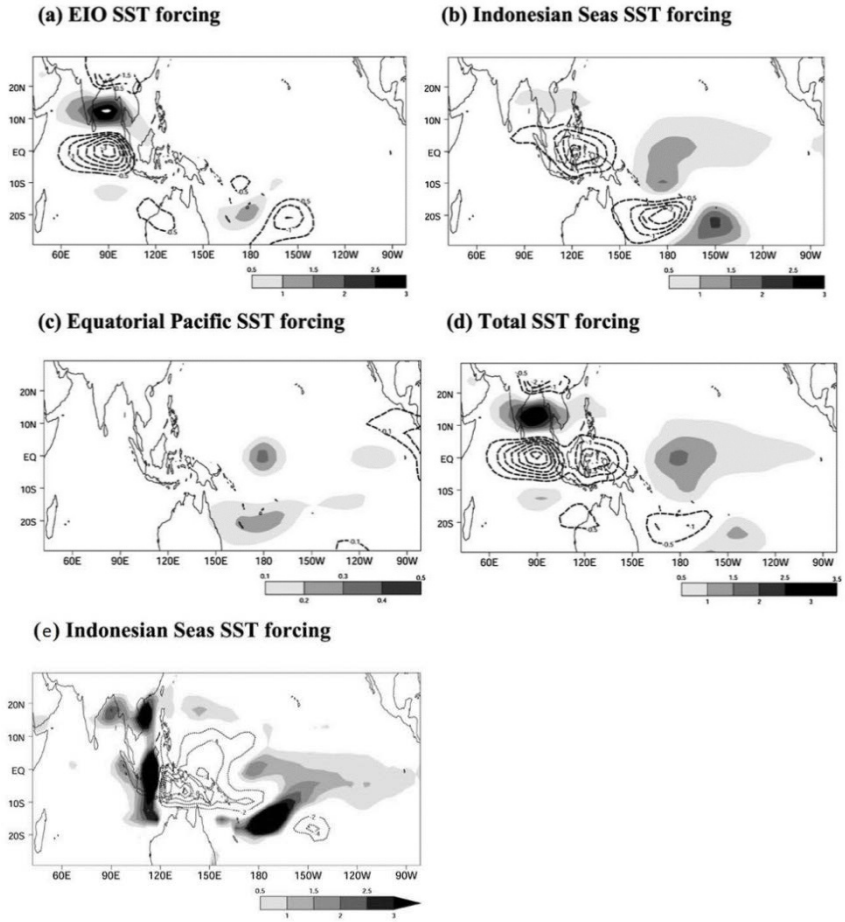

Figure 1.8: Linear atmospheric response to regional SST forcing. *850 mb zonal wind anomalies (m/s) results of regional SST forcing of the linear atmospheric model for the regions defined in Figure 1.7a for a) EIO, b) Indonesian Seas, c) Equatorial Pacific and d) total SST forcing. From [Annamalai et al., 2010] Figure 7. Figure e) shows the same as b) but for precipitation in mm/day (from Figure 8b of same paper ©American Meteorological Society. Used with permission.)*

forcing of the IODZM in [*Annamalai et al.*, 2005]. The linear experiments for the EPAC (Figure 1.8c) forcing also results in weak wind anomalies in the Pacific due to little additional generation of precipitation anomalies in this region. However, the impact of the Indonesian Seas on the atmospheric linear model is surprisingly strong and far reaching. Again cold SST forcing in the Indonesian Seas forces strong negative precipitation anomalies (see Figure 1.8e) which in turn force an atmospheric Kelvin response that is evident by easterlies over Indonesia and strong westerlies to the east over

the western equatorial Pacific (Figure 1.8b). Thus, when IODZM positive phase is in place, positive zonal wind anomalies occur over the equatorial western Pacific. Cold SST over the Indonesian Seas 1) reduces the normal east/west temperature gradient across the Pacific providing favorable conditions for westerly anomalies to develop, 2) suppresses convection over the Maritime continent and the resulting atmospheric Kelvin wave forces westerlies to the east, 3) leads to convergence of the westerlies that enhance western Pacific precipitation, and 4) results in an increased temperature gradient between Indonesia and the dateline further enhancing westerlies. These westerlies then lead to downwelling oceanic Kelvin waves further enhancing the growth of El Niño. [*Annamalai et al.*, 2010] conclude that regional IO SST and heating anomalies are not the primary cause but serve to enhance the development of El Niño and that IO ocean waves, triggered by IO wind anomalies, do not control Indonesian Sea SST but rather local wind effects dominate.

In summary, the IO can have strong influences for ENSO via either oceanic or atmospheric pathways. Enhanced western Pacific westerlies, enhanced precipitation, and intense freshening in the central Pacific are in place by closing the ITF. Regional coupling of basin-scale IO and Indonesian Seas SST anomalies force enhanced westerlies over the entire Pacific and increased ENSO forcing (Figure 1.6 and Figure 1.8). In addition, precipitation is enhanced in the same region where the zonal displacement of the warm/fresh pool is highly correlated with ENSO (e.g. Figure 1.8e). Keeping in mind that western Pacific precipitation is strongly influenced by the IO through both oceanic and atmospheric routes, and that precipitation is the major source of SSS anomalies in the

tropics, next the relevant research regarding SSS impacts on ENSO Indo-Pacific prediction via BLT dynamics is presented.

1.4 Role of Salinity and Fresh Water Forcing in the Indo Pacific Region

1.4.1 Impact of Barrier Layer Thickness on Coupled Predictions

Using coupled models and tuning the mixing to eliminate BLT for one year prior to El Nino, [*Maes et al.*, 2005] show that the heat buildup associated with BLT is a requirement for a large El Niño. These authors use the French coupled model (ARPEGE coupled to OPA) to investigate the impact of BLT on El Niño. Thirty years of model experiments show that prior to all El Niño, heat buildup occurs concurrently with the existence of BLT in the western Pacific (consistent with the observational findings of [*Bosc et al.*, 2009]). Correlations illustrate that both dynamic height (DH) and BLT are thickening in response to strengthened trade winds (i.e. easterlies) that sustain the heat buildup in the western Pacific prior to El Niño. In order to test the impact of BLT on El Niño an additional set of experiments are performed by [*Maes et al.*, 2005]. In the first stage, mixing is increased in the warm pool (defined as 4^{o}N-4^{o}S and SST > 28^{o}C) at the depth of the BLT in the year prior to El Niño so that salinity stratification is eroded. Then in the second stage the salinity mixing is returned to its original state and the model is restarted using the perturbed (i.e. no BLT) initial state and then run for the following El Niño year. Year 15 of the model, the example used in the paper, has a relatively strong El Niño (i.e. a NINO3.4 SST anomaly of 2.5^{o}C). The control (left) shows more heat stored for the top 250 m in the warm pool than for the perturbed (middle) experiment

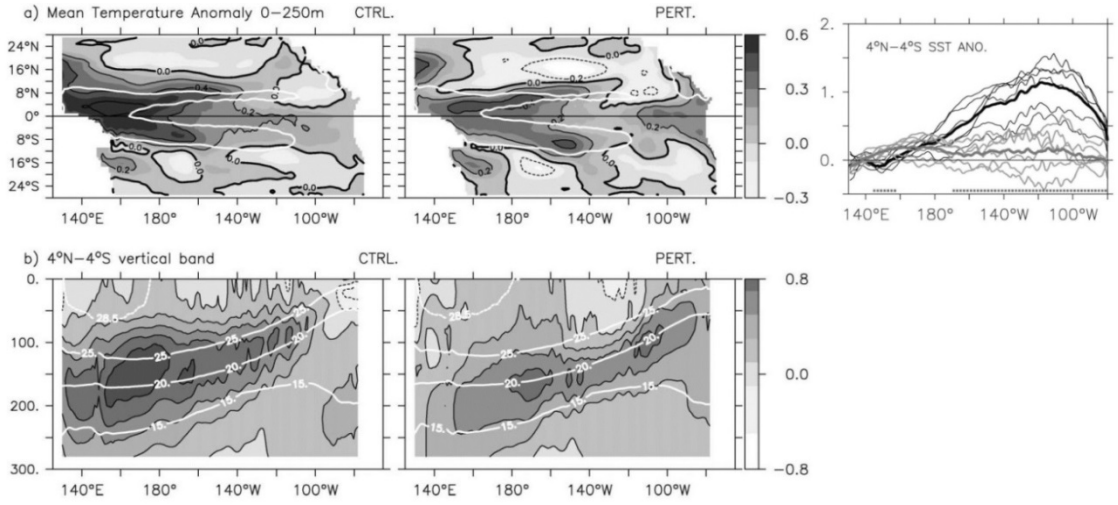

Figure 1.9: Impact of heat storage and BLT. *October-December mean for the year prior to El Niño (i.e. year 14 of the coupled model) minus 30 year climatology for (left) control and (right) perturbed for (top) 0-250 m mean temperature and (middle) longitude versus depth temperature along the equator(^{o}C). Right panel shows the following year's El Niño annual predictions (i.e. year 15). Black (control) and gray (perturbed) lines represent all 6 ensembles and heavy line shows the ensemble mean. From [Maes et al., 2005] Figures 6 and 7. The coupled model is comprised of the Meteo-France atmospheric and the ocean general circulation models from LODYC. The AGCM was adapted from the ARPEGE forecast model with T31 (3.75^{o}) and 19 levels. The OGCM comes from the Ocean Parallelise (OPA) for the Pacific basin with 1^{o} in longitude down to 0.5^{o} at the equator with 25 layers in the vertical. (©American Meteorological Society. Used with permission.)*

(Figure 1.9 top). In addition, temperature at the depth of the thermocline is increased for the control (i.e. with BLT heat storage) versus the perturbed (BLT removed via mixing - Figure 1.9 middle) in the western Pacific. For the eastern Pacific, the perturbed experiment shows higher temperature near the thermocline and at the surface. During the year prior to El Niño (i.e. year 14) the east to west SST gradient is reduced for the perturbed experiment, allowing a longer fetch for any westerly wind bursts. Plots of SST, zonal wind stress and D_{20} (not shown) confirm that equatorial Kelvin waves transport heat towards the east along the thermocline for the perturbed case in year 14 thus expending any heat buildup prior to El Niño. Thus, the net result of removing the BLT is to prematurely discharge heat to the east before the onset of El Niño.

Coupled forecasts are then initiated by [*Maes et al.*, 2005] and the annual mean El Niño year Figure 1.9 (right) shows that forecasts initiated from the control experiment (black curves) have a much larger SST signal along the equator than the perturbed experiments (gray curves). The perturbed experiment annual mean El Niño SST is less than 0.2^{o}C whereas the mean amplitude of the control is roughly 1^{o}C at 120^{o}W in the eastern Pacific. In other words, the removal of BLT results in an annihilation of the strong year 15 El Niño. The different terms of the mixed layer heat budget for the warm pool indicate that 1) the perturbed experiment has a deeper MLD (as expected with no BLT), 2) entrainment term is negative (cooling) for the perturbed and its amplitude dominates the MLD budget whereas this term is positive and relatively small for the control, 3) the atmospheric heating is large for the perturbed due to the increased MLD (deeper MLD can gain more solar heat flux), and 4) the reduction of surface currents forced by the wind working over deeper MLD for the perturbed experiment leads to slightly reduced advection term. Therefore, the presence of the BLT and the concomitant suppression of entrainment from below is a necessary requirement to store heat in the western Pacific to fuel the subsequent El Niño.

[*Maes et al.*, 2005] showed that accounting for the salinity structure is important for ENSO prediction. For this work, better estimates of the BLT lead to basin-scale changes in heat storage and corresponding changes in SST. In an idealized coupled model setting, we have seen that basin-scale changes in heat storage can lead to improved ENSO forcing predictions. Therefore, important questions about the role of salinity via BLT, heat storage, and SST still need to be addressed thus motivating this aspect of the dissertation research.

1.4.2 Impact of Salinity Assimilation on Coupled Predictions

Rather than perturbing coupled experiments as in the previous section, another way to investigate the impact of BLT is through assimilation of salinity in forced ocean models. A main focus of the operational seasonal climate prediction centers is the full utilization of recently implemented Argo S_z via ocean data assimilation. In a survey paper, [*Oke et al.*, 2009] highlights the relative importance of various observing systems to ocean analyses using the Global Ocean Data Assimilation Experiment (GODAE) models and they find that Argo is the only observing system that constrains subsurface temperature (T_z) and salinity (S_z). Specifically, the ECMWF ocean reanalysis system (ORA-S3) initialized with the atmospheric fluxes from the ERA-40 reanalysis (analyses after 2002) shows the impact of withholding different ocean observing systems at different locations [*Balmaseda and Anderson*, 2009]. Their coupled results (i.e. ORA-S3 coupled to operational global, Integrated Forecast System) indicate that inclusion of Argo data significantly improves SST hindcasts for most regions (except the Atlantic) and Argo outperforms both altimetry and mooring information for the western tropical Pacific i.e. NINO4 region and the entire tropical IO between 10^oN-10^oS. Earlier work suggested that Argo may correct errors in fresh water forcing, circulation, or water mass characteristics [*Balmaseda et al.*, 2007]. In this system the mean dynamic topography from the previous months ORA-S3 results is used to assimilate sea level. Assimilating altimetry does not significantly improve IO forecasts whereas Argo improves the SST forecasts for all IO regions tested. For the Pacific, altimetry assimilation outperforms Argo in the NINO3 and across the entire equatorial Pacific but Argo has higher validation

statistics in NINO4 region. Unfortunately, this work does not distinguish between the contribution of Argo T_z and S_z.

Using the NSIPP global Coupled General Circulation Model (the quasi-isopycnal Poseidon ocean model is coupled to the NSIPP AGCM - [*Vintzileos et al.*, 2003]), [*Yang et al.*, 2010] show that assimilating the subsurface structure of salinity accurately contributes to improved prediction of the 2006 El Niño. In particular, they show that assimilating both T_z and S_z into Pacific initial conditions captures the correct warming for 2006. The salinity assimilation improves the amplitude of the downwelling Kelvin wave, successfully capturing the two-stage deepening of the thermocline and the east/west displacement of the warm/fresh pool in the western Pacific. By swapping out variables from different techniques, these authors show that the salinity impact on stratification, especially near the thermocline in the western Pacific, is important for successful predictions.

[*Hackert et al.*, 2011] show that assimilation of gridded in situ SSS into initial conditions for our Pacific-only Hybrid Coupled Model (see Section 2.2.4 for details of similar model) improves the resulting coupled forecasts. Coupled experiments are initiated from these assimilation results and run for 12 months for each month, 1993-2007. The resulting hindcasts show that adding SSS to T_z assimilation improves coupled forecasts for 6-12 month lead times (see Figure 1.10a). The main benefit of SSS assimilation comes from improvement to the Spring Predictability Barrier (SPB) period. SSS assimilation increases correlation for 6-12 month forecasts by 0.2-0.5 (Figure 1.10b) and reduces RMS error by 0.3-0.6^{o}C for forecasts initiated between December and March, a period key to long-lead ENSO forecasts. The positive impact of SSS

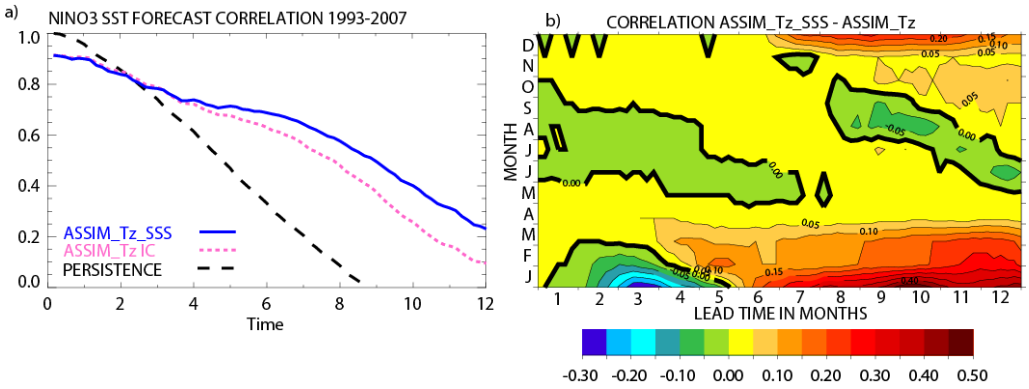

Figure 1.10: Coupled improvements due to SSS assimilation in the Pacific. *NINO3 SST anomaly statistics for a) correlation versus forecast lead time for observation persistence (dashed line), coupled experiments initiated from data assimilation of T_z (ASSIM_T_z - dotted) and T_z with SSS assimilation (ASSIM_T_z_SSS – solid) for 1993-2007 (r = 0.31, 95%) and b) start month versus lead time for correlation differences between ASSIM_T_z_SSS minus ASSIM_T_z. Note that inclusion of SSS in assimilation for initialization of ENSO hindcasts significantly improves the forecasts after 6 months especially for December to March starts From figures 4 and 5 [Hackert et al., 2011].*

assimilation originates from warm pool and Southern Hemisphere salinity anomalies. Improvements are brought about by fresh anomalies advected to the equator via subduction processes. Figure 1.11a shows both the SSS differences (i.e. with minus without SSS assimilation) as colors and the Bernoulli function for density surface 23.5 σ as contours. This panel shows that negative SSS anomalies flow towards the equator mostly from the Southern Hemisphere. Negative values of SSS (i.e. freshening) serve to increase the BLT near the equator (Figure 1.11b) which in turn leads to shallower mixed layer depth (Figure 1.11c). Thus, the net effect of assimilating SSS is to increase stability, reduce mixing, and shoal the thermocline (Figure 1.11d) which concentrates the wind impact of ENSO coupling. Monthly plots (not shown) indicate that this effect is most pronounced in June-August helping to explain the improvement in the SPB. In addition, regional assimilation of SSS determined that the western Pacific and the Southern Hemisphere has relatively greater influence on improving coupled forecasts

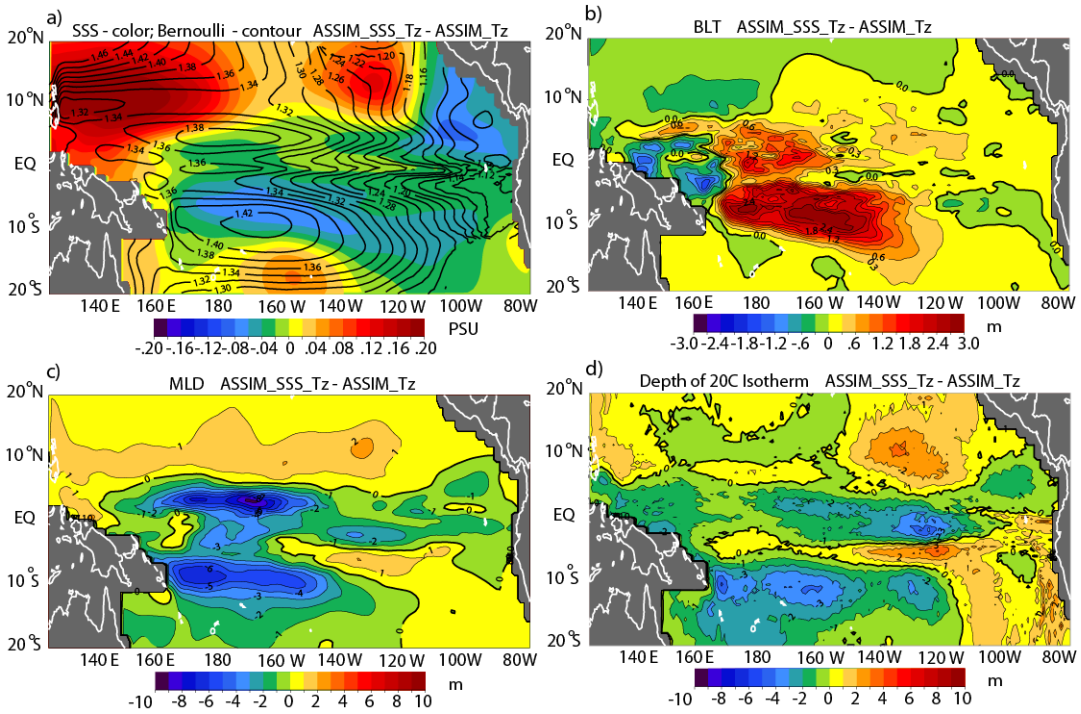

Figure 1.11: Initialization differences due to Pacific SSS assimilation. *Mean annual values for ASSIM_T_z_SSS minus ASSIM_T_z for (a) SSS (color) and ASSIM_T_z_SSS Bernoulli function using 23.5 σ (contours), (b) barrier layer thickness (BLT), (c) density criteria mixed layer depth (MLD), (d) depth of the 20°C isotherm (i.e., thermocline). Bernoulli streamlines are contoured every 0.2 cm and flow counterclockwise (clockwise) in the Northern (Southern) Hemisphere around low values. Missing contours correspond to regions where the 23.5 σ surfaces. MLD and BLT are defined using same criteria as used by [Sprintall and Tomczak, 1992].*

reaffirming the work of [*Ballabrera-Poy et al.*, 2002]. These are the precise regions where IO atmospheric coupling impacts the Pacific (see e.g. Figure 1.8e). Therefore, subducted off-equatorial and western Pacific salinity anomalies increase BLT along the equator in the western Pacific leading to improved MLD and more accurate air-sea coupling for ENSO predictions.

1.5 Objectives and Significance of Research

El Niño/Southern Oscillation (ENSO) has significant impacts on climate variability throughout the world and so has been the key focus for improving coupled

forecasts for the tropical Indo-Pacific. Given that El Niño and its related global teleconnections have dramatic societal impacts, examination of the role that IO variability plays in interannual predictions, both the amplitude and the character of this phenomenon, is a major objective of this dissertation. The analyses presented herein are especially critical now in light of the potential for testing recent theories explaining shortcomings of operational coupled models. For example, [*McPhaden*, 2015] and [*Santoso et al.*, 2015] suggested that a potential reason for the poor validation of the 2014 ENSO forecast was a lack of fully accounting for the impact of the IO on air/sea coupling in the tropical Pacific. The objective of this study is to understand the impact that the IO plays in the functioning of the coupled Indo-Pacific system through diagnosis of both the inter-basin oceanic and atmospheric teleconnections. In addition, we are interested in determining what impact IO data in general and fresh water flux (as diagnosed by salinity) in particular plays in the tropical Indo-Pacific ENSO predictability. Therefore, our research will answer the following questions: To what extent do oceanic and atmospheric teleconnections between the IO and Pacific impact ENSO predictability? Does inclusion of satellite and in situ observations in the IO improve coupled ENSO forecasts? And what is the role of sea surface salinity, both satellite and in situ, for improving near-surface density and what are the corresponding impacts on Indo-Pacific ENSO forecasts?

Given the results of previous idealized studies demonstrating both an oceanic and atmospheric teleconnection between the IO and ENSO, the main hypothesis of this dissertation is that the upstream influence of the IO plays an important role in advancing seasonal to interannual forecast skill of ENSO. First we present the role that forcing and

initial conditions play in the ENSO prediction problem to include the impact of the IO in initializing the coupled system. Specifically, we apply the previous generic/composite ENSO techniques for oceanic pathway (e.g. [*Song et al.*, 2007]) and atmospheric coupling (e.g. [*Wu and Kirtman*, 2004]) into the context of real ENSO predictions. For example, the impact of the ITF flow and wind/precipitation anomalies generated by IO SST anomalies are diagnosed for retrospective forecasts for 1993-present.

Next the impact satellite and in situ observations in the IO on ENSO predictions are addressed by comparing hindcasts that assimilate satellite SL, SST, SSS, and T_z and S_z in the IO with those that do not. By utilizing forced and coupled experiments and diagnosing differences between hindcasts with and without assimilation in the IO, the potential added benefits of satellite and in situ information in the IO are isolated and identified for improving ENSO predictions.

Lastly, we examine the impact fresh water flux (as measured by sea surface salinity) in the Indo-Pacific region may have on coupled ENSO predictions in light of poor precipitation forecasts in operational coupled models (e.g. [*Wang et al.*, 2010]). In the Pacific, previous work of [*Maes et al.*, 2005], [*Yang et al.*, 2010] and [*Hackert et al.*, 2011] showed the importance of salinity and accounting for heat storage in the BLT for ENSO predictions. However, it has yet to be fully demonstrated how improved salinity and mixed layer dynamics impact ENSO predictions. Therefore, a series of coupled experiment pairs are presented that isolate the impact of salinity assimilation versus those without. In addition, the relative quality and abundance of satellite versus in situ SSS assimilation has yet to be investigated in terms of ENSO prediction, so pairs of experiments are also presented that highlight how in situ salinity assimilation compares

with satellite derived SSS product. With the recent demise of Aquarius, the first NASA satellite designed specifically to measure sea surface salinity from space, and the questionable future for satellite salinity, it is now even more important to gain an improved understanding of the role of satellite salinity for ENSO prediction.

This dissertation is arranged in the following manner. The technical approaches (including data, model, and data assimilation descriptions) are presented in Section 2. Section 3 describes oceanic link of the IO via the ITF, Section 4 provides the results of the atmospheric teleconnections of the IO, Section 5 presents the impact of IO observations and Section 6 shows how SSS impacts ENSO predictability and compares satellite SSS relative to in situ observations. Finally, Section 7 contains the summary and conclusions.

2 Technical Approach and Methodology

The purpose of this dissertation is to identify what role the upstream influence of the IO plays on extending useful ENSO predictions, via the oceanic flow of the ITF, the atmospheric bridge of the IO to the Pacific, and the impact of assimilation in the IO. In addition, we assess the impact that fresh water flux through assimilation of sea surface salinity in the tropical Indo-Pacific region has on improving ENSO predictions. Our approach is to use a combination of satellite analysis, ocean models, data assimilation and coupled models to diagnose the impact of these various components on ENSO predictability. In this section we summarize these tools and the data that are used to isolate the impact of the IO and SSS on ENSO predictability.

2.1 Validation/Assimilation Data

Multi-satellite AVISO sea level data are used for assimilation and validation of ocean model and assimilation results (http://www.aviso.oceanobs.com/en/data/products/sea-surface-height-products/global/msla/index.html). In order to first homogenize the data from the different satellites (TOPEX/Poseidon, ERS, JASON 1, JASON 2, Envisat, GFO and Cryosat2), the best estimates for corrections, models, and references are applied to each satellite observation. Sea surface anomalies are calculated using each satellites repeat orbit mean or from a mean sea surface (MSS) when the satellite orbit does not repeat (ERS for April 1994-March 1995, Envisat since November 2010, and Cryosat2). A technique that minimizes the cross-over differences between satellites is applied in order to reduce the orbit error. Next, the mapping processing involves optimal interpolation (OI) of all available altimetry satellites (up to 4 e.g. Oct 2002-Sep 2005, J1+TPN+EN+GFO). The mapping procedure uses realistic correlation functions and

covariance functions are included that account for spatial and temporal scales using zonal and meridional propagation velocities which are estimated from five years of TP+ERS combined maps. In addition, 10% of the signal variance is included to take into account the sub-scale variability. Starting in October 1992 (i.e. start of TOPEX/Poseidon mission), research quality data are processed on a 7-day time-scale and typically have latency of 6 months. To acquire the latest data, near-real-time (NRT) daily data are also downloaded and averaged weekly to match the research quality data. All gridded fields have 1^{o}x1^{o} resolution from 60^{o}N-60^{o}S.

Weekly gridded 1^{o}x1^{o} SST data are available via http://www.esrl.noaa.gov/psd/data/gridded/data.noaa.oisst.v2.html and are comprised of in situ data from ships, drifting and moored buoys, and AVHRR data from satellite ([*Reynolds et al.*, 2002]). Satellite data are first tuned by regression to high-quality in situ SST data for day and night separately. Then OI is applied to the data in order to smoothly combine SST data from different sources. The first-guess field is the previous week's analysis and the random errors correspond to 1.3^{o}C, 0.5^{o}C, 0.5^{o}C and 0.3^{o}C for ship, buoy and, daytime and night-time satellite data, respectively. Note that the higher the random error, the lower the impact of the particular data source on the resulting OI. The zonal and meridional decorrelation scales are 850 km and 615 km, respectively. The data cover the period from November 1981 (i.e. start of AVHRR) to present with approximately 2 week data latency.

As part of our foundational work for assimilation, flexible software has been set up to access any subset of the available subsurface temperature (T_z) and salinity (S_z) data. The source data include the Global Temperature Salinity Profile Project (GTSPP),

TAO/RAMA, and World Ocean Database 2009 (WOD09 - [*Boyer et al.*, 2009]) observation data. For the GTSPP "best copy" data set [NODC, 2006] both real-time from the Global Telecommunications System (GTS) and delayed mode data received by the NODC are included in a continually managed database which maintains all available subsurface information removing duplicate entries. This data set includes profiles from instruments such as CTD and XBT measurements from ships, TAO buoys, and Argo profiling floats. Only data classified as "good", "probably good" or "modified" are included in our data set after location, date, gradient, density validation, climatological, and profile consistency tests are performed (http://www.nodc.noaa.gov/GTSPP/access_data/gtspp-bc.html). Daily mean TAO/RAMA data [McPhaden et al., 1998] are also included in this data set since mooring salinity data are handled inconsistently in both of the other data sets. All TAO/RAMA data except "lower quality" data were included (http://www.pmel.noaa.gov /tao/ data_deliv/). An additional data source, WOD09, includes research quality salinity and temperature profile data on standard levels (http://www.nodc.noaa.gov/OC5/WOA09/pr_woa09.html). Extensive quality controls are performed, and only data of "highest quality" (i.e. depth and salinity/temperature error flag=0) are retained in our database. In addition to the profile data, grids of the seasonal cycle for temperature and salinity provided by World Ocean Atlas 2009 (WOA09 -[Antonov et al., 2010; Locarnini et al., 2010]) are used to formulate anomalies. Prior to analysis, each profile is linearly interpolated to Levitus standard depths down to 1500 m and the closest matching WOA09 climatological value is subtracted to form an anomaly profile.

In order to extend the influence of the limited number of temperature and salinity profiles, and to remove the residual seasonal cycle after anomalies are formulated, the optimal interpolation (OI) technique of [Carton and Hackert, 1989] is employed to convert point-wise information to grids. Binning the data effectively removes redundant data from different data sources like GTSPP, WOD09 and TAO/RAMA so OI was performed on the binned data using decorrelation scales of 15^o longitude, 3^o latitude, and 1 month matching the values for SST estimated by [Meyers et al., 1991]. The process is repeated for each depth to obtain temperature and salinity anomaly grids with 1^ox1^ox1 month resolution at standard Levitus depths. As a final step the residual mean seasonal cycles (from the differences between the gridded observations and WOA09 gridded data) are removed for both T_z and S_z gridded OI data so that the EROKF assimilation procedure remains stationary.

In this work two different in situ SSS products are assimilated. To create the first one, all in situ salinity observations shallower than 10 m depth are binned in a 1^ox1^ox1month grid, anomalies are calculated using WOA09, and then OI was performed in a similar manner as T_z to produce a monthly SSS anomaly field. This SSS product is abbreviated as SSS_{ISMON} (for SSS in situ-monthly) and is comparable to satellite SSS since SSS errors estimated through cross-validation studies (e.g., performing several analyses by randomly withholding 10% data) provide an estimated salinity error of ~0.22 psu which is comparable to the expected accuracy of 0.2 psu for monthly grids of Aquarius retrievals ([Le Vine et al., 2007], [Yueh et al., 2001]).

The second SSS product is created from in situ salinity in order to capture the sampling coverage of Argo profilers with the same temporal resolution as the Aquarius

data. As before, profile anomalies are formulated with respect to the WOA09 climatology and the shallowest observations of the profile are binned for the tropical Indo-Pacific region on a weekly basis using a 10-day window. Now the OI is performed in the same manner as SSS_{ISMON} anomalies except that decorrelation scales are 9.5^{o} for longitude and 4.5^{o} for latitude matching those estimated using Aquarius SSS. This weekly product is differenced from the monthly product by designating it as SSS_{IS} (for SSS in situ). Note that gridding salinity data shallower than 10 m as surface observations is a reasonable preliminary assumption based on studies that have shown that over 84% of the time salinity differences between 1 m and 10 m are less than 0.05 psu for the TAO moorings ([Henocq et al., 2010]).

In addition to the gridded OI product using near-surface in situ salinity, this dissertation also utilizes the Aquarius satellite SSS product, the mapped (Level 3) Aquarius Version 2.9.1 data (ftp podaac.jpl.nasa.gov, cd L3/mapped/V3/7day/) ([Lilly and Lagerloef, 2008]). Since the innovation of the EROKF data assimilation technique is comprised of anomalies, these are formulated by subtracting the mean WOA09 SSS seasonal cycle from Aquarius data. In addition, the mean residual seasonal cycle of the in situ OI minus WOA09 is subtracted from the Aquarius SSS to remove the bias between the in situ and satellite SSS products.

The NINO3 (5^{o}S-5^{o}N, 90^{o}W-150^{o}W) SST anomaly from [*Reynolds et al.*, 2002] is used to validate all coupled and forced model results. In addition, the NINO3.4 region (5^{o}S- 5^{o}N, 120^{o}W-170^{o}W) differentiates the central Pacific from the eastern Pacific response of NINO3. For correlation, the effective degrees of freedom (df) is calculated using the technique of [*Quenouille*, 1952] (pp. 168-170) with the equation:

df=N/(1.+2.*r_a(1)*r_b(1)+2.*r_a(2)*r_b(2)+2.*r_a(3)*r_b(3)) where N is original number of observations and r_a and r_b are autocorrelations for time series a and b, respectively for 1, 2, and 3 months lags (indicated by indices). After the effective degrees of freedom are calculated the Students T test is used to establish significance of correlation values. For all statistics, a probability of p=0.05 that a correlation is not 0. (i.e. the null hypothesis), or a significance at the 95% level will be considered significant. In order to test the impact of the various pillars in this dissertation, forecast lead time correlations will be compared between different coupled model results. Since all experiments are validated against observed SST anomalies, and so share a common variable, these correlations are not independent (known as correlated correlations). Therefore, the Steiger's Z-test [*Steiger*, 1980] will be utilized to test the significance of the differences between correlations as applied in e.g. [*Uehara et al.*, 2014]. The details follow:

$Z = [Z_{ao} - Z_{bo}] * \frac{\sqrt{N-3}}{\sqrt{2}*[1-r_{ab}]*h}$ where Z_{ao}, Z_{bo} are Fisher Z transformations of r_{ao} and r_{bo} (the correlation of experiments a and b, respectively versus observations (o), N is the number of observations and r_{ab} is the correlation between the two forecast experiments, a and b, $h = \frac{1-[f*rm^2]}{1-rm^2}$, $f = \frac{1-r_{ab}}{2*[1-rm^2]}$, and $rm^2 = \frac{r_{ao}^2+r_{bo}^2}{2}$. This technique has the benefit of normal standard distribution, so its statistical significance was tested according to the condition that |Z| > 1.96 (p = 0.05). So if the Z-critical value exceeds 1.96 then the probability, p < 0.05, passes the 95% significance level. Correlated correlations exceeding the p=0.05 level are denoted by solid lines along the top x-axis (as defined by the figure captions). In addition, the lead time amplitude of the various forecasts will be validated against observed NINO3 SST anomaly using root mean square error differences

(RMS). Standard deviation and forecast mean will also be used to compare different forecasts versus observed values.

2.2 Models and Techniques

2.2.1 Ocean Model

The primitive-equation, sigma-coordinate model with variable depth oceanic mixed layer is described in *Gent and Cane* [1989] and *Murtugudde et al.* [1996]. This ocean model is described and validated in a series of simulation studies of circulation in all three tropical ocean basins [*Hackert et al.*, 2001; *Murtugudde and Busalacchi*, 1998; *Murtugudde et al.*, 1996; *Murtugudde et al.*, 1998] and proves accurate in analyzing subtropical cells and subduction pathways [*Chen et al.*, 1994a; *Luo et al.*, 2005; *Rothstein et al.*, 1998]. Solar radiation (Earth Radiation Budget Experiment - ERBE) and precipitation from a combination of *Xie and Arkin* [1998] and Global Precipitation Climate Project - GPCP [*Adler et al.*, 2003] are specified externally. Monthly anomalies of the cloud data [NCEP Reanalysis *Kalnay et al.*, 1996] are added to the Interannual Satellite Cloud Climatology Project –ISCCP seasonal cycle [*Rossow and Schiffer*, 1991] in order to provide a more realistic mean.

Our OGCM uses the hybrid vertical mixing scheme of *Chen et al.* [1994b] which combines the advantages of the traditional bulk mixed layer of *Kraus and Turner* [1967] with the dynamic instability model of *Price et al.* [1986]. This allows simulation of all three major processes of oceanic vertical turbulent mixing - atmospheric forcing is related to mixed layer entrainment/detrainment, gradient Richardson number accounts for shear flow, and instantaneous adjustment simulates high frequency convection in the

thermocline. It is important to note that implementation of this mixing scheme has led to accurate simulation of the mixed layer and subduction pathways [*Luo et al.,* 2005]. Surface fluxes are calculated interactively by coupling the OGCM to a thermodynamic atmospheric mixed layer model [*Murtugudde et al.*, 1996] thus allowing feedbacks between SST, SSS, and surface fluxes.

The model configuration used for all simulations covers the tropical Indo-Pacific basin (34°E -76°W, 30°N-30°S) with a homogeneous longitudinal grid and a variable latitudinal grid (down to 1/3° within 10° of the equator). This resolution is dense enough to allow mesoscale eddies and realistic ITF flow that averages 12 ± 4 Sv which closely matches observed values (e.g. [*Sprintall et al.,* 2009]). The open boundaries are treated as a sponge layer within 10° of the north and south borders smoothly relaxing to WOA09. The vertical structure consists of a variable depth mixed layer and 19 sigma layers with a deep motionless boundary being specified as T_{bottom} = 6°C and S_{bottom} = 35 PSU.

The model is spun up from rest using climatological winds with the initial conditions derived from WOA09 data and is allowed to come to equilibrium after 30 years of forcing by the *ECMWF* [1994] analysis climatology. Interannual runs are initialized from this climatological spin-up and the wind speeds required for sensible and latent heat fluxes are computed from interannual ECMWF wind converted to stress using the bulk formula (ρ = 1.2 kg/m^3, $C_D = 1.2 \times 10^3$).

The Indo-Pacific version of the G+C model is validated in Figure 2.1. SL, which is an integrated response to the entire model thickness, shows a good temporal correspondence to observed values. For the equatorial waveguide (i.e. 5°N-5°S), correlation exceeds 0.8 in the Pacific. In addition to accurately capturing the Pacific

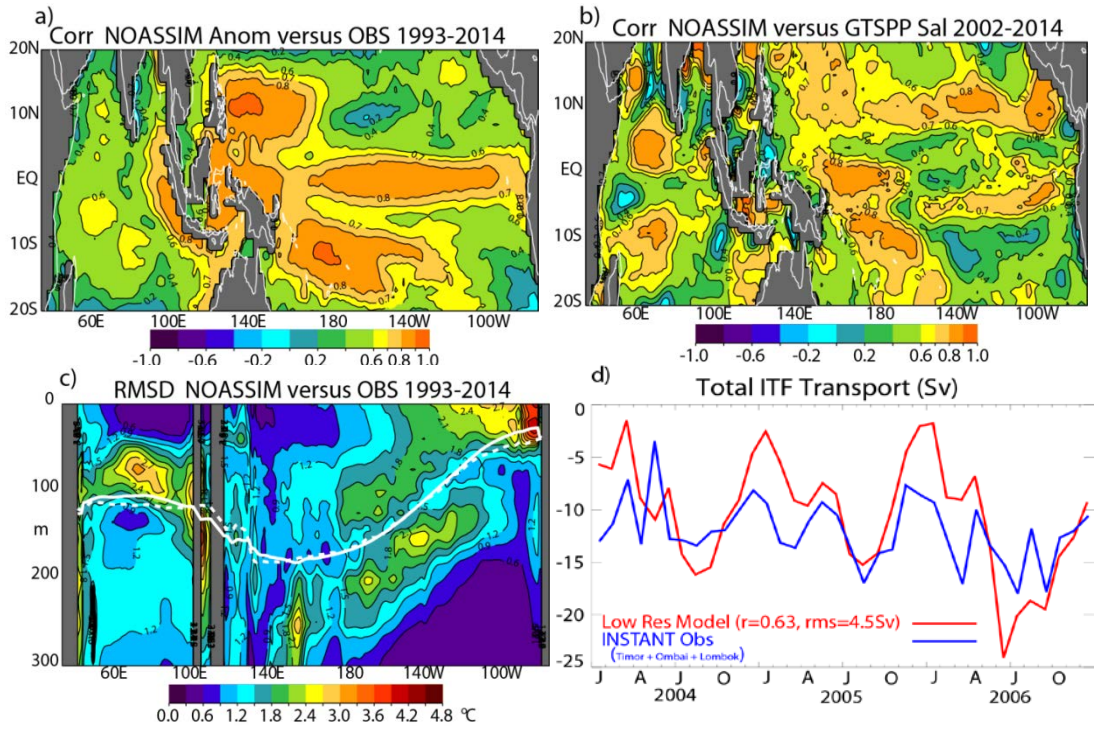

Figure 2.1: Ocean model validation. *Validation of the Indo-Pacific ocean model experiment forced by ECMWF wind stress, 1993-2014, a) correlation of SL' versus AVISO multi-satellite, b) correlation of SSS versus our gridded OI (detailed in Section 2.1), c) RMS (in ^{o}C) of equatorial T_z,, dashed (solid) lines are the mean observed (modeled) depth of the thermocline. Panel d) shows the ITF transport from this configuration of the ocean model (red) and INSTANT observations (blue line) for the period of INSTANT observations (January 2004 to December 2006).*

ENSO signal, the main interannual feature in the IO, the IODZM, is well represented in this model (Figure 2.1a). Correlation exceeds 0.6 for the western and 0.8 for the eastern dipole region of the IODZM, respectively. The equatorial subsurface temperature RMS error between model and observed is presented in Figure 2.1c. The model and observed T_z show a close correspondence with RMS errors rarely exceeding $2^{o}C$. In addition, the model (solid) and observed (dashed) mean depth of the $20^{o}C$ isotherm (representing the thermocline) overlay each other. This model is an improvement upon previous versions since riverine fresh water flux has been added using the river flow data of [*Dai and Trenberth*, 2002] . Figure 2.1b shows this improved correspondence between observed

and modeled SSS temporal signal. Note that this model is allowed to vary freely as a natural boundary condition ([*Huang*, 1993]) and only relaxes back to Levitus ([*Locarnini et al.*, 2010]) within the north and south boundary sponge layers. BLT will be a key element of this study so the good validation of SSS in the important BLT regions (i.e. northern BOB, eastern IO, Pacific warm pool, SPCZ, and ITCZ) is a particular advantage. This model also reproduces the flow of the ITF accurately as well. Figure 2.1d shows the time series of the ITF measured by the INSTANT moorings (solid) and the Sverdrup transport through 114^{o}E, between 21^{o}S-9^{o}S from the model. The ocean model reproduces the observed amplitude along with the intraseasonal to interannual variability (r=0.63, RMS=4.5 Sv).

2.2.2 Ensemble Reduced Order Kalman Filter Data Assimilation

As a baseline for some experiments, observations of satellite SL, SST, SSS, and in situ SSS, T_z, S_z anomalies are simultaneously assimilated into the model using an Ensemble Reduced Order Kalman Filter (EROKF). The equations of the reduced order Kalman filter are obtained by projecting the equations of the Kalman Filter upon a basis of Empirical Orthogonal Functions (EOFs) of the model from a long free run of the model (additional details and bibliographical references can be found in *Ballabrera-Poy et al.* [2001]).

Preliminary experiments have shown that 30 EOFs provide a reasonable compromise between accuracy, overfitting, and computational cost [*Hackert et al.*, 2007]. To reduce the pervasive effects of neglecting the complementary of the EOF subspace, which underestimates the analysis error covariance (see, for example *Cane et al.* [1996]),

an ensemble technique is used to estimate the analysis error covariance each month. At each assimilation cycle, the observations at the middle of the month are assimilated onto background states every 5 days. The numerical stability of the scheme is guaranteed by adding a constant diagonal matrix, **Q** (i.e. model forecast error), to the reduced order background error covariance which is empirically estimated from the residuals of the data-EOF fitting during the same period (see eq. (10) of *Verron et al.* [1999]).

An additional QC check to enforce the compatibility between observed and forecasted anomalies includes rejecting observed anomalies whose amplitude is larger than five standard deviations of the model anomalies at that point. This allows assimilating significant climate anomalies while filtering out data that are incompatible with the dynamics of the model. Our studies thus far have shown that typically less than 1% of the data are eliminated by this QC. Observations are projected onto the numerical grid. This approach strongly simplifies the forward observational operator, **H**. Subsurface observations are averaged if they fall within the same model grid box. For the control experiments, observational error is assumed to be 3 cm for SL [*Busalacchi et al.*, 1994] and 0.3°C for SST. The error values for the T_z and S_z were optimized by running a series of experiments assimilating each variable individually which led to values of 0.75°C and 0.31 PSU for temperature and salinity, respectively. For SSS, an observational error is chosen to be 0.2 PSU to correspond to the estimated error of Aquarius [*Lagerloef et al.*, 2008]. This value is conservative relative to the Version 2.9.1 Aquarius error estimates of -0.14 and -0.17 psu for the tropical Pacific and Indian Oceans, respectively (as reported by us in [*Lagerloef et al.*, 2013]).

2.2.3 Atmospheric Models

To investigate the coupled response of the ocean an HCM has been developed that couples the OGCM to a statistical atmospheric model (SAM) that estimates wind stress (τ) anomalies based on a singular value decomposition (SVD) analysis of the SST-τ covariance of a long simulation of the observed SST-forced ECHAM4.5 model ([*Zhang et al.*, 2006], [*Zhang and Busalacchi*, 2008], and [*Zhang and Busalacchi*, 2009]). The SST anomalies are from the extended SST reconstruction of [*Smith et al.*, 2008]; wind stress anomalies are simulated from the Max Planck Institute for Meteorology (MPI) Atmospheric GCM (ECHAM4.5; [*Roeckner*, 1996]). Wind stress data used to construct the τ model are the ensemble mean of a 24 member ECHAM 4.5 simulation for the period 1950-1999 with roughly 2.8^{o} resolution and 19 hybrid levels, forced by observed SST anomalies. As demonstrated by [*Barnett et al.*, 1993] and [*Syu et al.*, 1995], the seasonality of the atmosphere can have an important effect on the onset and evolution of El Niño. Thus, to construct seasonally dependent models for τ, the SVD analyses are performed separately for each calendar month, and so consist of 12 different sub-models, one for each calendar month. The first five SVD modes provide reasonable amplitudes of the wind stress from the model SST anomalies.

Our previously published coupled model uses the SAM which only provides monthly surface wind stress (e.g. [*Hackert et al.*, 2011]). Unfortunately, this limitation does not allow us to assess the impact of high-frequency winds and precipitation (intraseasonal to interannual variability) on coupled Indo-Pacific forecasts. Therefore, a more sophisticated atmospheric model is incorporated into our Indo-Pacific coupled

ocean model that allows separation of the wind and precipitation impacts of the IO on the coupled ENSO system. This intermediate complexity atmospheric general circulation model (AGCM), the International Centre for Theoretical Physics AGCM (nicknamed SPEEDY, for "Simplified Parameterizations, primitivE-Equation DYnamics") [*Molteni*, 2003]; [*Kucharski et al.*, 2006] follows our general coupling philosophy since it provides quality atmospheric model response yet it is relatively simple enough to be understood and efficient enough to allow many experiments to test various theories. We use SPEEDY Version 41 that has global T30 resolution (roughly 3.75^{o}) with 8 standard sigma layers (925 – 30 mb) and surface information. The winds in the tropics have been improved by adding cumulus momentum transport (CMT) to the convective parameterization code using the technique of [*Kim et al.*, 2008]. This technique transports momentum downward within subsidence regions surrounding regions of convection. Adding CMT to the atmospheric model shifts wind and western Pacific precipitation anomalies eastward, which are more in line with observations. In addition, the meridional extent of the wind is expanded due to the incorporation of the CMT. For example, [*Kim et al.*, 2008] show that 850 mb westerlies during ENSO expand from 15^{o}S-0^{o}N without CMT to 15^{o}S-10^{o}N with CMT. Implementation of CMT has also shown to improve intraseasonal precipitation, SST and winds such as those associated with e.g. Madden Julian Oscillations [*Zhou et al.*, 2012].

The winds and precipitation from SPEEDY have similar validation statistics as for other atmospheric models and observations. For example, the mean 925 mb winds of SPEEDY over the tropics closely match the European Centre for Medium-Range Weather Forecasts reanalysis (ERA - [*Gibson et al.*, 1997]). For precipitation, all the

major features of the observations (CMAP from [*Xie and Arkin*, 1998]) are reproduced by SPEEDY. However, the SPCZ has less abundant rainfall and relatively more precipitation over the tropical IO [*Molteni*, 2003]. For a full description of latest version of SPEEDY see [*Kucharski et al.*, 2013]. The SPEEDY AGCM has been successfully coupled with other ocean models for the Pacific (e.g. [*Kucharski et al.*, 2011]), Indian ([*Kucharski et al.*, 2006]), and Indo-Pacific regions (e.g. [*Kroeger and Kucharski*, 2011] [*Bracco et al.*, 2005]). Within the tropical Indo-Pacific region, our ocean model SST anomaly (SSTA) forces the SPEEDY AGCM. For the rest of the globe, the observed SSTA of HadISST [*Rayner et al.*, 2003] is used (i.e. similar to [*Kroeger and Kucharski*, 2011]).

2.2.4 Coupled Models

The ENSO simulation skill of our coupled models are comparable with most coupled systems which incorporate sophisticated ocean data assimilation (e.g., [*Ji et al.*, 1995]; [*Chen et al.*, 2000]). The overall time scale, structure, and coherent phase relationships among various atmosphere-ocean anomalies are consistent with the corresponding observations (e.g., [*Zhang and Levitus*, 1997]). While more efficient than the operational coupled models which use high resolution atmospheric models, the coupling of a SAM or SPEEDY allows multiple-sensitivity studies to quantify the impact of the ITF, atmospheric bridge, and regional assimilation on ENSO prediction and is justified since the atmospheric time scale is much shorter than the ocean's.

Our coupled models use the technique of anomaly coupling to couple the ocean and atmospheric models. Figure 2.2 schematically illustrates the SPEEDY coupling

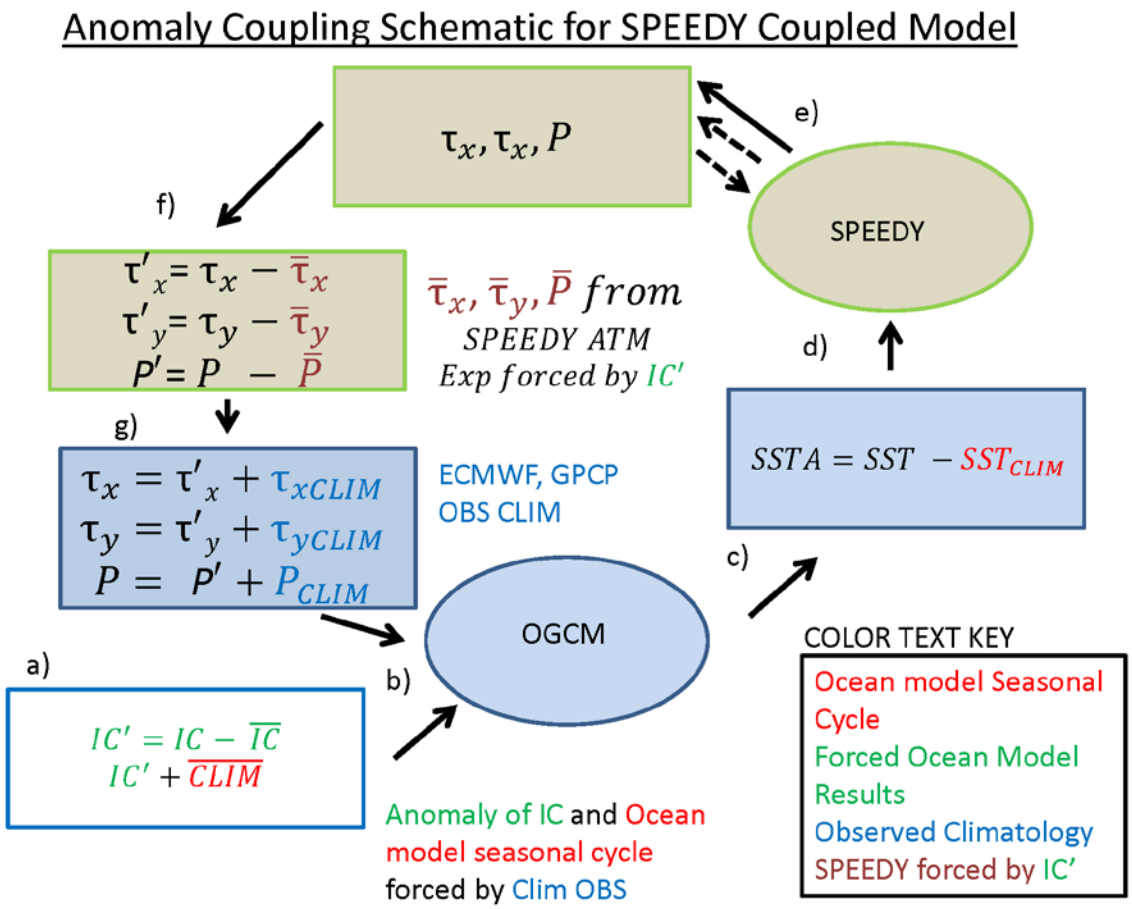

Figure 2.2: Coupled model schematic. *Schematic describing the SPEEDY coupled model. Ovals and boxes correspond to model and data, respectively. The light blue and light grey shapes correspond to ocean model and SPEEDY model, respectively. Superscript ' and overbars correspond to anomalies and means. τ and P are wind stress and precipitation, respectively and subscripts x and y stand for zonal and meridional components, respectively.*

technique. First (a) the initial conditions are formulated using the anomaly of the baseline forced ocean experiment (i.e. IC') added to the climatological mean. A typical example would be the anomaly with respect to the seasonal cycle of the IP_OPEN experiment added to the ECMWF climate forced ocean model results. These initial conditions are then used to force the ocean model (OGCM oval - b) for 30 days which produces an SST. The anomaly is formulated with respect to the ECMWF climate

experiment (SSTA – c) within the domain of the ocean model (i.e. the tropical Indo-Pacific) which is then used to force the SPEEDY atmospheric model (SPEEDY oval - d). Outside of the tropical Indo-Pacific, the observed HadISST [*Rayner et al.*, 2003] SSTA forces the global SPEEDY AGCM. The atmospheric model is spun up for 1 month and the resulting atmospheric model state is used as the initial conditions for the repeat SPEEDY experiment using the same SSTA (schematically indicated by double dashed arrows - e). Note that this is a necessary step since the atmosphere takes several weeks to spin up from rest. The SPEEDY model produces zonal and meridional wind stress (τ_x, τ_y) and precipitation (P). Anomalies are formulated with respect to the mean seasonal cycle of the similarly forced atmospheric model (f). For the IP_OPEN example, a long SPEEDY experiment was completed off-line using IP_OPEN SSTA for forcing for 1993-2014. The τ_x', τ_y', and P' anomalies are added to the ECMWF seasonal cycle (g) and used to force the OGCM for the next 30 days (back to b). Using this technique, one year forecasts are completed for each month for 1993-2014. The SAM model is simpler since the anomaly winds are determined directly by the SSTA values. The schematic (Figure 2.2) would have a line directly from the SSTA box to the box designating the forcing for the next OCGM step (but without the precipitation).

Daily wind stress, precipitation, and clouds provided by SPEEDY are important for ENSO forcing and these variables allow estimation of moisture flux from the IO to the Pacific, which is a key feature of the "atmospheric bridge" aspects of this current study. A disadvantage is that SPEEDY tends to underestimate the zonal winds associated with ENSO (e.g. [*Kroeger and Kucharski*, 2011]'s Figure 9). The advantages and disadvantages of the SAM/SPEEDY atmospheric models are demonstrated in Figure 2.3.

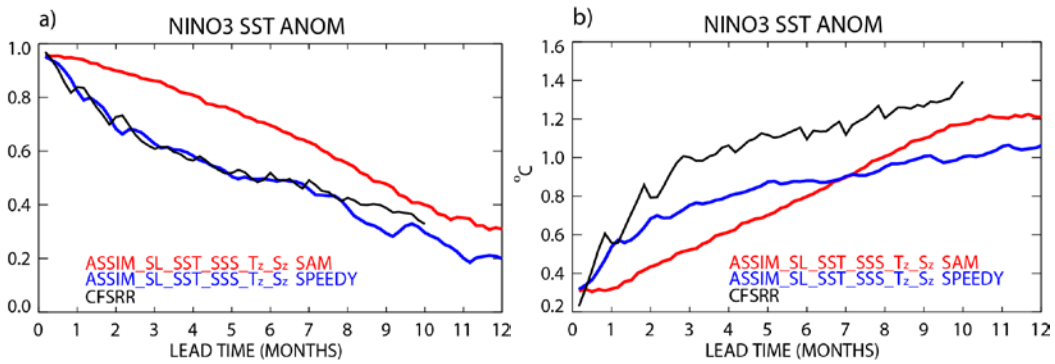

Figure 2.3: Validation of SAM and SPEEDY coupled models. *Our Indo-Pacific coupled models that assimilate all available satellite (SL, SST) and in situ information (SSS, T_z, S_z) for SAM (red) and SPEEDY (blue) are a) correlated and b) RMSD against observed NINO3 SST anomaly for Jan. 1993-Mar. 2011. CFSRR coupled model results (black) are included to put our HCM results into the context of a more widely known coupled model. Individual correlations exceed the 95% significance out to 10.4 (31), 8.3 (35) and 10 months (34) (effective degrees of freedom) for red, blue and black lines, respectively. Note that our HCM validation statistics are comparable to CFSRR system of NCEP and all validate well against observations.*

Although the SAM outperforms SPEEDY for the temporal validation (Figure 2.3a) both models have significantly better correlation than observation persistence after 4 months (not shown). For the amplitude, SPEEDY (blue) outperforms SAM (red) after 6 months (Figure 2.3b) and both outperform observation persistence after 3 months (not shown). Because of the advantages/disadvantages for the two different atmospheric models, both the SAM HCM along with this more sophisticated, SPEEDY version of the coupled code are executed to assess the impact of IO and SSS on ENSO coupled predictability depending on the problem being investigated. Utilizing both the statistical atmospheric model and the more complex SPEEDY atmospheric model will provide us an efficient set of tools to isolate the modes of the wind and precipitation.

In order to put our results in the context of operational models, we include the Climate Forecast System Reanalysis Reforecast ([*Saha et al.*, 2014]) as a reference (Figure 2.3 - black line). The coupled hindcasts are comprised of the atmospheric

assimilation/model with resolution ~38 km (detailed in [*Saha et al.*, 2010]) along with the MOM4 ocean model ([*Griffies et al.*, 2004]) with 0.5^{o} resolution within 30^{o}N-30^{o}S and the Global Ocean Data Assimilation System (GODAS) ocean assimilation ([*Behringer*, 2007]) of all available oceanic in situ data. The CFSRR model was chosen to substantiate our coupled model results since it is a well-known, state of the art, operational coupled model (i.e. the reanalysis, reforecast version of CFSv2). For Figure 2.3, the SAM results (red) outperform the CFSRR (black) as validated by correlation with observed NINO3 SST anomaly. However, for these long validation runs (i.e. January 1993 to March 2011), the SPEEDY correlation results (blue) are equivalent with the CFSRR forecasts. For RMSD validation, both the SAM and SPEEDY outperform the CFSRR for all lead times. CFSRR RMSD errors with observed NINO3 SST anomalies rise as high as 1.4^{o}C at 10 month lead times whereas SAM never exceed 1.2^{o}C and SPEEDY results are only 1^{o}C for the same lead time. In any case, the point of including the CFSRR results is to show that our coupled models validate at least as well as the NOAA operational model.

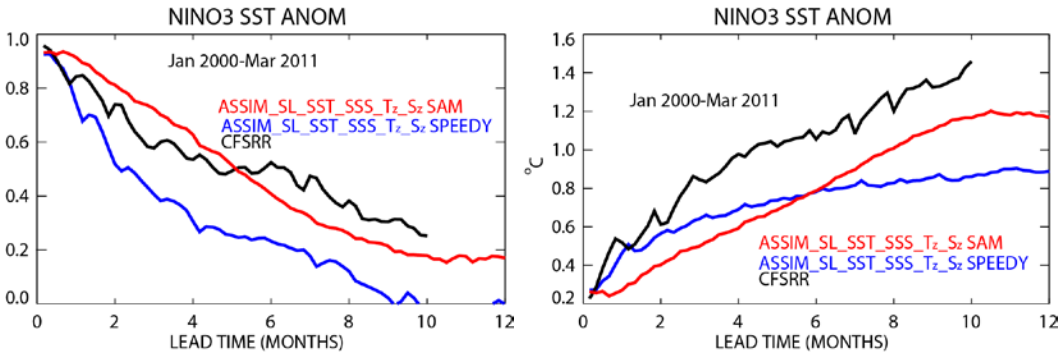

Figure 2.4: Validation of SAM and SPEEDY for independent period. *Same as Figure 2.3 but for January 2000 to March 2011, a period that is independent of training period for the SAM model (i.e. 1950-1999). Individual correlations exceed the 95% significance out to 5.5 (19), 2.8 (21) and 4.4 months (20) (effective degrees of freedom) for red, blue and black lines, respectively.*

Since the SAM model uses the period from 1950-1999 for training, the results from Figure 2.3a for January 1993 until March 2011 may contain artificial skill. Therefore, we include the validation of both SAM and SPEEDY coupled models against observations for the independent period, January 2000 to March 2011 in Figure 2.4 Not surprisingly, the overall skill is reduced for correlation since this period excludes the major ENSO event of 1997-98 and represents a similar degradation in skill as found in the IRI suite of operational models for 2002-2011 ([*Barnston et al.*, 2012]). However, both experiments outperform observed persistence after 5 months (not shown) and the relative relationship between SAM and SPEEDY remains similar but now the CFSRR results are more in line with SAM HCM. SAM probably outperforms SPEEDY for correlation since SAM has fewer degrees of freedom (i.e. only 5 SVD modes) and so generates less noise than SPEEDY (a dynamical model) with the same SST' forcing. In any case, the NINO3 RMS differences for both the SAM and SPEEDY experiments are similar and still have lower RMS with observations as compared with the CFSRR model results and they both have lower RMS than persistence (after 3 months, not shown).

As an additional first-order validation of the atmospheric components of the coupled models, the atmosphere-only model results for SAM and SPEEDY are correlated with observations that had previously been used to force the ocean model. Both the SAM and SPEEDY atmospheric models are forced by ocean model SST results that assimilate all available observations (i.e. SL, SST, SSS, T_z, and S_z) for 1993-2014. For example, Figure 2.5a shows the results of the SPEEDY atmosphere results versus ECMWF zonal wind. The correlation is generally high between 20^oS-20^oN. On the other hand, highest correlation is restricted to between 15^oS to 5^oN for the SAM results Figure 2.5c and so

the ITCZ is poorly reproduced. Since the SAM only retains 5 modes, only the large-scale ENSO wind signal is reproduced. In any case, both models validate well near the equator. For precipitation (Figure 2.5b), the SPEEDY results are validated against the GPCP forcing [*Adler et al.*, 2003]. The eastern Pacific, eastern ITCZ, SPCZ, and Indonesian Seas have the highest correlations. For a more comprehensive validation of the SPEEDY atmospheric model versus the European Centre for Medium-Range Weather Forecasts reanalysis (ERA -[*Gibson et al.*, 1997] over the period 1981-1990 see [*Molteni*, 2003].

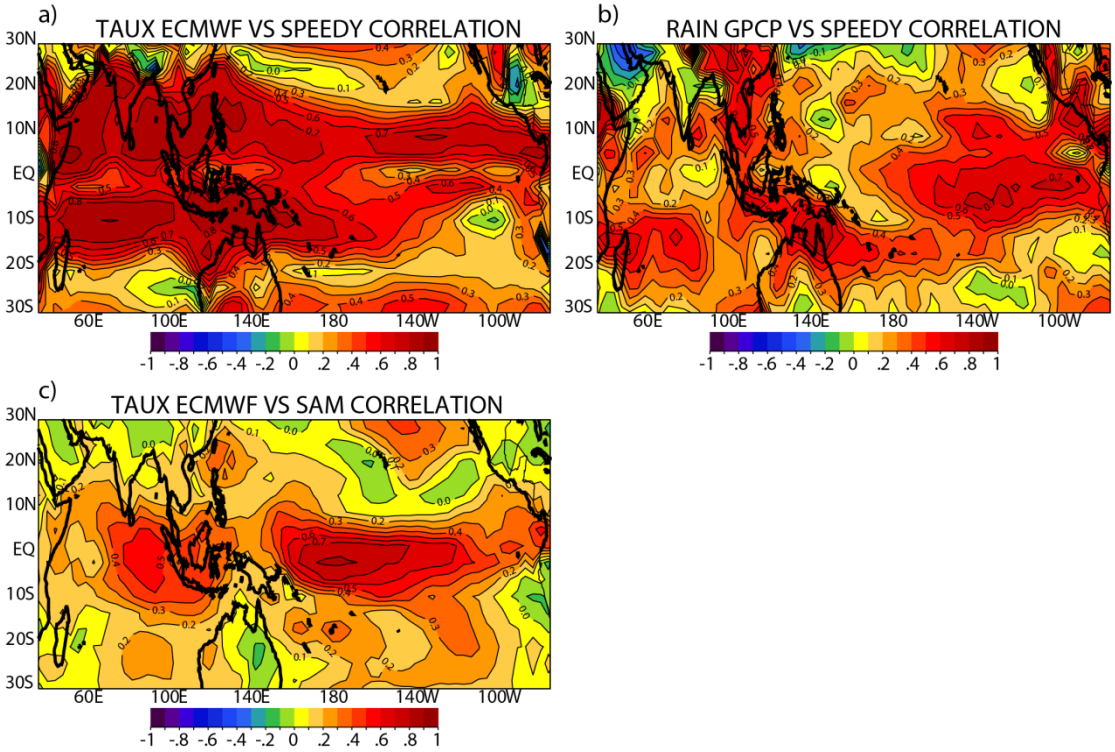

Figure 2.5: Validation of SPEEDY and SAM versus observations. *Correlation of SPEEDY a) zonal wind stress versus observed ECMWF winds and b) precipitation versus GPCP for 1993-2014. Panel c) same as a) but for SAM zonal wind stress. Correlations exceeding r=0.12 are significant at the 95% level for >180 estimated degrees of freedom.*

3 Role of the Indian Ocean Sector – Oceanic Impact on Coupled Predictability

Even though many operational models typically have relatively high resolution for the Indonesian Seas the Indonesian Throughflow (ITF) is not necessarily well represented. For example, the NCEP GODAS (i.e. the ocean model of the CFSv2) has 1^o x $1/3^o$ resolution [*Behringer*, 2007]) but represents the ITF as a single channel that flows from the Pacific to the IO between Sulawesi and the western tip of Western Papua New Guinea, closing the Makassar Strait and with it all the flow through the Banda Sea. The flow of the real ITF is more complicated as shown in Figure 1.1. In addition, the flow of the ITF is poorly observed and thus poorly validated in ocean models ([*Susanto and Song*, 2015]). Therefore, coupled hindcast experiments are performed with and without the ITF in order to test the potential for the oceanic contribution of the Indian Ocean for improving coupled ENSO forecasts.

By artificially closing the ITF, forced ocean and coupled models show the important impact that the IO has on the Pacific via the ITF (e.g. [*Hirst and Godfrey*, 1993]; [*Murtugudde et al.*, 1998], etc.). Later work by [*Schneider*, 1998], [*Wajsowicz and Schneider*, 2001] and [*Song et al.*, 2007] revealed that closing the ITF significantly impacts the Indo-Pacific circulation thus effecting ENSO. By closing the ITF in a coupled model, [*Santoso et al.*, 2011] and [*Kajtar et al.*, 2015] suggested an eastward shift of the biggest ENSO signal from the NINO3.4 region to the NINO3 region and attributed this to changes in the fetch of the Bjerknes coupling. Contrary to the earlier work of [*Song et al.*, 2007], [*Santoso et al.*, 2011] showed that closing the ITF led to weaker total variability. [*Yuan et al.*, 2013] and [*Schiller et al.*, 2010] showed that IO

Kelvin waves can penetrate the ITF and the former demonstrated how the IO Kelvin wave was significantly correlated with the following season NINO3.4 index. Thus, significant changes in the equatorial Pacific brought about by closing the ITF point towards the potential key importance of the IO for ENSO predictions. Unfortunately, all previous studies have focused on the impact of the IO using either forced ocean, idealized coupled model experiments or observational statistics. Therefore, here we present experiment pairs that isolate the role that the IO plays in ENSO predictability using a realistic hindcast model experiment design and anchoring our results by using observed NINO3 SST anomalies for 1993 to 2014.

3.1 Forced Ocean and Atmospheric Results: IP_OPEN – IP_NOITF

Experiment Name	Period	Model Geometry	Forcing
IP_OPEN	1993-2014	Indo-Pacific, 1^{o}x$1/3^{o}$ stretched, 34^{o}E-76^{o}W, 30^{o}N-30^{o}S, realistic coastlines, ITF open	Interannual Wind Stress from ECMWF, Precip. from a combination of GPCP and TRMM, and Clouds from NCEP reanalysis anomaly added to ISCCP seasonal cycle
IP_NOITF	1993-2014	Indo-Pacific, 1^{o}x$1/3^{o}$ stretched, 34^{o}E-76^{o}W, 30^{o}N-30^{o}S, realistic coastlines, ITF closed	Interannual Wind Stress from ECMWF, Precip. from a combination of GPCP and TRMM, and Clouds from NCEP reanalysis anomaly added to ISCCP seasonal cycle

Table 3.1: Open and NOITF Experiment description. *Table showing the model configuration and forcing for the IP_OPEN and IP_NOITF experiments. The ocean model is forced by ECMWF analysis 10m winds [ECMWF, 1994], NCEP Reanalysis cloud cover [Kalnay et al., 1996] and satellite derived precipitation estimates , GPCP [Adler et al., 2003] combined with TRMM [Kummerow et al., 2000] after October 2014. All these experiments are no assimilation.*

To highlight the impact of the IO oceanic contribution to ENSO forecast skill, forced model results with the ITF closed (IP_NOITF) are subtracted from those with the ITF open (IP_OPEN). Henceforth, these differences will be used synonymously with the phrase "oceanic contribution" or "oceanic process" of the IO. These two experiments are detailed in Table 3.1 and the results of these differences are shown in Figure 3.1 and Figure 3.2. Figure 3.1a shows the differences for currents. The flow through the ITF is emphasized by the red arrows. To the north of the Makassar Straight, the Mindanao current flows southward. To the south, the surface signature of the New Guinea coastal undercurrent along the New Guinea coast joins with the Pacific South Equatorial Current (SEC) to originate the flow into the Indonesian Seas. The ITF flows south in the Makassar Strait and exits into the IO via the Timor Passage. Note that this model configuration combines the outflow of Lombok, Ombai and Timor into a single passage as required by the coarse model resolution. Even with this limitation this model accurately reproduces the total and anomalous flow of the ITF (e.g. Figure 2.1d). After exiting the Indonesian Seas, the ITF flow merges with the IO South Equatorial Current (SEC). The current differences, are consistent with earlier work (e.g. [*Hirst and Godfrey*, 1993]). Figure 3.1b shows the corresponding SST differences. The entire Pacific is colder with the minimum centered in the upwelling region of the eastern Pacific. On the other hand, the IO is warmer with the maximum located in the outflow region of the ITF in the eastern IO at about 15^{o}S. This can be explained by the fact that the ITF normally transports warm, fresh water from the Pacific to the IO. When the ITF is closed, the warm water remains in the Pacific and the sign of the differences are negative in the Pacific and positive in the IO.

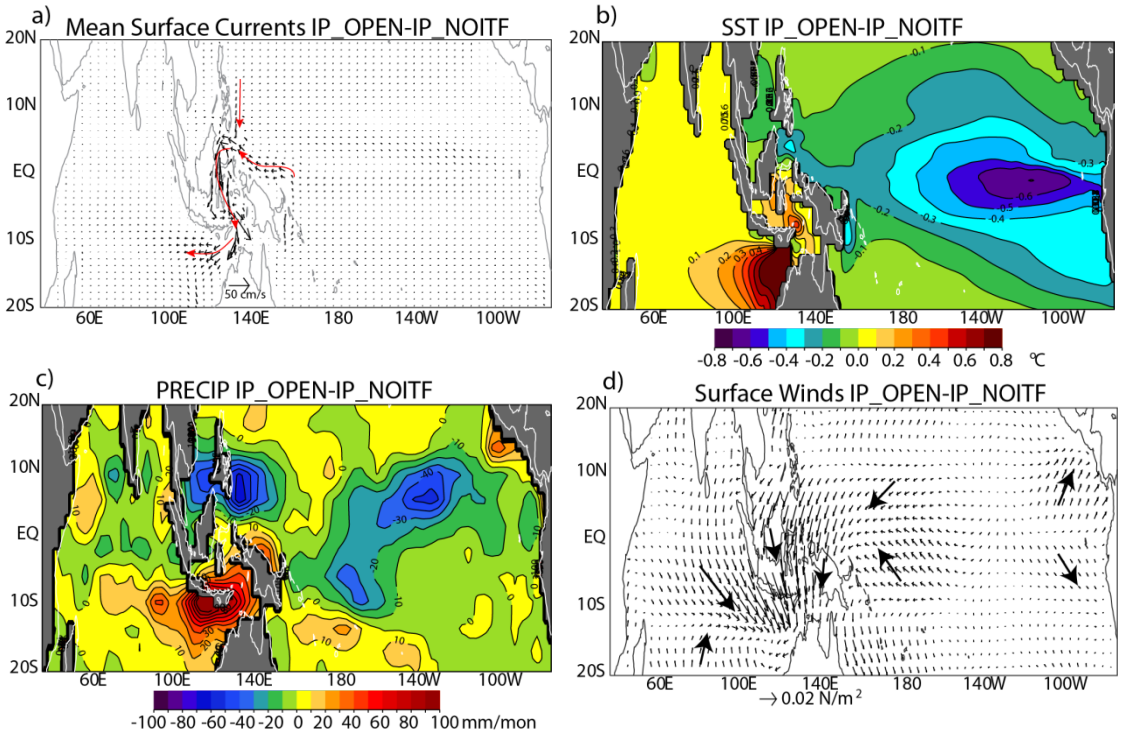

Figure 3.1: Spatial results of IP_OPEN minus IP_NOITF. *Annual mean oceanic contribution for 1993-2014 for a) mixed layer depth currents (red arrows highlight major features of the ITF), b) SST, c) precipitation, and d) surface wind stress (heavy arrows are added to emphasize wind direction). Note that wind stress and precipitation results are generated by forcing two SPEEDY atmospheric experiments with the forced ocean model SST anomalies and differencing the one forced by the IP_OPEN minus the IP_NOITF results. Absolute values exceeding 6.3 cm/s, 0.5^{o}C, 38.6 mm/mon, and 4.9x10^{-3} N/m^{2} are significant for the four panels, respectively.*

In order to diagnose the oceanic impacts (i.e. the ITF) on the atmosphere (i.e. not coupled), two sets of forced atmospheric model experiments are also completed. In one, the SST anomaly for IP_OPEN is used to force the SPEEDY atmosphere for 1993-2014. A similar atmospheric model experiment is forced by the IP_NOITF SST anomaly. Then the resulting winds and precipitation are differenced in the same manner as the ocean variables (i.e. IP_OPEN-IP_NOITF) over 1993-2014. Precipitation and wind stress results are presented in Figure 3.1c and d, respectively. For precipitation, largest differences correspond to important regions of convergence and divergence and SST anomalies. For example, the rainfall is mostly deficient in the Pacific. The rainfall is

especially lacking over the Inter-tropical Convergence Zone (ITCZ) at 5^{o}N, 140^{o}W and in the South Pacific Convergence Zone (SPCZ) at 10^{o}S, 170^{o}W due to the damping effect of cooler SSTs in the IP_OPEN versus IP_NOITF case. On the contrary, the eastern IO and Indonesian Seas show unusually abundant rainfall due to the enhanced atmospheric convection associated with the large SST anomaly near the outflow region of the ITF at 120^{o}E, 12^{o}S. The general character of the pattern of the precipitation differences is opposite to the errors found in the CFS. Namely, the CFS errors show too much rainfall over the ITCZ, SPCZ and too sparse precipitation for the Maritime Continent with respect to observations ([*Wang et al.*, 2010]).

In the eastern Pacific, east of the coldest SST, winds are weakly diverging away from the equator with northwesterlies to the south and southwesterlies to the north of the equator (Figure 3.1d). To the west of the coldest SST (about 140^{o}W), winds converge towards the equator with southeasterlies to the south and northeasterlies up to $1x10^{-2}$ N/m^2 to the north of the equator. In the very far western Pacific, northerly winds flow across Indonesia. Over the eastern half of the IO, the northwesterlies converge towards the warmest SST anomaly in the IO located near the exit of the ITF at 120^{o}E, 12^{o}S. To the south of there, southerlies converge towards 10^{o}S.

Figure 3.2e shows the average temperature between the surface and 300 m. Negative values predominate over the tropical Pacific consistent with the idea that the ITF carries warm water from the Pacific to the IO and IP_OPEN is thus cooler (i.e. negative) with respect to IP_NOITF. For salinity, the fresh water transported by the ITF makes the IO fresher with reduced SSS and at the same time mostly the entire tropical Pacific is saltier. Positive and negative maximum differences correspond to the

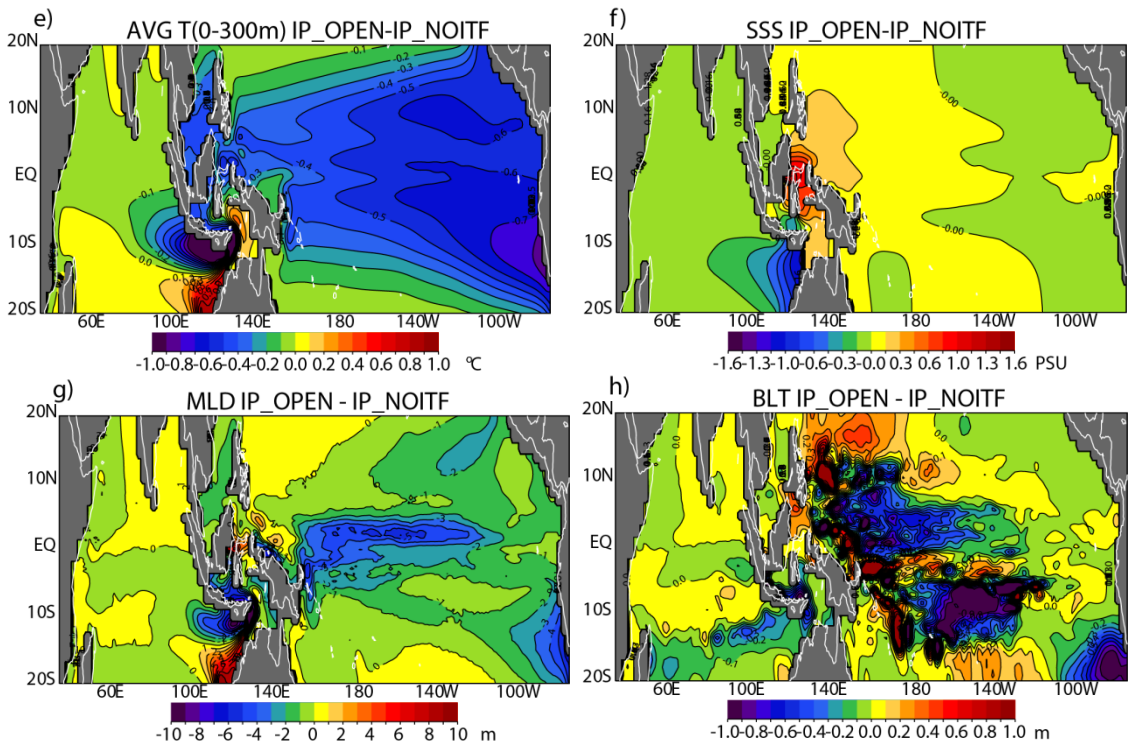

Figure 3.2: Spatial results of IP_OPEN minus IP_NOITF continued. *Same as Figure 3.1 for e) average temperature between 0-300 m (representing heat content), f) sea surface salinity (SSS), g)mixed layer depth (MLD) using the equivalent density criteria of 0.5^{o}C of [Sprintall and Tomczak, 1992], and h) barrier layer thickness (smoothed 5 times). Absolute values exceeding 0.83^{o}C, 0.3 PSU, 3.9m, and 0.85m are significant for the four panels, respectively.*

maximum regions of ITF transport in the western Pacific and in the eastern IO, respectively. The open ITF leaves a shallower mixed layer depth (MLD) for the Pacific but the impact is mostly felt just north of the equator in the western Pacific where differences are as big as -5 m (Figure 3.2g). In the IO, the MLD is deeper to the south and shallower to the north of the ITF exit due to the relative upwelling and downwelling associated with the positive/negative curl of ITF jet, respectively. Similar plots of the barrier layer thickness (BLT) (Figure 3.2h) shows shallower BLT for the open ITF over most of the western Pacific especially in regions where BLT are actually observed between 140^{o}E-180^{o}, 10^{o}S-5^{o}N (see Figure 1.3a). The IP_NOITF case allows more fresh

water to be trapped in the Pacific due to the land bridge and is thus available to form a deeper BLT, hence the negative values. For the IO, the negative values stretching from the mouth of the ITF towards the southwest are attributed to the fact that the IP_NOITF model produces a spurious BLT in boreal spring that is not present in the observations (Figure 1.3c).

If the sign is flipped, all of the results presented in Figure 3.1a-d and Figure 3.2e-f generally match those found in [*Song et al.*, 2007] Figure 1.5a-f. Note that the sign difference can be accounted for by the fact that Figure 1.5 is oriented NOITF-OPEN and Figure 3.1and Figure 3.2 are IP_OPEN - IP_NOITF. Also note that these results in Figure 3.1 and Figure 3.2 use real interannual forcing from 1993-2014 whereas Figure 1.5 uses 200 year simulation of a freely coupled model (i.e. CM2.1). For both, flow and transport of the ITF are clearly evident. When open, the ITF normally drains warm fresh water of the Pacific into the IO, winds are predominantly easterly over the western half of the equatorial Pacific and precipitation is deficient over the tropical Pacific. The IO is generally warmer and fresher, northwesterly winds converge at the mouth of the ITF, and precipitation is abundant over Indonesia and at 10^{o}S. The fidelity between the forced versus freely coupled model (i.e. for Figure 3.1, Figure 3.2 against Figure 1.5) shows consistent results and so reinforces the patterns for the oceanic impact of the ITF.

To test if the oceanic contribution of the IO impacts ENSO predictability we first investigate if the IP_OPEN – IP_NOITF differences have any relationship with observed ENSO. Therefore, the differences between NINO3 SST anomaly values from 1993-2014 (red line) are compared to the observed anomaly (blue line) in Figure 3.3. Although the scale of the differences, i.e. ~7% of the magnitude of the NINO3 anomalies, are relatively

smaller than those of [*Santoso et al.*, 2011] (i.e. 9% for Ekman to 39% for zonal advection terms of the Bjerknes coupled stability index) our results should be smaller since we are comparing two experiments forced with observed winds and precipitation whereas they use a freely coupled model. In any case, Figure 3.3 shows the high correspondence between the impact of the IO oceanic contribution and the observed

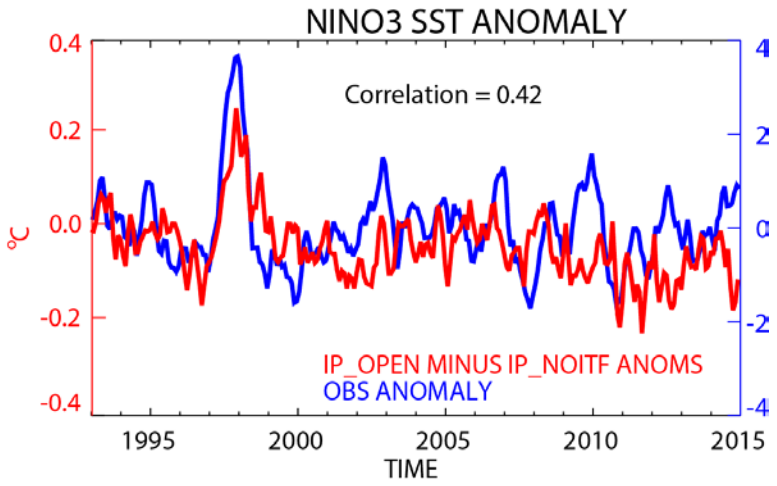

Figure 3.3: NINO3 SST IP_OPEN minus IP_NOITF anomalies versus observed. *Time series of NINO3 SST for IP_OPEN anomaly minus IP_NOITF anomaly (red) versus observed anomaly (blue). The correlation between the two lines is r=0.42 which is significant at the 99.9% level with 58 calculated effective degrees of freedom.*

NINO3 highlighting that the ENSO response of the IP_OPEN amplitude is larger than IP_NOITF. In other words, El Niño and La Niña amplitudes are larger for IP_OPEN versus IP_NOITF. Correlation between the time series is r=0.42 significant at the 99% level using 58 for the effective degrees of freedom (see Section 1.5 for details on how effective degrees of freedom are calculated). Thus, the IP_OPEN scenario allows for more variability of ENSO events for forced ocean model results and this aspect reinforces the work of [*Santoso et al.*, 2011].

Another way to envision the amplitude of IP_OPEN versus IP_NOITF is to show the recharge/discharge plots for the two experiments. [*Jin*, 1997] hypothesized that prior

to El Niño, heat is built up in the western Pacific and then heat is discharged to the east and poleward via both Kelvin and Rossby waves during El Niño. This process is conveniently illustrated using the amplitude of the NINO3 SST anomaly for the abscissa and average depth of the 20^{o}C isotherm anomaly for the western Pacific (5^{o}S-5^{o}N, 120^{o}E-180^{o}E) for the ordinate. This recharge paradigm is best demonstrated by the big El Niño of 1997 (Figure 3.4). Prior to the big event, from 1995 into 1996 (i.e. light green to yellow lines); the equatorial western Pacific recharges its heat and increasing the depth of the 20^{o}C isotherm. Then in 1997 (orange), the El Niño occurs with rising NINO3 SST anomalies (sliding to the right on this chart). At the same time the western Pacific heat content discharges (dropping down on the chart) and the values for the western Pacific heat content proxy (i.e. depth of the 20^{o}C isotherm) drop precipitously. After that, from 1998 until 2000 (deep orange to red line) the ocean recharges itself with the NINO3 SST anomaly drifting towards La Niña and the depth of the 20^{o}C isotherm climbing above zero. It is reassuring that the general character for the observations match those of the model results – for Figure 3.4, Figure 3.5, Figure 3.6 the right panel generally matches the left. For the purposes of this study, it is particularly interesting to note that the IP_NOITF experiment tends to underestimate the amplitude of both El Niño and La Niña. For example, the 1998 peak (Figure 3.4a) the IP_NOITF (orange dash line) shows weaker El Niño amplitude than the IP_OPEN (solid orange). The amplitude of IP_NOITF is weaker for the strong 2010-2012 La Niña as well (Figure 3.6a). On the contrary, for the weaker El Niños of 2002 and 2009 and La Niña of 2007, the relationships between the IP_NOITF and IP_OPEN are less conclusive (Figure 3.5a).

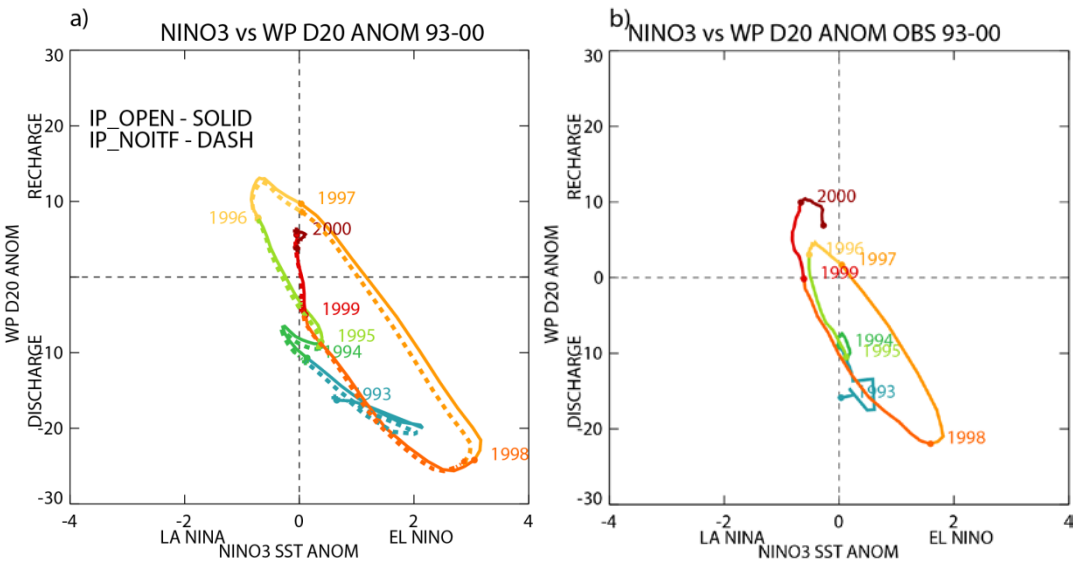

Figure 3.4: ENSO Recharge/discharge plots 1993-2000. *These plots represent the recharge/discharge of [Jin, 1997] and shows the NINO3 SST anomaly (abscissa) versus the depth of the 20°C isotherm (ordinate) for the western Pacific (120°E-180°E, 5°S-5°N). For a) each year is represented by a solid (dashed) line for the IP_OPEN (IP_NOITF) for 1993-2000. Dots and crosses and the year mark the beginning of each year for IP_OPEN and IP_NOITF, respectively. Similar calculations are compiled for observations (from the optimal interpolation of all available in situ temperature) and similar decades are presented in panels b).*

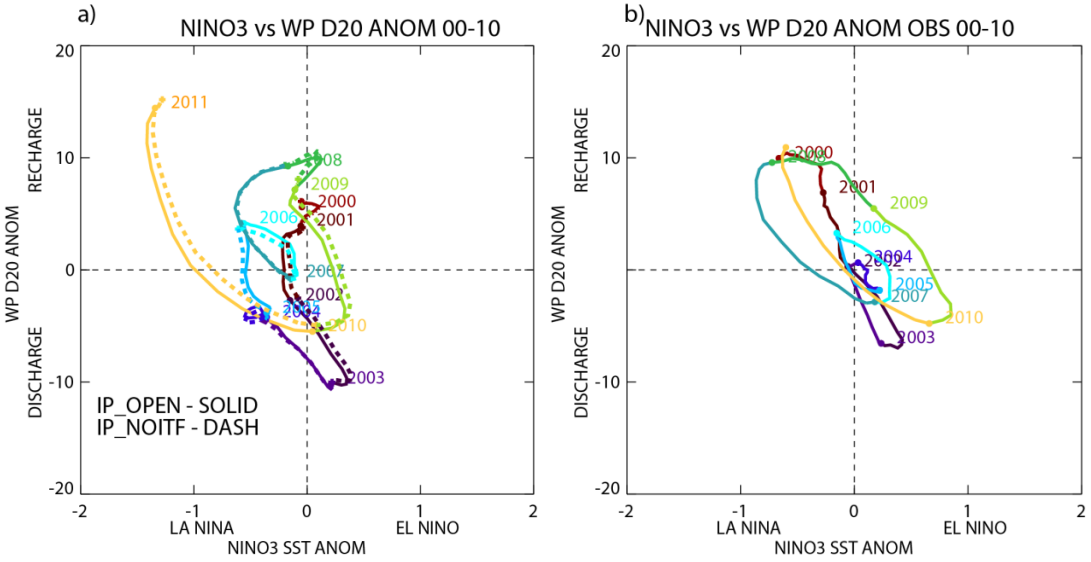

Figure 3.5: ENSO Recharge/discharge plots for 2000-2010. *Same as Figure 3.4 but for 2000-2010.*

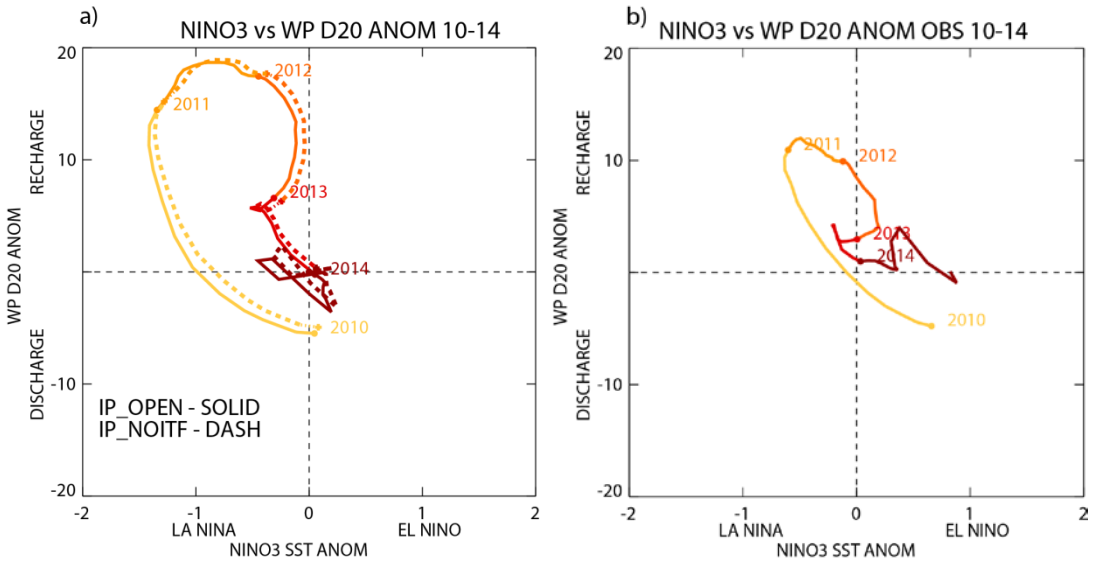

Figure 3.6: ENSO Recharge/discharge plots 2010-2015. *Same as Figure 3.4 but for 2010-2015.*

This feature for the 2000's and the change of the phase relationship seen after 2007 in Figure 3.3 may be attributed to lower variability and weaker predictability during this period as suggested by [*Barnston et al.*, 2012]. However, the relationship between IP_NOITF having weaker ENSO amplitude is broadly confirmed with these plots, matching the results of and the overall highly significant correlation of r=0.42 between the IP_OPEN – IP_NOITF differences and observed NINO3 SST anomaly.

One would expect that the IP_OPEN would have larger amplitude events given that the MLD is shallower for IP_OPEN (Figure 3.2g) and that both the IP_NOITF and the IP_OPEN experiments use the exact same forcing (both wind and fresh water flux). Identical forcing acting on a shallower MLD should yield higher amplitude large-scale oceanic Kelvin and Rossby waves leading to bigger ENSO signal. Another way to say this is that a thinner MLD would generate oceanic waves more efficiently. In order to test this hypothesis and to rule out that the amplitude of the IP_NOITF is damped due to changes in model geometry and large-scale ocean wave processes, a wind stress index

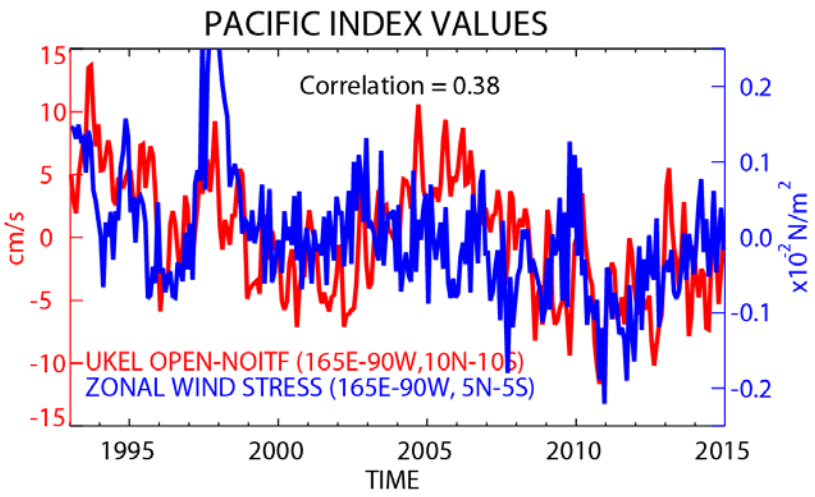

Figure 3.7: Kelvin currents versus index of zonal wind stress. *IP_OPEN and IP_NOITF SL results are first decomposed into longitude/time Kelvin/Rossby waves using the methodology of [Delcroix et al., 1994] and then differenced. The resulting Kelvin zonal current index (165°E-90°W, 10°S-10°N) in red is compared to the mean zonal wind stress anomaly index from the ECMWF analysis over the equatorial Pacific (165°E-90°W, 5°S-5°N) in blue. The correlation, r=0.38, is significant at the 99.9% level with 70 calculated effective degrees of freedom.*

covering the tropical Pacific (5°N-5°S, 165°E-90°W) is compiled using the anomalies of ECWMF analysis winds from 1993-2014 (i.e. those used to force both the IP_OPEN and IP_NOITF experiments). In addition, we have converted the model SL anomalies into the Kelvin and Rossby components for the IP_OPEN and IP_NOITF model results using the technique of [*Delcroix et al.*, 1994]. The Kelvin currents were differenced, IP_OPEN – IP_NOITF, and these were converted into an index for the tropical Pacific using the largest available land-free area possible (10°N-10°S, 165°E-90°W). Figure 3.7 shows the time series of this tropical Pacific Kelvin wave index versus zonal wind anomaly. The correlation of r=0.38 is significant at the 99.5% level and shows that the Kelvin wave differences are attributed to the wind dynamics acting upon the different model states (i.e. shallower MLD of IP_OPEN). In other words, the shallower MLD for the IP_OPEN generates higher amplitude Kelvin waves and has larger ENSO response even though the forcing is the same for IP_OPEN and IP_NOITF.

3.2 Coupled Model Results: IP_OPEN – IP_NOITF

Unlike all previous published research, the oceanic impacts of the ITF influence on the coupled ENSO response are tested here in realistic hindcast experiment scenarios. In order to isolate the impact of the IO on coupled ENSO forecasts, we compare and contrast two experiments, one has the ITF open (IP_OPEN) and the other artificially closes the ITF (IP_NOITF). For both experiments, IP_OPEN and IP_NOITF, the forced-ocean anomalies are used to initialize 12 month coupled experiments for each month from 1993 to 2014. The coupled results are validated using anomaly correlation coefficient and root mean square error (RMS) with observed NINO3 SSTA in Figure 3.8. These standard metrics measure the quality of the forecast pattern and the agreement of the amplitude of the anomalies, respectively [*Jin et al.*, 2008]. For the SPEEDY coupled model, the oceanic impact of IO has higher correlation from month 2 until month 10 with the IP_OPEN (red) generally outperforming the IP_NOITF (blue line) correlation results. Specifically, the individual validation of the IP_OPEN versus observations remains

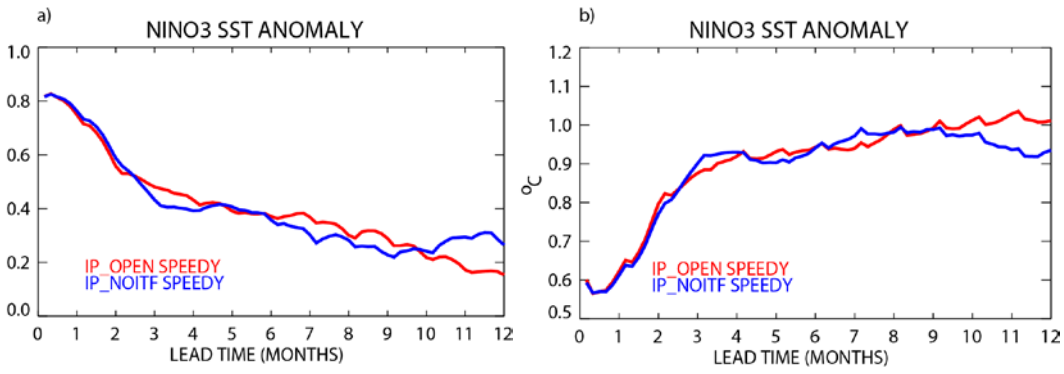

Figure 3.8: Validation of IP_OPEN and IP_NOITF coupled results. *Validation statistics for a) correlation and b) RMS differences between IP_OPEN (red) and IP_NOITF (blue) SPEEDY coupled model results. The experiments are validated with respect to the observed NINO3 SST anomaly for 1993-2014. Individual correlations exceed the 95% significance out to 8 (43) and 7 months (41) (effective degrees of freedom) for red and blue lines, respectively.*

significant from 0-8 month forecasts whereas the IP_NOITF experiment only surpasses the 95% level of significance out to 7 months. However, Figure 3.8a shows that the differences between the results initialized by the IP_OPEN and IP_NOITF give statistically similar results using the Steiger's Fisher Z test. For RMSD (Figure 3.8b), the story is similar since IP_OPEN (red) and IP_NOITF (blue) nearly overlay one another. Therefore, all that can be said is that both IP_OPEN and IP_NOITF have similar validation characteristics.

Although the correlation and RMSD differences between the coupled model results for IP_OPEN and IP_NOITF appear similar when validating against observations, it is important to note that the anomaly coupling technique used here specifically excludes the biases between the IP_OPEN and IP_NOITF (i.e. the patterns found in Figure 3.1 and Figure 3.2 are unaccounted for in the coupled model comparisons). In other words, the anomaly coupling technique uses internally consistent means for formulating initial conditions (see Figure 2.2a), SST anomalies (Figure 2.2c), and for creating the forcing anomalies (Figure 2.2f).

Due to the limitation of the anomaly coupling technique correlation and RMS statistics versus observed anomalies do not provide any unique insights. However, as pointed out earlier in Section 3.1 we demonstrated that the thinner MLD of the IP_OPEN experiment yields stronger Kelvin/Rossby waves leading to enhanced variability in the NINO3 region. To represent this variability, the standard deviation of the NINO3 and NINO3.4 region SST anomalies are presented in Figure 3.9a and Figure 3.9b, respectively. Both the standard deviation forecast statistics are larger for the IP_OPEN (red) versus IP_NOITF (blue). These results reconfirm those of [*Santoso et al.*, 2011]

who showed that the closed scenario has weaker total variability. Unlike [*Santoso et al.*, 2011] and [*Kajtar et al.*, 2015] who found that the region of highest variability shifted from NINO3 for IP_NOITF to NINO3.4 for IP_OPEN, the region of highest variability remains in the NINO3.4 region regardless of whether the ITF is open or closed for our experiments. An additional unique aspect of this current research is that the IP_OPEN experiment does a significantly better job of reproducing the real observed variability (as high as ~20% improvement). For both the NINO3 and NINO3.4 regions (Figure 3.9a and Figure 3.9b, respectively), the coupled model variability of the IP_OPEN results (red) more closely matches observed variability (signified by the dashed line) of 0.90°C and 0.86°C, respectively.

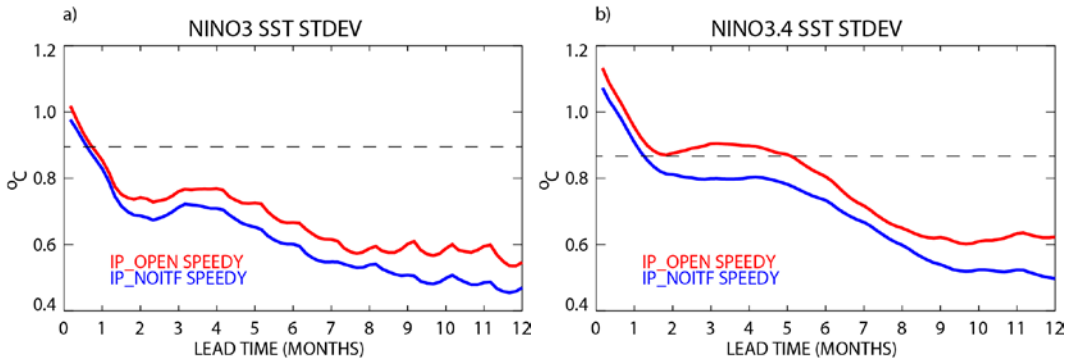

Figure 3.9: Standard deviation of IP_OPEN and IP_NOITF results. *Coupled model standard deviation statistics for SST anomaly for a) NINO3 and b) NINO3.4 regions for IP_OPEN (red) and IP_NOITF (blue). The dashed lines correspond to the observed values of 0.9°C and 0.86°C for the observed variability from 1993-2014 for the two regions, respectively.*

Although our standard anomaly coupling technique leads to inconclusive correlation and RMS of contribution of the IO as validated by observations, we can estimate the impact of the IP_OPEN versus IP_NOITF bias by manipulating the initialization of our coupled experiments. For example, we can devise an IP_OPEN experiment that utilizes the IP_NOITF mean seasonal cycle to formulate the anomalies to

initialize the coupled experiments instead of mean seasonal cycle of the IP_OPEN experiment. In other words, we subtract the patterns found in Figure 3.1 and Figure 3.2 from the IP_OPEN initial conditions at step Figure 2.2a of the coupled process. Among many other impacts (detailed in Section 3.1) this has the effect of increasing the MLD in the Pacific by roughly 2 m with the pattern defined by Figure 3.2g for initialization. After adding the patterns from Figure 3.1 and Figure 3.2 to the mean seasonal cycle, the IP_OPEN experiment is executed as before (i.e. same steps as for Figure 2.2b-g). In this way we can diagnose the impact of the NOITF bias on coupled experiments.

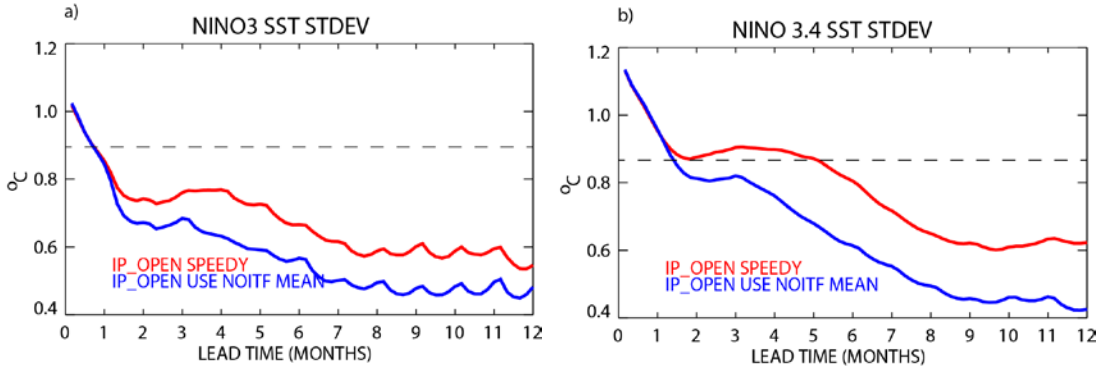

Figure 3.10: Standard deviation of IP_OPEN with IP_NOITF bias. *Standard deviation for IP_OPEN (red repeated from Figure 3.9) and IP_OPEN experiment with IP_NOITF bias added to initialization of coupled experiments (blue). The dash line corresponds to the observed standard deviation in the NINO3 region of a) 0.9°C and b) 0.86°C for NINO3 and NINO3.4 regions, respectively.*

As expected, the variability in the NINO3 region is reduced by imposing the IP_NOITF mean state due to the deeper MLD. The variability of the IP_OPEN experiment with IP_NOITF initial conditions is significantly reduced as can be seen in Figure 3.10a. For all months after 1 month lead time the IP_NOITF bias experiment has reduced variability by around 0.1°C (or ~15% of the total variability). In addition, the NINO3.4 region has similar results. Namely, the experiment that excludes the contribution of the IO bias has significantly lower variability than the standard IP_OPEN

experiment (Figure 3.10b) by around 0.15^{o}C after 1 month lead time. For both the NINO3 and NINO3.4 regions, the experiment that includes the IP_NOITF bias (blue) has lower variability than observed values (dashed) for all lead times with respect to the IP_OPEN experiment (red in Figure 3.10a and b).

These results tend to contradict the idea of [*Santoso et al.*, 2011] and [*Kajtar et al.*, 2015] who suggested that the change in ENSO variability was due to an eastward shift of the zonal extent of the Bjerknes coupling from the NINO3.4 region for IP_OPEN to NINO3 for the IP_NOITF case. However, our experiments indicate that an oceanic cause, namely the changes from the shallower for IP_OPEN to deeper MLD for IP_NOITF and the more efficient transmission of Kelvin/Rossby waves explains the higher variability and the good correspondence with observed variability for the IP_OPEN case.

3.3 Summary of Oceanic Contribution of the Indian Ocean

In this section, the oceanic contribution of the Indian Ocean to ENSO predictability has been highlighted by differencing experiments with the ITF open minus those with the ITF closed. This section has shown that oceanic processes are similar in character to previous results (e.g. [*Song et al.*, 2007]). In particular, the flow of the ITF currents from the western Pacific through the Indonesian Seas and beyond is readily apparent. The Pacific is generally cooler with minimum SST located just south of the eastern Pacific cold tongue while the IO SST is generally warmer with the maximum at the exit of the ITF. SSS is saltier in the Pacific and fresher in the IO with the largest positive and negative values in the entrance and exit regions of the ITF, respectively.

The atmosphere responds to these differences by showing equatorial convergence in the western and divergence in the eastern half of the Pacific. The precipitation is deficient in the Pacific and especially abundant over Indonesia and south of 5^{o}S in the IO. The winds over the IO are generally northwesterlies between the equator and 10^{o}S. The MLD and BLT are both shallower especially in the western Pacific, consistent with the idea that the ITF carries warm fresh water from the Pacific to the IO.

The ENSO response is larger for IP_OPEN versus IP_NOITF. Statistically significant high positive correlation between the NINO3 SST observations and the differences, IP_OPEN – IP_NOITF, reinforce the idea that IP_OPEN has higher amplitude for both El Niño and La Niña. In addition, plots of recharge/discharge show that the amplitude of the ENSO signal is larger for the IP_OPEN scenario than the IP_NOITF case. The Kelvin wave differences across the Pacific are highly correlated (statistically significant) with an index of the wind showing that the shallower MLD of the IP_OPEN is responsible for the higher sensitivity to the wind forcing versus the IP_NOITF experiment.

Next the coupled model response of the oceanic contribution of the IO at initialization was assessed. Although the IP_OPEN has generally higher correlation for coupled experiments and the individual correlation values are significant out to 8 and 7 months for IP_OPEN and IP_NOITF, respectively, results are too similar to make any statistically significant definitive statements about which is better. The similarity of the IP_OPEN versus IP_NOITF coupled validation is explained by the limitations of the anomaly coupling technique. SST anomalies are formulated with respect to the similarly-forced ocean model so the biases between IP_OPEN and IP_NOITF (as seen in Figure

3.1 and Figure 3.2) are left unaccounted for within the coupling process. It is important to remember that both the IP_OPEN and IP_NOITF coupled experiments use their own set of various means due to the anomaly coupling technique. However, the IP_OPEN experiment resulted in higher amplitude ENSO variability by as much as 20% and IP_OPEN better matches the observed variability in the NINO3 and NINO3.4 regions as compared to the IP_NOITF coupled experiment. These results were confirmed by modifying the IP_OPEN coupled experiment by adding the IP_NOITF bias to the initialization. These results also show that the IP_OPEN experiment has higher variability in the NINO3 and NINO3.4 regions and are more in line with observed variability.

In this Section real hindcast experiments and validation with observations are used for the first time to isolate the role of the IO. For the ocean, experiments with the ITF open minus those without show that the flow of the ITF through the Indonesian Seas drains the Pacific of warm and fresh water and reduces the MLD within ~7^{o} of the equator. High correlation between the IP_OPEN minus IP_NOITF and the observed NINO3 SST anomaly indicate that El Niño/La Niña and recharge/discharge estimates of ENSO are amplified by the oceanic contribution of the IO. Forced experiments show that the driving factor for this amplification is the shallower MLD when the ITF is open. The wind forced Kelvin wave signal is amplified for the IP_OPEN scenario versus IP_NOITF because similar forcing acts more efficiently on a shallower MLD. Even though the individual forecast correlation values are significant out to 7 months, unfortunately, the anomaly coupling technique used here explicitly excludes the biases between IP_OPEN and IP_NOITF at initialization so these coupled results are not statistically significant

different. On the other hand, the variability of the coupled experiments for IP_OPEN shows a much closer correspondence to observed variability over 1993 to 2014 and the highest variability remains in the NINO3.4 rather than the NINO3 region. Therefore, the ocean impact of the IO via the ITF is to modulate the amplitude of the ENSO signal by as much as ~20%. Unlike [*Santoso et al.*, 2011] and [*Kajtar et al.*, 2015] the NINO3.4 remains the region with maximum variability. They indicated that the reason for the shift was due to changes in the fetch of most intense Bjerknes coupling. However, our results suggest that the reason is due to the oceanic link. In particular, the impact of the shallower MLD for the IP_OPEN case allows Kelvin waves to be effectively amplified.

4 Role of the Indian Ocean Sector – Impact of Atmospheric Coupling

Another way to try to extend our understanding of ENSO is to separate out the impact of the IO atmosphere. In previous work, [*Wu and Kirtman*, 2004] (see e.g. Figure 1.6d) and [*Annamalai et al.*, 2005] proposed that cold IO sea surface temperature anomalies (SST') could generate an atmospheric Kelvin wave that would manifest as equatorial westerlies over the western Pacific which in turn could impact the thermocline in the eastern Pacific via large-scale oceanic Kelvin wave processes (e.g. [*Kessler et al.*, 1995]) which would then enhance an ongoing El Niño. In addition, [*Annamalai et al.*, 2010] attributed Pacific westerlies to cold SST' in the Indonesian Seas. However, all previous approaches idealized SST' forcing (either the 1st EOF mode of SST, symmetric basin-scale or IODZM SST' patterns, or differencing El Niño years with and without strong IODZM from coupled models) and then diagnosed the impact of these SST anomalies with linear atmospheric models. These techniques only go as far as producing an idealized wind anomaly in the Pacific and the authors are limited to conjecture on the impact on ENSO predictability due to the IO SST' forcing. In any case, all these studies fall short of actually addressing the impact of IO atmospheric teleconnections on real coupled ENSO forecasts as validated by observations.

4.1 Forced Ocean and Atmospheric Model Results

In this section we will examine the forced atmospheric response between the IO and the Pacific using a similar methodology as [*Wu and Kirtman*, 2004] but with the full (i.e. not idealized) ocean forcing and an intermediate complexity, non-linear, atmospheric model. These SPEEDY atmosphere-only experiments are initiated using different SST'

for the IO basin to isolate the ocean forcing impacts via the atmosphere on the coupled Indo-Pacific system. In this work, the Pacific (abbreviated PAC) is defined as 30°N-30°S, 130°E-70°W and the Indian Ocean (IO) is defined as 30°N-30°S, 30°E-129°E. Outside the tropical Indo-Pacific region, the interannual SST' from the Hadley Centre (HadISST, [*Rayner et al.*, 2003]) is used to force the global SPEEDY model and climatological values are used for other atmospheric model boundary conditions such as surface albedo, climatological SST, sea ice, snow depth, vegetation, heat flux parameters, and soil moisture (matching those described in [*Kucharski et al.*, 2013]). Within the Indo-Pacific region, experiments were initiated that are designed to isolate the impact of the IO region surface forcing on the atmosphere.

Experiment Name	Period	Model Geometry	Indo-Pacific Forcing
INT_PAC, INT_IO	1993-2014	Global/Indo-Pacific	Interannual SST' forcing for Pacific and IO
INT_PAC, CLIM_IO	1993-2014	Global/Indo-Pacific	Interannual SST' forcing for Pacific, climatological seasonal cycle SST for IO

Table 4.1: Experiment description for impact of interannual IO SST forcing. *Table defining the ocean forcing for the various SPEEDY experiments. The far left column describes the experiments, "INT" and "CLIM" stand for interannual and climatological forcing and "PAC" and "IO" stand for Pacific (30°N-30°S, 130°E-70°W) and Indian Oceans (30°N-30°S, 30°E-129°E), respectively. The far right column describes the SST anomaly forcing (SST') for the Indo-Pacific region. In order to isolate the impact of the IO, differences between INT_PAC, INT_IO – INT_PAC, CLIM_IO are presented. Note that SST' are formulated with respect to the 1983-2014 mean seasonal cycle using [Reynolds et al., 2002] OI SST.*

Table 4.1 shows the experiments used in this study. The experiments either use interannual (i.e. INT) SST' forcing or climatology seasonal cycle (CLIM) SST separated by basin, PAC and IO. For example, forcing SPEEDY using interannual SST' for the Pacific and IO is abbreviated as INT_PAC, INT_IO. Following the similar methodology of e.g. [*Wu and Kirtman*, 2004], we subtract the results from these different experiments

in order to isolate the impact of the IO sector ocean forcing. Thus, subtracting INT_PAC, CLIM_IO results from INT_PAC, INT_IO will isolate the impact of the IO SST' via the atmospheric teleconnections to the Pacific. We will use "atmospheric teleconnection" "atmospheric impact" or "atmospheric bridge" interchangeably throughout the following text for this impact.

The results of the SPEEDY atmospheric model differences are designed to isolate the impact of the IO and are presented in Figure 4.1a-f for zonal, meridional wind stress, precipitation, curl and divergence of the wind stress, respectively. By differencing experiments with full coupling in the IO minus those with decoupled IO, the impact of the variations in the IO summer monsoon is readily apparent for both precipitation and wind stress. For precipitation (Figure 4.1c), positive anomalies can be seen stretching from the equator to 10^{o}N in the eastern Arabian Sea (AS), at 7^{o}N to 12^{o}N in the Bay of Bengal (BOB), and 10^{o}N to 20^{o}N in the South China Sea (SCS). Abundant rainfall is consistent with deceleration (i.e. convergence) of the monsoon flow starting south of the equator as southeasterlies, recurving to southerlies near the equator and decelerating as southwesterlies in the AS, BOB, and SCS (Figure 4.1d and f). These southwesterlies converge into northeasterlies found north of 10^{o}N in the BOB and SCS. In the Southern Hemisphere, between 10^{o}S and the equator, negative precipitation anomalies generally predominate west of 95^{o}E. Again these precipitation patterns are consistent with the general divergence of the winds in these regions as they feed into the northward monsoon flow. In addition, positive precipitation is found over the southern Indonesian islands between 95^{o}E and 130^{o}E stretching between 12^{o}S to 5^{o}S. This feature is due to the onshore convergence of the westerlies winds found west of 95^{o}E and is consistent with

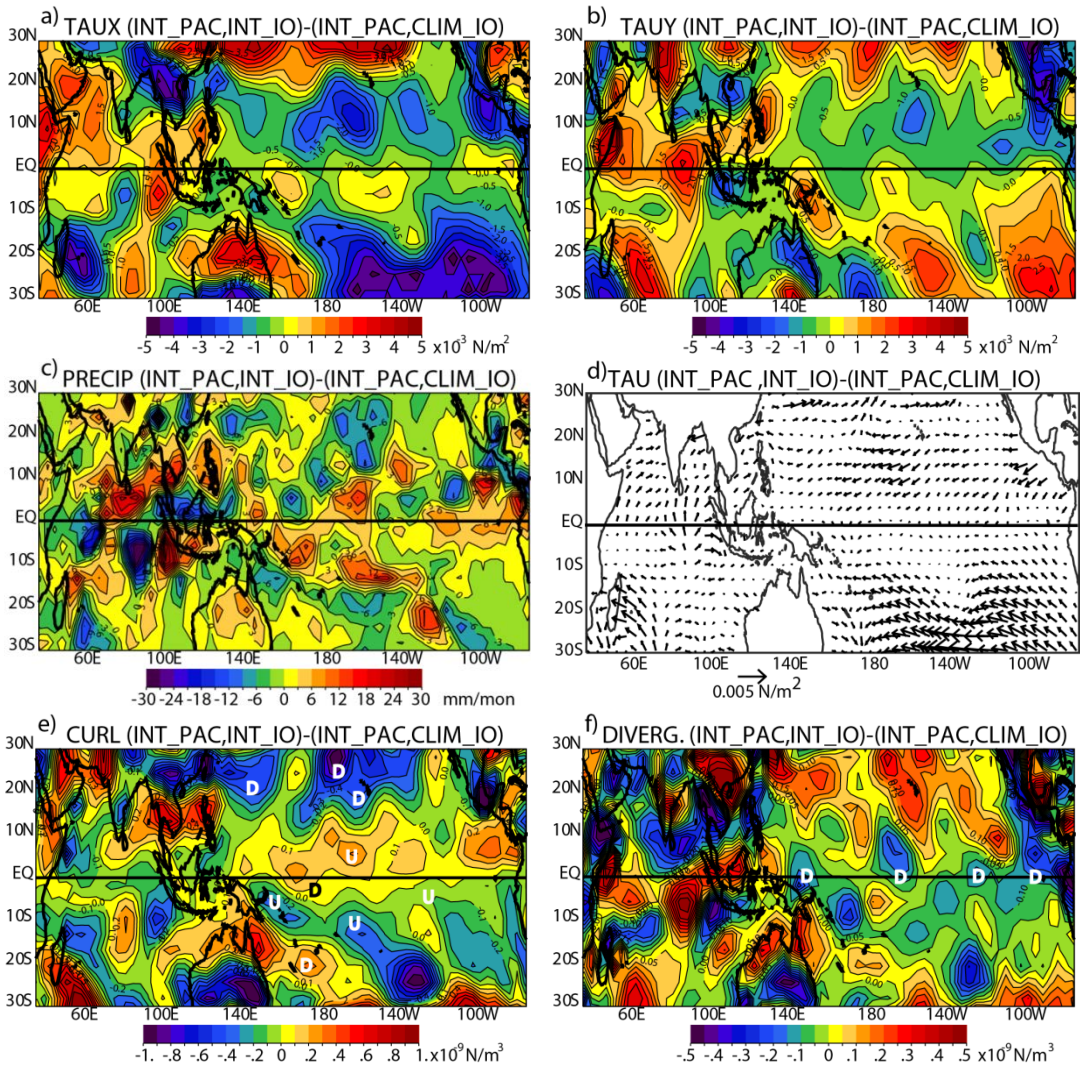

Figure 4.1: Impact of interannual IO SST forcing. *Differences between two sets of SPEEDY experiments for a) zonal, b) meridional wind stress, c) precipitation, d) vector representation of a) and b), e)curl and f) divergence of the wind stress. Differences are full SST anomaly forcing over the Indo-Pacific region (i.e. INT_PAC, INT_IO) minus the experiment that uses climatological seasonal cycle forcing over the IO (INT_PAC, CLIM_IO). Letters "U" and "D" represent regions of upwelling and downwelling favorable winds and absolute values greater than 3.3x10^{-3} N/m^2, 2.7x10^{-3} N/m^2, 13.2 mm/mon, 0.53x10^{-9} N/m^3, 0.35x10^{-9} N/m^3 are significant at the 95% level for a), b) c), e), and f), respectively.*

anomalies that are associated with the transition of the northwest to summer monsoons (e.g. in February). In the southwest IO between 25^{o}S-15^{o}S and west of 80^{o}E, a band of positive precipitation is evident just to the east of Madagascar and is the result of southeasterlies to the south converging with northwesterlies to the north (Figure 4.1f).

Warm SST leads to atmospheric advection, enhanced inflow, convergence and abundant atmospheric convection and precipitation. The patterns in the IO are consistent with the anomalies of the monsoon wind and precipitation patterns (i.e. those patterns associated with interannual minus climatological seasonal cycle SST forcing in the IO). These patterns from the IO atmospheric teleconnection in the IO are somewhat similar to the validation of the CFSR model. For example, CFSR is deficient by about 30 mm/mon with respect to the observed precipitation across the entire IO within a few degrees of the equator ([*Wang et al.*, 2010]) and CFSR is too rainy over southern India and Southeast Asia by about 15 mm/mon.

In the Pacific, Figure 4.1c shows generally abundant precipitation differences off the equator at 5^{o}N, 15^{o}S centred near 160^{o}W. In addition, positive anomalies are seen in the upwelling region of the eastern equatorial Pacific east of 130^{o}W and in the South Pacific Convergence Zone (SPCZ) at 10^{o}S, 160^{o}E. To the north of 10^{o}N and south of 20^{o}S, negative precipitation generally predominates. As stated before, the CFSR is too rainy over the Pacific ITCZ and SPCZ and dry over the Maritime continent.

In the Pacific strong easterlies can be seen between equator and 20^{o}N and south of 15^{o}S across the entire basin (Figure 4.1a). North of 20^{o}N, strong westerlies prevail. Between 10^{o}S and the equator, wind differences are generally very weak westerly. The meridional winds (Figure 4.1b) converge to roughly 5^{o}S with northerlies to the north and southerlies to south especially east of the dateline. Along 20^{o}N winds are generally divergent for the meridional wind plot. The relatively weak winds near the equator match those of [*Annamalai et al.*, 2005] who used a simple linear atmospheric model (i.e. the moist linear baroclinic model – LBM of [*Watanabe and Jin*, 2003]) to show that the

atmospheric Kelvin wave of the western dipole of the IODZM cancelled that of the eastern dipole (see for example their Figures 8b, 10d). However, our results show the importance of not only the near-equatorial winds but also the off-equatorial zonal and meridional winds for the diagnosis of the IO SST' teleconnections to Pacific ENSO.

The off-equatorial easterlies represented in Figure 4.1a are a prominent feature but are lacking in previous work (e.g. Figure 1.6d and Figure 1.8b). There are several reasons why the simple atmospheric models that were used to highlight the IO atmospheric teleconnections to the Pacific (i.e. [*Wu and Kirtman*, 2004] and [*Annamalai et al.*, 2010]) might lack the off-equatorial easterlies like the SPEEDY results shown here. For the previous results, the SST field in the IO is idealized in some way or another. Either the 1st EOF of the coupled model results or the SST differences with and without IODZM for El Niño is utilized to simplify the SST forcing. In addition, these models have been linearized about different mean states for specific seasons (JJAS and MJ, respectively) so the seasonal cycle remaining in SPEEDY may play a role in forming the off-equatorial easterlies. When we limit the SST' forcing in the IO to just the 1st EOF (not shown but a similar pattern as e.g. Figure 1.6a for the IO) for the forced SPEEDY AGCM, the westerly signal near the equator is enhanced (i.e. the atmospheric Kelvin wave found in both previous papers) but the easterlies off the equator remain.

The lack of a strong signal off the equator for the LBM results of the previous authors is surprising considering the results of [*Watanabe and Jin*, 2003]. They used a similar model (i.e. LBM) as previous authors and force it with El Niño minus La Niña observed SST' limited to the IO region. Their Figure 8c indicates that a basin-scale cooling in the IO (their M3 region) results in a positive precipitation response symmetric

within 15^{o} of the equator that is centered at 140^{o}E. West of the dateline, the 850 mb streamfunction response to this heating shows nearly collocated cyclonic flow and easterlies between 10^{o}N-35^{o}N, westerlies for 5^{o}N-10^{o}S, and easterlies between 15^{o}S-30^{o}S west of the dateline, which are broadly similar to our results. On the other hand, our precipitation results have this maximum centered to the east, at roughly 160^{o}W (Figure 4.1c), so this displacement of the precipitation heating might explain the elongated off-equatorial easterlies found in the SPEEDY results (Figure 4.1a).

Another potential difference between previous work and the current wind results is the amplitude and location of the precipitation anomalies in the Pacific. For example, [*Annamalai et al.*, 2010] (Figure 1.8c) shows the strong positive precipitation anomalies centered at 10^{o}S and 5^{o}N centered at 180^{o}, roughly similar to our results. However for these previous results there is also a strong negative anomaly with similar zonal extent and amplitude to the west, centered at 150^{o}E that may act to offset any off-equatorial signal in the winds. Our precipitation results (Figure 4.1c) show that there are no such offsetting precipitation anomalies to the west of the main positive values located between 160^{o}E to 160^{o}W centered at 10^{o}S and 5^{o}N. Therefore, off-equatorial easterlies are not opposed by westerlies for the SPEEDY results.

The last and most likely potential reason for off-equatorial easterlies may be the convective scheme within the SPEEDY results. [*Kim et al.*, 2008] show that implementation of CMT leads to enhanced off-equatorial precipitation (i.e. roughly 5^{o}-15^{o} off the equator) and decreased precipitation between 5^{o}S-5^{o}N. The wind response to implementation of CMT is increased 850 mb westerlies between 10^{o}S-10^{o}N and also easterlies poleward of the enhanced precipitation. However, these results are only valid

west of 150^{o}W for the December - February climatological forcing used for the [*Kim et al.*, 2008] example. A fundamental concept of CMT is that upper atmosphere momentum is transported to the surface via downdrafts around convection. In our example, general enhanced precipitation (Figure 4.1c) between 15^{o}S-5^{o}N drags westerly momentum from upper branch of the Walker circulation to the surface (Figure 4.1a). At the same time, weaker precipitation for the coupled IO with respect to the decoupled IO does the opposite leaving enhanced easterlies between 5^{o}N-20^{o}N and south of 15^{o}S. Thus, implementation of CMT within SPEEDY, but not within any of the linear model results, may also contribute to the off-equatorial easterlies found in the SPEEDY results. Although there are multiple potential reasons for differences between the nonlinear LBM and SPEEDY atmospheric results, exploring differences further is beyond the scope of the current dissertation, and we proceed analyzing the (presumably more accurate) AGCM from SPEEDY.

The combined impact of the zonal and meridional winds in the Pacific on the ocean can be conveniently summarized by diagnosing the differences of the SPEEDY experiments using curl and divergence of the wind stress. On the equator, surface convergence of the wind leads to convergence of the surface currents, downwelling in the ocean, a deepening of the thermocline, and an increase in sea level values. The divergence of the atmospheric teleconnections is presented in Figure 4.1f and this shows pervasive downwelling all along the entire equator. Off the equator, the curl can be used to estimate the sense of Ekman pumping velocity as a measure of upwelling or downwelling. Figure 4.1e shows that upwelling favorable wind (i.e. positive in the Northern Hemisphere and negative in the Southern Hemisphere) is predominant between

15°S to 10°N in the Pacific. However, the curl just to the south of the equator between 160°E-140°W is positive indicating a narrow band of downwelling favorable curl. North of ~10°N and in the southeast Pacific (off Australia) downwelling curl is also prevalent.

To summarize, atmospheric model experiments were differenced to isolate the impact of IO SST' forcing on the tropical Indo-Pacific atmosphere. These differences highlighted the strong interannual signature of variations in the monsoon that is evident in both the precipitation and wind stress difference plots in the IO. In the Pacific, strong easterlies prevail south of 15°S and between the equator to 20°N. Also differences show weak westerlies near the equator between 10°S and the equator. For the meridional component, winds converge towards 5°S especially over the eastern half of the basin with abundant precipitation in the eastern Pacific cold tongue region near the equator. In addition, differences show strong positive precipitation anomalies in the central Pacific. Convergence along the equator indicates that there is pervasive downwelling favourable conditions present at initialization of the coupled system along the equator. However, off the equator between 15°S-10°N the prevailing curl indicates that IO SST' is generally forcing upwelling in this region. As [*Annamalai et al.*, 2005] noted, the weak winds within the waveguide may allow nascent El Niño/La Niña events to grow unencumbered. Unfortunately, all previous studies (i.e. [*Wu and Kirtman*, 2004], [*Annamalai et al.*, 2005], and [*Annamalai et al.*, 2010], etc.) used idealized SST' patterns and simplified linear atmospheric models to show impacts of the IO on the wind field without assessing observed ENSO predictability. On the contrary, in the next subsection we use a full intermediate complexity AGCM (i.e. SPEEDY) and real interannual forcing to diagnose

the development of the mean forecast forced by atmospheric teleconnection of the IO to the Pacific ENSO.

In a similar vein as previous work, there are weak westerlies near the equator (10^oS-0^oN) across the entire Pacific. However, our diagnosis suggests that the atmospheric response is more complicated than previously thought and a previously unaccounted-for significant signal corresponds to strong easterlies south of 15^oS and between 0^oN to 20^oN. The simplified linear atmospheric models used by previous studies lack these easterlies presumably due to the simplification of the full IO SST forcing (using either EOF patterns or seasonal phase locking), negative precipitation anomalies over the far western Pacific in the linear model that may serve to offset the winds from the linear but not the SPEEDY results, or the impact of implementation of CMT within SPEEDY. Since the SPEEDY model is in good agreement with observations and operational reanalyses ([*Molteni*, 2003]) and improved further using the CMT of [*Kim et al.*, 2008] and SPEEDY does not suffer from the potential shortcomings of the linear model results documented above, we proceed to analyze the impact of the IO SST' forcing on real ENSO prediction via the atmospheric bridge using the coupled model incorporating the SPEEDY nonlinear AGCM.

4.2 Coupled Model Results

A series of coupled experiments designed to isolate the full impact of the interannual IO SST' forcing is executed. Operationally the same initial conditions are used, i.e. the ECMWF-forced experiment, to initialize all coupled experiments since the goal is to completely eliminate any potential impacts caused by different initialization. However, within the coupling procedure (at step d) in Figure 2.2) we replace the regional

SST anomaly with zeros effectively substituting the interannual SST forcing with climatological seasonal cycle values. Following the same nomenclature as Figure 4.1, a series of two 12 month coupled experiments were completed for each month from 1993-2014 (for each experiment a total of 264 12 months runs were completed). The two experiments are 1) INT_PAC, INT_IO (this is identical to the IP_OPEN coupled experiment described earlier and has interannual SST anomaly forcing for the Pacific as well as for the IO) and 2) interannual Pacific, climatological IO (INT_PAC, CLIM_IO). Just like the atmospheric experiments earlier in this section, the experiments with similar Pacific forcing are compared, e.g. INT_PAC, INT_IO versus INT_PAC, CLIM_IO. The validation of these two experiments versus observed NINO3 SST' over all 12 month lead times, 1993-2014, can be found in Figure 4.2. Both experiments individually exceed the 95% significance versus observations from the beginning of the experiment out to 5.5 months. After 3 month lead times, the correlation of the full coupling begins to outperform the INT_PAC, CLIM_IO coupled experiment. Correlation differences climb to r=0.16 by 7 month lead times. At this time the Steiger Z Test ([*Steiger*, 1980]) shows that the differences are significant (thick dashed line on top x axis in Figure 4.2a). After that, the differences drop to about r=0.1 out to 10 month lead times when the differences are no longer significant. The important result of this plot is that the interannual forcing of the IO significantly improves coupled forecasts for ENSO. For the RMS differences, Figure 4.2b provides a similar story. Over most of the forecast period especially between 2 to 9 month lead times, interannual SST forcing in the IO improves (reduces) the RMS differences as measured by NINO3 SST' observations. Therefore, including the impacts

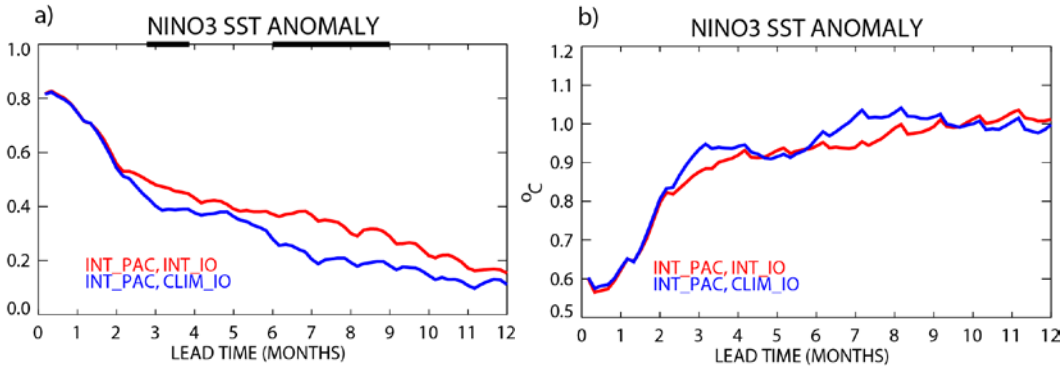

Figure 4.2: Impact of IO interannual forcing on coupled NINO3 SST results. *Validation statistics for a) correlation and b) RMS differences between coupled experiments with full atmospheric coupling (i.e. INT_PAC, INT_IO which is the same as IP_OPEN SPEEDY in Figure 3.8) in red and interannual coupling in the Pacific and climatological forcing in the IO (i.e. INT_PAC, CLIM_IO) in blue. The coupled experiments are validated against observed NINO3 SST anomaly for 1993 to 2014. Individual correlations exceed the 95% significance out to 8 (43) and 5.8 months (41) (effective degrees of freedom) for red and blue lines, respectively. The thick black line on the top x-axis shows where the red line is significantly larger than the blue line using the Steiger-Z test.*

of the IO atmospheric teleconnection serves to improve the coupled predictability as validated with real observations over 1993 to 2014.

The next step is to examine why the interannual SST forcing of the IO improves the coupled forecasts. Figure 4.3 shows the mean and standard deviation of the NINO3 SST' of all the 12 month forecasts from 1993-2014. The mean plot (Figure 4.3a) shows that the experiment with interannual IO forcing has higher mean values (i.e. relative warming signal in the NINO3 region) after 3 months. On the other hand, the INT_PAC, INT_IO and INT_PAC, CLIM_IO standard deviation lines in Figure 4.3b practically overlay one another. Therefore, we conclude that the interannual signal in the IO serves to warm the mean state in the eastern Pacific after 3 months rather than impact the variability.

In order to further diagnose the source of the warming after 3 months, the mean forecast difference, INT_PAC, INT_IO minus INT_PAC, CLIM_IO, is presented for all

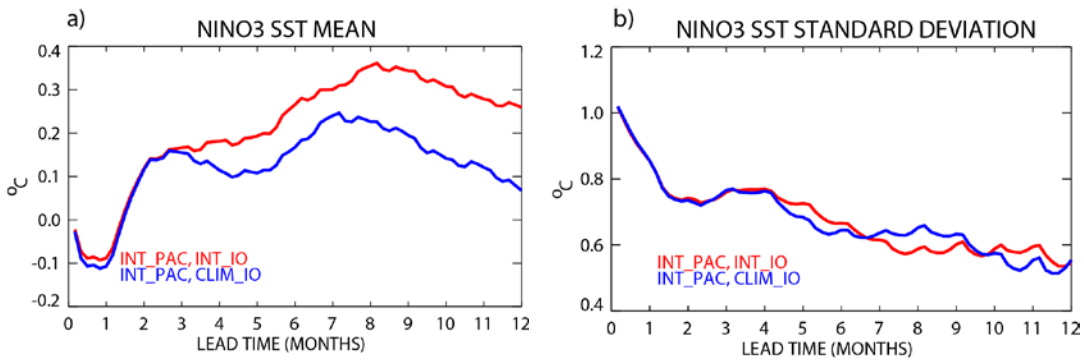

Figure 4.3: Variability of NINO3 SST for impact of interannual IO SST forcing. *Plots showing the NINO3 SST a) mean forecast and b) variability for INT_PAC, INT_IO (red) and INT_PAC, CLIM_IO (blue) for all forecasts from 1993-2014.*

12 months of lead times. Longitude versus time plots track the evolution over the average forecast in Figure 4.4. Early in the average forecast difference, prior to month 3, easterly winds along the equator between 140°E-160°E and between 180°-140°W (Figure 4.4c) set off upwelling Kelvin waves (Figure 4.5a), cooling SST' (Figure 4.4a), and inducing westward flow across the entire Pacific (Figure 4.4d). This is consistent with the general upwelling favorable curl in the initial conditions (i.e. Figure 4.1e) between 15°S-10°N. After this slight upwelling and cooling in the central Pacific associated with equatorial easterlies is spent, the SST in the NINO3 region begins to warm after 3 month lead times (Figure 4.4a). In the east, westerlies centered at approximately 130°W generate a downwelling Kelvin wave that arrives at the eastern boundary at month 4 (Figure 4.5a). At this time the NINO3 region begins to warm (Figure 4.4a). In the west, westerlies on the equator west of 140°E and near the dateline act in the equatorial Pacific setting off a second downwelling Kelvin wave (identified by positive sea level anomaly and eastward flow - Figure 4.4b, d and Figure 4.5a) that starts in month 4 that traverses the Pacific and arrives at the eastern boundary by month 6. The cumulative effects of the downwelling Kelvin waves after month 5 are to continue to warm the NINO3 region.

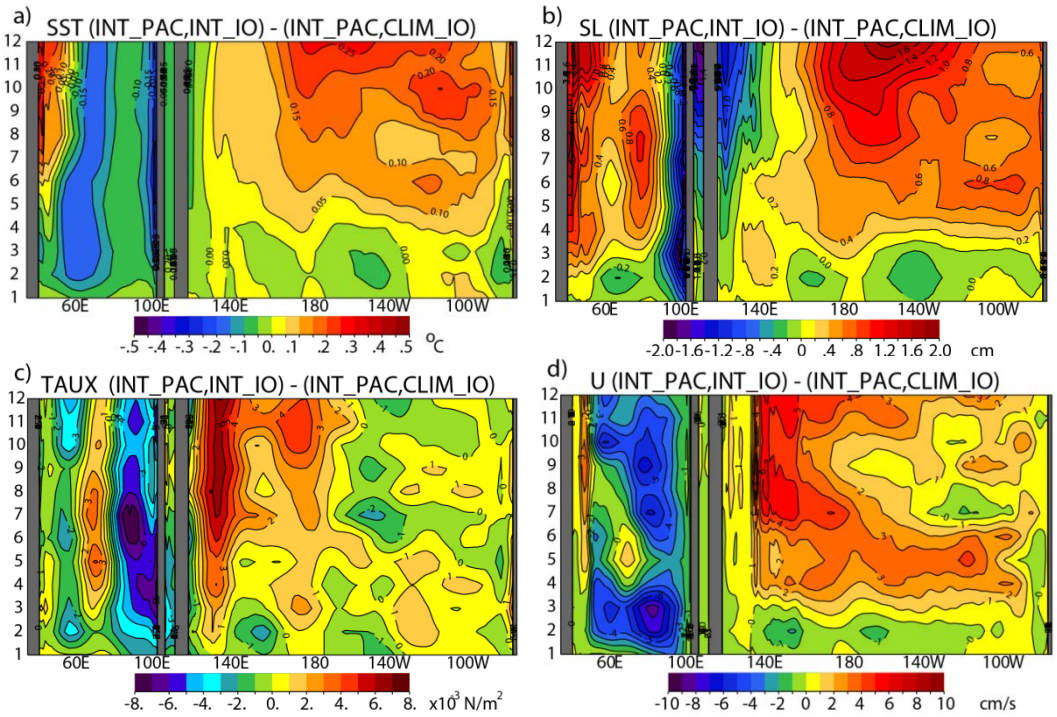

Figure 4.4: Hovmöller plots of impact of interannual IO SST forcing. *Plots showing the mean temporal evolution of the impact of IO atmospheric coupling using longitude versus lead time (in months) averaged between 2°N and 2°S for a) SST, b) SL, c) zonal wind stress, and d) zonal currents. The mean is taken for the average forecast differences, INT_PAC, INT_IO minus INT_PAC, CLIM_IO, over all months from 1993 to 2014.*

For month 6 through 8, warmest SST' is building in the central Pacific between 160°E and 140°W. Westerlies to the west and easterlies to the east converge into this warm region (Figure 4.4c) near the dateline. A weak upwelling Kelvin wave (Figure 4.5a dashed line) is initiated that is associated with these easterlies east of the dateline. At this time, the prevailing eastward flow is interrupted and westward currents are found in the eastern Pacific between months 6-8 (Figure 4.4d). The SST' in the NINO3 region briefly cools (Figure 4.4a) in month 7. At this same time (forecast months 6-8), westerlies prevail from the western boundary all the way to the dateline. The next downwelling Kelvin wave is initiated in the west and arrives at the eastern boundary roughly at forecast month 9. As it enters the NINO3 region this downwelling Kelvin wave warms

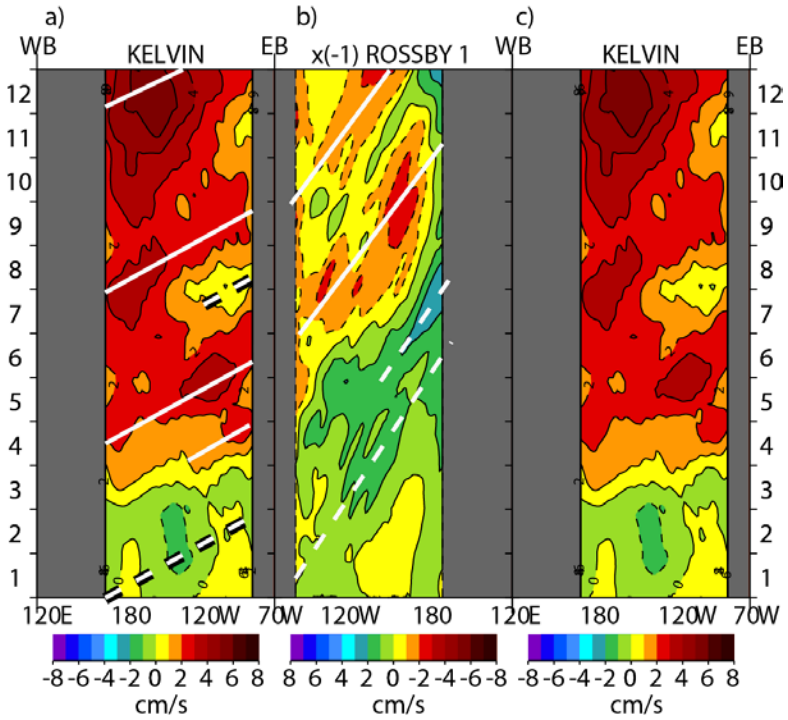

Figure 4.5: Kelvin/Rossby wave decomposition of interannual IO SST forcing. *Longitude versus time distribution of the equatorial (a) Kelvin and (b) the first meridional mode of equatorial Rossby waves through their signature in zonal surface current deduced from the average forecast SL differences, (INT_PAC, INT_IO) – (INT_PAC, CLIM_IO). In order to follow possible wave reflections on the western (WB) and eastern (EB) boundaries, the Rossby panel (b) is inverted and the Kelvin wave pattern is repeated (c). The color scale for the Rossby panel is also inverted since reflection on meridional boundaries results in zonal currents of opposite sign. Solid lines (downwelling) and dashed lines (upwelling) represent theoretical wave speeds for Kelvin (2.5m/s) and Rossby waves (-0.8m/s or ~5months to cross this Pacific basin at 5^{o}N) on each plot.*

the SST'. The warmest SST' fills in to the west and by month 10 some of the warmest SST' is located just east of the dateline. Bjerknes coupling becomes entrenched and westerlies to the west of the SST' maximum converge with easterlies to the east (Figure 4.4c).

Careful examination of the equatorial signal and Kelvin/Rossby wave decomposition of the ocean waves helps to explain the timing and sign of the differences in the mean state in Figure 4.3a. After 3 month forecasts, downwelling Kelvin waves that

are forced by westerlies in the western Pacific, start to warm the eastern Pacific. After 7 month lead times, the Bjerknes feedback mechanism begins to lock in leading to enhanced westerlies over the western Pacific (Figure 4.4c) and enhanced air-sea coupling. The atmospheric impact of including the interannual forcing in the IO is to impart a large-scale downwelling favorable signal in the Pacific, increasing the warming in the NINO3 region after the 3 months. By 7 month lead times, the El Niño signal is enhanced/reinforced due to Bjerknes coupling.

To a large part, the previous discussion reinforces the conjecture of e.g. [*Annamalai et al.*, 2010] who suggested that the impact of the IO would be to enhance the westerlies along the equator and amplify an ongoing El Niño. However, examination of the various fields besides equatorial Hovmöller plots suggests that the initialization and growth of the warming in the NINO3 region is influenced by off-equatorial factors and by not only zonal but also meridional wind stress. Therefore, the discussion will now focus on the Pacific basin using plots of the mean forecast for 3, 5, 7, and 10 month lead times for SST', sea level anomaly, curl and divergence differences for INT_PAC, INT_IO minus INT_PAC, CLIM_IO results (Figure 4.6 to Figure 4.9).

On the equator, Ekman pumping velocity is undefined (since the Coriolis parameter is in the denominator). However, near the equator the wind stress divergence can be diagnosed to infer regions of upwelling or downwelling. By month 3 of the mean forecast, divergence corresponds to upwelling between 140^{o}E-150^{o}W on the equator and convergence is found between 140^{o}W-110^{o}W (Figure 4.6d). Off the equator, downwelling favorable curl (i.e. curl <0 in the Northern Hemisphere and > 0 in the Southern Hemisphere) can be seen west of 140^{o}W generally within 10^{o} of the equator

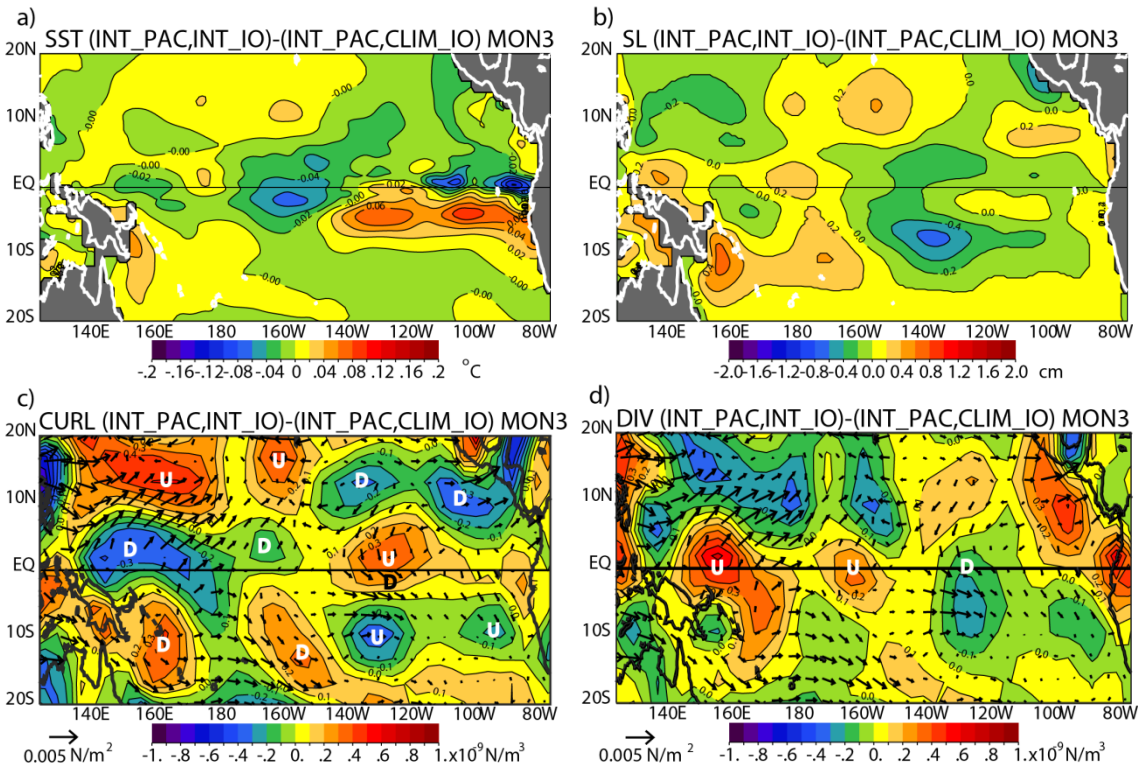

Figure 4.6: Average 3 month forecast INT_PAC, INT_IO-INT_PAC, CLIM_IO. *Average forecast values for month 3 for a) SST, b) sea level, c) curl of the wind stress (color) and wind stress (vector), and d) divergence of the wind stress (color) and wind stress (vector). The scale of the vector plot is indicated in the bottom left of the panel. For the reader's convenience, regions of upwelling and downwelling are marked by letters U and D, respectively.*

(Figure 4.6c). West of 160°W in the far western Pacific downwelling favorable curl off the equator corresponds to positive sea level anomalies off New Guinea (Figure 4.6b). This feature is important since it initiates the transition from the upwelling prior to month 3 across the basin to overall downwelling after that time. In other words, the off-equatorial curl initializes a downwelling Rossby wave and positive sea level anomaly in the far western Pacific that soon reflects as a downwelling Kelvin wave that begins the eventual transition to warm SST' in the NINO3 region by month 7. This is an instance where the off-equatorial signal (i.e. a downwelling Rossby wave) contributes to converting upwelling to downwelling along the equator and so features prominently in

ENSO predictability. Unfortunately, this downwelling in the west is not well represented by the Kelvin/Rossby decomposition plot (Figure 4.5) since it lies west of 160^{o}E which is the western extent of the land-free symmetric box that is required by this decomposition analysis. However, the subsequent downwelling Kelvin wave (spawned from the reflected Rossby wave) in the far west starting in month 4 is well diagnosed.

To the east, a pair of upwelling-favorable (i.e. negative in the Northern Hemisphere positive in the Southern Hemisphere) curl patches are located within 10^{o} of the equator between 140^{o}W-110^{o}W (Figure 4.6c). This feature corresponds with a pair of negative sea level anomalies centered at 5^{o}N and 12^{o}S at 130^{o}W and is identified as an upwelling Rossby wave in the Kelvin/Rossby diagnosis in Figure 4.5b. East of 160^{o}W, an upwelling Rossby wave at 140^{o}W acts to shoal the thermocline at 5^{o}N and 10^{o}S reshaping the meridional gradient to help focus the downwelling Kelvin wave train along the equator coming later in the average forecast.

So to summarize, downwelling Rossby waves forced by wind stress curl off the equator in the far western Pacific reflect to downwelling Kelvin waves eventually transitioning the NINO3 region to warming. The upwelling Rossby wave at 140^{o}W at month 3 shapes the meridional gradient to focus intensification on the equator.

By month 5 the downwelling Rossby wave hitting the western boundary in month 3 has reflected into a downwelling Kelvin wave and this wave has propagated eastward across the Pacific as far as ~140^{o}W (Figure 4.7b and Figure 4.5a). The effects of this downwelling Kelvin wave are demonstrated by positive sea level and SST anomaly throughout the waveguide (+/- 2^{o}) across the entire Pacific (Figure 4.7a). The average negative values, respectively in Figure 4.7c) and these upwelling features are echoed in

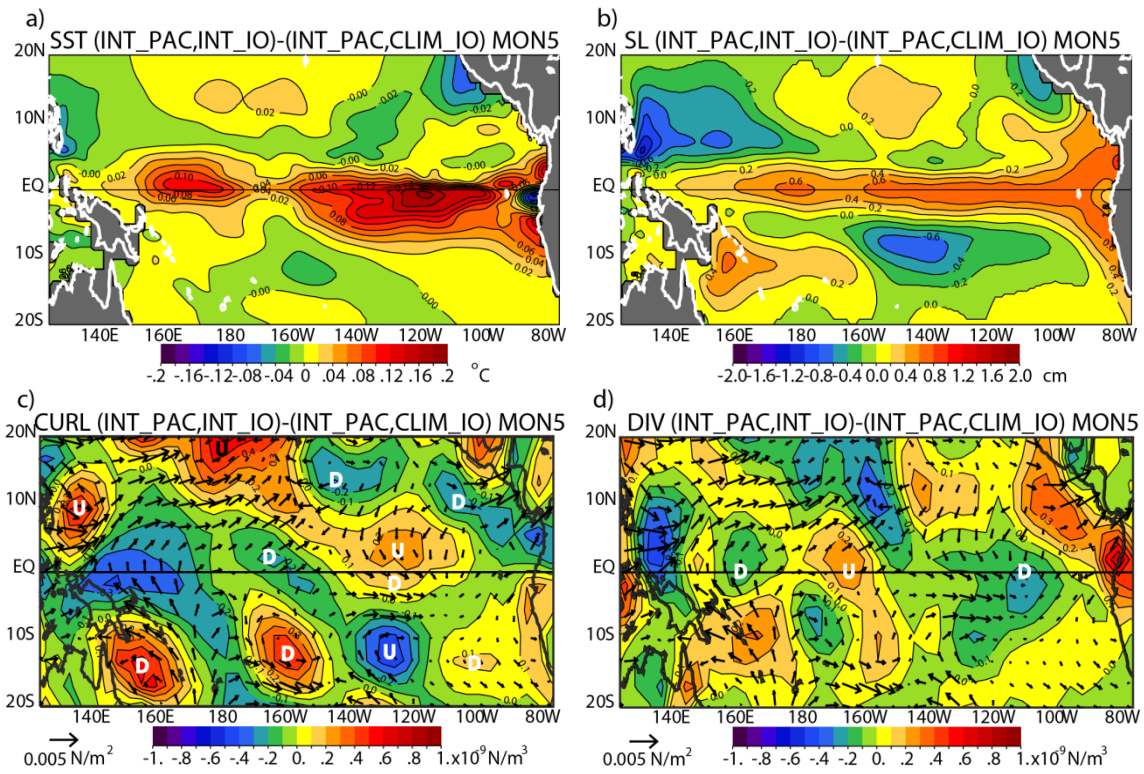

Figure 4.7: Average 5 month forecast INT_PAC, INT_IO-INT_PAC, CLIM_IO. *Same as previous but for 5 month average forecasts.*

forecast upwelling curl signal is still present at 130°W, 5°N and 12°S (positive and the negative sea level at 5°N and 10°S at 145°W. The NINO3 region is warming and SST' is largest at about 120°W on the equator. It is also interesting to note that the warmest SST' is just south of the equator whereas the sea level anomaly maximum is centered on the equator. Convergence found on the equator and positive curl and downwelling just to the south (5°S-0°S, 140°W-110°W) coincide with maximum SST'. Going from 5°N to 12°S along 130°W winds are starting northerly recurving to northwesterlies just south of the equator. West of the dateline and south of 5°S, pervasive positive curl (i.e. downwelling favorable) is collocated with positive sea level anomaly against New Guinea and Australia coasts. To the north of the equator, positive curl and upwelling are found with negative sea level west of 150°E off the Philippines. Thus the southeasterlies to the south recurving to southwesterlies north of the equator in the far western Pacific act to

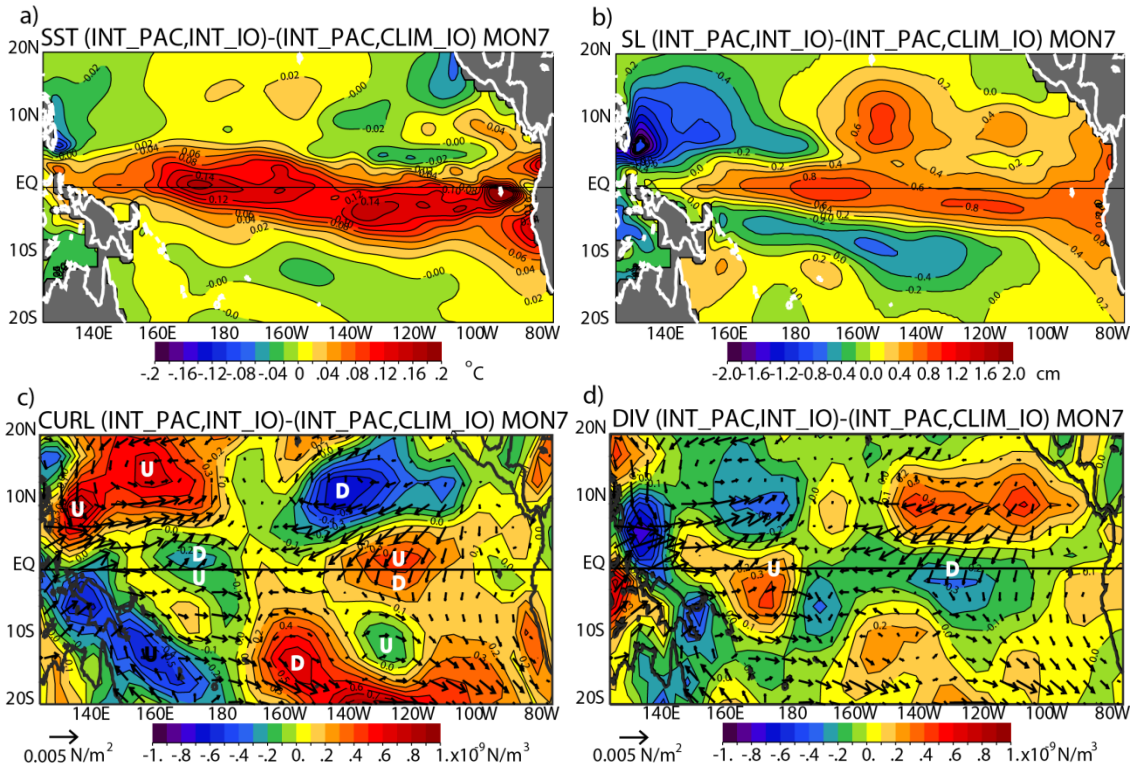

Figure 4.8: Average 7 month forecast INT_PAC, INT_IO-INT_PAC, CLIM_IO. *Same as previous but for 7 month lead forecast mean.*

deepen and shoal sea level, respectively. So to reiterate, not only are the equatorial signals important for the diagnosing the impact of the IO on ENSO, but the off-equatorial impacts such as oceanic Rossby wave formation and propagation are also important.

By month 7 the second Kelvin wave has reflected at the eastern boundary as a downwelling Rossby wave as evident by positive sea level at 10°N, 5°S at 120°W (Figure 4.8b and Figure 4.5b). Another positive sea level and SST' maximum is centered on the equator at ~170°W (Figure 4.8a, b). Equatorial westerlies, best demonstrated by the westerly wind burst in Figure 4.4c that extends from the western boundary to 160°E (note the $2x10^{-3}$ N/m^2 contour), force this downwelling Kelvin wave. To the north, downwelling curl corresponds to positive sea level and to the south negative sea level is collocated with upwelling favorable wind stress curl at 10°N, 10°S at 150°W,

respectively. Off the equator, west of 160°E the curl is positive to the north and this forces upwelling 0-10°N and negative sea level. It is also interesting to note that upwelling curl within 5° of the equator in the NINO3 region (particularly at 120°W) is causing weak upwelling and cold SST' at 5°N driving the warmest SST south of the equator (Figure 4.8a).

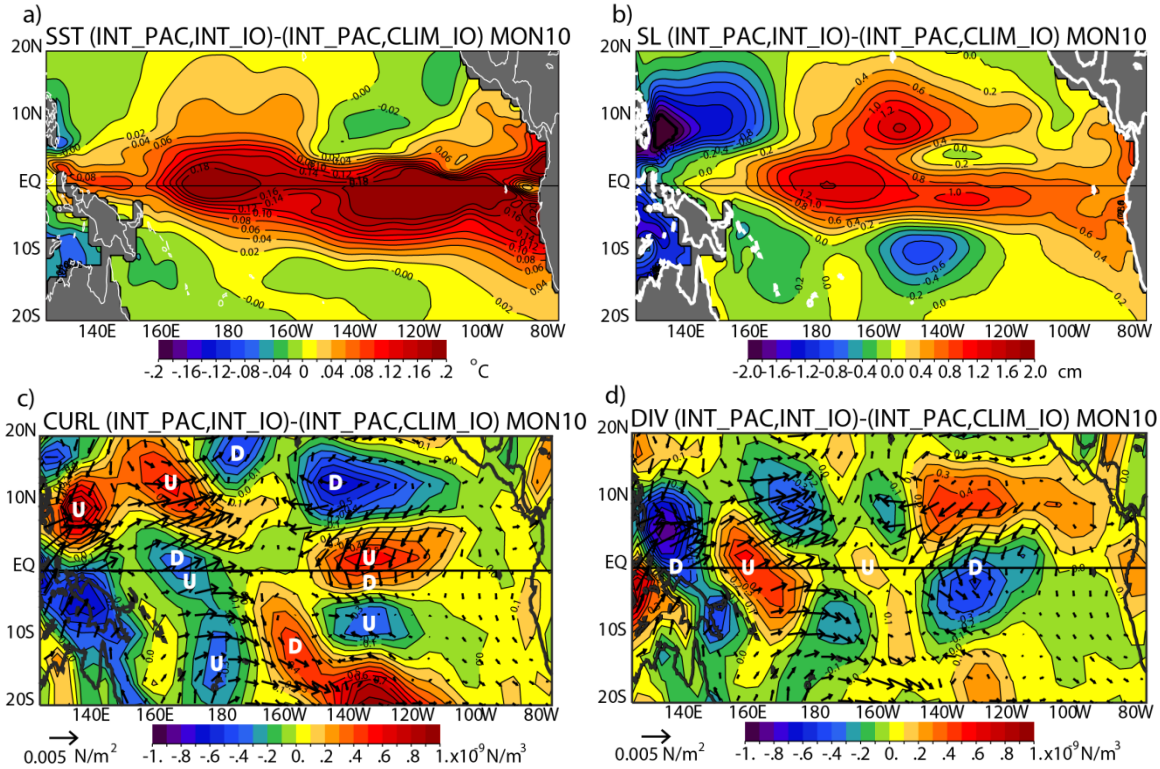

Figure 4.9: Average 10 month forecast INT_PAC, INT_IO-INT_PAC, CLIM_IO. *Same as previous but for 10 month forecast mean.*

By month 10 the Bjerknes coupling has locked in (Figure 4.9). SST' is positive throughout the equatorial band between 160°E to the eastern boundary. The negative sea level horseshoe pattern is evident off the equator in the west and positive values east of 160°E near the equator typically associated with a mature El Niño. On the equator, winds are diverging between 150°E-175°E and converging to the east of there between 150°W-100°W. To the east of 150°W and off the equator, the curl and sea level are in good

agreement. At 10°N, 150°W, downwelling curl corresponds with positive sea level anomaly. At 2°N, 135°W positive curl overlays with a small region of negative sea level. Just south of the equator at 135°W, downwelling curl coincides with a maximum of sea level and SST'. Further to the south at 10°S and 140°W upwelling curl and negative sea level coincide. Thus the pattern of upwelling/downwelling curl of the wind maintains the meridional sea level gradient east of 160°W. Off the equator west of 160°W, upwelling curl is acting to reinforce the negative sea level off the Philippines and off the coast of New Guinea and Australia. To summarize, the mean forecast by 10 month lead times shows winds that are primarily diverging away from the equator west of the dateline (i.e. southwesterlies to the north and northwesterlies to the south of the equator) and converging towards the equator east of the dateline (with northeasterlies north of the equator slowing and turning towards northwesterlies at the equator). These diagnostics of the average coupled forecast reveals that the response of the ENSO system in the Pacific is more complicated than simply triggering a westerly wind burst in the western Pacific on the equator and setting off downwelling Kelvin waves eventually warming the NINO3 region as suggested by e.g. [*Annamalai et al.*, 2010].

4.3 Summary of Atmospheric Teleconnections

In order to investigate the atmospheric teleconnections of the IO to the Pacific ENSO, two experiments were contrasted. In one, the full Indo-Pacific region atmosphere is forced by observed interannual SST anomalies (INT_PAC, INT_IO). In the other, the IO is forced by climatological SST (INT_PAC, CLIM_IO). Differences between these two forced atmospheric model experiments, point out the impact of the interannual

forcing in the IO on the Indo-Pacific. These differences spotlight a much richer wind response pattern in the Pacific than previous work that used idealized forcing and simple linear atmospheric models. Weak westerlies are found near the equator between 10^{o}S and the equator similar to previous literature (e.g. [*Annamalai et al.*, 2005]). However, at initialization strong easterlies between 30^{o}S to 10^{o}S and 0^{o}N to 25^{o}N and equatorial convergence of the meridional winds across the entire Pacific are unique findings from this dissertation. Coupled forecasts that include IO interannual forcing are significantly improved relative to the decoupled IO with respect to the 1993 to 2014 observed NINO3 SST anomaly. The reason for this improvement comes from the prevailing wind patterns in the Pacific generated from interannual IO SST coupling. Generally these wind patterns correspond to large-scale equatorial divergence west of the dateline and northeasterly-to-northwesterly cross-equatorial flow converging on the equator east of the dateline. In addition, off-equatorial curl impacts large-scale oceanic waves (i.e. Kelvin and Rossby waves) in response to the interannual atmospheric forcing of the IO via atmospheric teleconnections to the Pacific ENSO. After 3 months, downwelling Kelvin waves increase the NINO3 SST and eventually Bjerknes feedback takes hold in the eastern Pacific which allows this warm anomaly to grow. Therefore, the atmospheric impact of the IO is to increase the warming in the NINO3 region for 1993 to 2014 and improve coupled forecasts.

5 Role of the Indian Ocean Sector – Impact of Observations

Earlier work of [*Balmaseda and Anderson*, 2009] highlighted the importance of observations for SST analyses in the IO. For example, including Argo data significantly improved SST forecasts throughout the tropical IO. In addition, [*Huang et al.*, 2008] show that incorporation of real salinity profiles from Argo, led to improved vertical structure and more realistic barrier layer thicknesses in the tropical IO. More realistic mixed layer depths result in better estimates of modeled SST and so should lead to better forecasts. Observations in the IO are also important for measuring the long-term SST trend and fixing forced ocean model solutions. For example, the observed trend averaged over the entire tropical IO (20^oS-20^oN) for 1992-2014 is $1.5x10^{-2}$ $^oC/yr$ from the observed satellite SST product [*Reynolds et al.*, 2002] whereas the model alone (i.e. the IP_OPEN experiment) is $-0.7x10^{-3}$ $^oC/yr$ over the same region and time. When assimilation of all available observations takes place (i.e. ASSIM_SL_SST_SSS_T_z_S_z to be discussed later in this section), the trend becomes more realistic ($0.8x10^{-3}$ $^oC/yr$) with the correct sign and approximate amplitude. Therefore observations from satellite and in situ observations in the IO help to improve simulation of SST warming in the IO.

Operational coupled models routinely assimilate most available observations with the goal of improving ocean circulation and forcing at initialization. However, these previous results are comprised of model-only experiments and so the potential positive impacts of observations in the IO have not yet been fully considered. In the previous section we have seen that the interannual variability of the SST anomalies in the IO have a significant impact for improved ENSO forecasts. Thus, improved initialization of the coupled system due to assimilation in the IO may help to constrain the Pacific-to-IO

oceanic pathway (via e.g. modulation of the ITF flow) and the atmospheric teleconnection from the IO-to-Pacific by improving SST forecasts and the resulting air-sea coupling throughout the Indo-Pacific region. For example, [*Yuan et al.*, 2013] and [*Izumo et al.*, 2014] suggest that including IO observations (i.e. IODZM events) can extend useful ENSO predictions. Although many forecast studies have focused on how assimilation in the Pacific improved ENSO forecasts (e.g. [*Ji et al.*, 2000] and [*Hackert et al.*, 2011]), the impact of IO observations on ENSO predictability has been relatively neglected. Therefore, the main goal of this section is to assess the impact of IO observations through assimilation of available satellite and in situ data into initialization of coupled ENSO predictions.

5.1 Forced Ocean and Atmospheric Model Results

The most straight forward way of determining the impact of IO observations on coupled ENSO predictability is to compare an experiment that is initialized with the full impact of observations throughout the Indo-Pacific region (i.e. assimilation of SL, SST, SSS, T_z, and S_z abbreviated as ASSIM_SL_SST_SSS_T_z_S_z) versus one that masks assimilation in the IO and only assimilates data in the Pacific (i.e. ASSIM_SL_SST_SSS_T_z_S_z_MASKIND - for masked IO). Throughout this section the jargon for these model differences is either 'IO data impact' or 'FULL minus MASKED IO'. The longitude, 130^{o}E, is the demarcation between the IO and Pacific for assimilation purposes since it marks a convenient narrow passageway of the western ITF. Data that are assimilated include the multi-satellite blended sea level data from the AVISO using all available altimetry, the OI combination of AVHRR satellite and in situ

SST from NOAA, the OI of all available near-surface in situ salinity (using all data within 10m of the surface) and individual in situ temperature and salinity profiles. These observations are detailed in Section 2.1. Experiments were limited to the period, 2002-

Experiment Name	Period	Model Geometry	Assimilation Data/Region
ASSIM_SL_SST_SSS_T_z_S_z (abbreviated as "FULL")	2002-2014	Global/Indo-Pacific	Anomalies of SL, SST, SSS, T_z, S_z / for Pacific and IO
ASSIM_SL_SST_SSS_T_z_S_z_MASKIND (abbreviated as "MASKIND")	2002-2014	Global/Indo-Pacific	Anomalies of SL, SST, SSS, T_z, S_z / for Pacific only

Table 5.1: Experiment description isolating the impact of observations in the IO. *This Table defines the data assimilation methodology for the various experiments. The far left column is the experiment name. The data that are assimilated include: SL - the global multi-satellite sea level anomaly from AVISO, SST - OI of all satellite and in situ sea surface temperature from NOAA, SSS – the OI of all near surface salinity within 10m of surface and subsurface temperature and salinity profiles (T_z, S_z) mostly from Argo. See Section 2.1 for full details about the assimilation data. The delineation between the Indian and Pacific Oceans for data assimilation is defined as 130^{o}E in the Indonesian Seas. Anomalies are formulated with respect to the 1993-2014 mean seasonal cycle.*

2014, since the Argo array is only well established during this period and there are enough in situ data so that SSS, T_z and S_z are reasonably well populated in the IO. The experiments for this section are defined in Table 5.1, have the same specifications as those described in Section 2.2.1 for the model validation and use the EROKF technique detailed in Section 2.2.2. Differences of coupled experiments initialized by the full Indo-Pacific minus masked IO assimilation show the impact of IO observations on ENSO prediction.

The differences at initialization, for the impact of IO assimilation, are displayed in Figure 5.1. As expected, the biggest impacts of observations are found in the IO. For SL (Figure 5.1a) the pattern shows negative values in the eastern IO, BOB, and AS and

positive values stretching out from the western IO boundary centered at roughly 12^{o}S. In the Pacific west of 160^{o}W, negative sea level predominates with minimum values found at 5^{o}S and 8^{o}N just west of the dateline. Sea level is positive at 15^{o}S, along the equator, and 12^{o}N east of 140^{o}W. One could envision the pattern in the Pacific as an upwelling Rossby wave with negative sea level in the western half and downwelling Kelvin wave reflecting as a downwelling Rossby wave with positive sea level in the eastern half of the basin. Remember that these differences are only due to the regional assimilation but with identical forcing. For SST (Figure 5.1b), the largest values are found in the IO with the maximum at roughly 65^{o}E, 12^{o}S coincident with the location of the largest positive SL differences. These warm SST differences are consistent with the observed warming trend in the IO over recent decades (e.g. [*Luo et al.*, 2012]).

For the Pacific, the differences due to IO assimilation are generally negative. The coolest values correspond to differences less than -0.05^{o}C between 15^{o}S and 10^{o}N with minimum values between 130^{o}W-80^{o}W at 10^{o}S, 140^{o}W-100^{o}W at the equator, and145^{o}W-130^{o}W at 10^{o}N. However, all these values are very small compared to the IO. For Figure 5.1c, the differences of the observations in the IO generally bring about deeper MLD throughout the IO. For the Pacific, the strong shoaling of the MLD due to the influence of assimilation of observations in the IO is evident between 15^{o}S-8^{o}N and west of 120^{o}W. East of there in the far eastern Pacific, the MLD deepens within 10^{o} of the equator.

In the same way as previous sections, the output of the SPEEDY atmospheric model forced by FULL and MASKIND data assimilation results are differenced to

explain the IO observational impact on the atmosphere at initialization. Figure 5.1d shows the SPEEDY model results (forced not coupled) for wind stress (vectors) and

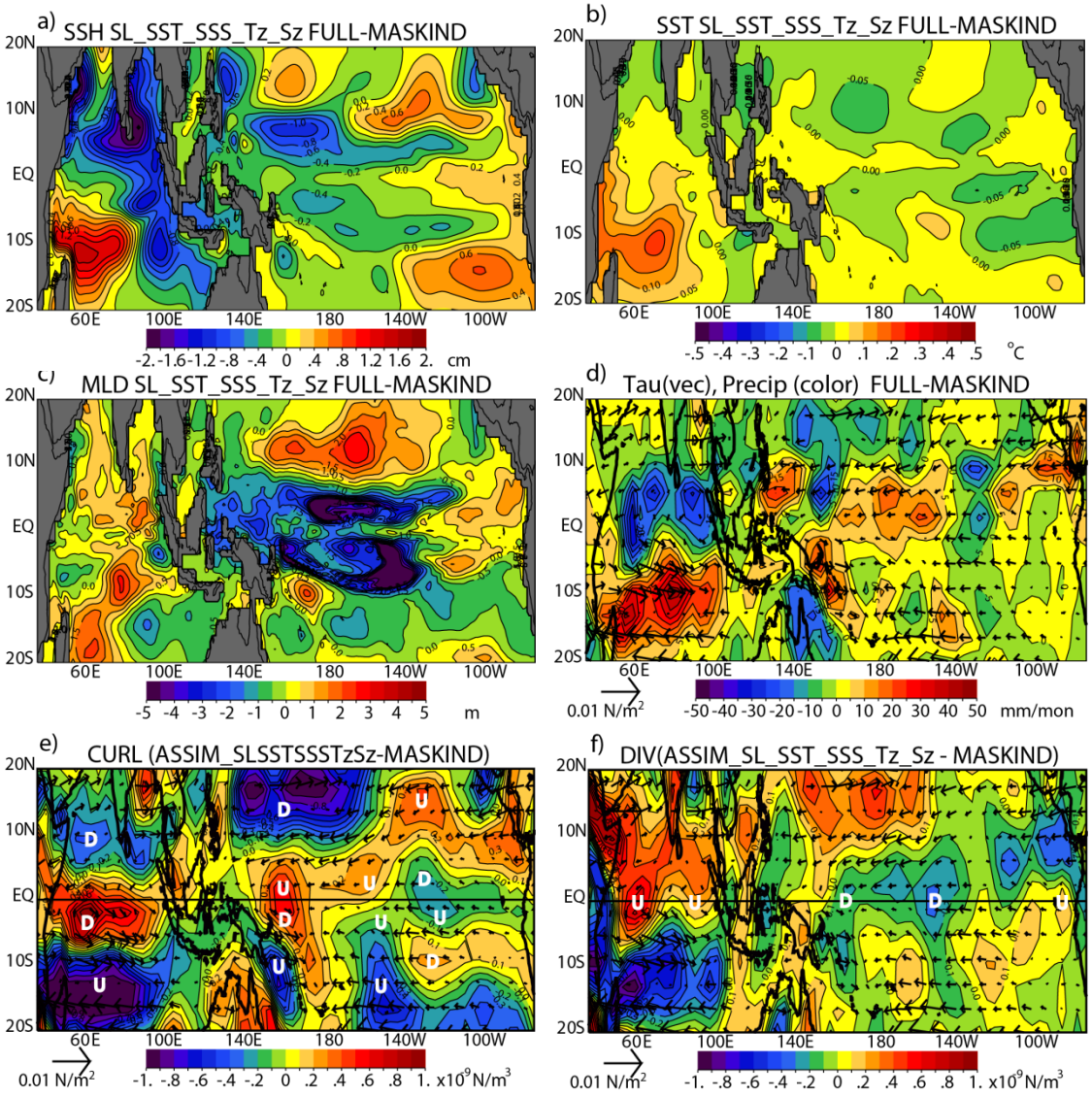

Figure 5.1: Differences FULL minus MASKIND at initialization. *The mean differences for full Indo-Pacific assimilation of SL, SST, SSS, T_z and S_z (i.e. ASSIM_SL_SST_SSS_T_z_S_z) minus the experiment that only assimilates in the Pacific (ASSIM_SL_SST_SSS_T_z_S_z_ MASKIND) are presented for all months 2002-2014. The panels show a) sea level, b) SST, c) MLD, d) SPEEDY atmospheric results for precipitation (color) and wind stress (arrows), e) curl (color) and wind stress (arrows) and f) divergence (color) and wind stress vectors(arrows). "U" and "D" on panels e) and f) represent regions on upwelling and downwelling favorable conditions, respectively. Absolute values exceeding 1.1 cm, 0.1°C, 2.7 m, [6.9x10^{-3} N/m^2; 18.25 mm/mon], 0.85x10^{-9} N/m^3 and 0.55 N/m^3 are significant for the six panels, respectively.*

precipitation (colors). This plot shows that weak northeasterlies just north of the equator in the IO recurve into northwesterlies converging towards the warmest water as seen in Figure 5.1b. Warm SST' in the southern IO leads to atmospheric convection, abundant rainfall, and convergence of the winds at the surface. The precipitation pattern shows negative values north of 5^{o}S in the IO and positive in the Southern Hemisphere again consistent with convergence (Figure 5.1f) towards and positive precipitation anomalies over the warmest anomaly. At initialization downwelling favorable curl (negative in the Northern Hemisphere and positive south of the equator) is evident everywhere north of the warmest SST in the IO and upwelling can be found south of 10^{o}S (Figure 5.1e). Apparent inconsistences between the curl and sea level (e.g. in the northern IO) are evident since these plots show the initialization state and coupling of the system has yet to occur.

In the Pacific, there are small areas of westerlies between 20^{o}S-5^{o}S and north of 15^{o}N west of the dateline. However, easterly flow predominates throughout most of the basin. This is consistent with the work of [*Annamalai et al.*, 2005] who noted that basin warming in the IO (i.e. their "basin-mode SST anomaly") would lead to easterlies in the western Pacific (their Figure 9a,c). The general pattern is abundant precipitation extending out from the Maritime continent to about 140^{o}W near the equator again consistent with enhanced Walker circulation. In addition, a feature in the eastern Pacific precipitation is the negative values that overlay with the negative SST anomalies found east of 140^{o}W. These patterns of negative precipitation are in line with the overall cooling and suppressed convection in the eastern Pacific. Figure 5.1e shows the curl of the wind stress for the differences brought about by observations in the IO. Over most of

the Pacific, upwelling favorable curl (i.e. positive in the Northern Hemisphere and negative in the Southern Hemisphere) predominates. These results document the differences in the initial conditions for the coupled experiments. So to summarize, the impact of observations in the IO leads to warm SST over most of the IO basin. Warm SST leads to atmospheric convergence and enhanced precipitation. The easterly trade winds over the western Pacific flow into this IO warm anomaly and the Walker circulation is enhanced. Sea level and MLD are shoaled between 12°S-8°N west of 140°W concomitant with anomalous easterlies and general upwelling.

5.2 Coupled Model Results

Results of coupled experiments initialized using assimilation of all available observations in the IO (i.e. ASSIM_SL_SST_SSS_T_z_S_z) are contrasted with those lacking the influence of observations in the IO (i.e. ASSIM_SL_SST_SSS_T_z_S_z_ MASKIND) in order to assess the impact of IO observations on ENSO predictability.

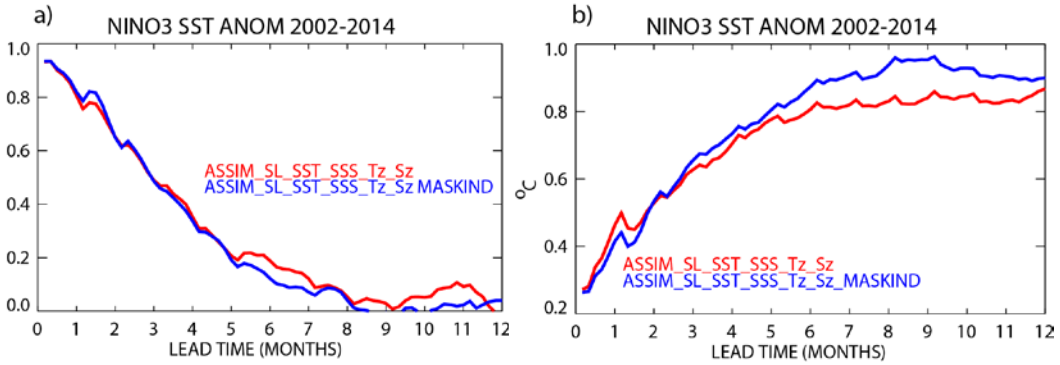

Figure 5.2: NINO3 statistics of IO observations assimilation. *Validation statistics for SPEEDY coupled model results for a) correlation and b) RMS differences between full Indo-Pacific assimilation of SL, SST, SSS, T_z and S_z (i.e. ASSIM_SL_SST_SSS_T_z_S_z shown as red curve) and the experiment that only assimilates in the Pacific, masking assimilation in the IO (ASSIM_SL_SST_SSS_T_z_S_z_ MASKIND, blue). The experiments are validated with respect to the observed NINO3 SST anomaly for 2002-2014. Individual correlations exceed the 95% significance out to 3.7 (23) and 3.5 months (22) (effective degrees of freedom) for red and blue lines, respectively.*

For each month for 2002-2014 12-month coupled forecasts are initialized from these two experiments. As with previous experiments, we validate these two coupled experiments using observed SST anomalies in the NINO3 region [*Reynolds et al.*, 2002]. In Figure 5.2a, both the full assimilation and the experiment that masks assimilation in the IO are individually significant only to about 3.5 months. Correlation differences generally remain below r=0.05 but peak at 6 and 11 month lead times. However, the differences never climb to the statistically significant threshold. In Figure 5.2b the improvement brought about by full assimilation is more readily apparent than for the correlation validation. For example, the RMS for the full assimilation is lower by as much as 0.07°C and 0.13°C for lead-times of 6 and 9 months, respectively. Over most of the forecast, the RMS values are smaller for the FULL assimilation case. Although the correlation differences are small and thus not significant, the full assimilation still outperforms the experiment masking assimilation in the IO for RMS. In other words, the impact of all available observations in the IO slightly improves coupled forecasts as validated by NINO3 observed SST anomalies.

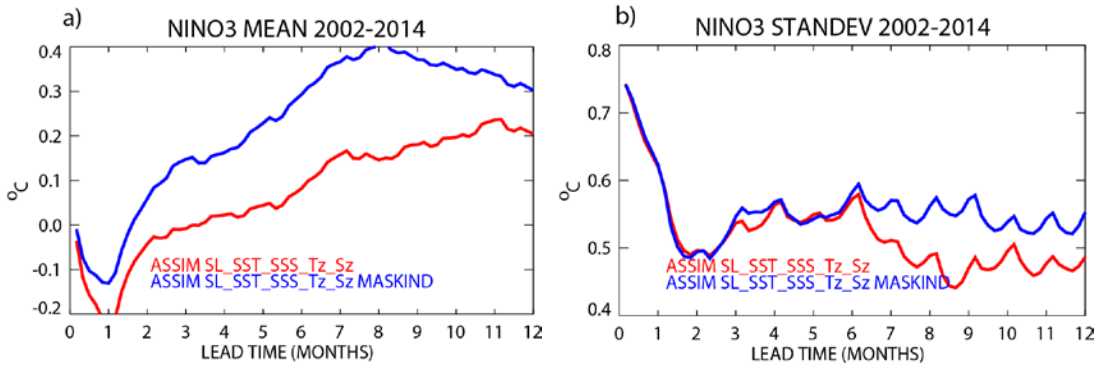

Figure 5.3: Impact of IO assimilation for NINO3 mean and standard deviation. *Forecasts lead-time statistics for SPEEDY coupled model results for a) mean and b) standard deviation for the NINO3 region for full Indo-Pacific assimilation of SL, SST, SSS, T_z and S_z (i.e. ASSIM_SL_SST_SSS_T_z_S_z shown as red curve) and the experiment that only assimilates in the Pacific (ASSIM_SL_SST_SSS_T_z_S_z_MASKIND, blue).*

In order to diagnose how inclusion of observations in the IO improves upon the experiment that masks assimilation in the IO, the mean forecasts for the NINO3 region are presented. The mean for the full assimilation is considerably lower than the coupled experiment that masks assimilation in the IO. Figure 5.3a shows that for all lead times the coupled forecasts for the ASSIM_SL_SST_SSS_T_z_S_z (red curve) have lower means. For the variability, the two experiments are relatively indistinguishable until roughly 6 month lead-times. After that time, the full assimilation has weaker variability of around 0.48^{o}C as opposed to 0.55^{o}C. In summary, inclusion of observations in the IO somewhat improves the forecast statistics for RMS. In addition, the mean forecast is substantially

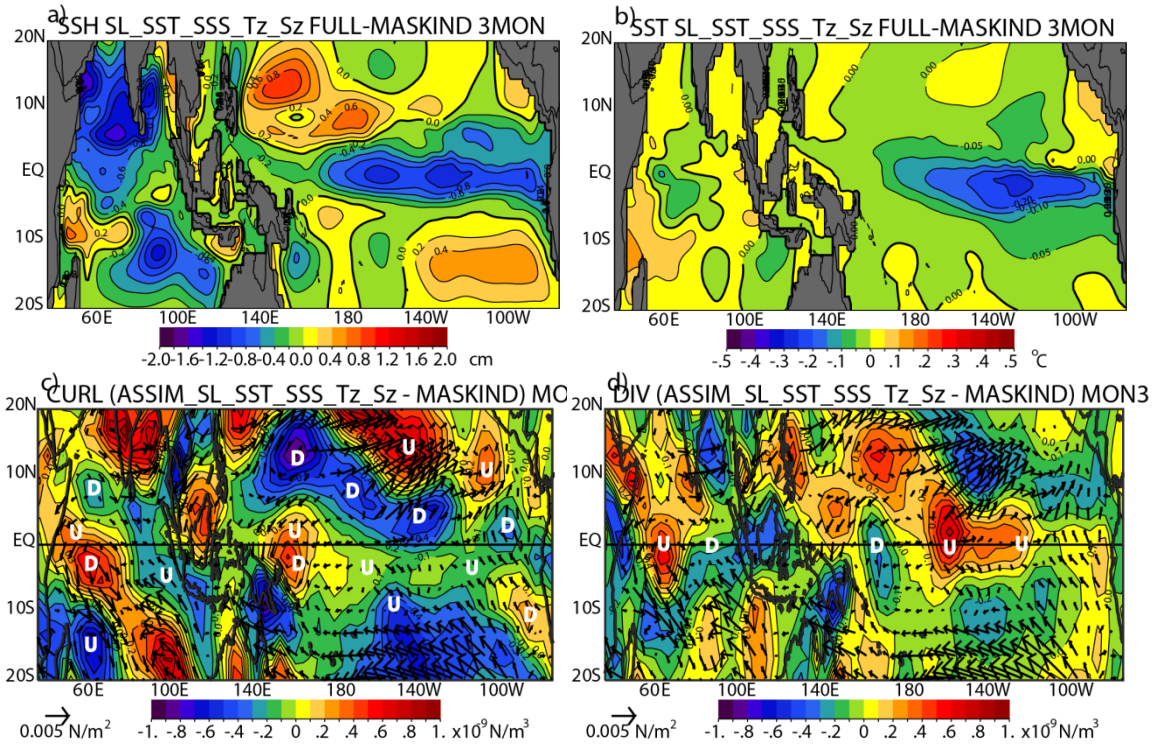

Figure 5.4: Differences FULL minus MASKIND at 3 month forecast lead time. *The mean differences for 3 month lead-time SPEEDY forecasts are presented for the full Indo-Pacific assimilation minus the experiment that only assimilates in the Pacific. Average forecast values for month 3 for a) sea level, b) SST, c) curl of the wind stress (color) and wind stress (vector), and d) divergence of the wind stress (color) and wind stress (vector). The scale of the vector plot is indicated in the bottom left of the panel. For the reader's convenience, regions of upwelling and downwelling are marked by letters U and D, respectively.*

cooler but the variability is weaker only after 6 month lead-times for the full versus the masked IO assimilation experiments.

To show how the coupled forecasts develop and how the coupled forecast statistics evolve leading to the results of Figure 5.2 and Figure 5.3, the mean forecast differences after 3 month lead time, FULL-MASKIND coupled results, are presented in Figure 5.4. Easterlies present in the western Pacific in the initial conditions enhance the Walker circulation and continue over the 0-3 month forecast lead times serving to effectively decrease sea level the eastern Pacific. Anticyclonic winds and downwelling favorable curl (negative) north of 5^{o}N centered at 160^{o}E over the western half of the Pacific combine with downwelling curl (positive) just off New Guinea to deepen sea level off the equator in the western Pacific (Figure 5.4a). These features are identified as a downwelling Rossby wave in Figure 5.5b arriving at the dateline in month 3. At that same time diverging winds along the equator (Figure 5.4d) contribute upwelling signal east of the dateline in the Pacific. Upwelling along the equator and just south of the equator (Figure 5.4c) corresponds to lower sea level on the equator and cooler SST just south of the equator east of the dateline (Figure 5.4a, b, respectively). The predominant upwelling Kelvin waves, driven by the persistent easterlies in the western Pacific and diverging winds west of the dateline along the equator, are clearly demonstrated in Figure 5.5a (dashed lines) and these have propagated from the west serving to cool the NINO3 region (Figure 5.4b) cooling by as much as 1.5^{o}C. Hovmöller diagram (not shown) of the sea level differences indicate that the upwelling Kelvin wave arriving at the eastern boundary in month 3 has its origins in the reflected upwelling Rossby wave identified in the sea level at initialization (negative sea level at 5^{o}N, 5^{o}S and 160^{o}E in Figure 5.1a).

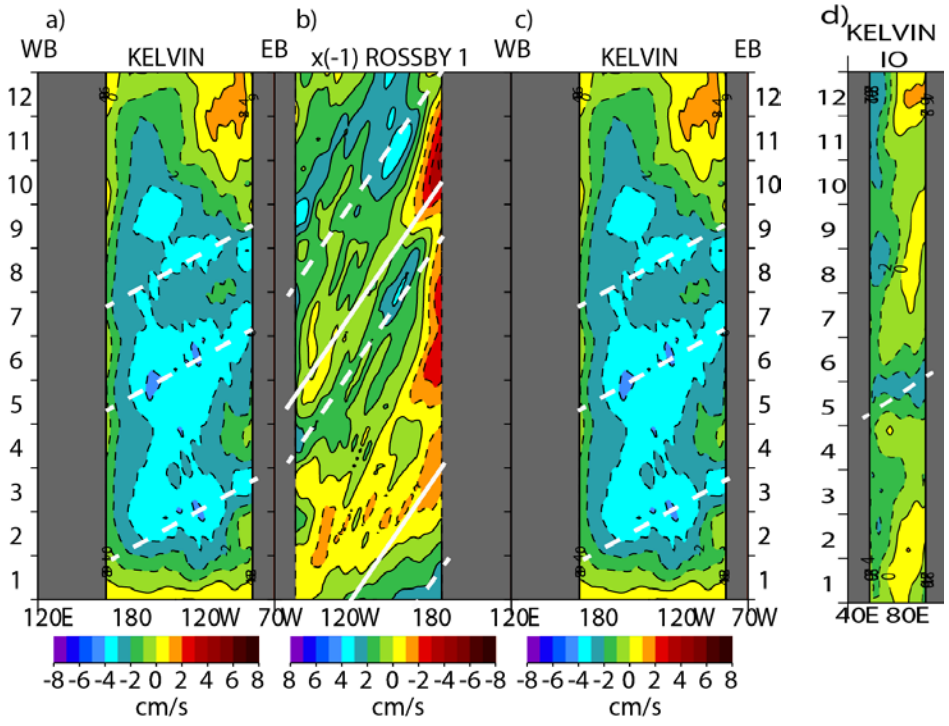

Figure 5.5: Kelvin/Rossby decomposition of FULL minus MASKIND results. *Longitude versus time distribution of the equatorial (a) Kelvin and (b) the first meridional mode of equatorial Rossby waves through their signature in zonal surface current deduced from the average forecast SL differences, (ASSIM_SL_SST_SSS_T_z_S_z) – (ASSIM_SL_SST_SSS_T_z_S_z_MASKIND). In order to follow possible wave reflections on the western (WB) and eastern (EB) boundaries of the Pacific, the Rossby panel (b) is inverted and the Kelvin wave pattern is repeated (c). The color scale for the Rossby panel is also inverted since reflection on meridional boundaries results in zonal currents of opposite sign. Solid lines (downwelling) and dashed lines (upwelling) represent theoretical wave speeds for Kelvin (2.5m/s) and Rossby waves (-0.8m/s or ~5months to cross this Pacific basin at 5^{o}N) on each plot. Panel d) corresponds to the IO Kelvin decomposition with the same color scale as a).*

Traces of this upwelling Rossby wave can also be found in Figure 5.5b and the timing matches the reflection into the primary upwelling Kelvin wave in Figure 5.5b to Figure 5.5c at month ~1.5.

By 6 month forecasts, warm SST can be found west of 145^{o}E and so the SST gradient across 140^{o}W to 140^{o}E in the Pacific enhances the easterlies of the Walker circulation (Figure 5.6d) and then Bjerknes coupling fully takes hold in the Pacific.

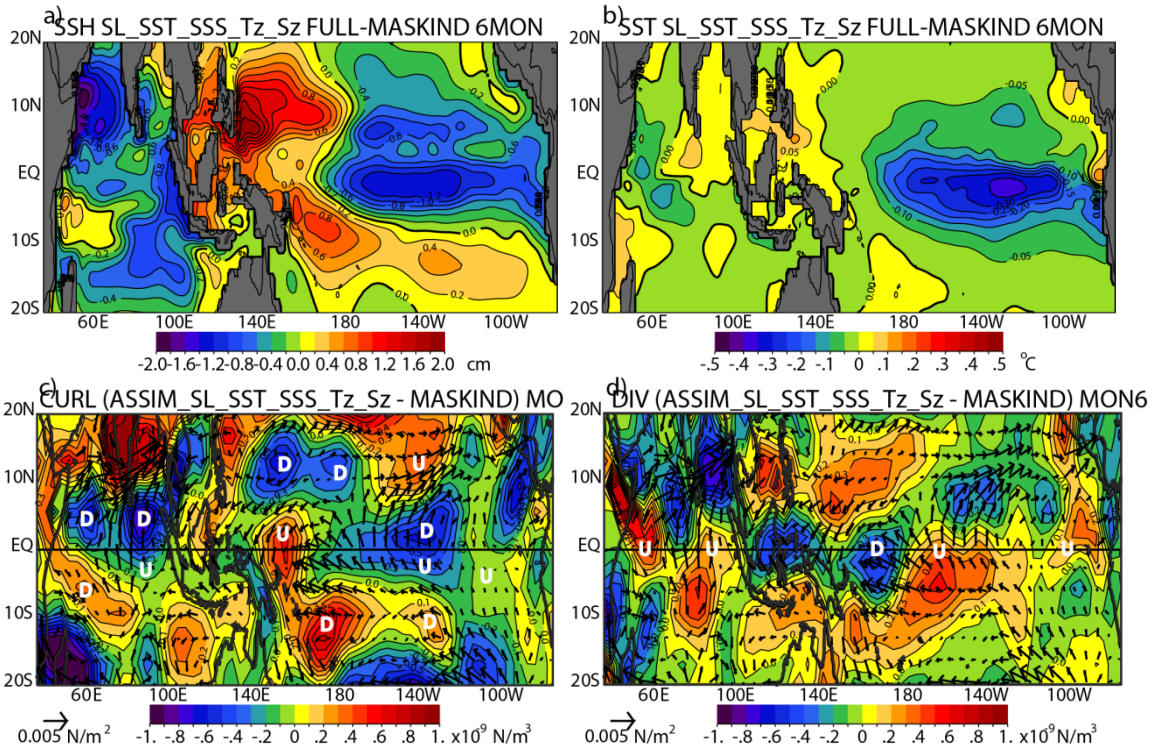

Figure 5.6: Differences FULL minus MASKIND for 6 month forecast lead times. *Same as Figure 5.4 but for 6 month forecast lead times.*

Differences in the Pacific now strongly resemble the typical La Niña pattern, namely the SST is negative in the cold tongue region of the eastern Pacific (Figure 5.6b), the sea level has a positive horseshoe shape in the western Pacific and negative values in the eastern Pacific near the equator (Figure 5.6a), easterly trades are enhanced along the equator west of 120^{o}W. Downwelling favorable curl (Figure 5.6c) reinforces the positive sea level horseshoe pattern 10^{o} off the equator in the western Pacific and wind divergence (Figure 5.6d) along the equator reinforces the cold upwelling east of the dateline. Thus, the impacts of observations in the IO at initialization serve to eventually intensify the cold tongue and explain the differences in the mean forecast found in Figure 5.3a where the mean NINO3 SST' is reduced by 0.21^{o}C at 6 months relative to the MASKIND experiment.

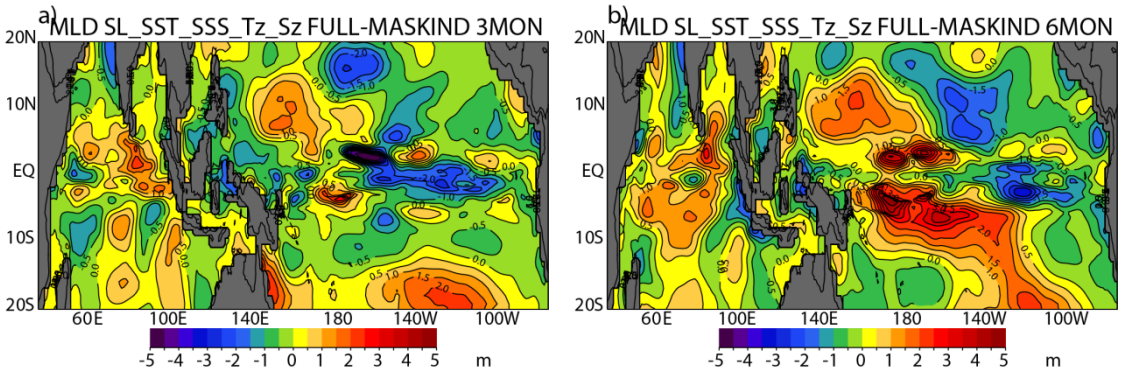

Figure 5.7: Forecast evolution of MLD for FULL minus MASKIND. *Average Mixed layer depth differences ASSIM_SL_SST_SSS_Tz_Sz minus ASSIM_SL_SST_SSS_Tz_Sz_MASKIND for a) 3 month and 6 month forecast lead times.*

As far as the variability of the NINO3 region is concerned, the differences between the FULL and MASKIND experiments in Figure 5.3b can be explained by the progression of the MLD plots from Figure 5.1 and Figure 5.7. The MLD is shallower for ASSIM_SL_SST_SSS_T_z_S_z than for ASSIM_SL_SST_SSS_T_z_S_z_MASKIND at initialization between 10^{o}N-10^{o}S west of 120^{o}W (Figure 5.1c). Over time the MLD follows the same progression as sea level. In the western Pacific (west of 180^o at ~10^{o}S and 10^{o}S) downwelling favorable curl increases sea level as well as deepens the MLD. Upwelling on the equator shoals the MLD so that by 3 month forecasts (Figure 5.7a), the MLD is shallower in the cold tongue and the western Pacific MLD difference values are generally small along the equator. However, by 6 month forecasts, when the variability in the NINO3 region decreases in Figure 5.3b, MLD differences west of 160^{o}W are significantly deeper so the Kelvin wave-generating winds are expended on a much deeper MLD in the western Pacific. Thus, after 6 months the variability is reduced. Another way to envision the falling variability in the NINO3 region after 6 months lead times is that the Kelvin wave signal in the Pacific is dissipating after 6 month forecasts for the mean difference, FULL minus MASKIND, as illustrated in Figure 5.5a.

In the IO, the pattern remains similar as for the initialization (Figure 5.1) but with the SL and SST differences decreasing over time. For example, the maximum SL gradient across the IO at 10^{o}S starts at 6.5 cm (Figure 5.1a). By 3 month lead times, this gradient has dropped to 4.5 cm (Figure 5.4a) and by 6 month lead time the gradient is only 3 cm (Figure 5.6a). The warm SST found in the initial conditions (0.2^{o}C - Figure 5.1b) quickly cools to no more than 0.1^{o}C for 3 and 6 month forecasts (Figure 5.4b and Figure 5.6b, respectively). Another major feature to note is the upwelling Kelvin wave found in the IO for forecast lead times of 5-6 months (Figure 5.5d). This Kelvin wave is generated by widespread divergence due to the transition of southeasterlies to southwesterlies as they cross the equator (Figure 5.6c) and is reflected in the sea level since values drop significantly just to the west of Sumatra for month 6 as this Kelvin wave arrives at the eastern boundary (Figure 5.6a) of the IO.

The previous discussion has not yet focused on the impact on the Indonesian Throughflow (ITF) brought about by observations in the IO. Examining the SL forecast differences after 6 months, one would envision that the ITF flow should increase for the FULL assimilation versus the MASKED IO assimilation case. Figure 5.6a shows the strong positive SL anomaly at the mouth of the ITF just off the Philippines Islands and the negative values at the exit region just west of Sumatra. [*Wyrtki*, 1987], [*Potemra*, 2005] and more recently [*Susanto and Song*, 2015] all deduced that an increased pressure head between the Pacific and the IO would lead to increased ITF flow. The indices of sea level differences, FULL - MASKIND, for the eastern IO (EIO) and the western Pacific (WP) are presented for the 0-12 month lead times in Figure 5.8a. These regions are meant to roughly reproduce those used by [*Potemra*, 2005] to estimate the ITF

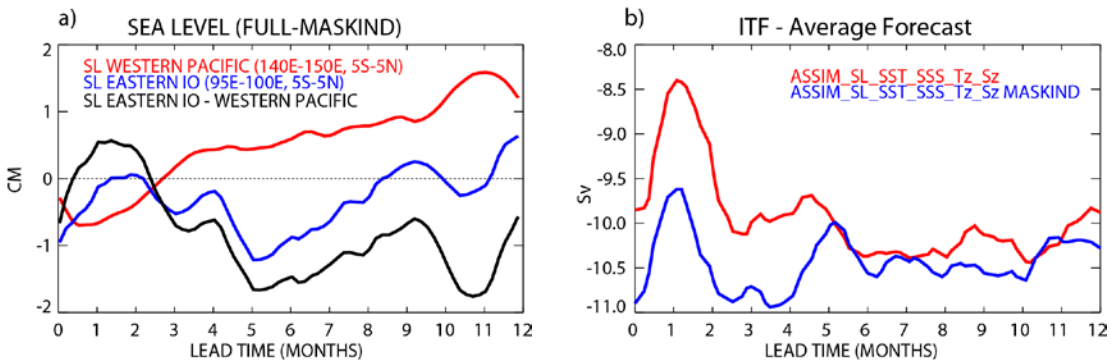

Figure 5.8: ITF flow of mean forecast for FULL versus MASKIND experiments. *Plot a) shows the sea level indices for the western Pacific (red), eastern Indian Ocean (blue) and the sea level gradient across the ITF (i.e. eastern IO minus western Pacific - black) for the ASSIM_SL_SST_SSS_Tz_Sz (i.e. FULL) minus ASSIM_SL_SST_SSS_Tz_Sz_MASKIND results. Plot b) shows the ITF flow for the FULL assimilation in the Indo-Pacific region in red and the experiment that MASKS assimilation in the IO in blue. Negative values for a) and b) represent westward flow. Regions are defined in the key for a).*

transport using sea level gradient. For the western Pacific (red line), the sea level differences rise over the entire average forecast period due to the aforementioned sea level rise and associated downwelling curl off the equator and converging winds on the equator west of the dateline. For the EIO (blue line), the values remain weak until roughly month 6 when the upwelling Kelvin wave (seen in Figure 5.5d and forced by upwelling along the equator in Figure 5.6d) arrives in the EIO. The differences, EIO minus WP (black line), lead to an increased pressure head and the experiment that includes observations in the IO has a significant jump for the values for the ITF at 6 month lead time (Figure 5.8b). In other words, the upwelling Kelvin wave arrives at the eastern boundary and traverses the Indonesian Seas carrying westward flow with it, increasing the amplitude of the ITF. After it passes, the ITF has larger westward flow (i.e. larger negative values) and the FULL assimilation experiment matches the magnitude of the MASKIND experiment after that time. In this case, the increase in ITF magnitude corresponds to both a deeper MLD in the western Pacific and a decrease in the

NINO3 SST variability. However, these results are at odds with the results of Section 3, namely that the IP_OPEN minus IP_NOITF (i.e. the extreme case of larger ITF flow) leads to shallower MLD and increased NINO3 variability. Therefore, in the case of the impact of the IO observations for ENSO we judge that the IO atmospheric teleconnections to the Pacific ENSO have a bigger influence than the impact of the ITF.

5.3 Summary of the IO Observation Impact on ENSO

The impact of observations in the IO on ENSO forecasts are diagnosed using the output of two experiments. In one, all the available satellite and in situ observations for the Indo-Pacific region are assimilated into the initial conditions for coupled experiments (ASSIM_SL_SST_SSS_T_z_S_z). In the second, observations are excluded from the IO region but included in the Pacific sector (ASSIM_SL_SST_SSS_T_z_S_z_ MASKIND). Coupled experiments are then initiated from both these experiments for each month from 2002-2014 and these show that ENSO predictions are improved when observations in the IO are incorporated. ENSO forecasts, validated using observed NINO3 SST values, show that RMS is slightly improved and the mean and variability (only after 6 months) are reduced when the impact of observations in the IO are accounted for. Basin-wide warming in IO brought about by assimilation in the IO, leads to atmospheric Kevin waves with easterlies predominating over the western Pacific enhancing Walker circulation. These easterlies near the equator generate upwelling oceanic Kelvin waves that traverse the Pacific leading to upwelling and lower SST' in the NINO3 region. At the same time downwelling-favorable curl, centered ~10^o off the equator in the western Pacific, deepens the thermocline and MLD, and raises the sea level and SST in the west.

As the forecast continues, warming in the west and cooling in the east maintains/enhances the Pacific SST gradient and Bjerknes coupling takes hold. A La Niña-like pattern becomes entrenched with enhanced trades in the tropical Pacific and cooling in the cold tongue region. Although the variability in the NINO3 region is reduced after 6 month lead times due to deepening of the MLD in the western Pacific and the associated damping of the Kelvin waves, the ITF flow is enhanced at this same time as a result of an upwelling (i.e. westward flow enhanced) Kelvin wave from the IO entering the Indonesian Seas.

6 Impact of Sea Surface Salinity on Coupled ENSO Prediction

In the previous sections we have demonstrated the critical importance of SST and mixed layer processes for the impacts of the IO on ENSO predictability. For example, a shallower MLD in the Pacific produces enhanced ENSO variability when the ITF is open, interannual SST' forcing in the IO results in equatorial and off-equatorial teleconnections to the Pacific that eventually lead to improved ENSO forecasts, and IO basin-scale warming (as isolated by IO observations) causes enhancement of the Walker circulation through Pacific SST gradients and enhanced Bjerknes coupling. However, coupled models generally have a hard time producing accurate fresh water flux due to suboptimal precipitation forecasts. For example, SPEEDY, the AGCM component of our coupled model, is too dry over the SPCZ and too wet over the tropical IO ([*Molteni*, 2003]). In addition, operational coupled models such as CFSv2 are known to be lacking in forecasting precipitation particularly in the Pacific ITCZ and SPCZ where rainfall is overabundant and in the western Pacific and near Indonesia where rainfall is deficient ([*Wang et al.*, 2010], [*Kumar et al.*, 2010], [*Saha et al.*, 2014]). Less than ideal fresh water forcing from SPEEDY and CFSv2 coupled models could potentially impact SST through inaccurate specification of mixed layer density and mixing. Therefore, we attempt to address the potential issues with inaccurate fresh water flux by assessing how assimilation of sea surface salinity in the Indo-Pacific region affects ENSO predictability. Specifically, the Hybrid Coupled Model (HCM) is utilized since this statistical atmospheric model specifies observed precipitation climatology from GPCP ([*Adler et al.*, 2003]) rather than using some suboptimal precipitation forecast.

This question of how improved sea surface salinity via data assimilation in the Indo-Pacific region affects ENSO predictability has yet to be fully addressed. In June 2011, NASA launched Aquarius which is the first satellite that was designed to monitor SSS on a global scale. Up until remote sensing of SSS, achieving a high resolution, uniform global view of surface salinity had not been possible due to sparse in situ salinity measurements. The overlaying scientific goal of the Aquarius mission was to quantify and understand the linkages among ocean circulation, the global water cycle and climate by accurately measuring SSS [*Lagerloef et al.*, 2008]. As in previous sections, a combination of ocean models, coupled ocean-atmosphere models, and data assimilation of satellite and in situ data, are used to investigate if satellite SSS data help to improve short-term ENSO predictions. (Note that this research has been published during Hackert's PhD candidacy [*Hackert et al.*, 2014]).

6.1 Salinity Observations and Long-Term SSS Coupled Model Validation

The current study extends the previous works of [*Hackert et al.*, 2011] and [*Ballabrera-Poy et al.*, 2002] by expanding to the tropical Indo-Pacific region from the Pacific and by incorporating assimilation of Aquarius and in situ SSS products. The impact of SSS is assessed by comparing an experiment that assimilates SSS data versus one that does not. The reference simulation assimilates subsurface temperature (ASSIM_T_z) only. Previous authors have shown that assimilation of subsurface temperature has been shown to produce reasonable coupled ENSO forecasts ([*Ruiz et al.*, 2005], [*Drosdowsky*, 2006], [*Lima et al.*, 2009]). The reference simulation does not assimilate SST and SL data, as these variables overly constrain the initialization of the

coupled ocean-atmosphere model, and given their covariance with SSS muddle the impact of SSS assimilation.

The purpose of this section is to show how SSS data impact the initialization of coupled ENSO predictions in general and how in situ SSS initialization compares to Aquarius. Thus, the role of the SSS data will be investigated using two different SSS products. One is an optimal interpolation (OI) of all available in situ mixed layer salinity observations and the other is the satellite SSS product provided by the Aquarius project. The general philosophy of this section is to difference coupled model experiments with SSS assimilation minus the baseline without SSS assimilation using the NINO3 (i.e. 5^{o}S-5^{o}N, 150^{o}W-90^{o}W) SST anomaly index as the validation target.

In addition to the assimilation of subsurface temperature data, weekly gridded fields (i.e. Level 3 data) of SSS from both Aquarius Version 2.9.1 ($ASSIM\_T_z\_SSS_{AQ}$) and our weekly in situ SSS product ($ASSIM\_T_z\_SSS_{IS}$) are assimilated to assess the impact of SSS on initialization of coupled forecasts. Gridded SSS products are detailed in Section 2.1. Each SSS data assimilation experiment is initialized using the $ASSIM\_T_z\_SSS_{ISMON}$ results for July 2011 and then assimilation of additional various SSS data takes place starting from August 2011 to February 2014. The different experiments discussed in this section are summarized in Table 6.1 and detailed in the following: the ocean model is run for 30 years using ECMWF climatological forcing. Then, starting in 1993, subsurface temperature is assimilated (abbreviated as $ASSIM\_T_z$) until February 2014 using realistic interannual forcing (both ECMWF winds and GPCP/TRMM precipitation). Another experiment that assimilates the monthly SSS in situ product along with T_z is run from 1993 until February 2014 (abbreviated as

Experiment Name	Period	Assimilation Variables
ASSIM_T_z	Jan 1993 - Feb 2014	T_z
ASSIM_T_z_SSS_{ISMON}*	Jan 1993- Feb 2014	SSS from OI of all available near surface salinity with depth ≤ 10 m and T_z, monthly
ASSIM_T_z_SSS_{IS}	Aug 2011 – Feb 2014	SSS from OI of all available near surface salinity with depth ≤ 10 m and T_z, weekly
ASSIM_T_z_SSS_{AQ}	Aug 2011 – Feb 2014	SSS from Aquarius Version 2.9.1 Level 3 data and T_z, weekly
ASSIM_T_z_$SSS_{AQ@IS}$	Aug 2011- Feb 2014	SSS from OI of Aquarius along-track data subsampled at in situ locations and times and T_z, weekly

Table 6.1: SSS assimilation experiments. *Summary of the salinity coupled model experiments used in this section. The first column is the experiment designation, the second indicates the period, and the third describes the data used to initialize these coupled model experiments. T_z stands for subsurface temperature. The asterisk indicates that the ASSIM_T_z_SSS_{ISMON} experiment is used to initialize all other assimilation experiments that assimilate SSS starting in August 2011.*

ASSIM_T_z_SSS_{ISMON}). Monthly OI is required prior to the Aquarius period due to the scarcity of in situ SSS observations (e.g. Argo) early in the record. Two additional experiments that, in addition to T_z, also assimilate weekly gridded Aquarius SSS (ASSIM_T_z_SSS_{AQ}) and an OI of in situ SSS (ASSIM_T_z_SSS_{IS}) are initialized from July 2011 ASSIM_T_z_SSS_{ISMON} results and cover the period from August 2011 until February 2014 (30 months). Anomalies are formulated for each SSS experiment with respect to the 1993-2013 mean seasonal cycle of the ASSIM_T_z_SSS_{ISMON} experiment and then these anomalies are added to the climatological ECMWF results and used as initial conditions for coupled experiments. Then for each month from August 2011 until February 2014, free SAM coupled model experiments are initiated from the three forced

experiments and are run for 12 months each (for a total of 360 months). Note that adding anomalies to ECMWF climatology model results are required since the SAM needs a fixed seasonal cycle of model SST (ref. Figure 2.2).

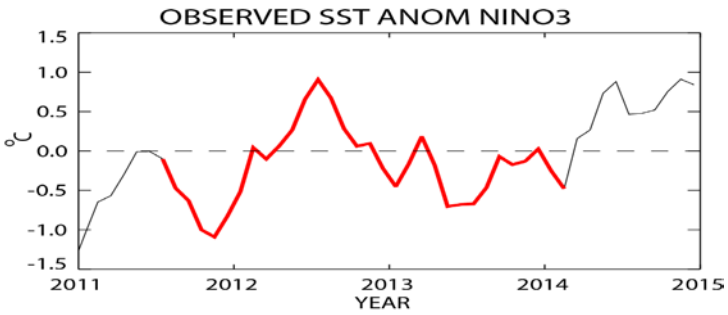

Figure 6.1: NINO3 SST anomaly for the Aquarius period. *The observed NINO3 SST anomaly is highlighted in red for the Aquarius period (i.e. 8/11-2/14).*

The period under consideration in this study is from August 2011 until February 2014. During this period, the NINO3 index (Figure 6.1) indicates a minor La Niña from September 2011 to January 2012 (i.e. NINO3 region SST anomaly less than -0.5^{o}C) with a minimum of -1^{o}C in December 2011. During 2012, the NINO3 SST anomaly rose peaking in July 2012 at 0.92^{o}C. While this warming was taking place, many coupled models predicted El Niño for late 2012 (see, e.g., the forecast discussion provided in http://iri.columbia.edu/climate/ENSO/currentinfo/archive/201207/SST_table.html). However, these El Niño forecasts proved inaccurate. Instead, cooling returned in the eastern Pacific for early 2013 with minimum negative anomalies in January 2013 of -0.57^{o}C. After that, cooling subsided in Boreal spring but returned in May to August 2013 (as low as -0.69^{o}C in June). The repeated cooling episodes correspond to an overall mean weak La Niña state (-0.25^{o}C) for the tropical eastern Pacific from August 2011 until February 2014.

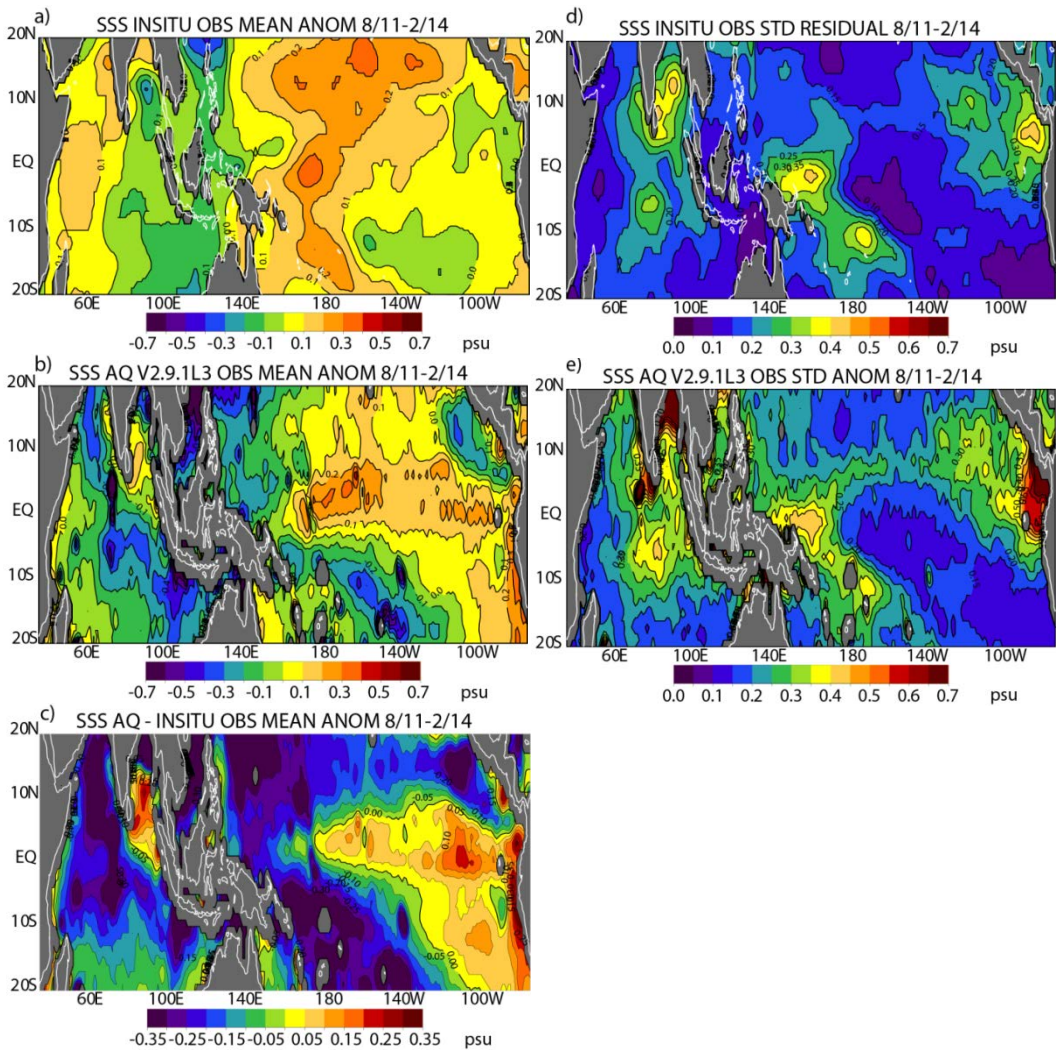

Figure 6.2: Gridded SSS Observations. *Mean of SSS anomaly for a) OI of all near-surface in situ data (SSS_{IS}), b) Aquarius L3 gridded product (SSS_{AQ}). Plot c) shows the mean difference between Aquarius minus in situ. (Note that the color bar is half that of the means.) Standard deviation is also presented for d) in situ and e) satellite SSS. Anomalies are all formulated with respect to Levitus SSS. All observations cover the period, 8/11-2/14 and all panels have been smoothed for plotting using a bilinear smoother.*

The mean and standard deviation of the in situ SSS and Aquarius SSS anomalies over the Aquarius period (August 2011-February 2014) are presented in Figure 6.2. Despite the many similarities between the two products there are important differences between the Aquarius satellite SSS and in situ SSS product (Figure 6.2c). An example is the relatively saltier values for Aquarius east of 180^{o} near the equator and east of 120^{o}W

in the Southern Hemisphere. In addition, Aquarius minus in situ SSS shows negative values in the ITCZ between 5^{o}N to 20^{o}N and in the SPCZ in the Pacific. In the Indian Ocean, Aquarius is generally fresher especially from the equator to 10^{o}S and in the Arabian Sea with the exception of the Bay of Bengal.

Although there are significant differences between the mean SSS, most of the features of the variability are similar in both the in situ and Aquarius SSS plots (Figure 6.2d and e, respectively). High variability in the far western Pacific along the equator stretches east and south into the South Pacific Convergence Zone (SPCZ) at roughly 170^{o}W, 15^{o}S. Common regions of high variability can also be seen in the eastern/central Indian Ocean to the Bay of Bengal and in the far eastern Pacific under the ITCZ and especially at 5^{o}N at the eastern boundary for both products. The other interesting feature is that the amplitude of the Aquarius variability is significantly larger than the in situ SSS product.

In order to validate the spin up for the Aquarius-period experiments, coupled experiments are completed with and without SSS assimilation for January 1993 to August 2011. Figure 6.3 validates the correlation and Root Mean Square (RMS) of the model results against the observed NINO3 SST anomaly ([*Reynolds et al.*, 2002]). The experiments reported in Figure 6.3 are ASSIM_T_z (black solid line), ASSIM_T_z_SSS_{ISMON} (blue dashed line) and the NCEP Climate Forecast System Reanalysis Reforecast (CFSRR) results. The CFSRR coupled hindcasts (Figure 6.3, red dotted line) represents operational coupled model forecast skill (see Section 2.2.4 for a description of the CFSRR data). Figure 6.3 confirms that both the CFSRR and our HCM results validate well against observations with significant correlations extending to the

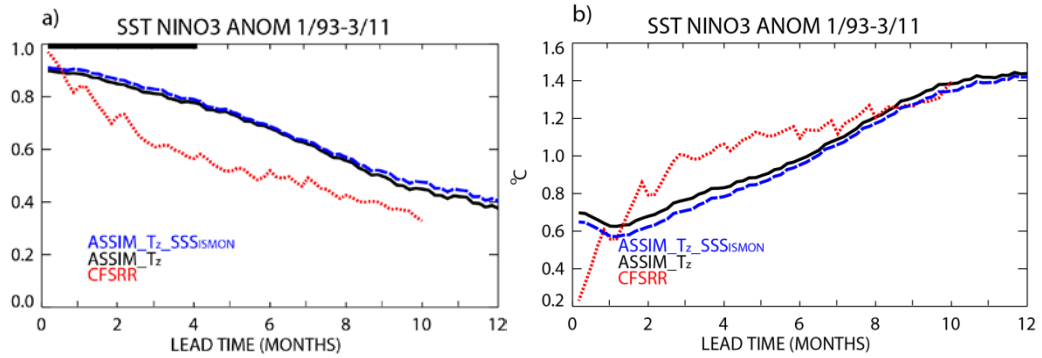

Figure 6.3: Validation of coupled spin up versus CFSRR. *Our Indo-Pacific HCM experiments and CFSRR coupled model results are validated with observed NINO3 SST anomaly for January 1993 - March 2011 using a) correlation and b) RMS. ASSIM_T_z assimilates all subsurface temperature information (black) and ASSIM_T_z_SSS_{IS} additionally assimilates the monthly SSS product (blue dash), whereas the NCEP CFSRR (red dotted line) coupled model assimilates SST and in situ salinity (S_z) in addition to T_z. Individual correlations exceed the 95% significance out to 12 (32), 12 (32) and 10 months (34) (effective degrees of freedom) for blue, black and red lines, respectively. The thick black line on the top x-axis shows where the blue line is significantly larger than the black line using the Steiger-Z test. Note that our HCM validation statistics are comparable to the NCEP operational CFSRR results and all validate well against observations. March 2011 (rather than July 2011) is chosen as the end of the validation period since this date corresponds to the last available CFSRR data.*

end of the respective experiments. In addition, RMS difference validation of our HCMs using NINO3 SST anomaly observations is comparable to the CFSRR results after 1 month lead times. Note that early in the forecast period the high correlation and low RMS for CFSRR are attributed to the fact that CFSRR assimilates SST (i.e. including assimilation in the NINO3 region) whereas our coupled models were specifically formulated to allow independent SST evolution (i.e. no SST assimilation). Thus, both these models provide useful and independent tools to diagnose ENSO prediction improvements brought about by SSS assimilation. This validation shows that our model/data assimilation/coupled model system which are initialized using only T_z and

additionally SSS_{ISMON} are comparable to other, widely used, operational systems that assimilate SST, T_z, and S_z. It is also important to note that the experiment that assimilates gridded monthly OI of SSS ($ASSIM\_T_z\_SSS_{ISMON}$ – blue line in Figure 6.3) has persistently higher correlation (significant from 0-4 month lead times) and lower RMS than $ASSIM\_T_z$. These results are consistent with those of [*Hackert et al.*, 2011] and foreshadow the positive impact of SSS on ENSO forecasts.

6.2 Impact of SSS Assimilation on Coupled Forecasts

In order to assess the impact of satellite SSS on ENSO predictability we distinguish between coupled experiments initialized using Aquarius assimilation ($ASSIM\_T_z\_SSS_{AQ}$) versus those without ($ASSIM\_T_z$). The observed NINO3 region SST anomaly from [*Reynolds et al.*, 2002] is used as a target to judge the quality of a particular forecast. For all experiments, we calculate mean statistics, correlation and RMS differences, over the period August 2011 to February 2014. Figure 6.4 displays the correlation and RMS versus lead time for three simulations, $ASSIM\_T_z$, $ASSIM\_T_z\_SSS_{IS}$, and $ASSIM\_T_z\_SSS_{AQ}$. For short term forecasts, from month 1 to month 3, the experiment that includes assimilation of in situ SSS outperforms $ASSIM\_T_z$. Forecast results are indistinguishable from one another from 3 to 5 month lead times. However, between 5 to 10 month forecast lead times, $ASSIM\_T_z\_SSS_{IS}$ correlations significantly outperform $ASSIM\_T_z$. The Steiger Z statistic (from [*Steiger*, 1980]) indicates that such an increase of correlation is 95% significant for these lead times (indicated by blue dotted line along the upper x-axis). Thus, assimilation of in situ OI SSS product significantly improves coupled forecasts with respect to subsurface temperature assimilation alone for this period.

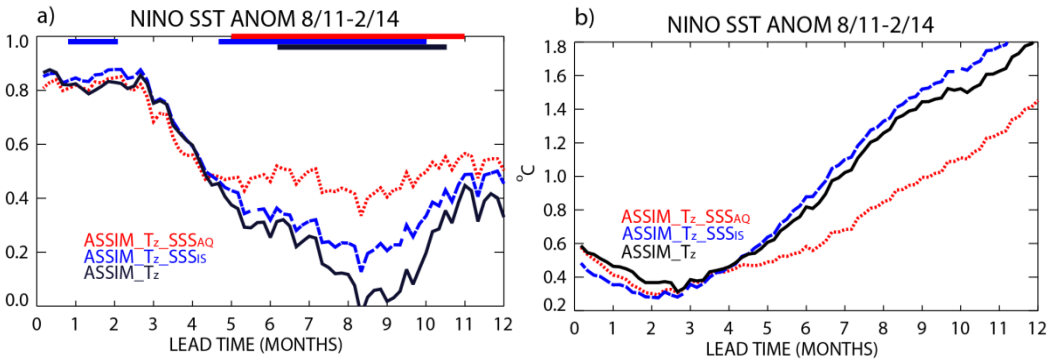

Figure 6.4: NINO3 validation of experiments that assimilate SSS observations. *Validation of coupled model results for the Aquarius period, August 2011 to February 2014 using a) correlation and b) RMS versus observed NINO3 SST anomaly. The solid black curve is initialized using assimilation of subsurface temperature (ASSIM_T_z), the thick dotted red curve from T_z and Aquarius SSS (ASSIM_T_z_SSS_{AQ}) and the dash blue curve from T_z and weekly OI of all available near-surface salinity (ASSIM_T_z_SSS_{IS}). The thick red (blue) lines on the top x-axis show where the ASSIM_T_z_SSS_{AQ} (ASSIM_T_z_SSS_{IS}) significantly outperforms the control. The black line shows where ASSIM_T_z_SSS_{AQ} is significantly bigger than ASSIM_T_z_SSS_{IS} using the Steiger-Z test.*

These results agree with previous work of [*Ballabrera-Poy et al.*, 2002] and [*Hackert et al.*, 2011] who found that SSS did not so much impact short-term coupled forecasts, but after 6-9 months SSS information did significantly improve ENSO forecasts. As will be detailed later, the existence of such a lag is explained by the fact that anomalies of the salt concentration modulate ENSO Kelvin/Rossby waves especially in the western equatorial Pacific via density perturbations above the depth of the thermocline.

The RMS differences between the predicted and observed NINO3 SST anomalies are shown in Figure 6.4b. Although the differences between the curves associated with ASSIM_T_z (black line) and ASSIM_T_z_SSS_{IS} (blue dash) are small, assimilation of in situ SSS actually degrades the statistics after 5 month lead time forecasts. This result is inconsistent with [*Hackert et al.*, 2011] who found that RMS is reduced when coupled predictions are initialized with in situ gridded SSS starting with 3 month lead times. The

degradation of ASSIM_T_z_SSS_{IS} RMS versus ASSIM_T_z is also inconsistent with the longer assimilation experiments shown in Figure 6.3b.

Figure 6.4 also highlights the impact of Aquarius SSS data (ASSIM_T_z_SSS_{AQ} - red dotted line). Like the weekly gridded in situ SSS results, inclusion of Aquarius SSS improves the correlation of the coupled forecasts. This is especially evident by month 6, when the correlation for ASSIM_T_z_SSS_{AQ} versus observed NINO3 SST anomaly is r=0.46 while the ASSIM_T_z experiment correlation is only r=0.25. By month 9, the results have bifurcated further since ASSIM_T_z_SSS_{AQ} remains at r = 0.40 while the ASSIM_T_z results falls to r = 0.0. In this case the differences between ASSIM_T_z_SSS_{AQ} and the baseline (i.e. ASSIM_T_z) are highly statistically significant. The Steiger Z statistic shows that the experiment that includes Aquarius SSS is significantly larger than the baseline between 5-11 month lead times (solid red along upper x-axis). The impact of the SSS assimilation is felt after 5 months and differences peak at 9 month lead times matching previous work (e.g. [*Ballabrera-Poy et al.*, 2002]). Therefore, inclusion of assimilation of satellite SSS significantly improves the temporal evolution of coupled forecasts after 5 month lead times.

Unlike ASSIM_T_z_SSS_{IS}, now the RMS results for ASSIM_T_z_SSS_{AQ} are consistently lower than ASSIM_T_z for all lead times (Figure 6.4b). Prior to month 5 these differences are small. However, after 5 month lead times the differences climb to an average of roughly 0.3^{o}C with ASSIM_T_z_SSS_{AQ} having a lower RMS than ASSIM_T_z by 0.45^{o}C at 9 month lead times. For each lead time the ASSIM_T_z_SSS_{AQ} results (red dotted line) have lower RMS and thus outperform the ASSIM_T_z experiments.

A key result of this study to this point is that not only does satellite SSS significantly improve coupled forecasts in general, but that Aquarius gives better results than the in situ SSS product alone. Figure 6.4 shows the validation versus observed NINO3 SST anomalies of both ASSIM_T_z_SSS_{IS} (blue dash) and ASSIM_T_z_SSS_{AQ} (red dotted). The correlation plots show that Aquarius outperforms the in situ SSS assimilation for five month lead forecasts. Correlations of ASSIM_T_z_SSS_{AQ} exceed ASSIM_T_z_SSS_{IS} by an average of roughly r = 0.15 for months 6.5 to 10.5. During this period the significance of the differences, as measured by the Steiger Z test (black line along top x-axis), exceeds the 95% significance level. Therefore, coupled experiments that account for satellite SSS (i.e. Aquarius) significantly improve coupled forecasts for 6 to 10 month lead times with respect to assimilation of in situ SSS. The improved statistics for satellite versus in situ SSS assimilation is similar for validation using RMS differences with observed NINO3 SST anomalies. Even though the RMS is similar prior to 5 month lead time forecasts, Figure 6.4b shows that after 5 month lead times, the assimilation of satellite SSS outperforms the in situ SSS by an average of 0.4^{o}C RMS (compare red dotted to blue dash lines).

In order to diagnose why assimilation of SSS improves coupled forecasts, mean differences between the ASSIM_T_z_SSS_{IS}, and ASSIM_T_z data assimilation results (i.e. the initialization of the coupled models over August 2011 until February 2014), are presented. It is important to note that these differences include not only the short-term impact of weekly SSS assimilation (i.e. August 2011 to February 2014), but also the long-term (January 1993 to July 2011) bias between assimilation scenarios built into the initial conditions. Remember that ASSIM_T_z was initialized from its continuing,

identical long-term experiment whereas ASSIM_T_z_SSS_{IS} was initialized in August 2011 using the July 2011 ASSIM_T_z_SSS_{ISMON} experiment. In other words, these differences contain both the long-term bias between experiments, but also the differences due to assimilation of salinity for August 2011 to February 2014.

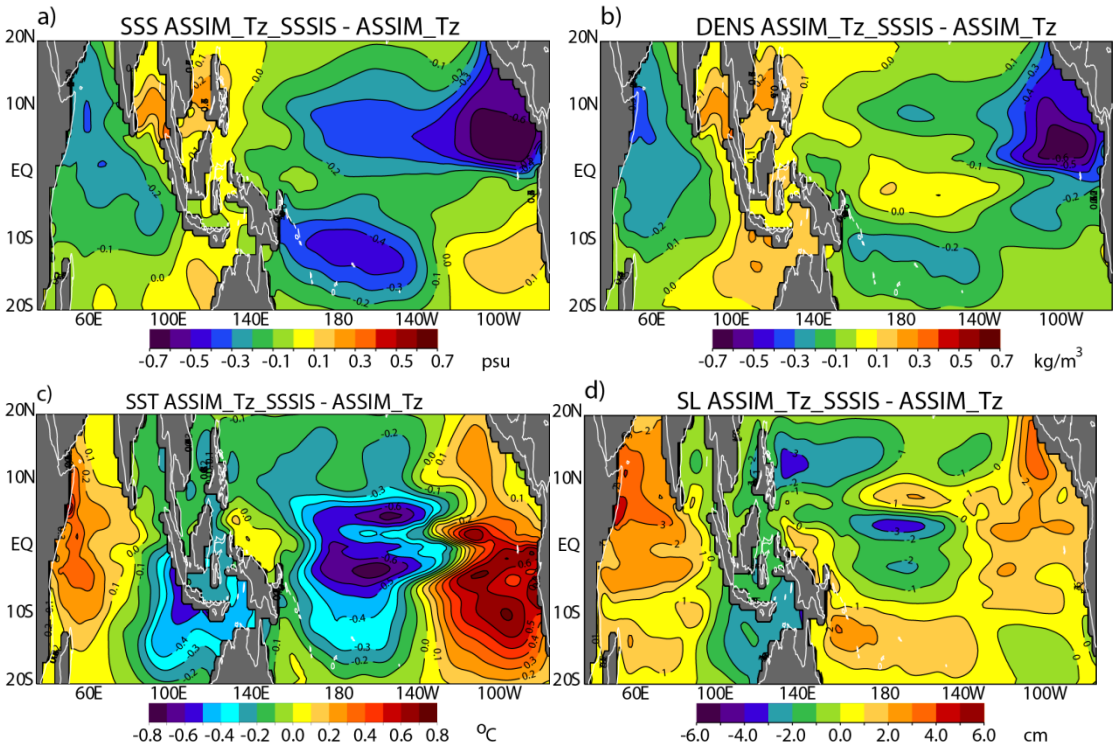

Figure 6.5: Initialization difference between ASSIM_T_z_SSS_{IS} minus ASSIM_T_z. *Results of the mean difference between ASSIM_T_z_SSS_{IS} minus ASSIM_T_z initial conditions for a) SSS, b) mixed layer density, c) SST and d) sea level for August 2011 to February 2014. Units are psu, kg/m^3, ^oC and cm, respectively. Absolute values exceeding 0.52 PSU, 0.42 kg/m^3, 0.68^oC and 3.2 cm are significant for the four panels, respectively.*

In Figure 6.5a, the model SSS for ASSIM_T_z_SSS_{IS} minus ASSIM_T_z is presented. The SSS assimilation experiment is fresher over most of the Indian Ocean with the exception of the Bay of Bengal. Over the Indonesian Seas, in a zonal band between roughly 100^{o}E and 140^{o}E, assimilation of in situ SSS produces anomalous salting with respect to the ASSIM_T_z experiment. In the Pacific, both in the ITCZ (east

of 160°E, between the equator and 10°N) and in the South Pacific Convergence Zone (SPCZ) (5°S-15°S from the coast of New Guinea to 140°W) negative differences show that the ASSIM_T_z_SSS_{IS} is fresher than the ASSIM_T_z experiment.

Inclusion of in situ SSS leads to density changes in the mixed layer. Figure 6.5b shows that density differences generally mirror those of SSS. However a major difference can be seen within 5° of the equator between 160°E and 140°W. This feature, with higher density, corresponds with reduced buoyancy and enhanced mixing. The mixing of cooler water from below is evident in the SST plots (Figure 6.5c). For example, note the negative region, reminiscent of an equatorial upwelling Rossby wave, between 160°E to 140°W. Here ASSIM_T_z_SSS_{IS} has lower SST than ASSIM_T_z with lowest values (lower than -0.5°C) located in a zonal band roughly 5° off the equator. This feature is also found in the sea level ASSIM_T_z_SSS_{IS} minus ASSIM_T_z difference plot (Figure 6.5d). The main feature here is again suggestive of an upwelling Rossby wave with negative values at 5° straddling the equator near the dateline. South of the equator, the minor asymmetric values peak at -2 cm whereas the Northern Hemisphere values are -4 cm.

The feature in the mean fields of SL and SST that looks similar to a Rossby wave is actually the result of two separate Rossby waves during our study period. The first is spawned in the far eastern Pacific in December 2011 to February 2012. This feature, evident in a longitude versus time analysis (not shown) as negative SSS ASSIM_Tz_SSS_{IS} minus ASSIM_T_z differences, travels west starting from 120°W to 100°W along 3°N and arrives at the dateline by June/July 2012. A weaker but symmetric fresh SSS feature can be found in the Southern Hemisphere. As the negative SSS Rossby

wave traverses west, the surface layer density and model thickness is reduced with the biggest impact between 170^{o}W and 130^{o}W at 3^{o}N for April to July 2012. Somewhat lagging the reduction in the model surface layer thickness, sea level shoals between 160^{o}E to 150^{o}W at 3^{o}N for May to August 2012. The timing and location of the SST signal is well synchronized with SL and SSS diagnoses. During this period, SST is primarily negative with the biggest signal between 160^{o}E to 170^{o}W at 5^{o}N coinciding with the upwelling SL signal. For all these variables the timing of the symmetric feature in the Southern Hemisphere brought about by SSS assimilation is similar but the amplitude is somewhat weaker. Later in the study period, a second Rossby wave is initiated due to SSS assimilation in February 2013. These features along with the relative positive SSS values in the NINO3 region are important components of the coupled forecast improvements brought about by SSS assimilation and so will be discussed in more detail later.

A similar set of plots as the previous figure is presented for the differences between the Aquarius assimilation (ASSIM_T_z_SSS_{AQ}) minus ASSIM_T_z for August 2011 to February 2014 (Figure 6.6). Mostly all of the features are similar for salinity differences, Figure 6.6a and Figure 6.5a. Namely, negative salinity differences are seen over most of the Indian Ocean except the Bay of Bengal, negative values can be seen in the ITCZ and SPCZ in the Pacific, and positive salting in the southeast Pacific. Again the density pattern for the ASSIM_T_z_SSS_{AQ} minus ASSIM_T_z (Figure 6.6b) generally matches those of SSS. Lower density in the ITCZ and SPCZ regions of the tropical Pacific matches regions of lower SSS from Figure 6.6a. However, the main feature to focus on is the higher density water in the mixed layer within 5^{o} of the equator and

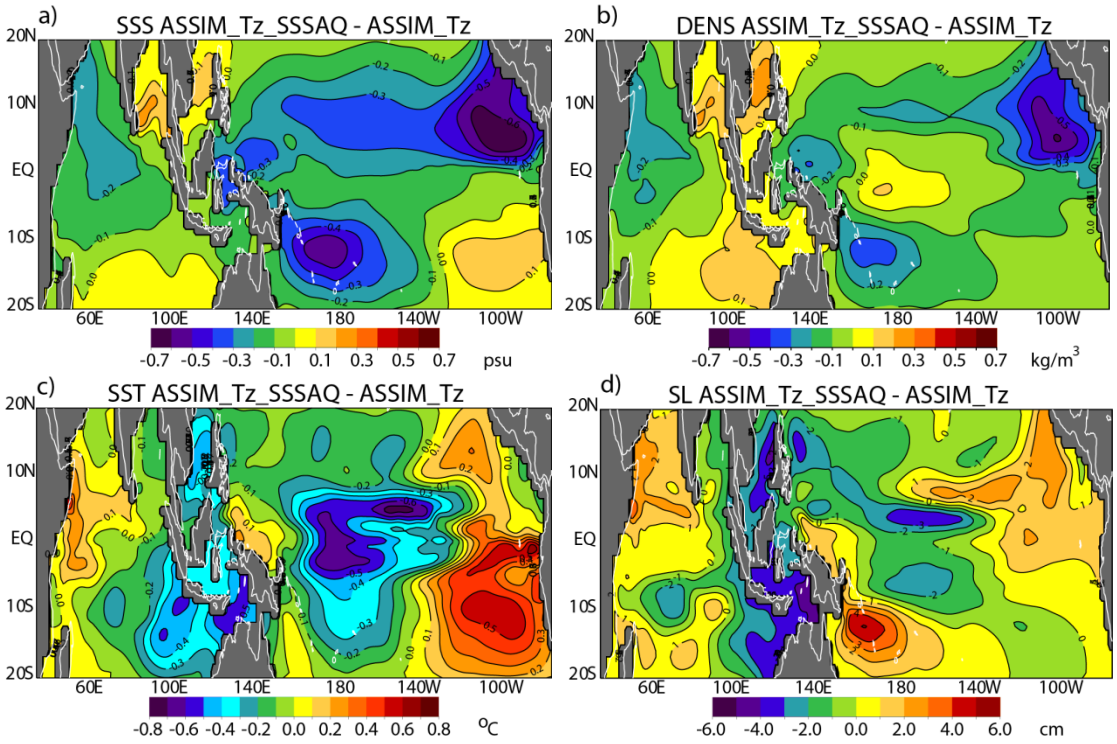

Figure 6.6: Initialization differences for ASSIM_T_z_SSS_{AQ} minus ASSIM_T_z. *Results of the mean difference between ASSIM_T_z_SSS_{AQ} minus ASSIM_T_z initial conditions for a) SSS, b) mixed layer density, c) SST, and d) SL for August 2011 to February 2014. Units are psu, kg/m^3, ^{o}C, and cm respectively. Absolute values exceeding 0.51 PSU, 0.36 kg/m^3, 0.61^{o}C and 3.4 cm are significant for the four panels, respectively.*

between 160^{o}E and 150^{o}W. This region of higher density corresponds to enhanced mixing (not shown), and colder SST. This feature for the ASSIM_T_z_SSS_{AQ} minus ASSIM_T_z SST results (Figure 6.6c), is clearly evident by the meridional banding with differences colder than -0.5^{o}C at 5^{o}S and 5^{o}N with minimum values at 180^o and 150^{o}W, respectively. This pattern, that strongly resembles an upwelling Rossby wave signature, generally matches the corresponding SST differences in Figure 6.5c. Higher density leads to enhanced mixing and upwelling of cooler SST from below. This leads to shoaling of the mixed layer and thermocline and so the sea level shoals as well. Negative sea level differences, corresponding to this upwelling can be seen in Figure 6.6d

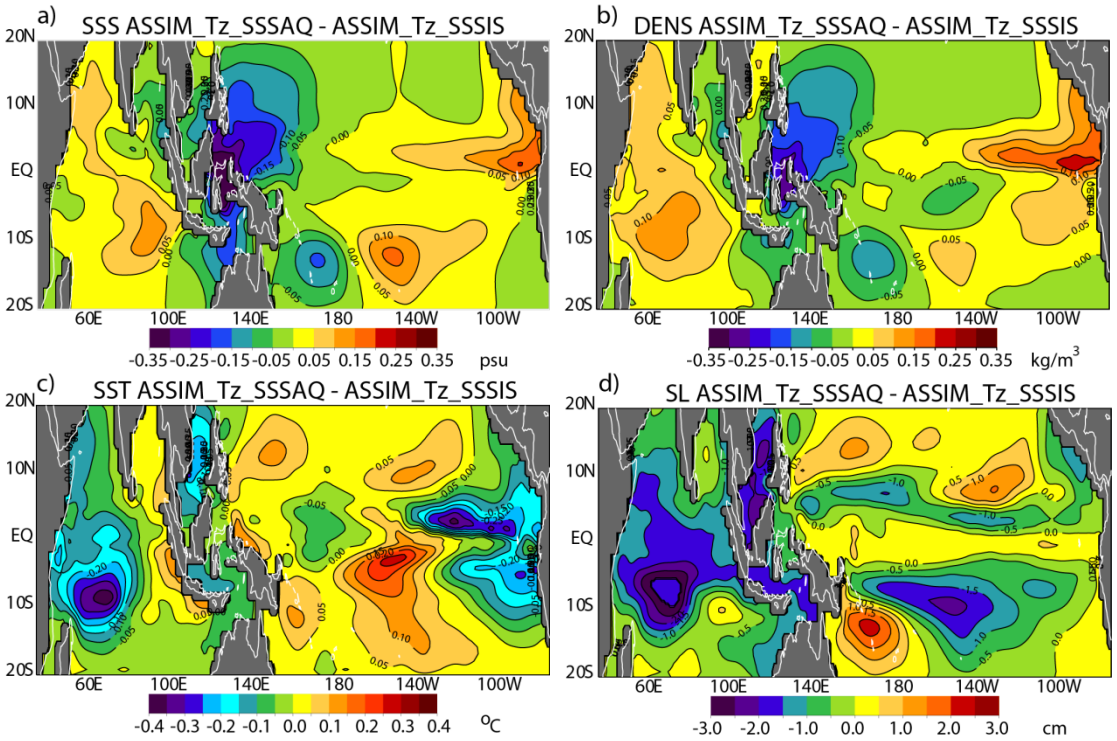

Figure 6.7: Initialization differences ASSIM_T_z_SSS_{AQ} minus ASSIM_T_z_SSS_{IS}. *Same as Figure 6.6 but for mean difference, ASSIM_T_z_SSS_{AQ} minus ASSIM_T_z_SSS_{IS}. Absolute values exceeding 0.17 PSU, 0.15 kg/m^3, 0.23^{o}C, and 2.2 cm are significant for the four panels, respectively.*

straddling the equator near the dateline representing an upwelling Rossby wave in these mean difference plots.

Besides showing the impact of the individual SSS products another goal of this dissertation is to show the potential added benefit of satellite versus in situ SSS. The main differences between Figure 6.6a and Figure 6.5a are found in the off-equatorial western Pacific and in the Indonesian Seas region where assimilation of Aquarius gives fresher results than the in situ product. In addition, ASSIM_T_z_SSS_{IS} is significantly fresher than ASSIM_T_z_SSS_{AQ} in the NINO3 region of the eastern Pacific just north of the equator. A more convenient way to highlight the differences between SSS assimilation experiments is to difference these directly. Figure 6.7a shows the ASSIM_T_z_SSS_{AQ} minus ASSIM_T_z_SSS_{IS} differences. Here the differences in the

Indonesian Seas and off equatorial western Pacific are evident with ASSIM_T_z_SSS_{AQ} having a fresher mean than ASSIM_T_z_SSS_{IS} results. The other significant region is the eastern Pacific north of the equator (0^o-5^oN, 140^oW-90^oW) where ASSIM_T_z_SSS_{AQ} is saltier than ASSIM_T_z_SSS_{IS} assimilation results by as much as 0.15 psu. It is reassuring to note that in the Pacific our data assimilation differences (i.e. Figure 6.7a) are qualitatively consistent with observation differences of Aquarius minus in situ SSS found in Figure 6.2c.

The ASSIM_T_z_SSS_{AQ} experiment is warmer than ASSIM_T_z_SSS_{IS} over most of the western/central Pacific between Indonesia and 130^oW with maximum positive differences at 10^oN and 5^oS at 155^oW and at the western boundary. An exception is the weak negative pattern (-0.05^{o}C) at the eastern edge of the warm pool centered along the equator at 170^oE. East of 130^oW, the ASSIM_T_z_SSS_{IS} experiment SST is warmer than the ASSIM_T_z_SSS_{AQ} experiment (compare Figure 6.5c to Figure 6.6c) and these differences manifest as a cold La Niña pattern with negative values within 10^o of the equator east of 140^oW in the eastern Pacific (Figure 6.7c). Just considering the equator in the eastern Pacific, strong east to west gradient of SST differences (ASSIM_T_z_SSS_{AQ} minus ASSIM_T_z_SSS_{IS}) should lead to relative enhanced easterlies, Bjerknes feedback, and cooling in the upwelling region of the eastern Pacific. We shall see that these SST differences and the resultant relative SST gradient across the equatorial Pacific are critical for improved Aquarius forecasts as opposed to assimilation of in situ SSS.

The ASSIM_T_z_SSS_{AQ} minus ASSIM_T_z_SSS_{IS} has positive SL in the equatorial western Pacific stretching east all the way to the eastern boundary within 3^o of the equator (Figure 6.7d). In addition, negative values (i.e. lower SL for ASSIM_T_z_SSS_{AQ}

versus ASSIM_T_z_SSS_{IS}) are present in the western half of the Pacific at 8^{o}N connecting negative values at 5^{o}N, 140^{o}W in the eastern half. In the Southern Hemisphere, the negative values stretch across most the basin and the minimum is centered on 10^{o}S, 150^{o}W. The overall pattern of Figure 6.7b can be envisioned as a downwelling Kelvin wave being followed by an upwelling Rossby wave whereas Figure 6.5b and Figure 6.6b look more like an upwelling Rossby wave centered just east of the dateline.

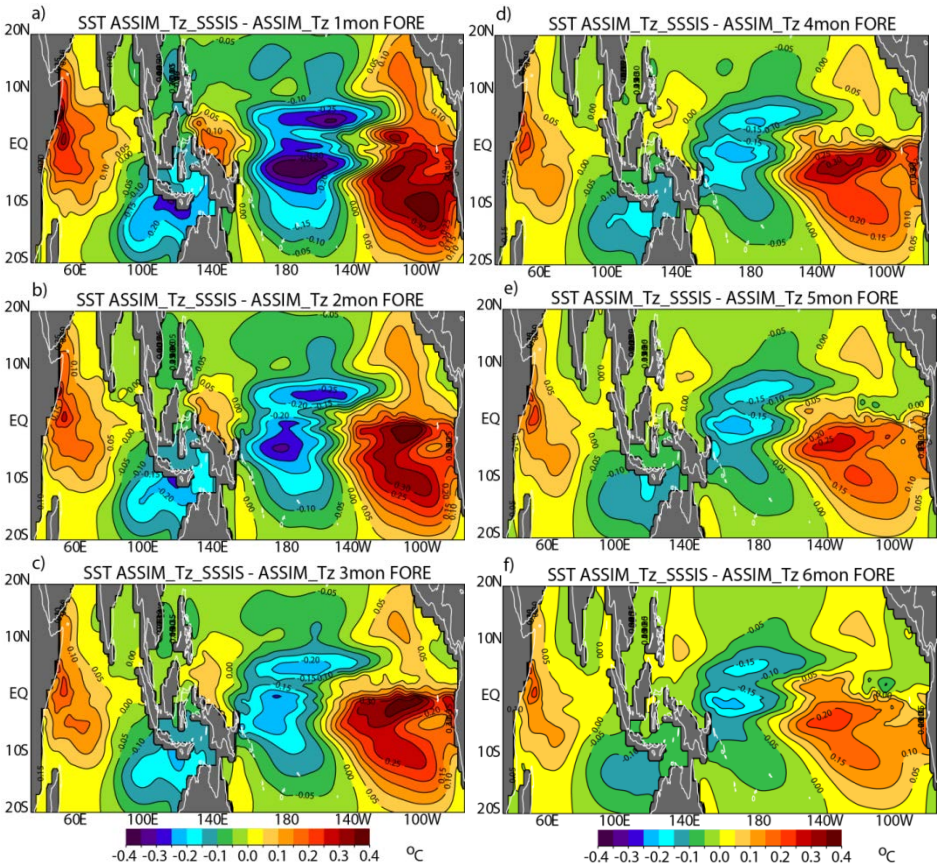

Figure 6.8: Evolution of mean forecasts for ASSIM_T_z_SSS_{IS} minus ASSIM_T_z. *SST results for ASSIM_T_z_SSS_{IS} minus ASSIM_T_z forecast means for a) 1 month, b) 2 month, c) 3 month, d) 4 month, e) 5 month and f) 6 month forecast lead times averaged over all start months, August 2011 to February 2014. Units are in ^{o}C.*

In order to examine the impact on ENSO forecasts, the temporal evolution of the mean forecast difference ASSIM_T_z_SSS_{IS} minus ASSIM_T_z is presented. For each month from August 2011 until February 2014 the average of all 1 month, 2 month, and so

on to 6 month forecast differences are presented for SST (Figure 6.8a-f). Recall that Figure 6.4a showed that ASSIM_T_z_SSS_{IS} had improved forecast validation with respect to ASSIM_T_z only after 7 months. The evolution of the mean forecast differences provides an explanation about the reason for this lead time in NINO3 forecast improvement. In month 1, SST in the NINO3 region for ASSIM_T_z_SSS_{IS} is warmer than for ASSIM_T_z with SST differences as large as 0.3°C (Figure 6.8a). The negative differences over the central Pacific straddle the equator with values lower than -0.3°C, but dissipate with time. On the contrary, the once-positive values in the NINO3 region have cooled with values reduced to near 0°C (Figure 6.8f).

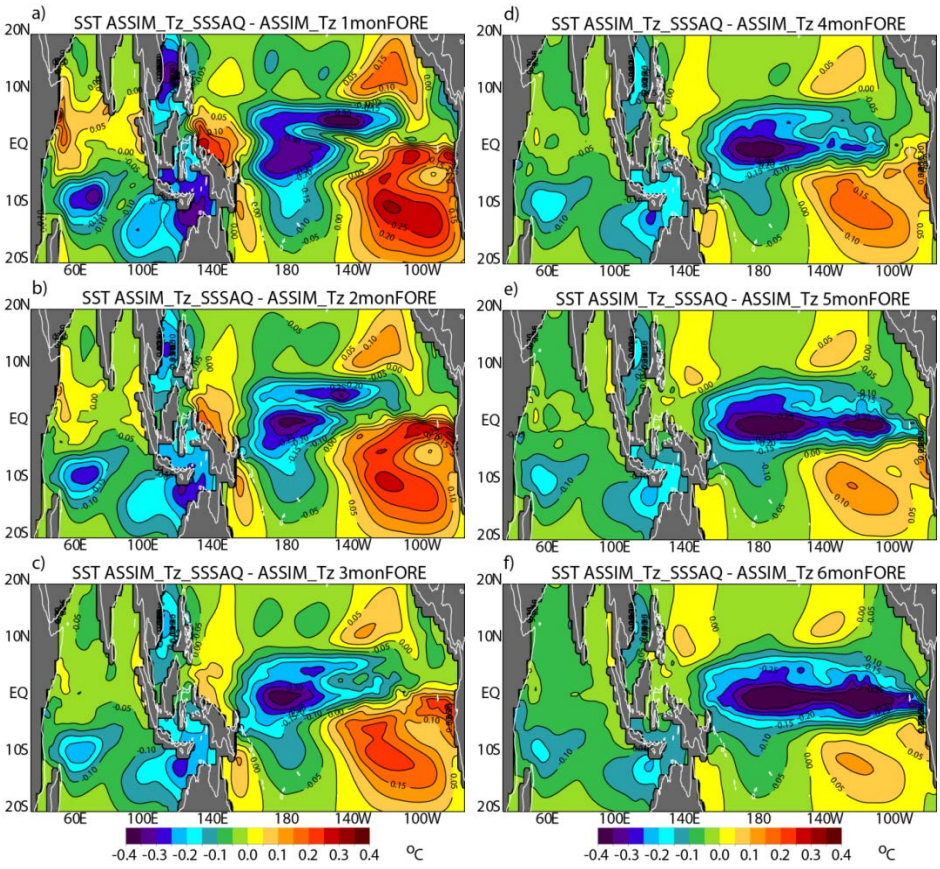

Figure 6.9: Evolution of mean forecast for ASSIM_T_z_SSS_{AQ} minus ASSIM_T_z. *SST results for ASSIM_T_z_SSS_{AQ} minus ASSIM_T_z forecast means for a) 1 month, b) 2 month, c) 3 month, d) 4 month, e) 5 month, and f) 6 month forecast lead times averaged over all start months, August 2011 to February 2014. Units are in °C.*

Similar plots for ASSIM_T_z_SSS_{AQ} minus ASSIM_T_z (Figure 6.9) show a more dramatic story. Propagation from the central to eastern Pacific and amplification in the eastern Pacific is readily apparent (resembling La Niña cooling). For SST (Figure 6.9a-f) the time sequence looks very much like an upwelling Rossby wave reflecting at the western boundary into an upwelling Kelvin wave arriving at the eastern boundary in month 6 (Figure 6.9f). For Figure 6.9a the NINO3 SST starts out weak and near 0.^{o}C in month 1. As time progresses, the negative differences drop in month 6 (Figure 6.9f) with contours as low as -0.35^{o}C. Also note that the coolest contours arrive in the eastern tropical Pacific at the very time when the coupled forecast begins to show significant improvement from Figure 6.4a, b in month 5. As we shall see, the impact of satellite SSS assimilation is to pull the forecast more towards the observed weakly negative conditions rather than towards an El Niño condition as is the tendency without SSS assimilation.

Another way to envision the relative impact of SSS assimilation is to examine the longitude versus time history of the equatorial mean of the differences averaged over all start months. Figure 6.10 shows the Hovmöller plot averaged within 2^{o} of the equator for SST and the resulting differences in zonal wind stress anomaly from the coupled model statistical atmospheric model (SAM). Figure 6.10a shows that early in the mean forecast, ASSIM_T_z_SSS_{IS} minus ASSIM_T_z SST is positive east of 135^{o}W peaking at 110^{o}W prior to month 3. By month 5 the positive values have diminished and after month 7 the values in the NINO3 region begin to turn negative. In the central Pacific, the negative values of SST centered at the dateline dissipate from months 6 to 9. The corresponding plot of zonal wind stress (TAUX) is presented in Figure 6.10b. As expected, winds react to the SST differences by converging into warm water and diverging from cold SST

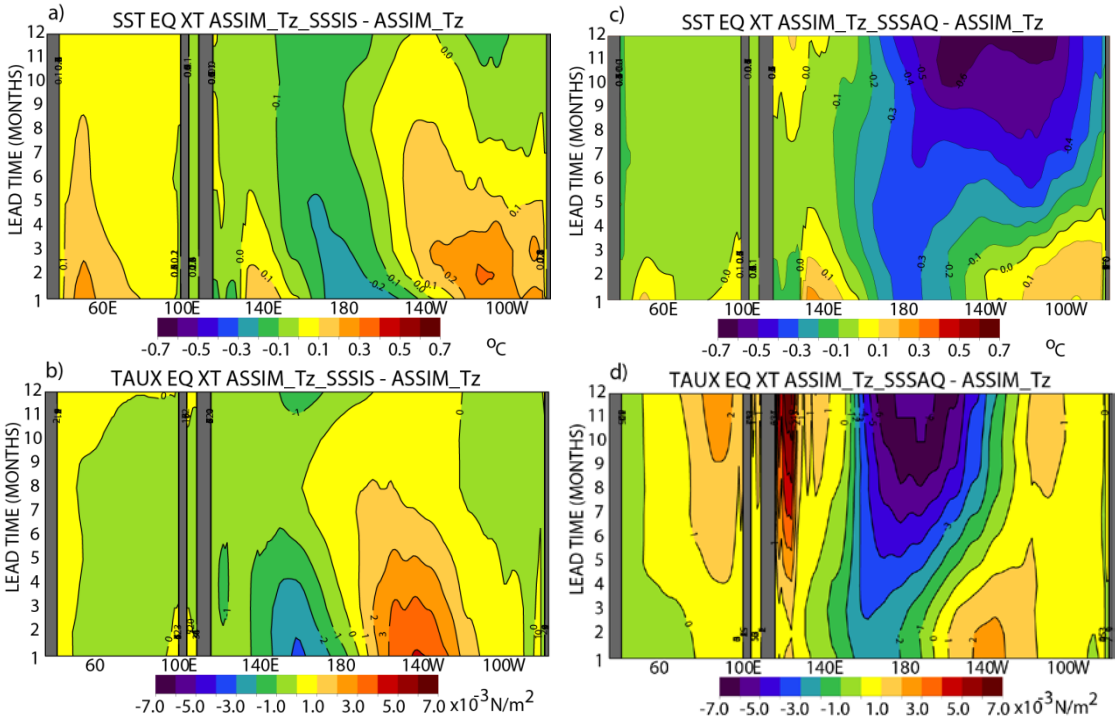

Figure 6.10: Hovmöller plots of mean forecast evolution. *Equatorial Indo-Pacific longitude versus time sections for forecast mean of ASSIM_T_z_SSS_{IS} minus ASSIM_T_z for a) SST and b) zonal wind stress within 2^o of the equator. The x-axis is longitude and the y-axis is forecast lead time (increasing length forecasts up). On the right is the same for ASSIM_T_z_SSS_{AQ} minus ASSIM_T_z for c) SST and d) zonal wind stress.*

differences. During the strongest west-to-east zonal gradient from month 0 to month 5, westerly winds, just to the west of the warmest water, converge into the NINO3 region and easterly winds just to the west of the coldest differences are seen west of the dateline. In this case, the downwelling signal associated with the east Pacific SST gradient should somewhat offset any western Pacific upwelling signal. However, this coupling in the east breaks down by month 6 and the winds die down leaving the NINO3 region slightly cooler for the ASSIM_T_z_SSS_{IS} experiment versus ASSIM_T_z. After forecast lead time of 5 months the relatively cooler waters in the central and eastern Pacific are reinforced by weak easterlies east of the dateline.

The forecast trajectory is quite different for the longitude-versus-time plots of the ASSIM_T_z_SSS_{AQ} minus ASSIM_T_z results in Figure 6.10c (SST) and Figure 6.10d (TAUX). Here the small area of positive SST differences in the NINO3 region vanishes by month 3. In this case the upwelling in the west/central Pacific grows unencumbered by any downwelling signal in the east (as is the case for the ASSIM_T_z_SSS_{IS} minus ASSIM_T_z). As time progresses, negative values intensify so that by month 8 the negative values for ASSIM_T_z_SSS_{AQ} minus ASSIM_T_z are less than -0.5^{o}C. Note that the start of the coldest anomaly in the NINO3 region, i.e. month 9, is the same forecast lead time that corresponds to the most significant improvement brought about by satellite SSS assimilation as seen in Figure 6.4a. Not coincidentally month 9 also corresponds to the maximum relative upwelling signal below the mixed layer (not shown). The wind response shows weak easterlies at the beginning of the mean forecast period strengthening and migrating slightly eastward (from 170^{o}E to roughly 170^{o}W). The coupled response of the ASSIM_T_z_SSS_{AQ} minus ASSIM_T_z is typical of a relative growing La Niña pattern.

In summary, the general impact of the assimilation of SSS during this period is to cool the NINO3 region. Figure 6.8f, Figure 6.9f, Figure 6.10a and Figure 6.10c all show that assimilation of SSS cools the eastern Pacific to some degree. In particular, the assimilation of satellite SSS from Aquarius (ASSIM_T_z_SSS_{AQ}) is more effective at cooling the NINO3 region than the in situ product.

In order to highlight the impact of SSS assimilation on coupled forecasts, the mean forecast for all start months, August 2011 to February 2014, is presented. Figure 6.11 shows the NINO3 SST anomaly results for all coupled experiments discussed

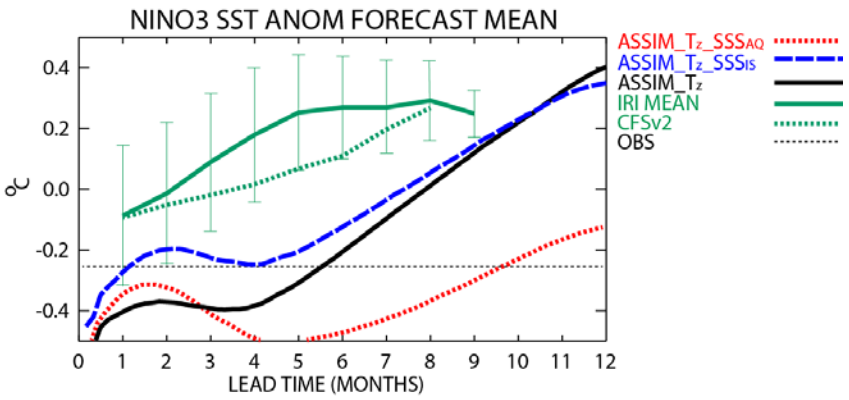

Figure 6.11: Mean forecasts for different coupled experiments. *Mean forecast for NINO3 SST forecast anomaly (^oC) from August 2011 to February 2014 for ASSIM_T_z (solid black), ASSIM_T_z_SSS_{IS} (blue –dash) and ASSIM_T_z_SSS_{AQ} (red – dotted). In addition, the IRI dynamical model mean for NINO3.4 region is provided (solid green line to show the model consensus) along with the NOAA operation model, CFSv2, results (green dash). The one standard deviation about the mean for IRI is illustrated by the green error bars. All these mean forecasts are normalized using the long-term mean, 1993-2013, for our HCM results and presumably 1970-2000 for IRI and CFSv2. The horizontal black dashed line corresponds to the mean observation anomaly over this period, -0.25^oC.*

previously (ASSIM_T_z – black solid, ASSIM_T_z_SSS_{IS} – blue dash, and ASSIM_T_z_SSS_{AQ} – red dotted). In addition, we present the dynamical model mean from the IRI web site (http://iri.columbia.edu/climate/ENSO/currentinfo/archive/index.html – solid green line) for the NINO3.4 region (5^{o}N-5^{o}S, 120^{o}W-170^{o}W) and NOAA operational forecast results, CFSv2, for all forecasts initiated for the Aquarius period. Although referring to a slightly different region, these results are included to show general features of community forecasts and the specific example of the national forecast (i.e. CFSv2) for this period. All our HCM results along with the IRI mean and CFSv2 tend towards warming over time in the eastern Pacific. The extreme example of this is the mean forecast for ASSIM_T_z which rises past 0.4^{o}C by 12 month forecasts. After 10 month lead forecasts, ASSIM_T_z_SSS_{IS} is a slight improvement on ASSIM_T_z tending more towards the real observation mean of -0.25^{o}C over this period (thin

horizontal black dashed line in Figure 6.11). Overall the most realistic forecast is the ASSIM_T_z_SSS_{AQ} result that overlays ASSIM_T_z until about 3 month forecast lead times. After that, ASSIM_T_z_SSS_{AQ} clearly diverges from ASSIM_T_z approaching the slightly negative mean conditions that prevailed over this period (i.e. -0.25^{o}C). In addition, this representation shows the clear bifurcation of the forecast trajectories for ASSIM_T_z_SSS_{AQ} versus ASSIM_T_z_SSS_{IS}. The Aquarius assimilation tends more towards the cooler/neutral conditions after about 5 months, while ASSIM_T_z_SSS_{IS} starts tending away from -0.25^{o}C and more towards warmer NINO3 reiterating the timing and sense of the results of Figure 6.4a.

6.3 Role of Aquarius Data Sampling

The high correspondence between in situ and Aquarius observations ([*Lagerloef et al.*, 2013]) would lead one to assume that the gridded fields of in situ SSS should look similar to the satellite SSS. However, there are clear differences between the mean salinity patterns. To address the question of whether the sampling of the relatively sparse in situ observations impacts the mean fields, the Aquarius Version 2.9.1 data have been subsampled along-track (i.e. Level 2 data) using the nearest collocation to available near surface in situ observations. Data were rejected if any Aquarius radiometer flag failed at the moderate level (e.g. RFI, rain, land, ice, etc.) matching the validation data flagging of [*Lagerloef et al.*, 2013]. Only the closest Aquarius data point was included if it fell within 1^o and within the same day of the in situ observation. After subsampling the Aquarius data at in situ observation times and locations, the data were gridded using the same technique as for the weekly in situ data. The results of this OI of Aquarius data at

in situ collocations are presented for the mean and standard deviation in Figure 6.12a and b, respectively.

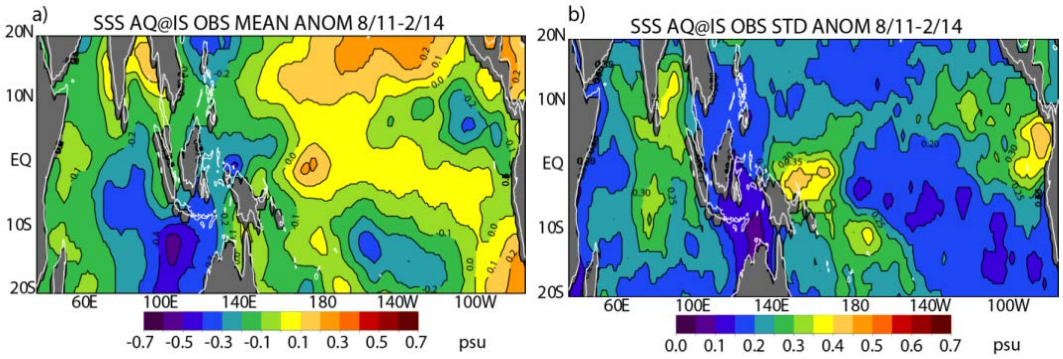

Figure 6.12: Gridded SSS for Aquarius subsampled at in situ locations/times. *SSS a) mean and b) standard deviation of OI anomalies of Aquarius along-track data subsampled at nearest collocation with in situ observations.*

The gridded fields of Aquarius SSS subsampled at in situ locations/times (Figure 6.12a) reproduce much of the patterns found in the original Aquarius fields (Figure 6.2b). For example, the subsampled Aquarius product has positive SSS anomalies along theequator with the maximum just to the west of the dateline, negative values in the SPCZ (180^{o}-100^{o}W, 10^{o}S-20^{o}S), western Pacific (west of 160^{o}E), in the IO, and at the eastern boundary of the Pacific at 5^{o}N. However, the mean for the subsampled OI of Aquarius is quite different from the original Aquarius data product along the equator especially in the eastern Pacific. For the full Aquarius L3 data, the maximum of the NINO3 region is greater than 0.2 psu (Figure 6.2b). In this same region, the subsampled product is more in line with the in situ product shown in Figure 6.2a having slightly negative values to the north and positive SSS anomaly to the south of the equator. In other words, subsampling Aquarius data at the in situ locations fails to reproduce the key salty anomaly in the eastern Pacific. Note that although visual inspection of the data coverage maps of the in situ locations reveals relatively consistent coverage from one

week to the next, the overall number of observations is small relative to Aquarius satellite coverage. For example, only 5-8% of the bins have in situ data for the NINO3 region for any particular week. Therefore, the general similarity between the subsampled Aquarius data (Figure 6.12a) and gridded in situ data (Figure 6.2a) suggests that differences between the full Aquarius gridded and in situ products are mostly due to the sparse distribution of in situ data.

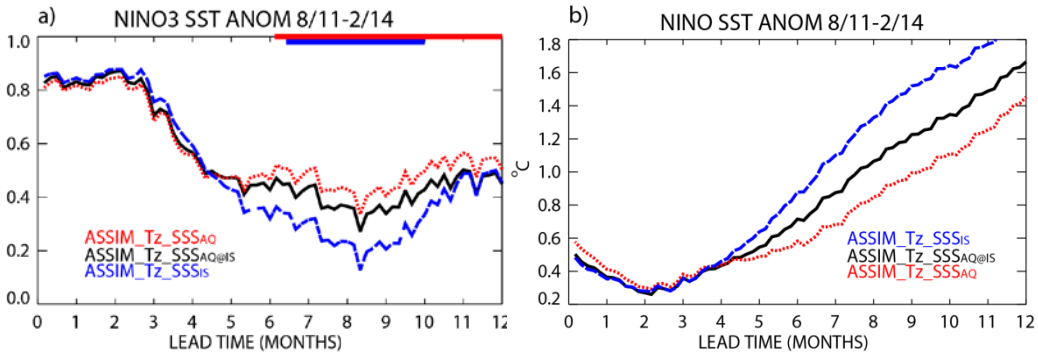

Figure 6.13: Validation of Aquarius subsampled at in situ locations. *Validation of coupled model results for the Aquarius period, August 2011 to February 2014 using a) correlation and b) RMS versus observed NINO3 SST anomaly. Dashed blue curve is initialized from the experiment that assimilates weekly OI of all available near-surface salinity and subsurface temperature (ASSIM_T_z_SSS_{IS}), solid black curve is the experiment that assimilates the OI of Aquarius data at the closest collocation with in situ and subsurface temperature (ASSIM_T_z_$SSS_{AQ@IS}$) and the dotted red curve is initialized using weekly gridded Aquarius SSS and subsurface temperature (ASSIM_T_z_SSS_{AQ}). The thick red (blue) lines on the top x-axis show where the ASSIM_T_z_SSS_{AQ} (ASSIM_T_z_$SSS_{AQ@IS}$) is significantly bigger than ASSIM_T_z_$SSS_{AQ@IS}$ (ASSIM_T_z_SSS_{IS}) using the Steiger-Z test.*

To test what relative impact the subsampled Aquarius product would have on ENSO predictions, we completed an additional assimilation experiment using the optimal interpolation product that subsampled Aquarius SSS at the in situ locations and times. Comparing the results of this experiment versus the full Aquarius gridded product would highlight the impact of satellite versus in situ data coverage and comparing the subsampled Aquarius against the in situ product would point out the impact of the

different data sources. The subsampled-Aquarius at in situ locations experiment is abbreviated as ASSIM_T_z_$SSS_{AQ@IS}$ (for Aquarius at in situ locations). Just like the other experiments, the assimilation results were used as initial conditions and the coupled experiments were run for 12 months for each month from August 2011 until February 2014. The results indicate that ASSIM_T_z_$SSS_{AQ@IS}$ is degraded with respect to the ASSIM_T_z_SSS_{AQ} experiment. For correlation, the ASSIM_T_z_$SSS_{AQ@IS}$ and ASSIM_T_z_SSS_{AQ} are indistinguishable until about 6 months (Figure 6.13a). After that time the Aquarius subsampled SSS product (ASSIM_T_z_$SSS_{AQ@IS}$) is significantly degraded for all lead times. The Steiger Z test indicates that the significance of the difference exceeds the 95% confidence limits (thick dashed red line on the top x-axis on Figure 6.13a). On the other hand, the subsampled Aquarius gridded product (ASSIM_T_z_$SSS_{AQ@IS}$) has a higher correlation than the in situ product (ASSIM_T_z_SSS_{IS}) after 6.5 month forecast lead time. Again the Steiger Z test indicates that ASSIM_T_z_$SSS_{AQ@IS}$ is higher than ASSIM_T_z_SSS_{IS} and the significance of the differences generally exceed 95% from 6.5 to 10 month lead times (thick blue line on top x-axis in Figure 6.13a). The RMS differences presented in Figure 6.13b reiterate the conclusion that the subsampled Aquarius product has forecast statistics that are degraded with respect to ASSIM_T_z_SSS_{AQ}, but still outperform the ASSIM_T_z_SSS_{IS}. Therefore, we conclude that both the spatial resolution afforded by satellite SSS and the quality of individual Aquarius observations is what makes initialization of Aquarius superior to the in situ product for coupled predictions. However we note that the degraded Aquarius product is still superior to the in situ results.

6.4 Summary of Impact of SSS

To summarize, adding SSS to T_z assimilation generally improves the forecast skill of coupled forecasts versus observed NINO3 SST anomalies. Correlation is improved when the in situ SSS product is assimilated (i.e. ASSIM_T_z_SSS_{IS}). In addition, when Aquarius SSS is assimilated into the initial conditions (ASSIM_T_z_SSS_{AQ}), both the correlation and RMS are improved with respect to the ASSIM_T_z experiments. When testing the relative improvement of SSS assimilation, satellite SSS outperforms in situ SSS for correlation with the significance of the differences exceeding 95% for months 6.5 to 10.5 and RMS is lower for all lead times after 5 months.

In general, SSS assimilation gives cool, upwelling in the central Pacific which manifests as an upwelling Rossby wave. This feature is consistent for both experiments that assimilate SSS and is present in the initial conditions for ASSIM_T_z_SSS_{IS} (Figure 6.5b, c) and for ASSIM_T_z_SSS_{AQ} (Figure 6.6b, c). For example, the relative upwelling (i.e. ASSIM_T_z_SSS_{AQ} – ASSIM_T_z) is strong and positive early in the mean forecast whereas ASSIM_T_z_SSS_{IS} – ASSIM_T_z is near zero at the base of the mixed layer. After month 2 lead times, the vertical velocity is positive (i.e. upwelling) for both SSS assimilation scenarios relative to ASSIM_T_z with Aquarius tending towards stronger upwelling than in situ SSS assimilation. As the forecast develops, this upwelling signal makes its way to the NINO3 region (Figure 6.8, Figure 6.9a-f) where it reduces the tendency for the HCM to forecast too-warm NINO3 SST anomalies. This tendency for warm NINO3 forecast is not only a problem for our ASSIM_T_z forecasts, but is also habitual for coupled models in general as is evident by the warm forecasts for the IRI

dynamic mean and the CFSv2 results in Figure 6.11 (solid, dashed green line, respectively).

The two SSS assimilation experiments differ in that the eastern Pacific is relatively warmer for ASSIM_T_z_SSS_{IS} than ASSIM_T_z_SSS_{AQ} (compare Figure 6.10a to c) at the forecast initialization. Thus the more intense SST gradient for ASSIM_T_z_SSS_{IS} from the dateline to the eastern boundary leads to stronger westerlies and a relative downwelling signal (compare Figure 6.10b to d). This downwelling signal offsets the upwelling in the central Pacific leading to a muted cooling for ASSIM_T_z_SSS_{IS} with respect to ASSIM_T_z_SSS_{AQ} for the NINO3 region (see Figure 6.10a and c). Another way to look at it is that ASSIM_T_z_SSS_{AQ} has a larger east to west SST gradient (see especially Figure 6.7c) leading to enhanced easterlies, enhanced Bjerknes coupling, and more intense NINO3 upwelling. Therefore, the mean forecast for ASSIM_T_z_SSS_{AQ} is closer to the observed conditions than ASSIM_T_z_SSS_{IS} due to this enhanced cooling in the eastern Pacific (Figure 6.11) counteracting the general tendency towards warm ASSIM_T_z NINO3 for this period.

So why it is that ASSIM_T_z_SSS_{AQ} has cooler SST in the NINO3 region and warmer SST in the far west than ASSIM_T_z_SSS_{IS}? As is shown in Figure 6.2c and Figure 6.7a, Aquarius SSS is saltier in the eastern Pacific and fresher in the far western Pacific. In the NINO3 region this relatively high SSS leads to a density increase and decreased buoyancy forcing. Vertical mixing is increased leading to increased entrainment of cold water from the bottom of the mixed layer resulting in decreased SST in the NINO3 region. In the west, the opposite is true. Relatively fresher SSS leads to increased stratification decreased mixing, and warmer SST when Aquarius SSS is

assimilated. The increased east to west SST gradient at the initialization of the forecasts leads to broadly enhanced easterlies for the forecast period and enhanced upwelling in the east.

Lastly, the relative impact of the spatial sampling versus the observation quality of Aquarius was tested against in situ observations by producing a subsampled version of the Aquarius data. These plots showed that the subsampled Aquarius outperformed the in situ results but was degraded with respect to the full Aquarius gridded product.

7 Summary and Conclusions

Variations in El Niño/Southern Oscillation (ENSO) impacts atmospheric and oceanic circulation across the globe (e.g. [*Ropelewski and Halpert,* 1987]) and so has widespread socioeconomic ramifications ([*Glantz,* 2001]). Therefore, it is a worthwhile goal to try to better understand the factors influencing ENSO predictability. In 2014 coupled forecasts called for a strong El Niño matching the unprecedentedly strong 1997 event. However, operational forecasts such as CFSv2 predicted ~2.5^{o}C for the NINO3.4 SST' for November from April 2014 but did not validate as an El Niño peaking only at 0.6^{o}C [*Zhu Jieshun et al.*, 2016]. [*McPhaden,* 2015] and [*Santoso et al.*, 2015] suggested that the fundamental reason for this suboptimal forecast was that air/sea coupling and precipitation did not follow the strong SST anomalies in the central Pacific as envisioned by [*Bjerknes,* 1969] and one factor that may have been important was that precipitation anomalies in the Pacific were anchored near the Maritime Continent due to the influence of the IO. Another factor that may impact this recent forecast is the inadequate validation of precipitation in operational coupled models. In particular , [*Wang et al.*, 2010] showed that CFSv2 was particularly poorly validated in the western Pacific and regions of large-scale atmospheric convergence. Therefore, we further explore how the IO may influence ENSO predictability and examine if sea surface salinity can provide surrogate information for less-than-ideal coupled model precipitation.

Although operational modeling groups now generally use global model configurations, the contribution of various ocean basins, particularly the IO, has yet to be fully explored. For example, the ITF is relatively poorly resolved in ocean models (e.g.

Hypothesis Tested	Technique	ENSO Validation	Impact on ENSO	Comments
Oceanic impact of IO improves ENSO predictions	IP_OPEN minus IP_NOITF	Weak positive impact (not significant) on ENSO correlation after 3 month lead times	IP_OPEN has improved variability for both NINO3 and NINO3.4 regions due to a shallower MLD for the IP_OPEN case	If the IP_NOITF bias is imposed on IP_OPEN initialization, the validation is significantly degraded
Atmospheric impact of IO improves ENSO predictions	Fully coupled for Indo-Pacific minus IO atmosphere decoupled from ocean	ENSO predictions are significantly improved 3-9 months with peak improvement at 7 month lead times	IO atmospheric coupling increases NINO3 mean after 3 months with peak at 7 month lead times	Off-equatorial large-scale downwelling curl in the Pacific leads to downwelling Kelvin wave warming entering NINO3 region with maximum warming for 7 month forecasts
Data assimilation in the IO improves ENSO predictions	Full assimilation of SL, SST, SSS, T_z, S_z in the Indo-Pacific minus assimilation only in Pacific	ENSO predictions are slightly improved (not significant) after 5 months	Significant cooling in NINO3 mean (cooling by as much as 0.2^oC)	Basin-scale warming in the IO leads to enhanced trades in the Pacific and La Niña-like Bjerknes coupling
Assimilating SSS improves ENSO predictions	Assimilate SSS minus without SSS assimilation	1) Assimilating any in situ or satellite SSS significantly improves ENSO skill after 5 months 2) satellite significantly outperforms in situ SSS	Including SSS impacts mixed layer density serving to enhance upwelling near the dateline, which propagates to the east, eventually cooling the NINO3 region offsetting the pervasive warming for this period	Satellite outperforms in situ SSS due to both Aquarius observation quality and improved satellite sampling

Table 7.1: Dissertation Summary: *Summary of all hypothesis components covered in this dissertation.*

GODAS with $1/3^{o}$ resolution and a single ITF passageway) as part of operational coupled model systems and so the impact of the oceanic contribution of the IO may be suboptimal. In addition, observations of the ITF are sparse (due to Argo grounding and mooring vandalism) and so the model ITF flow is poorly validated ([*Susanto and Song*, 2015]). In addition, constraining near-surface density using satellite SSS is still largely unexploited within operational coupled models. Therefore, the potential for in situ and Aquarius SSS to improve coupled forecasts is also assessed.

The IO impacts ENSO via an oceanic pathway through variability of the Indonesian Throughflow (ITF) as well as by forcing atmospheric teleconnections modulating the Walker circulation across the entire Indo-Pacific region. Rather than attempting to track the air/sea coupling and the impact of fresh water flux over the Indo-Pacific using model forecast precipitation (which is known to be suboptimal e.g. [*Wang et al.*, 2010]), we test the potential for improving ENSO forecasts by constraining near-surface density by specifying sea surface salinity (SSS) using data assimilation. The main results of the oceanic impact via the ITF, the atmospheric teleconnections of the IO, and the impact of data (including SSS) in the IO on ENSO hindcasts are summarized in Table 7.1

Previous work of [*Santoso et al.*, 2011] and [*Kajtar et al.*, 2015] comparing experiments with open ITF versus artificially closed ITF indicate that changes in ENSO variability are due to differing fetch of the Bjerknes coupling and the highest variability shifts eastward from NINO3.4 to NINO3 regions when closing the ITF. These results point out the potential of the ITF circulation to help improve ENSO predictions.

Following a similar methodology but in predictive mode, we find that the oceanic impact of the ITF is to slightly improve coupled forecast validation as validated by observations. Although this impact of the open ITF circulation is not significant for correlation validation, the strong model biases, with versus without the ITF circulation, help to explain that the ENSO forecast variability is significantly stronger for the ITF open case (as much as a 20% increase in the variability) and better matches the observed values. *When the ITF is open, warm and fresh water drains from the Pacific, shoaling the MLD, and amplifying the impact of wind stress on large-scale oceanic Kelvin and Rossby waves. Thus, we conclude that a shallower MLD in the IP_OPEN case is the cause of the improved variability* and not the extended fetch of Walker circulation.

Judging by the substantial impact of the ITF on ENSO variability, a major recommendation for the oceanographic community and operational centers would be to optimize technology to better observe the ITF. For example, incorporation of high resolution altimetry into ocean data assimilation procedures could be used to improve estimation of the flow of the ITF. The Surface Water & Ocean Topography (SWOT – expected to be launched in 2020) will provide cross-track, high resolution (120 km swath and roughly 10 km resolution) sea level. These observations will provide high enough resolution SL to estimate geostrophic currents within the Indonesian Seas providing observations to validate model simulations and data to improve data assimilation reconstructions of the ITF. Currently no such in situ data exist ([*Susanto and Song*, 2015]), so satellite observations such as these should be included in operational coupled data assimilation initialization (as they become available) to provide improved observational coverage of the ITF.

Another key potential source of improvement for ENSO predictions is the impact of atmospheric teleconnections originating from the IO. In order to isolate the impacts of atmospheric teleconnections from the IO to the Pacific, several previous researchers (e.g. [*Wu and Kirtman*, 2004]) contrasted experiments that allow coupling throughout the Indo-Pacific region with those that only allow coupling in the Pacific and decouple the IO by utilizing climatological SST forcing in the IO. However, they only go as far as to characterize ENSO in general terms and simplify the atmospheric impact using linear atmospheric models and idealized SST anomaly forcing patterns. They generally find that Pacific wind anomalies, generated by idealized IODZM SST anomaly patterns tend to cancel one another. For example, opposite sign SST anomaly in the western and eastern IO generate atmospheric Kelvin waves that tend to cancel one another. On the other hand, idealized basin-scale anomalies in the IO, force opposite sign wind anomalies in the Pacific. For example, negative SST in the IO generate prevailing westerlies between 20^{o}S to 20^{o}N in the Pacific (see e.g. [*Wu and Kirtman*, 2004] and Figure 1.6a, d). However, coupled experiments described herein that are initialized with the full observed SST forcing and utilize a nonlinear atmosphere indicate that this atmospheric response in the Pacific to interannual IO forcing has more details. Like earlier authors, we find that winds are weak westerly between 10^{o}S to the equator for the differences between coupled minus decoupled IO forced experiments. However, unlike preceding research, trade winds are enhanced off the equator and strong easterlies prevail between 30^{o}S to 15^{o}S and the equator to 25^{o}N. The differences between the previous linear atmospheric model and our AGCM (i.e. SPEEDY) results may be due to either simplification of IO forcing, displacement of precipitation (and heating) to the east with

no compensating anomaly, or most likely, the convective momentum transport in SPEEDY. These off-equatorial winds have profound impact in that they generate wind stress curl that act to amplify the oceanic Rossby wave signal which eventually impact the eastern Pacific by way of reflected Kelvin waves.

Differences between coupled experiments show that including the impact of interannual teleconnections from the IO have significantly higher ENSO correlation (exceeding the 95% significance level from 3-9 months) and lower RMS validation statistics. The reason for this is a combination of equatorial and off-equatorial coupling that eventually warms the NINO3 region. Early in the forecast period, prior to 3 month lead times, equatorial upwelling in the western Pacific weakly cools the NINO3 region via propagation of upwelling Kelvin waves. After that time, off-equatorial downwelling favorable curl in the western Pacific helps to amplify the transition from cooling to warming in the NINO3 region by way of reflected downwelling Rossby to downwelling Kelvin waves. Downwelling Kelvin waves, amplified by equatorial convergence, warm the eastern Pacific and improve correlation validation after 3 month lead times with respect to observations. The improvement in correlation peaks at 7 months which corresponds with the time it takes for the transmission of the reflected downwelling Rossby wave to reflect into the downwelling Kelvin wave then to propagate across the Pacific into the NINO3 region. *Therefore, a main conclusion from these results is that the interannual variability of IO SST forcing is responsible for overall somewhat lagged widespread downwelling in the Pacific, assisted by off-equatorial curl, leading to warmer NINO3 SST anomaly and improved validation after 3 month lead times.*

Currently ENSO forecast discussions (e.g. http://origin.cpc.ncep.noaa.gov/products/GODAS/ocean_briefing_gif/global_ocean_monitoring_current.ppt) include descriptions of large-scale ocean waves present in the initialization of coupled forecasts. However, these discussions only assess the state of the oceanic Kelvin wave (using the Ocean Kelvin Wave Index, an extended EOF technique) and this would suggest a lack of emphasis on off-equatorial processes in coupled model initialization. On the contrary, the results of the impact of the teleconnections from the IO to the Pacific (i.e. Section 4) presented herein demonstrate the important significance of the off-equatorial processes that generate oceanic Rossby waves. Therefore, we recommend that the impact of the Rossby waves on ENSO should be included in forecast discussions. We have shown that the impact of the IO atmospheric teleconnections to ENSO significantly improve coupled forecasts from 3-9 month lead times so these off-equatorial processes should be considered/included as an important ENSO forecast tool.

In addition to assessing the oceanic pathway and atmospheric teleconnections of the IO to ENSO, the impact of observations in the IO is tested for the first time. The main feature for the impact of all available satellite and in situ observations in the IO is the strong basin-scale warm SST anomaly in the subtropical southern IO at initialization. This SST anomaly forces an atmospheric Kelvin wave signal that enhances easterly winds of the Walker circulation in the Pacific especially west of the dateline. These easterly winds drive upwelling oceanic Kelvin waves that propagate to the east eventually serving to cool the NINO3 region. After 3 month forecasts, the IO SST anomaly dissipates. However, the east-to-west temperature gradient in the Pacific is enhanced due to upwelling and associated cool SST reaching the far eastern Pacific. At that same

time, off-equatorial downwelling curl serves to warm the western Pacific. When comparing the experiment that accounts for all available observations in the IO and the one that masks assimilation in the IO, the net result is that the validation statistics, correlation and RMS, are slightly (not significantly) improved. However, the mean forecast anomaly is dramatically reduced (by about 0.2^{o}C) and the full IO assimilation experiment is in better agreement with observed values. *Thus, more accurate attribution of the warming SST trend in the IO via data assimilation of all available observations leads to cooling the NINO3 region and slightly improved ENSO validation.*

Besides assessing ENSO predictability, a better understanding of the upstream influence of the Indian Ocean sector may also shed light on longer time-scale Indo-Pacific interactions. For example, [*Lee et al.*, 2015] used output of an ocean model (CESM1 - [*Danabasoglu et al.*, 2012]) and observations from the World Ocean Atlas 2013 ([*Locarnini et al.*, 2013]) to investigate the impacts of decadal change in the Pacific. The global ocean heat content for 0-700 m (OHC_{700}) from observations and the model has steadily increased over the last three decades ([*Lee et al.*, 2015]). Although the Pacific OHC_{700} rose steadily from 1983 until 2003, it actually decreased in the latest period from 2003-2012 corresponding to the multiple occurrences of La Niña. On the other hand, the IO OHC_{700} was steady and near zero prior to 2003 but it rose dramatically from 2003 until 2013. The ocean model budget analysis of OHC_{700} in the IO indicates that the primary driver of the warming was the horizontal advection term leading to the conclusion that ITF transported excess heat in the latest decade from the Pacific to the IO via the ITF. Our model (i.e. IP_OPEN) shows that ITF trend is -0.04 Sv/yr where negative values indicate an increase in the normal westward ITF flow. In addition,

observations of the ITF generally support the idea of increased ITF transport over time. The observed ITF from 2004-2006 of ~15 Sv ([*Sprintall et al.*, 2009]) was greater than that estimated to be 10.8 Sv ([*Vranes et al.*, 2002]) in 1997 (but the ITF is known to be weak during El Niño). In summary, [*Lee et al.*, 2015] show that the latest hiatus in Pacific warming is due to an increase in ITF flow transporting an increased amount of warm water from the Pacific and storing it in the top 700 m of the IO. This matched our results to the extent that the impact of the ITF was to cool the NINO3 region.

A better appreciation of the role that observations in the IO sector and inter-basin teleconnections play may also improve our understanding of decadal time-scale Indo-Pacific interactions. For example, [*Luo et al.*, 2012], found that the IO was warming faster than the Pacific from 1983-2013 (0.1^{o}C/decade versus 0.037^{o}C/decade, respectively) using NOAA SST [*Reynolds et al.*, 2002]. In addition, for 1993-2014 Pacific easterlies have intensified (i.e. Figure 3.7 trend = $-6\text{x}10^{-3}$ N/m^2/yr with 99.9% significance using a Monte-Carlo technique) over the tropical Pacific trending towards La Niña conditions with cooler SST in the NINO3 region (trend = -0.05^{o}C/yr). Thus, changes in the last decade (i.e. 2000-2009 anomaly with respect to 1983-2006) resemble La Niña with increased Walker circulation, increased thermocline slope, and enhanced upwelling in the eastern Pacific and cooler NINO3 SST [*Luo et al.*, 2012]. This paper used a similar methodology as our impact of observations experiments (they assimilated the observed SST trend into their coupled model for the IO between 20^{o}N-20^{o}S, and relaxed to climate conditions elsewhere) and found a similar result as Section 5, namely that adding the observed warming trends in the IO SST for 2000-2013 lead to enhanced easterlies in the western Pacific, and La Niña-like response. They also performed

experiments using prescribed SST trends in the IO varying from 0.025 to 0.1^{o}C/decade, representing a range of warming differences between the IO and Pacific. Again multi-decadal warming differences between the IO and the Pacific enhance the Walker circulation and produce a La Niña–like state. Our results from Section 5 and these results from [*Luo et al.*, 2012] confirm that the IO/eastern Pacific SST differences in the trends are the likely cause of the predominant La Niña state for the recent decade.

Recent theory has suggested the general circulation, including the Walker circulation, would weaken under a global warming scenario (e.g. [*Vecchi et al.*, 2006]). However, analysis of recent coupled climate models suggests that this is not the case. For example, [*Luo et al.*, 2012] examined 163 CMIP3 and CMIP5 with various greenhouse gas forcing and representative concentration pathways (RCP) scenarios. They found that Pacific warming was proportional to anthropogenic forcing but there was no clear relationship between anthropogenic forcing and Pacific trades. However, they found that there was a strong relationship between the temperatures in the eastern Pacific (200-280^{o}E, 20^{o}S-20^{o}N) minus the IO SST (40^{o}E-120^{o}E, 20^{o}S-20^{o}N) trends and the trend of the Pacific trades (150^{o}E-240^{o}E, 10^{o}S-10^{o}N). Therefore, under climate change scenarios, Pacific wind changes, the strength of the Walker circulation, and ENSO are related to the gradient of SST between the IO and the eastern Pacific rather than the global SST trends.

Besides the contribution of downstream influence of the IO, the improved characterization of mixed layer density via prescription of SSS plays an important role in ENSO predictability. In a series of coupled experiments, the impact of SSS is assessed for the Indo-Pacific region. Any SSS product, either in situ or Aquarius satellite,

significantly improves coupled forecasts with respect to a coupled experiment that lacks SSS assimilation. The mechanism that allows SSS to improve coupled forecasts is described in the following: SSS assimilation improves the near-surface density field. Relatively saltier/denser water straddling the equator in the central Pacific near the dateline results in enhanced mixing leading to cooler SST in the central Pacific. This cooler water first migrates west as an upwelling Rossby wave then reflects as an upwelling Kelvin wave propagating to the east. Once these Kelvin waves arrive in the NINO3 region, Bjerknes feedback takes hold leading to substantially cooler NINO3 SST anomalies. During this period, the IRI dynamic model mean, CFSv2 operational forecasts, and our forecast lacking the influence SSS (i.e. ASSIM_T_z) show a warming trend over the mean forecast (see Figure 6.11). Thus, *the beneficial impact of Aquarius SSS assimilation is to improve the mixed layer density, enhance mixing, and setting off upwelling that eventually cools the eastern Pacific after 6 months, counteracting the pervasive warming and improving ENSO validation.* Aquarius data are more efficient at improving the coupled forecasts than the OI of in situ SSS due to both the quality of the individual observations and the spatial and temporal resolution advantage of the satellite SSS.

In order to put these impacts of SSS assimilation into the perspective of global operational coupled models that typically do not include the impacts of SSS, our coupled experiments, with minus without Aquarius assimilation, are compared to the observational/CFSRR bias. Exploiting the CFSRR product as an example of an operational model is justified since it uses the same version of the coupled model, i.e.

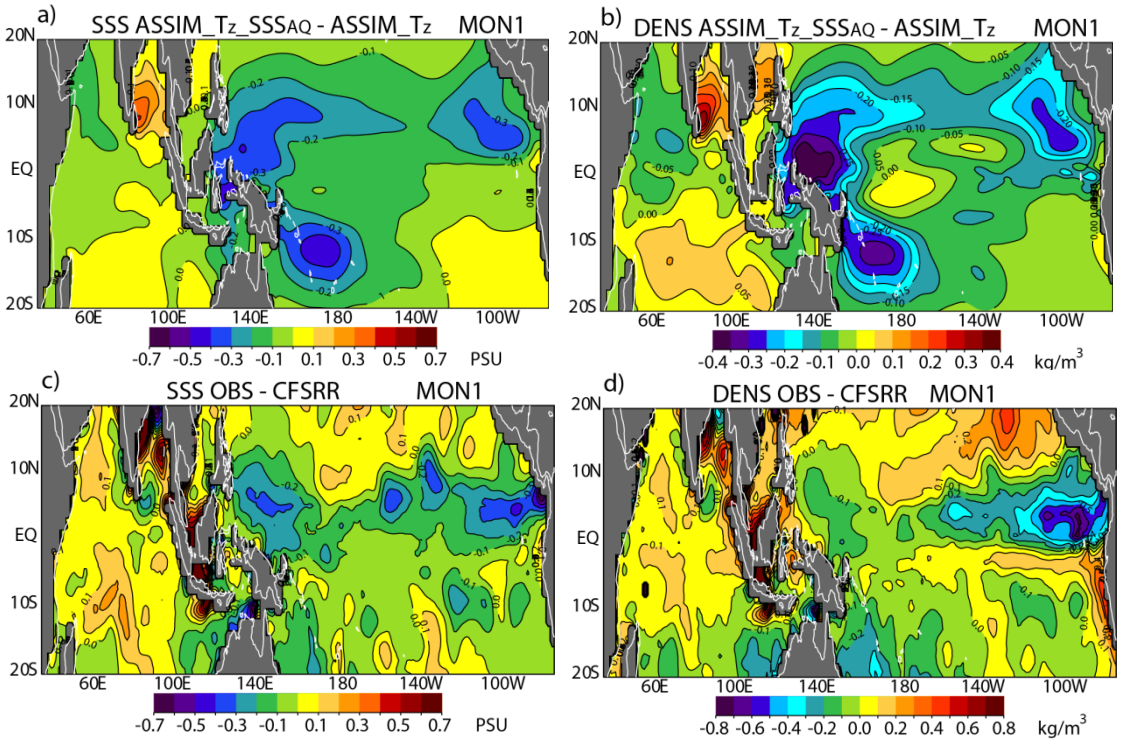

Figure 7.1: Impact of SSS and operational model biases. *Top panels show impact of including SSS in initialization for 1 month SPEEDY forecast differences, $ASSIM\_T_z\_SSS_{AQ} - ASSIM\_T_z$ for a) SSS and b) density in the mixed layer for Sep. 2011 – Oct. 2014. Bottom panels show the corresponding observational/CFSRR ([Saha et al., 2014]) model biases for Jan. 1993 – Mar. 2011. The mixed layer density observations are derived from the 10 m OI of salinity and temperature from all available in situ observations (see Section 2.1 for details). Also note that the color scale for d) is twice that of b).*

CFSv2 as the current operational setup at NCEP except the Reanalysis 2 state is used for initialization. (The CFSRR model is detailed in Section 2.2.4.)

Figure 7.1 shows the impacts of Aquarius assimilation for SSS and density (top) versus the observational bias of the CFSRR model (bottom). For ease of comparison, the operational coupled model bias plots are formulated such that the sign matches the sense of the coupled model difference plots for those with SSS (i.e. observations and $ASSIM\_T_z\_SSS_{AQ}$) minus those without SSS (i.e. CFSRR and $ASSIM\_T_z$). Although the observation/CFSRR biases are displaced somewhat southward and correspond to a

different period, our results from the top panels generally contain similar features as the operational model biases (bottom panels). For both, fresh SSS differences span most of the Pacific between the equator and 10^{o}N. In addition, both Figure 7.1a and Figure 7.1c have negative values over the southwest subtropical Pacific in the region of the SPCZ.

For density, the impact of SSS (Figure 7.1b) looks similar to the observational/CFSRR biases (Figure 7.1d) as well. For example, the negative zonal band under the ITCZ and SPCZ are common to both. Most importantly the key region with positive density differences near the dateline (roughly 160^{o}E-140^{o}W, 5^{o}S-5^{o}N) is evident in both figures. Recall that this positive density feature for the impact of Aquarius results (Figure 6.6b) is the driving impetus behind enhanced mixing and upwelling of cold water to the surface that eventually makes its way to the eastern Pacific and improves the coupled forecasts (as discussed in the previous Section 6.2). Also it is important to note that the CFSv2 forecast results have an unrealistic warming trend for the NINO3 region (i.e. green dashed line Figure 6.11). Since the CFSv2 model generally drifts towards too warm NINO3 SST anomalies, SSS assimilation cools the eastern Pacific, and our coupled model differences caused by SSS assimilation look similar enough to the observation/CFSRR biases, we are encouraged to believe that SSS assimilation will improve the CFSv2 ENSO forecasts. *Therefore a major prediction of this dissertation is that operational coupled models will benefit from imposing an improved fresh water flux by specifying SSS, constraining near-surface density, and cooling the NINO3 region, offsetting the pervasive and unrealistic warming of the operational CFSv2 model forecast.*

Finally, the purpose of this dissertation is to test the hypothesis that the upstream influence of the Indian Ocean, through the oceanic flow of the ITF, the atmospheric teleconnections forced from the IO to the Pacific, and observations in the IO, all play an important role in extending useful ENSO predictions. In addition, improving the fresh water flux estimation by assimilating sea surface salinity in the Indo-Pacific region improves the near-surface ocean quantities, such as density, leading to better ENSO predictions. Each principle of this hypothesis has been isolated by comparing coupled experiments with and without each particular feature and these results have been validated using correlation and RMS against NINO3 observations. For example, the impact SSS has been isolated by validating experiments with SSS assimilation versus

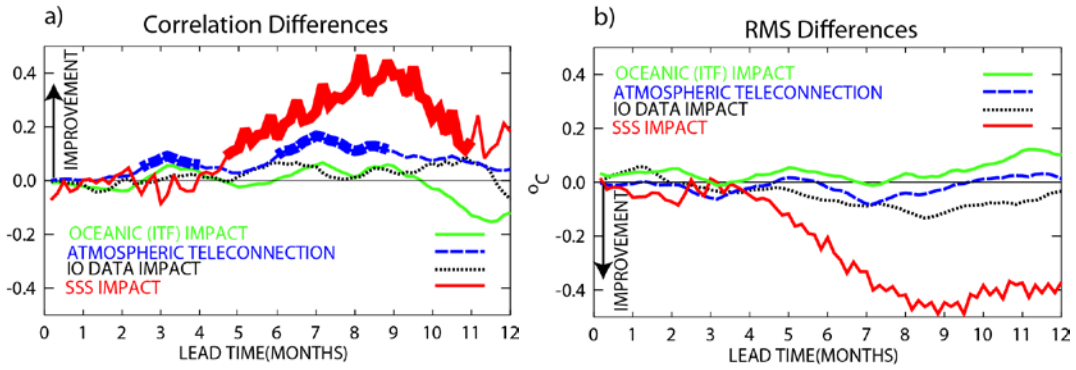

Figure 7.2: Summary of impacts of IO and satellite SSS assimilation. *This Figure shows differences for a) correlation and b) RMS NINO3 validation between the various experiments designed to isolate the IO oceanic impacts of the ITF (i.e. IP_OPEN – IP_NOITF – green for 1993-2014), the atmospheric teleconnection of the IO to ENSO (i.e. INT_PAC, INT_IO – INTPAC_CLIMIO – blue dash for 1993-2014), impact of assimilation in the IO (i.e. ASSIM_SL_SST_SSS_T_z_S_z - ASSIM_SL_SST_SSS_T_z_S_z_MASKIND – black dotted for 2002-2014) and impact of Aquarius SSS assimilation (i.e. ASSIM_ T_z _SSS_{AQ} – ASSIM_T_z – red line for Aug. 2011-Feb. 2014). For example, the green curve represents the differences, IP_OPEN minus IP_NOITF curves in Figure 3.8. For correlation, positive differences correspond to ENSO validation improvement. Especially thick sections denote differences which pass the 95% significance test using the Steiger Z technique. For b) RMS values below zero represents improvement brought about by the various impacts of the IO or SSS.*

those without SSS assimilation (i.e. in Figure 6.4). A convenient way to visualize and summarize all the impacts of the various principles is to simply difference the correlation that includes the impact of a particular component minus the correlation lacking it. Any correlation difference greater than zero would mean that particular component would improve ENSO forecasts. For example, the ASSIM_T_z_SSS_{AQ} – ASSIM_T_z correlation differences correspond to the red line in Figure 7.2. If this red line is above zero that would mean that ASSIM_T_z_SSS_{AQ} has higher correlation so the impact of SSS is to improve ENSO forecast predictability. In a similar way, any line below zero for the RMS differences would mean that particular component improves ENSO forecasts. Examination of Figure 7.2a and b shows that mostly all the components positively enhance ENSO predictability. In other words, mostly all the lines fall above for correlation and below the zero line for RMS. Although the various contributions of the IO generally account for ENSO predictability improvements, the biggest contributor is clearly the impact of specifying fresh water flux via salinity assimilation that significantly improves correlation by as much as r=0.4 and almost 0.5^{o}C for RMS at around 9 month forecast lead times. So in summary, *the hypothesis that the influence of the IO region and SSS improves coupled ENSO predictability has been affirmed.*

Global operational coupled models now include the impacts of the IO via both the oceanic pathway (with less than ideal ITF flow) and the atmospheric teleconnections (with realistically forced dynamical atmospheric models). Both these impacts along with the influence of assimilating oceanographic data in the IO have proven to improve coupled ENSO forecasts to varying degrees. Herein we detail to what extent the IO impacts ENSO forecasts. However, most operational coupled models have yet to

incorporate satellite SSS into their routine forecasts. We provide evidence that operational centers could benefit from assimilating sea surface salinity into their coupled models and the concomitant relative cooling due to improved density specification at initialization. The impact of assimilating SSS serves to counteract the warming tendency currently found in operational coupled models (as represented by CFSv2 results). In addition, initialization of coupled models "fixing" the fresh water flux via SSS assimilation would help to address known problems with precipitation in the e.g. CFSR coupled model. Therefore, a main prediction of this dissertation is that operational coupled models will benefit from including SSS assimilation into their routine initialization procedure.

7.1 Future Research Interests

The Tropical Ocean Global Atmosphere (TOGA) experiment led to a better understanding of the tropical Pacific and ENSO dynamics ([*McPhaden et al.*, 2010]). However, it is proving more and more challenging to sustain the tropical Indo-Pacific observing system. To address this issue, a workshop was held to evaluate the observing system requirements to continue to support ENSO modeling research and forecasting [*Anderson and Suga*, 2014]. The key conclusion of this meeting emphasized the overarching and persistent importance of long-term climate observations near the equator. The goals of this project, known as Tropical Pacific Observing System 2020 (TPOS 2020) are to "1) define the best observing system to monitor, observe and predict the state of ENSO and advance scientific understanding of its causes, 2) determine the most efficient method for sustained observations to support prediction systems, 3)

advance the knowledge of the predictability horizon of the tropical Pacific variability, and 4) determine interannual and multi-decadal variability" [*Anderson and Suga*, 2014]. However, it remains an open question which observing systems give the best return on investment for observing, monitoring and predicting ENSO. Although TPOS 2020 is focused only in the Pacific, we plan to provide comparable and complementary information for the IO. Therefore, we will evaluate how the observing system in the IO impacts ENSO monitoring and forecasting.

Observing system simulation experiments (OSSE) will be performed to isolate the impact of various components of the IO observing system on ENSO predictions. This work follows the same goals as the TPOS 2020, but we extend the evaluation of the observing systems to the IO to determine how each component of the system impacts ENSO monitoring, forecasting, and improving our understanding of fundamental ENSO mechanisms. For each data type – SL, SST, SSS from satellite and SSS, T_z and S_z from in situ (Argo and RAMA moorings), we will assess how these observations (combined together and individually) will impact ENSO predictions by utilizing salt/heat/eddy kinetic energy (EKE) budget analysis to determine the impact of heat/salt/momentum storage, advection, etc. in the mixed layer. Changes in the mixed layer and barrier layer formation will in turn impact buoyancy forcing and SST in the Indo-Pacific and we will determine how these changes impact ITF flow and air-sea coupling associated with ENSO.

Next we plan to examine the specific impact of salinity in the IO on coupled ENSO predictions. In the Pacific, previous work of [*Maes et al.*, 2005], [*Yang et al.*, 2010] and [*Hackert et al.*, 2011] all showed the importance of salinity and accounting for

heat storage in the BLT for ENSO predictions. In addition, [*Huang et al.*, 2008] and [*Seo et al.*, 2009] demonstrated the impact of salinity assimilation for constraining SST in the IO for monsoon prediction. However, no one has yet shown how improved salinity and BLT in the IO could impact ENSO predictions. In light of the significant impact of salinity assimilation for the Indo-Pacific region described herein, we will show how observation-constrained salinity in the IO will lead to improved ITF flow (via adjusted density and SL) and more accurate inter-basin atmospheric coupling (via improved SST). We will execute a series of forced and coupled experiment pairs that differentiate the impact of salinity assimilation in the IO. These pairs of experiments will also highlight how assimilation of salinity in the IO interacts with other satellite observations such as SL. (This future research has been recently funded by NASA Physical Oceanography Grant NNX16AH62G.)

Although the conceptual ENSO models of [*Jin*, 1997] and [*Schopf and Suarez*, 1988] provide a good reference, ENSO development is rarely so well behaved in nature. The often confusing juxtaposition of conflicting Kelvin and Rossby waves, heat storage, and triggering wind events make a definitive forecast often difficult. For example, in June 2014 the consensus forecast from IRI called for El Niño for December 2014 prompting NOAA to issue an El Niño watch. Subsurface conditions and heat storage rivaled the big ENSO event of 1997. However, in reality the 2014 event fizzled out. [*McPhaden*, 2015] suggested that the lack of coupling between the atmosphere and ocean was the main reason for this poor forecast and one possibility (besides the impact of the IO or SSS) for this prediction failure was negative feedbacks such as upwelling ocean (i.e. Rossby) waves may have damped warm ENSO sea surface temperature anomalies.

Thus, a future research goal is to focus on isolating the impact of the large-scale ocean/atmospheric coupled processes play in extending useful ENSO predictions through analysis of heat content and ocean waves.

[*Zhu Jieshun et al.*, 2016] tested the impact of off-equatorial SST anomalies in the operational CFSv2 – ([*Saha et al.*, 2014]) ENSO forecast system by substituting April initial conditions into the coupled model forecast in June of 2014. A particular problem of the CFSv2 is that in June 2014 the SST anomaly was too cool in the northwest Pacific due to too strong winds (their term is wind-evaporation-SST feedback) and too warm in the southeast Pacific due to a lack of stratus clouds. Their hypothesis was that known problems with the model stratus clouds and winds lead to erroneous SST anomalies and correcting such should lead to improved ENSO forecast. However, correcting the SST anomaly only improved the forecast by 40% so much of the forecast error remains unexplained. This result would imply that problems with the CFSv2 initialization are more than just related to SST. Thus, our hypothesis is that unaccounted-for heat content anomalies and large-scale ocean waves in the CFSv2 initialization impacts mixed layer processes and SST and contributes to the degraded 2014 ENSO forecast. Therefore, we plan to diagnose how well coupled systems account for large-scale ocean heat content and ocean waves using a combination of all available satellite and in situ observations, ocean models, data assimilation, coupled models, and CFSv2 ocean and coupled model results.

Differencing experiments with real initialization of the ocean state (through data assimilation) minus ocean experiments initialized with the climatological mean state isolates the impact of the ocean initial state on ENSO development. Next the statistical

atmospheric model (SAM) is applied to these differences (illustrating the passive response of the atmosphere) as well as applying an intermediate coupled model (i.e. SPEEDY, defining the active atmospheric response of the ocean initial conditions). Comparison of both the passive and active atmospheric response to the real (observed) atmospheric winds and precipitation during the ENSO event allows us to diagnosis to what degree initialization of the coupled system impacted the success of a particular ENSO forecast. In addition, analyzing the NOAA operational initialization and atmospheric model results (i.e. GODAS and CFSv2, respectively) in a similar manner puts these results into the context of real operational ENSO forecasts. The objective of this project is to diagnose potential issues in the initialization and forcing of retrospective ENSO forecasts using all other available ocean observations with the ultimate goal of improving operational coupled ENSO forecasts. (All the proposed research contained in the previous three paragraphs has been submitted to the NASA ROSES 2016 OSTST Solicitation.)

8 References

Adler, R. F., et al. (2003), The version-2 global precipitation climatology project (GPCP) monthly precipitation analysis (1979-present), *Journal of Hydrometeorology*, *4*(6), 1147-1167.

Alexander, M. A., I. Blade, M. Newman, J. R. Lanzante, N. C. Lau, and J. D. Scott (2002), The atmospheric bridge: The influence of ENSO teleconnections on air-sea interaction over the global oceans, *Journal of Climate*, *15*(16), 2205-2231.

Anderson, D., and T. Suga (2014), Volumn 1: Workshop Report and Recommendations, paper presented at Ocean Observations Panel for Climate - Tropical Pacific Observing System, 2020 Workshop (TPOS 2020), Scripps Institution of Oceanography, San Diego, Ca., USA.

Annamalai, H., S. Kida, and J. Hafner (2010), Potential Impact of the Tropical Indian Ocean-Indonesian Seas on El Nino Characteristics, *Journal of Climate*, *23*(14), 3933-3952.

Annamalai, H., S. P. Xie, J. P. McCreary, and R. Murtugudde (2005), Impact of Indian Ocean sea surface temperature on developing El Niño, *Journal of Climate*, *18*(2), 302-319.

Antonov, J. I., D. Seidov, T. P. Boyer, R. A. Locarnini, A. V. Mishonov, H. E. Garcia, O. K. Baranova, M. M. Zweng, and D. R. Johnson (2010), World Ocean Atlas 2009, Volume 2: Salinity., in *NOAA Atlas NESDIS 69*, edited by Secondary Antonov, J. I., D. Seidov, T. P. Boyer, R. A. Locarnini, A. V. Mishonov, H. E. Garcia, O. K. Baranova, M. M. Zweng, and D. R. Johnson, p. 184 pp., U.S. Government Printing Office, Washington, D.C.

Ballabrera-Poy, J., A. J. Busalacchi, and R. Murtugudde (2001), Application of a reduced-order Kalman filter to initialize a coupled atmosphere-ocean model: Impact on the prediction of El Niño, *Journal of Climate*, *14*(8), 1720-1737.

Ballabrera-Poy, J., R. Murtugudde, and A. J. Busalacchi (2002), On the potential impact of sea surface salinity observations on ENSO predictions, *Journal of Geophysical Research-Oceans*, *107*(C12), 10.1029/2001JC000834.

Balmaseda, M., and D. Anderson (2009), Impact of initialization strategies and observations on seasonal forecast skill, *Geophysical Research Letters*, *36*(1), 10.1175/2008MWR2668.1171.

Balmaseda, M., D. Anderson, and A. Vidard (2007), Impact of Argo on analyses of the global ocean, *Geophysical Research Letters*, *34*(16), 6.

Barnett, T. P., M. Latif, N. Graham, M. Flugel, S. Pazan, and W. White (1993), ENSO and ENSO-Related Predictability .1. Prediction of Equatorial Pacific Sea-Surface Temperature with a Hybrid Coupled Ocean-Atmosphere Model, *Journal of Climate*, *6*(8), 1545-1566.

Barnston, A. G., M. K. Tippett, M. L. L'Heureux, S. Li, and D. G. DeWitt (2012), Skill of Real-Time Seasonal ENSO Model Predictions during 2002–11: Is Our Capability Increasing?, *Bulletin of the American Meteorological Society*, *93*(5), 631-651.

Behringer, D. (2007), The Global Ocean Data Assimilation System (GODAS) at NCEP, paper presented at 11th Symp. on Integrated Observing and Assimilation Systems for Atmosphere, Oceans and Land Surface, American Meteorological Society San Antonio, TX [Available online at http://ams.confex.com/ams/pdfpapers/119541.pdf].

Bjerknes, J. (1969), Atmospheric Teleconnections from Equatorial Pacific, *Monthly Weather Review*, *97*(3), 163-&.
Bosc, C., T. Delcroix, and C. Maes (2009), Barrier layer variability in the western Pacific warm pool from 2000 to 2007, *Journal of Geophysical Research-Oceans*, *114*.
Boyer, T. P., et al. (2009), World Ocean Database 2009, paper presented at NOAA Atlas NESDIS 66, U.S. Government Printing Office, Washington, D.C.
Bracco, A., F. Kucharski, F. Molteni, W. Hazeleger, and C. Severijns (2005), Internal and forced modes of variability in the Indian Ocean, *Geophysical Research Letters*, *32*(12).
Busalacchi, A. J., M. J. McPhaden, and J. Picaut (1994), Variability in Equatorial Pacific Sea-Surface Topography During the Verification Phase of the Topex/Poseidon Mission, *Journal of Geophysical Research-Oceans*, *99*(C12), 24725-24738.
Cane, M. A., A. Kaplan, R. N. Miller, B. Y. Tang, E. C. Hackert, and A. J. Busalacchi (1996), Mapping tropical Pacific sea level: Data assimilation via a reduced state space Kalman filter, *Journal of Geophysical Research-Oceans*, *101*(C10), 22599-22617.
Carton, J. A., and E. C. Hackert (1989), Application of Multi-Variate Statistical Objective Analysis to the Circulation in the Tropical Atlantic-Ocean, *Dynamics of Atmospheres and Oceans*, *13*(3-4), 491-515.
Carton, J. A., G. Chepurin, X. H. Cao, and B. Giese (2000), A Simple Ocean Data Assimilation analysis of the global upper ocean 1950-95. Part I: Methodology, *Journal of Physical Oceanography*, *30*(2), 294-309.
Chen, D., A. J. Busalacchi, and L. M. Rothstein (1994a), The Roles of Vertical Mixing, Solar-Radiation, and Wind Stress in a Model Simulation of the Sea-Surface Temperature Seasonal Cycle in the Tropical Pacific-Ocean, *Journal of Geophysical Research-Oceans*, *99*(C10), 20345-20359.
Chen, D., L. M. Rothstein, and A. J. Busalacchi (1994b), A Hybrid Vertical Mixing Scheme and Its Application to Tropical Ocean Models, *Journal of Physical Oceanography*, *24*(10), 2156-2179.
Chen, D., C. M. Cane, S. E. Zebiak, R. Cañizares, and A. Kaplan (2000), Bias correction of an ocean-atmosphere coupled model, *Geophysical Research Letters*, *27*(16), 2585-2588.
Cronin, M. F., and M. J. McPhaden (2002), Barrier layer formation during westerly wind bursts, *Journal of Geophysical Research-Oceans*, *107*(C12).
Dai, A. G., and K. E. Trenberth (2002), Estimates of freshwater discharge from continents: Latitudinal and seasonal variations, *Journal of Hydrometeorology*, *3*(6), 660-687.
Danabasoglu, G., S. C. Bates, B. P. Briegleb, S. R. Jayne, M. Jochum, W. G. Large, S. Peacock, and S. G. Yeager (2012), The CCSM4 Ocean Component, *Journal of Climate*, *25*(5), 1361-1389.
Delcroix, T., and J. Picaut (1998), Zonal displacement of the western equatorial Pacific "fresh pool", *Journal of Geophysical Research-Oceans*, *103*(C1), 1087-1098.
Delcroix, T., and M. McPhaden (2002), Interannual sea surface salinity and temperature changes in the western Pacific warm pool during 1992-2000, *Journal of Geophysical Research-Oceans*, *107*(C12).
Delcroix, T., J. P. Boulanger, F. Masia, and C. Menkes (1994), Geosat-Derived Sea-Level and Surface Current Anomalies in the Equatorial Pacific During the 1986-1989

El-Niño and La-Niña, *Journal of Geophysical Research-Oceans*, *99*(C12), 25093-25107.
Dirmeyer, P. A. (2013), Characteristics of the water cycle and land–atmosphere interactions from a comprehensive reforecast and reanalysis data set: CFSv2, *Climate Dynamics*, *41*(3), 1083-1097.
Drosdowsky, W. (2006), Statistical prediction of ENSO (Nino 3) using sub-surface temperature data, *Geophysical Research Letters*, *33*(3), 10.1029/2005GL024866.
ECMWF (1994), The description of the ECMWF/WCRP Level III-A Global Atmospheric Data Archive, *Tech. Attach.Rep.*, 72 pp. pp, European Centre for Medium-Range Weather Forecasts, Reading, England, U.K.
England, M. H., and F. Huang (2005), On the interannual variability of the Indonesian Throughflow and its linkage with ENSO, *Journal of Climate*, *18*(9), 1435-1444.
Gent, P. R., and M. A. Cane (1989), A Reduced Gravity, Primitive Equation Model of the Upper Equatorial Ocean, *Journal of Computational Physics*, *81*(2), 444-480.
Gibson, J. K., P. Kallberg, S. Uppala, F. Hernandez, R. Nomura, and Y. Serrano (1997), ECMWF re-analysis. *Rep.*, European Centre for Medium-Range Weather Forecasts, Reading (UK).
Glantz, M. H. (2001), *Currents of Change: El Nino and La Nina Impacts on Climate and Society*, 252 pp., Cambridge University Press, Cambridge, UK.
Godfrey, J. S. (1989), A SVERDRUP MODEL OF THE DEPTH-INTEGRATED FLOW FOR THE WORLD OCEAN ALLOWING FOR ISLAND CIRCULATIONS, *Geophysical and Astrophysical Fluid Dynamics*, *45*(1-2), 89-112.
Gordon, A. L. (1986), INTER-OCEAN EXCHANGE OF THERMOCLINE WATER, *Journal of Geophysical Research-Oceans*, *91*(C4), 5037-5046.
Griffies, S. M., M. J. Harrison, R. C. Pacanowski, and A. Rosati (2004), Techical Guide to MOM4, in *GFDL Ocean Group Technical Report 5* edited by Secondary Griffies, S. M., M. J. Harrison, R. C. Pacanowski, and A. Rosati, p. 337, GFDL GFDL Princeton, NJ [Available online at www.gfdl.noaa.gov/~fms].
Hackert, E., A. Busalacchi, and J. Ballabrera-Poy (2014), Impact of Aquarius sea surface salinity observations on coupled forecasts for the tropical Indo-Pacific Ocean, *Journal of Geophysical Research, Oceans*, *119*(doi: 10.1002/2013JC009697).
Hackert, E., J. Ballabrera-Poy, A. J. Busalacchi, R. H. Zhang, and R. Murtugudde (2007), Comparison between 1997 and 2002 El Nino events: Role of initial state versus forcing, *Journal of Geophysical Research-Oceans*, *112*(C1).
Hackert, E., J. Ballabrera-Poy, A. Busalacchi, R. H. Zhang, and R. Murtugudde (2011), Impact of sea surface salinity assimilation on coupled forecasts in the tropical Pacific, *Journal of Geophysical Research-Oceans*, *116*(C05009), 10.1029/2010JC006708.
Hackert, E. C., A. J. Busalacchi, and R. Murtugudde (2001), A wind comparison study using an ocean general circulation model for the 1999-1998 El Niño, *Journal of Geophysical Research-Oceans*, *106*(C2), 2345-2362.
Hendon, H. H. (2003), Indonesian rainfall variability: Impacts of ENSO and local air-sea interaction, *Journal of Climate*, *16*(11), 1775-1790.
Henocq, C., J. Boutin, F. Petitcolin, G. Reverdin, S. Arnault, and P. Lattes (2010), Vertical Variability of Near-Surface Salinity in the Tropics: Consequences for L-Band Radiometer Calibration and Validation, *Journal of Atmospheric and Oceanic Technology*, *27*(1), 192-209.

Hirst, A. C., and J. S. Godfrey (1993), The Role of Indonesian Throughflow in a Global Ocean GCM, *Journal of Physical Oceanography*, *23*(6), 1057-1086.
Horel, J. D., and J. M. Wallace (1981), PLANETARY-SCALE ATMOSPHERIC PHENOMENA ASSOCIATED WITH THE SOUTHERN OSCILLATION, *Monthly Weather Review*, *109*(4), 813-829.
Huang, B. Y., Y. Xue, and D. W. Behringer (2008), Impacts of argo salinity in NCEP global ocean data assimilation system: The tropical Indian ocean, *Journal of Geophysical Research-Oceans*, *113*(C8), 10.1029/2007JC004388.
Huang, R. X. (1993), Real Fresh-Water Flux as a Natural Boundary-Condition for the Salinity Balance and Thermohaline Circulation Forced by Evaporation and Precipitation, *Journal of Physical Oceanography*, *23*(11), 2428-2446.
Izumo, T., M. Lengaigne, J. Vialard, J.-J. Luo, T. Yamagata, and G. Madec (2014), Influence of Indian Ocean Dipole and Pacific recharge on following year's El Nio: interdecadal robustness, *Climate Dynamics*, *42*(1-2), 291-310.
Ji, M., A. Leetmaa, and J. Derber (1995), An Ocean Analysis System for Seasonal to Interannual Climate Studies, *Monthly Weather Review*, *123*(2), 460-481.
Ji, M., R. W. Reynolds, and D. W. Behringer (2000), Use of TOPEX/Poseidon sea level data for ocean analyses and ENSO prediction: Some early results, *Journal of Climate*, *13*(1), 216-231.
Jin, E. K., et al. (2008), Current status of ENSO prediction skill in coupled ocean-atmosphere models, *Climate Dynamics*, *31*(6), 647-664.
Jin, F. F. (1997), An equatorial ocean recharge paradigm for ENSO. Part I: Conceptual model, *Journal of the Atmospheric Sciences*, *54*(7), 811-829.
Kajtar, J. B., A. Santoso, M. H. England, and W. Cai (2015), Indo-Pacific Climate Interactions in the Absence of an Indonesian Throughflow, *Journal of Climate*, *28*(13), 5017-5029.
Kalnay, E., et al. (1996), The NCEP/NCAR 40-year reanalysis project, *Bulletin of the American Meteorological Society*, *77*(3), 437-471.
Kessler, W. S., M. J. McPhaden, and K. M. Weickmann (1995), Forcing of Intraseasonal Kelvin Waves in the Equatorial Pacific, *Journal of Geophysical Research-Oceans*, *100*(C6), 10613-10631.
Kim, D., J. S. Kug, I. S. Kang, F. F. Jin, and A. T. Wittenberg (2008), Tropical Pacific impacts of convective momentum transport in the SNU coupled GCM, *Climate Dynamics*, *31*(2-3), 213-226.
Kraus, E. B., and J. S. Turner (1967), A One-Dimensional Model of Seasonal Thermocline .2. General Theory and Its Consequences, *Tellus*, *19*(1), 98-&.
Kroeger, J., and F. Kucharski (2011), Sensitivity of ENSO characteristics to a new interactive flux correction scheme in a coupled GCM, *Climate Dynamics*, *36*(1-2), 119-137.
Kucharski, F., F. Molteni, and J. H. Yoo (2006), SST forcing of decadal Indian Monsoon rainfall variability, *Geophysical Research Letters*, *33*(3).
Kucharski, F., I. S. Kang, R. Farneti, and L. Feudale (2011), Tropical Pacific response to 20th century Atlantic warming, *Geophysical Research Letters*, *38*.
Kucharski, F., F. Molteni, M. P. King, R. Farneti, I.-S. Kang, and L. Feudale (2013), On the Need of Intermediate Complexity General Circulation Models A "SPEEDY" Example, *Bulletin of the American Meteorological Society*, *94*(1), 25-30.

Kumar, A., M. Chen, and W. Wang (2010), An analysis of prediction skill of monthly mean climate variability, *Climate Dynamics*, *37*(5), 1119-1131.
Kummerow, C., et al. (2000), The status of the Tropical Rainfall Measuring Mission (TRMM) after two years in orbit, *Journal of Applied Meteorology*, *39*(12), 1965-1982.
Lagerloef, G., et al. (2013), Aquarius Salinity Validation Analysis; Data Version 2.0 (ftp://podaac-ftp.jpl.nasa.gov/allData/aquarius/docs/v2/AQ-014-PS-0016_AquariusSalinityDataValidationAnalysis_DatasetVersion2.0.pdf) *Rep.*, 36 pp, Jet Propulsion Lab, Pasdena, Ca. .
Lagerloef, G., et al. (2008), THE AQUARIUS/SAC-D MISSION: DESIGNED TO MEET THE SALINITY REMOTE-SENSING CHALLENGE, *Oceanography*, *21*(1), 68-81.
Lau, N. C., and M. J. Nath (2003), Atmosphere-ocean variations in the Indo-Pacific sector during ENSO episodes, *Journal of Climate*, *16*(1), 3-20.
Lee, S.-K., W. Park, M. O. Baringer, A. L. Gordon, B. Huber, and Y. Liu (2015), Pacific origin of the abrupt increase in Indian Ocean heat content during the warming hiatus, *Nature Geosci*, *advance online publication*.
Lilly, J. M., and G. Lagerloef (2008), Aquarius Level 3 processing algorithm theoretical basis document. Version 0.9. (ftp://podaac-ftp.jpl.nasa.gov/allData/aquarius/docs/v2/AquariusLevel3_GriddingSmoothingPaper_Lilly&Lagerloef2008.pdf)*Rep.*, 14 pp, Jet Propulsion Lab, Pasadena, CA.
Lima, C. H. R., U. Lall, T. Jebara, and A. G. Barnston (2009), Statistical Prediction of ENSO from Subsurface Sea Temperature Using a Nonlinear Dimensionality Reduction, *Journal of Climate*, *22*(17), 4501-4519.
Locarnini, R. A., A. V. Mishonov, J. I. Antonov, T. P. Boyer, H. E. Garcia, O. K. Baranova, M. M. Zweng, and D. R. Johnson (2010), World Ocean Atlas 2009, Volume 1: Temperature, NOAA Atlas NESDIS 68, edited by Secondary Locarnini, R. A., A. V. Mishonov, J. I. Antonov, T. P. Boyer, H. E. Garcia, O. K. Baranova, M. M. Zweng, and D. R. Johnson, p. 184 pp., U.S. Government Printing Office, Washington, D.C.
Locarnini, R. A., et al. (2013), *World Ocean Atlas 2013, Volume 1: Temperature*, , 43 pp., S. Levitus, Ed., A. Mishonov Technical Ed., NOAA Atlas NESDIS 73.
Lukas, R., and E. Lindstrom (1991), The Mixed Layer of the Western Equatorial Pacific-Ocean, *Journal of Geophysical Research-Oceans*, *96*, 3343-3357.
Luo, J.-J., W. Sasaki, and Y. Masumoto (2012), Indian Ocean warming modulates Pacific climate change, *Proceedings of the National Academy of Sciences of the United States of America*, *109*(46), 18701-18706.
Luo, Y. Y., L. M. Rothstein, R. H. Zhang, and A. J. Busalacchi (2005), On the connection between South Pacific subtropical spiciness anomalies and decadal equatorial variability in an ocean general circulation model, *Journal of Geophysical Research-Oceans*, *110*(C10), 10.1029/2004jc002655.
Maes, C., and S. Belamari (2011), On the Impact of Salinity Barrier Layer on the Pacific Ocean Mean State and ENSO, *Sola*, *7*, 97-100.
Maes, C., J. Picaut, and S. Belamari (2002), Salinity barrier layer and onset of El Niño in a Pacific coupled model, *Geophysical Research Letters*, *29*(24).
Maes, C., J. Picaut, and S. Belamari (2005), Importance of the salinity barrier layer for the buildup of El Niño, *Journal of Climate*, *18*(1), 104-118.

Maes, C., K. Ando, T. Delcroix, W. S. Kessler, M. J. McPhaden, and D. Roemmich (2006), Observed correlation of surface salinity, temperature and barrier layer at the eastern edge of the western Pacific warm pool, *Geophysical Research Letters*, *33*(6).
McPhaden, M. J. (2015), Playing hide and seek with El Nino, *Nature Clim. Change*, *5*(9), 791-795.
McPhaden, M. J., A. J. Busalacchi, and D. L. T. Anderson (2010), A TOGA RETROSPECTIVE, *Oceanography*, *23*(3), 86-103.
McPhaden, M. J., et al. (1998), The tropical ocean global atmosphere observing system: A decade of progress, *Journal of Geophysical Research-Oceans*, *103*(C7), 14169-14240.
Meyers, G. (1996), Variation of Indonesian Throughflow and the El Niño Southern Oscillation, *Journal of Geophysical Research-Oceans*, *101*(C5), 12255-12263.
Meyers, G., R. J. Bailey, and A. P. Worby (1995), Geostrophic Transport of Indonesian Throughflow, *Deep-Sea Research Part I-Oceanographic Research Papers*, *42*(7), 1163-1174.
Meyers, G., H. Phillips, N. Smith, and J. Sprintall (1991), Space and Time Scales for Optimal Interpolation of Temperature - Tropical Pacific-Ocean, *Progress in Oceanography*, *28*(3), 189-218.
Mignot, J., C. d. B. Montegut, A. Lazar, and S. Cravatte (2007), Control of salinity on the mixed layer depth in the world ocean: 2. Tropical areas, *Journal of Geophysical Research-Oceans*, *112*(C10).
Molteni, F. (2003), Atmospheric simulations using a GCM with simplified physical parametrizations. I: model climatology and variability in multi-decadal experiments, *Climate Dynamics*, *20*(2-3), 175-191.
Murtugudde, R., and A. J. Busalacchi (1998), Salinity effects in a tropical ocean model, *Journal of Geophysical Research-Oceans*, *103*(C2), 3283-3300.
Murtugudde, R., R. Seager, and A. Busalacchi (1996), Simulation of the tropical oceans with an ocean GCM coupled to an atmospheric mixed-layer model, *Journal of Climate*, *9*(8), 1795-1815.
Murtugudde, R., A. J. Busalacchi, and J. Beauchamp (1998), Seasonal-to-interannual effects of the Indonesian Throughflow on the tropical Indo-Pacific Basin, *Journal of Geophysical Research-Oceans*, *103*(C10), 21425-21441.
National Academies of Sciences, E., and Medicine (2016), *Next Generation Earth System Prediction: Strategies for Subseasonal to Seasonal Forecasts*, 290 pp., The National Academies Press, Washington, DC.
National Research Council (2010), *Assessment of intraseasonal to interannual climate prediction and predictability*, National Academies Press, Washington, D.C. :.
NODC (2006), NODC Operational Oceanographic Data Group: Global Temperature Salinity Profile Program, February 2006*Rep.*, U.S. Department of Commerce, National Oceanic and Atmospheric Administration, National Oceanographic Data Center, Silver Spring, MD 20910.
Oberhuber, J. (1988), An Atlas based on the COADS data set: The budgets of heat, buoyancy and turbulent kinetic energy at the surface of the global ocean, in *Rep 15*, edited by Secondary Oberhuber, J., Max-Plank-Institut fur Meteorologie, Hamburg.

Oke, P. R., M. A. Balmaseda, M. Benkiran, J. A. Cummings, E. Dombrowsky, Y. Fujii, S. Guinehut, G. Larnicol, P. Y. Le Traon, and M. J. Martin (2009), OBSERVING SYSTEM EVALUATIONS USING GODAE SYSTEMS, *Oceanography*, *22*(3), 144-153.

Picaut, J., M. Ioualalen, C. Menkes, T. Delcroix, and M. J. McPhaden (1996), Mechanism of the zonal displacements of the Pacific warm pool: Implications for ENSO, *Science*, *274*(5292), 1486-1489.

Potemra, J. (2005), Indonesian Throughflow Transport variability estimated from satellite altimetry, *Oceanography*, *18*(4), 98-107.

Potemra, J. T., M. E. Luther, and J. J. Obrien (1991), THE SEASONAL CIRCULATION OF THE UPPER OCEAN IN THE BAY OF BENGAL, *Journal of Geophysical Research-Oceans*, *96*(C7), 12667-12683.

Price, J. F., R. A. Weller, and R. Pinkel (1986), Diurnal Cycling - Observations and Models of the Upper Ocean Response to Diurnal Heating, Cooling, and Wind Mixing, *Journal of Geophysical Research-Oceans*, *91*(C7), 8411-8427.

Quenouille, M. H. (1952), *Associated measurements*, 242 pp., Buterworths, London.

Rayner, N. A., D. E. Parker, E. B. Horton, C. K. Folland, L. V. Alexander, D. P. Rowell, E. C. Kent, and A. Kaplan (2003), Global analyses of sea surface temperature, sea ice, and night marine air temperature since the late nineteenth century, *Journal of Geophysical Research-Atmospheres*, *108*(D14).

Reid, J. L. (2003), On the total geostrophic circulation of the Indian Ocean: flow patterns, tracers, and transports, *Progress in Oceanography*, *56*(1), 137-186.

Reynolds, R. W., N. A. Rayner, T. M. Smith, D. C. Stokes, and W. Q. Wang (2002), An improved in situ and satellite SST analysis for climate, *Journal of Climate*, *15*(13), 1609-1625.

Rodgers, K. B., M. A. Cane, N. H. Naik, and D. P. Schrag (1999), The role of the Indonesian Throughflow in equatorial Pacific thermocline ventilation, *Journal of Geophysical Research-Oceans*, *104*(C9), 20551-20570.

Roeckner, E., et al. (1996), The atmospheric general circulation model ECHAM-4: Model description and simulation of present-day climate, *Technical Report 218, Max-Planck Institute for Meteorology, Hamburg, Germany, 90 pp.*

Ropelewski, C. F., and M. S. Halpert (1987), Global and Regional Scale Precipitation Patterns Associated with the El-Niño Southern Oscillation, *Monthly Weather Review*, *115*(8), 1606-1626.

Rossow, W. B., and R. A. Schiffer (1991), Isccp Cloud Data Products, *Bulletin of the American Meteorological Society*, *72*(1), 2-20.

Rothstein, L. M., R. H. Zhang, A. J. Busalacchi, and D. Chen (1998), A numerical simulation of the mean water pathways in the subtropical and tropical Pacific Ocean, *Journal of Physical Oceanography*, *28*(2), 322-343.

Ruiz, J. E., I. Cordery, and A. Sharma (2005), Integrating ocean subsurface temperatures in statistical ENSO forecasts, *Journal of Climate*, *18*(17), 3571-3586.

Saha, S., et al. (2014), The NCEP Climate Forecast System Version 2, *Journal of Climate*, *27*(6), 2185-2208.

Saha, S., et al. (2010), THE NCEP CLIMATE FORECAST SYSTEM REANALYSIS, *Bulletin of the American Meteorological Society*, *91*(8), 1015-1057.

Saji, N. H., B. N. Goswami, P. N. Vinayachandran, and T. Yamagata (1999), A dipole mode in the tropical Indian Ocean, *Nature*, *401*(6751), 360-363.
Santoso, A., W. Cai, M. H. England, and S. J. Phipps (2011), The Role of the Indonesian Throughflow on ENSO Dynamics in a Coupled Climate Model, *Journal of Climate*, *24*(3), 585-601.
Santoso, A., W. Cai, M. Collins, M. McPhaden, and F.-F. Jin (2015), ENSO EXTREMES AND DIVERSITY Dynamics, Teleconnections, and Impacts, *Bulletin of the American Meteorological Society*, *96*(11), 1969-1972.
Schiller, A., S. E. Wijffels, J. Sprintall, R. Molcard, and P. R. Oke (2010), Pathways of intraseasonal variability in the Indonesian Throughflow region, *Dynamics of Atmospheres and Oceans*, *50*(2), 174-200.
Schneider, N. (1998), The Indonesian Throughflow and the global climate system, *Journal of Climate*, *11*(4), 676-689.
Schopf, P. S., and M. J. Suarez (1988), Vacillations in a Coupled Ocean Atmosphere Model, *Journal of the Atmospheric Sciences*, *45*(3), 549-566.
Seo, H., S.-P. Xie, R. Murtugudde, M. Jochum, and A. J. Miller (2009), Seasonal Effects of Indian Ocean Freshwater Forcing in a Regional Coupled Model, *Journal of Climate*, *22*(24), 6577-6596.
Shi, G., J. Ribbe, W. Cai, and T. Cowan (2007), Multidecadal variability in the transmission of ENSO signals to the Indian Ocean, *Geophysical Research Letters*, *34*(9).
Smith, T. M., R. W. Reynolds, T. C. Peterson, and J. Lawrimore (2008), Improvements to NOAA's historical merged land-ocean surface temperature analysis (1880-2006), *Journal of Climate*, *21*(10), 2283-2296.
Song, Q., A. L. Gordon, and M. Visbeck (2004), Spreading of the Indonesian Throughflow in the Indian Ocean, *Journal of Physical Oceanography*, *34*(4), 772-792.
Song, Q., G. A. Vecchi, and A. J. Rosati (2007), The role of the Indonesian Throughflow in the Indo-Pacific climate variability in the GFDL Coupled Climate Model, *Journal of Climate*, *20*(11), 2434-2451.
Sprintall, J., and M. Tomczak (1992), EVIDENCE OF THE BARRIER LAYER IN THE SURFACE-LAYER OF THE TROPICS, *Journal of Geophysical Research-Oceans*, *97*(C5), 7305-7316.
Sprintall, J., S. E. Wijffels, R. Molcard, and I. Jaya (2009), Direct estimates of the Indonesian Throughflow entering the Indian Ocean: 2004-2006, *Journal of Geophysical Research-Oceans*, *114*, 19.
Steiger, J. H. (1980), TESTS FOR COMPARING ELEMENTS OF A CORRELATION MATRIX, *Psychological Bulletin*, *87*(2), 245-251.
Susanto, R. D., and Y. T. Song (2015), Indonesian throughflow proxy from satellite altimeters and gravimeters, *Journal of Geophysical Research: Oceans*, *120*(4), 2844-2855.
Syu, H. H., J. D. Neelin, and D. Gutzler (1995), Seasonal and Interannual Variability in a Hybrid Coupled GCM, *Journal of Climate*, *8*(9), 2121-2143.
Talley, L. D. (2008), Freshwater transport estimates and the global overturning circulation: Shallow, deep and throughflow components, *Progress in Oceanography*, *78*(4), 257-303.

Tozuka, T., J.-J. Luo, S. Masson, and T. Yamagata (2007), Decadal modulations of the Indian Ocean dipole in the SINTEX-F1 coupled GCM, *Journal of Climate*, *20*(13), 2881-2894.
Trenberth, K. E. (1984), Signal Versus Noise in the Southern Oscillation, *Monthly Weather Review*, *112*(2), 326-332.
Uehara, H., A. A. Kruts, H. Mitsudera, T. Nakamura, Y. N. Volkov, and M. Wakatsuchi (2014), Remotely propagating salinity anomaly varies the source of North Pacific ventilation, *Progress in Oceanography*, *126*, 80-97.
Uppala, S. M., et al. (2005), The ERA-40 Reanalysis, *Quarterly Journal of the Royal Meteorological Society*, *131*(612), 2961-3012.
Vecchi, G. A., B. J. Soden, A. T. Wittenberg, I. M. Held, A. Leetmaa, and M. J. Harrison (2006), Weakening of tropical Pacific atmospheric circulation due to anthropogenic forcing, *Nature*, *441*(7089), 73-76.
Verron, J., L. Gourdeau, D. T. Pham, R. Murtugudde, and A. J. Busalacchi (1999), An extended Kalman filter to assimilate satellite altimeter data into a nonlinear numerical model of the tropical Pacific Ocean: Method and validation, *Journal of Geophysical Research-Oceans*, *104*(C3), 5441-5458.
Vintzileos, A., M. Rienecker, M. Suarez, S. K. Miller, P. J. Pegion, and J. T. Bacmeister (2003), Simulation of the El Nino-Southern Oscillation phenomenon with NASA's Seasonal-to-Interannual Prediction Project coupled general circulation model. , *Clivar Exchanges No. 28*, *8*(4), 25-27.
Vranes, K., A. L. Gordon, and A. Ffield (2002), The heat transport of the Indonesian Throughflow and implications for the Indian Ocean heat budget, *Deep-Sea Research Part II-Topical Studies in Oceanography*, *49*(7-8), 1391-1410.
Wajsowicz, R. C., and E. K. Schneider (2001), The Indonesian throughflow's effect on global climate determined from the COLA coupled climate system, *Journal of Climate*, *14*(13), 3029-3042.
Wang, W., M. Chen, and A. Kumar (2010), An Assessment of the CFS Real-Time Seasonal Forecasts, *Weather and Forecasting*, *25*(3), 950-969.
Watanabe, M., and F. F. Jin (2003), A moist linear baroclinic model: Coupled dynamical-convective response to El Nino, *Journal of Climate*, *16*(8), 1121-1139.
Webster, P. J., A. M. Moore, J. P. Loschnigg, and R. R. Leben (1999), Coupled ocean-atmosphere dynamics in the Indian Ocean during 1997-98, *Nature*, *401*(6751), 356-360.
Wijffels, S. E., G. Meyers, and J. S. Godfrey (2008), A 20-yr average of the Indonesian throughflow: Regional currents and the interbasin exchange, *Journal of Physical Oceanography*, *38*(9), 1965-1978.
Wu, R. G., and B. P. Kirtman (2004), Understanding the impacts of the Indian Ocean on ENSO variability in a coupled GCM, *Journal of Climate*, *17*(20), 4019-4031.
Wyrtki, K. (1987), Indonesian through-Flow and the Associated Pressure-Gradient, *Journal of Geophysical Research-Oceans*, *92*(C12), 12941-12946.
Xie, P. P., and P. A. Arkin (1997), Global precipitation: A 17-year monthly analysis based on gauge observations, satellite estimates, and numerical model outputs, *Bulletin of the American Meteorological Society*, *78*(11), 2539-2558.
Xie, P. P., and P. A. Arkin (1998), Global monthly precipitation estimates from satellite-observed outgoing longwave radiation, *Journal of Climate*, *11*(2), 137-164.

Yang, S. C., M. Rienecker, and C. Keppenne (2010), The Impact of Ocean Data Assimilation on Seasonal-to-Interannual Forecasts: A Case Study of the 2006 El Nino Event, *Journal of Climate*, *23*(15), 4080-4095.
Yu, J. Y., C. R. Mechoso, J. C. McWilliams, and A. Arakawa (2002), Impacts of the Indian Ocean on the ENSO cycle, *Geophysical Research Letters*, *29*(8).
Yuan, D., H. Zhou, and X. Zhao (2013), Interannual Climate Variability over the Tropical Pacific Ocean Induced by the Indian Ocean Dipole through the Indonesian Throughflow, *Journal of Climate*, *26*(9), 2845-2861.
Yuan, D., J. Wang, T. Xu, P. Xu, Z. Hui, X. Zhao, Y. Luan, W. Zheng, and Y. Yu (2011), Forcing of the Indian Ocean Dipole on the Interannual Variations of the Tropical Pacific Ocean: Roles of the Indonesian Throughflow, *Journal of Climate*, *24*(14), 3593-3608.
Yueh, S. H., R. West, W. J. Wilson, F. K. Li, E. G. Njoku, and Y. Rahmat-Samii (2001), Error sources and feasibility for microwave remote sensing of ocean surface salinity, *Ieee Transactions on Geoscience and Remote Sensing*, *39*(5), 1049-1060.
Zhang, R. H., and S. Levitus (1997), Interannual variability of the coupled tropical Pacific Ocean-atmosphere system associated with the El Niño Southern Oscillation, *Journal of Climate*, *10*(6), 1312-1330.
Zhang, R. H., and A. J. Busalacchi (2008), Rectified effects of tropical instability wave (TIW)-induced atmospheric wind feedback in the tropical Pacific, *Geophysical Research Letters*, *35*(5), 10.1029/2007gl033028.
Zhang, R. H., and A. J. Busalacchi (2009), Freshwater Flux (FWF)-Induced Oceanic Feedback in a Hybrid Coupled Model of the Tropical Pacific, *Journal of Climate*, *22*(4), 853-879.
Zhang, R. H., A. J. Busalacchi, and R. G. Murtugudde (2006), Improving SST anomaly simulations in a layer ocean model with an embedded entrainment temperature submodel, *Journal of Climate*, *19*(18), 4638-4663.
Zhou, L., and R. Murtugudde (2010), Influences of Madden-Julian Oscillations on the eastern Indian Ocean and the maritime continent, *Dynamics of Atmospheres and Oceans*, *50*(2), 257-274.
Zhou, L., R. B. Neale, M. Jochum, and R. Murtugudde (2012), Improved Madden-Julian Oscillations with Improved Physics: The Impact of Modified Convection Parameterizations, *Journal of Climate*, *25*(4), 1116-1136.
Zhou, X. B., Y. M. Tang, and Z. W. Deng (2009), Assimilation of historical SST data for long-term ENSO retrospective forecasts, *Ocean Modelling*, *30*(2-3), 143-154.
Zhu Jieshun, J., A. Kumar, B. Huang, M. A. Balmaseda, and Z.-Z. Hu (2016), The role of off-equatorial surface temperature anomalies in the 2014 El Niño prediction, *Scientific Reports*, *6*.